

Die approbierte Originalversion dieser
Dissertation ist in der Hauptbibliothek der
Technischen Universität Wien aufgestellt und
zugänglich.
<http://www.ub.tuwien.ac.at>

Diese Dissertation haben begutachtet:



The approved original version of this thesis is
available at the main library of the Vienna
University of Technology.

<http://www.ub.tuwien.ac.at/eng>



TECHNISCHE
UNIVERSITÄT
WIEN

Vienna University of Technology

DISSERTATION

Correlation between 3D microstructure and thermo-mechanical behavior of near eutectic piston alloys

ausgeführt zum Zwecke der Erlangung des akademischen Grades eines Doktors der
technischen Wissenschaften unter der Leitung von

Assoc. Prof. Dipl.Ing. Dr.techn. Guillermo Carlos Requena

E308 Institut für Werkstoffwissenschaft und Werkstofftechnologie

eingereicht an der Technischen Universität Wien,

Fakultät für Maschinenwesen und Betriebswissenschaften

von

Dipl.Ing. Robert Koos

Matrikelnummer: 0025990

Missindorfstrasse 4/6

1140 Wien

Wien, am 12.November 2014

Contents

Acknowledgements	5
Kurzfassung	6
Abstract	8
1. State of the art	9
1.1. Al-Si alloys	9
1.1.1. Eutectic silicon network in Al-Si alloys after solidification	10
1.1.2. Spheroidization of eutectic and primary silicon	12
1.1.3. Aluminides in Al-Si piston alloys	13
1.1.4. Precipitation strengthening in Al-Si piston alloys	15
1.2. Mechanical properties of Al-Si piston alloys	17
1.3. Tomography	24
1.3.1. Serial sectioning tomography	24
1.3.2. X-ray tomography	25
1.3.2.1. Synchrotron tomography	26
1.4. Hypothesis	29
2. Experimental	30
2.1. Materials	30
2.2. Heat treatment	31
2.3. Experimental methods	31
2.3.1. Determination of the region of trust	31
2.3.2. Cooling of the piston after solution treatment	32
2.3.3. Metallography	32
2.3.4. Light optical microscopy	33
2.3.5. Scanning electron microscopy	33
2.3.6. Light optical tomography	33
2.3.6.1. Mechanical serial sectioning	34
2.3.6.2. Ion milling serial sectioning	35
2.3.7. Synchrotron tomography	37
2.3.7.1. Reconstruction, segmentation and image processing	37
2.3.7.2. Morphological analysis	40
2.3.8. Hardness tests	41

2.3.9.	Nanohardness of matrix	41
2.3.10.	Thermo-mechanical tests.....	42
2.3.10.1.	Compression tests	42
2.3.10.2.	Tensile tests.....	42
2.3.10.3.	Coefficient of thermal expansion	43
2.3.10.4.	Young's modulus	44
2.3.10.5.	Thermo-mechanical fatigue	44
3.	Results.....	47
3.1.	Cooling of the pistons after solution treatment.....	47
3.2.	Region of trust	47
3.3.	Light optical microscopy.....	49
3.3.1.	Effect of solution treatment time.....	49
3.4.	SEM.....	55
3.4.1.	Effect of solution treatment time	55
3.4.2.	Effect of ageing time at 300°C	57
3.4.3.	Element mapping.....	58
3.5.	Light optical tomography	67
3.5.1.	Mechanical serial sectioning	67
3.5.2.	Ion milling serial sectioning.....	69
3.6.	Synchrotron X-ray micro-computed tomography (S μ CT)	70
3.6.1.	Volume fraction, interconnectivity and Euler number of aluminides	70
3.6.2.	Euler number of eutectic and primary silicon	74
3.6.3.	Morphology of aluminides	76
3.6.3.1.	Morphology of Silicon.....	91
3.7.	Hardness evolution during ageing	100
3.8.	Hardness of matrix.....	103
3.9.	Thermo-mechanical tests	103
3.9.1.	Compression tests	103
3.9.2.	Tensile tests.....	106
3.9.3.	Thermo-mechanical fatigue	112
3.9.3.1.	Coefficient of thermal expansion and dynamic mechanical analysis ..	112
3.9.3.2.	Thermo-mechanic fatigue.....	114
3.9.3.2.1.	$\Delta T=50-300^{\circ}\text{C}$, $\sigma=50\text{MPa}$	114
3.9.3.2.2.	$\Delta T=50-380^{\circ}\text{C}$, $\sigma=35\text{MPa}$	121

4. Discussion of results.....	129
4.1. Evolution of the microstructure during solution treatment	129
4.1.1. Qualitative changes of the rigid networks	129
4.1.2. Changes in the network of aluminides.....	130
4.1.3. Changes in the network of eutectic and primary silicon.....	132
4.1.4. Changes in the hybrid network formed by silicon and aluminides	134
4.2. Thermo-mechanical properties correlated with internal architecture	137
5. Conclusions	140
5.1. Experimental imaging methods	140
5.2. Evolution of the microstructure during solution treatment	140
5.3. Correlation of thermo-mechanical properties with internal architecture	143
6. References.....	145

Acknowledgements

First and foremost I would like to express my gratitude to Prof. Guillermo Requena for his guidance, support and invaluable input which made this doctoral thesis possible. His inspiring enthusiasm for work and scientific research ignited the needed driving force to overcome every obstacle presenting itself during the preparation of this thesis.

I am in debt to Prof. Frank Mücklich for accepting to be one of the examiners of this work.

I thank Elodie Boller and Alexander Rack both from the ID19 beamline of the ESRF, for their contributions to the tomographic measurements, preprocessing and reconstructions.

I would like to thank Prof. Hans-Peter Degischer for his interest and helpful advices during my work.

The group of structural metallic materials and composites: Ricardo, my wingman at nearly every synchrotron nightshift, Martin, Pere, David, Simon and our departed colleagues Cecilia, Domonkos, Marta, Warcho and Zahid I would like to thank all for creating a great working environment and for their fruitful discussions.

The technical solutions that were worked out for this thesis would not have been possible without the aid of Christian and Edith. Thank You!

I would like to thankfully point out the help of Thomas Koch with the nano hardness tests.

The support of the colleagues at the institute of Material science and Technology is deeply appreciated.

I gratefully acknowledge the financial support of the FWF project P-22876-N22, the K-project ZPT within the COMET and the company Kolbenschmidt for the provision of the investigated alloys.

Finally, I would like to thank my entire family for their unconditional support throughout all these years.

Kurzfassung

Die dreidimensionale (3D) Mikrostruktur der nah-eutektischen AlSi10Cu6Ni2Mg, AlSi12Cu5Ni2Mg, AlSi12Cu5Ni3Mg, AlSi12Cu5Ni2 Legierungen sowie einer hypereutektischen AlSi17Cu4Mg Legierung wurden als Funktion der Lösungsglühzeit bei einer Temperatur von 500°C mittels Synchrotron Mikrotomographie unter der Verwendung von Absorption- und Phasenkontrast-Imaging untersucht.

Diese Legierungen werden durch eutektisches und primäres Si sowie von Aluminiden in einer aushärtbaren α -Al Matrix gebildet. Die rigiden Phasen (Si und Aluminide) bilden im Gusszustand mit einem Gehalt von ~25vol% ein dicht verbundenes lasttragendes Netzwerk, das zur Festigkeit der Legierungen beiträgt. Diese 3D Mikrostruktur wurde zusätzlich mit einer neu entwickelten Sektionierungsmethode, die mittels Ionenmühle kleine Abtragsraten während dieses Sektionierungsprozesses ermöglicht, durchgeführt. Die Entwicklung der Volumengehalte, Interkonnektivität, Kontiguität und Morphologie der Phasen wurde mittels Tomographie an denselben Proben nach 0h, 1h und 4h Lösungsglühzeit quantifiziert. Die hypereutektische AlSi17Cu4Mg Legierung zeigt eine Verringerung des Volumengehaltes der Aluminide von ~6vol% zu 4vol% nach 4h Lösungsglügen, welche auf die partielle Auflösung des, während der Erstarrung segregiertem, Al_2Cu zurückzuführen ist. Des Weiteren nimmt die Interkonnektivität des Aluminidnetzwerkes dieser Legierung von ~90% auf 70% ab während die spezifische Euler Nummer um ~34% ansteigt. Diese Parameter bleiben für die nah-eutektischen Legierungen, welche 10-13vol% Aluminide mit einer Interkonnektivität von ~95-98% aufweisen, praktisch konstant. Die Euler Nummer des Aluminidnetzwerkes der nah eutektischen Legierungen bleibt ebenso konstant.

Das eutektische und primäre Si besitzt eine große Kontiguität mit dem Aluminidnetzwerk insbesondere bei den nah eutektischen Legierungen, welche in einer hohen Stabilität der Interkonnektivität während des Lösungsglühprozesses resultiert. Die Quantifizierung der Interkonnektivität zeigt, dass die Ausdehnung des größten Si Partikel nach dem Lösungsglügen unverändert bleibt. Die Entwicklung der (spezifischen) Euler Nummer und der Morphologie abgeleitet von der Oberflächenkrümmungsverteilung des Si Netzwerkes zeigt bestimmte Änderungen des Netzwerkes nach 1h lösungsglügen. Das Hybridnetzwerk aus Si und Aluminiden zeigt Veränderungen in der Si Interkonnektivität, die eine Konsequenz der beobachteten Entwicklung der individuellen Netzwerke während des Lösungsglühens darstellt. Die tomographischen Ergebnisse werden mit Druck- (RT, 300°C, 380°C)

und Zugfestigkeiten (300°C, 380°C) sowie mit dem thermomechanischen Ermüdungswiderstand der Legierungen nach denselben Lösungsglühzeiten korreliert, um die mikrostrukturellen Parameter für deren Verhalten zu identifizieren.

Abstract

The three-dimensional (3D) microstructure of near-eutectic AlSi10Cu6Ni2Mg, AlSi12Cu5Ni2Mg, AlSi12Cu5Ni3Mg, AlSi12Cu5Ni2 alloys and that of a hypereutectic AlSi17Cu4Mg alloy is studied as function of solution treatment (ST) time at 500°C by synchrotron microtomography using absorption and phase contrast imaging.

The alloys are formed by eutectic plus primary Si and aluminides embedded in an age hardenable α -Al matrix. The rigid phases (Si and aluminides) in as-cast condition with an amount of ~25vol% form a highly interconnected network able to carry load and, thus, contribute to the strength of the alloys. This 3D microstructure is additionally investigated by a newly developed serial sectioning method using an ion mill to obtain small depth removal during the sectioning procedure. The evolution of the volume fraction, interconnectivity, contiguity and morphology of phases are quantified from tomographies of the same sample after 0h, 1h and 4h ST. The hypereutectic AlSi17Cu4Mg alloy shows a decrease in the volume fraction of aluminides from ~6vol% to 4vol% after 4h ST owing to partial dissolution of Al₂Cu segregated during solidification. Furthermore, the interconnectivity of the aluminides network in this alloy decreases from ~90% to ~70% while, the specific Euler number shows an increase of ~34%. These parameters remain practically constant for the near-eutectic alloys, which present 10-13vol% of aluminides with ~95-98% interconnectivity. The (specific) Euler numbers of the networks of aluminides in the near eutectic alloys remain constant as well.

The eutectic and primary Si present a large contiguity with the aluminides network, especially for the near eutectic alloys, which results in high stability of the interconnectivity during the solution heat treatments. Quantification of the interconnectivity shows that the size of the largest Si particle is stable after solution treatment. The evolution of the (specific) Euler Number and the morphology derived from the surface curvature distribution of the Si network show distinct changes in the network after 1h ST. The hybrid network formed by Si and aluminides shows Si interconnectivity changes that are a consequence of the evolution observed for the individual networks during solution treatment. The tomographic results are correlated with the compressive (RT, 300°C, 380°C) and tensile strength (300°C, 380°C) as well as the thermo-mechanical fatigue resistance of the alloys after the same ST times aiming at identifying the microstructural parameters responsible for their behavior.

1. State of the art

1.1. Al-Si alloys

Al-Si alloys are widely used in shape casting manufacturing [1]. The Al-Si alloying system, depicted in Fig. 1.1, is well suited to produce sound castings with good mechanical properties.

Eutectic Al-Si alloys are two-phase materials formed by α -Al and the rigid Si segregated during eutectic solidification. The amount, grain size and morphology of primary α -Al have been shown to be important for the castability of alloys [2]. The morphology of the eutectic Si is determined during solidification by the mean temperature gradient in the melt and the growth rate of the solidification front [3,4]. The eutectic point is at $\sim 577^\circ\text{C}$ and at a Si concentration of $\sim 12.6\text{ wt}\%$. In the as cast condition the eutectic Si in Al-Si alloys usually forms long-range interconnected structures embedded in the α -Al matrix as it was originally shown by deep etching of the α -Al matrix [5].

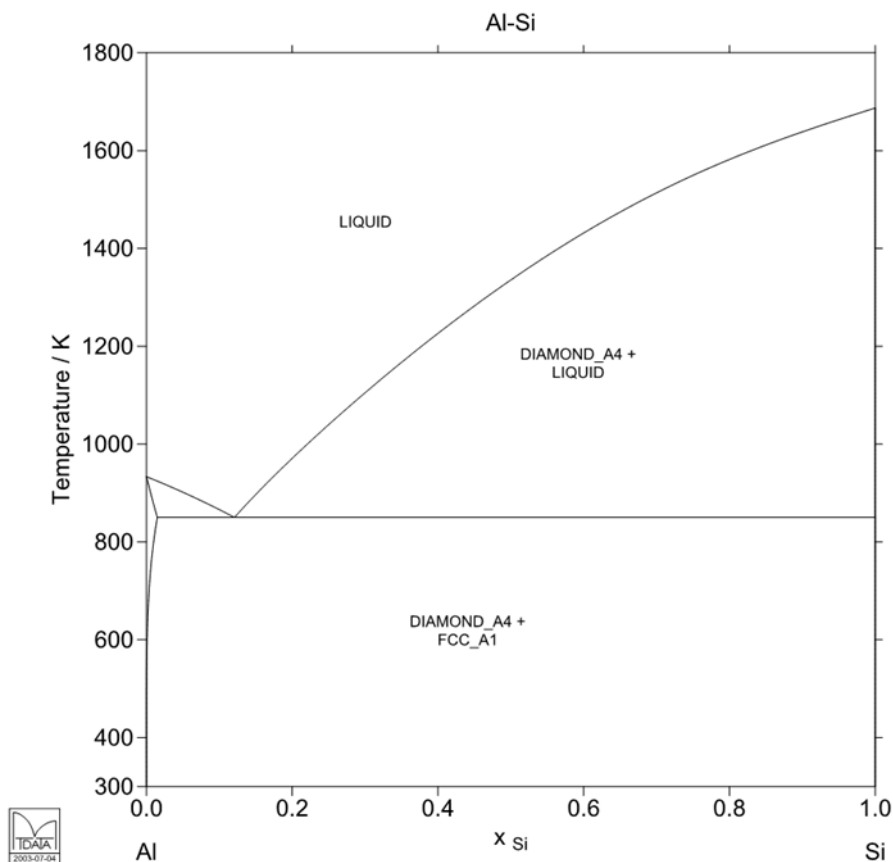


Fig. 1.1: Al-Si phase diagram [6].

1.1.1. Eutectic silicon network in Al-Si alloys after solidification

The formation of a silicon network during solidification of Al-Si alloys is affected by the mean temperature gradient of the melt, the solidification rate [3,7] and the presence of modifiers such as Sr, Na, Ca, Ti and Sb [8-13]. Hosch et al. [7] investigated eutectic silicon morphologies, shown in Fig. 1.2, after directional solidification of an AlSi12 alloy with a temperature gradient of 7-14 K/mm over a solidification velocity range of 10-950 $\mu\text{m/s}$. It was found that a flake-to-fiber transition occurred within two overlapping but distinct solidification rate intervals. One interval, 100-500 $\mu\text{m/s}$, was characterized by an increase of in-plane breakup of broad silicon plates into skeletal plate- and rod-like structures (Fig. 1.2b). This indicates the activation of multiple in-plane $\{111\}$ growth directions. The next interval, from 500-950 $\mu\text{m/s}$, showed the activation of out-of-plane silicon growth, leading to a fibrous rod structure and three-dimensional (3D) growth (Fig. 1.2c).

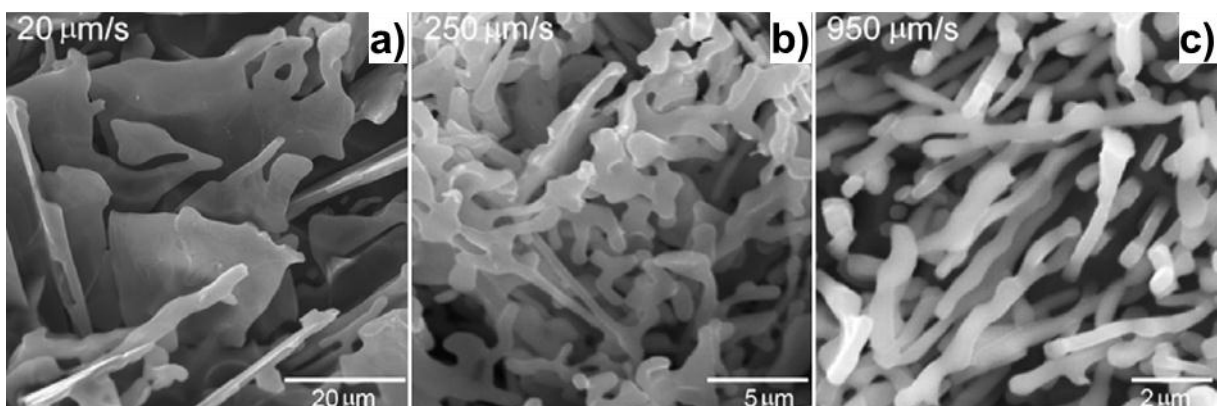


Fig. 1.2: SEM images of deep etched samples of an AlSi12 alloy solidified at different cooling rates [7], increasing unidirectional solidification from left (flake-like) to right (fibrous-like).

Lasagni et al. [9] investigated morphological changes of eutectic silicon in Sr-modified and unmodified AlSi7 and AlSi12 alloys by focused ion beam (FIB) tomography (Fig. 1.3). The addition of 0.017 wt% Sr led to a complete modification of the eutectic Si from flake- to a coral-like fibrous structure. The connecting nodes were thicker, $\sim 1\text{-}4 \mu\text{m}^2$, in the unmodified AlSi7 than in the Sr-modified alloy. The fibrous branches of 0.2-0.4 μm in diameter and a length of 3-5 μm in many directions showed connecting nodes of 0.05-0.1 μm^2 in the AlSi7 alloy.

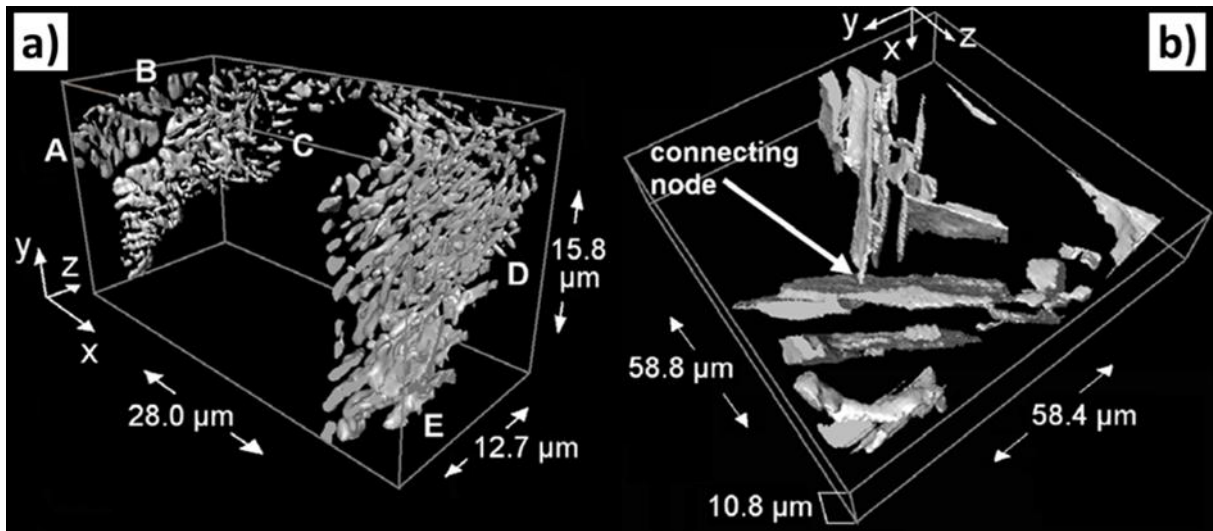


Fig. 1.3: (a) Sr-modified and (b) unmodified eutectic Si structure in the as cast condition of an AlSi7 alloy [9].

Besides modifiers which change the morphology of eutectic Si grain nucleators for primary Si such as P, and for α -Al such as Ti, B, Zr and V are often used in near-eutectic and hypereutectic Al-Si alloys [14,15]. Recently, Liang et al. [16] calculated the Al-Si-P ternary system and determined the necessary content of P and Si for the formation of AlP. This phase results in a coarsening of the eutectic Si plates. Thus, according to these investigations the P-threshold for the formation of AlP is up to 7.4 ppm for hypoeutectic alloys. Ludwig et al. [10] studied the combined effects of Ca and P on the microstructure of a high purity AlSi7 alloy (Fig. 1.4). The coarsening of the Al-Si eutectic is associated with a higher number of potential nucleation sites [10]. The main effect of Ca is the reduction of P-based nucleants for the eutectic Si by the formation of the pre-eutectic $\text{Al}_2\text{Si}_2\text{Ca}$ phase, which nucleates on AlP, and by the formation of the Ca_3P_2 phase [10].

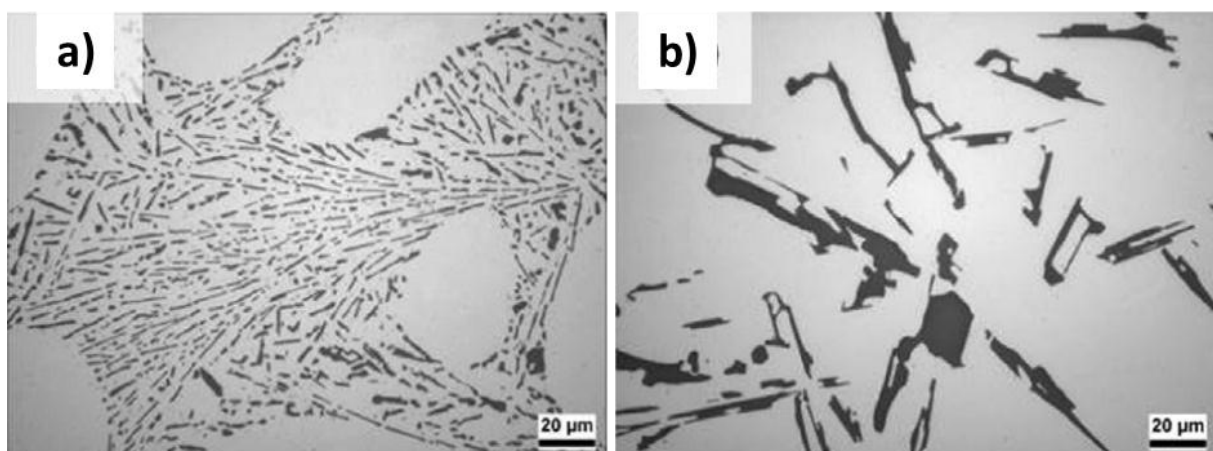


Fig. 1.4: Effect of the addition of P on the morphology of Si in a high purity AlSi 7wt% alloy a) 0.5 ppm P and b) 20 ppm P [10].

1.1.2. Spheroidization of eutectic and primary silicon

The shape and size of eutectic and primary Si can be altered by heat treatments such as hot isostatic pressing [17] and solutionizing [18] which result in a spheroidized Si morphology [19]. This morphological change is driven by surface tension during heat treatment resulting in a minimization of the total free-energy or the ratio between interface areas and particle volumes.

Zhu et al. [20] investigated the spheroidization of Si in an AlSi13 alloy and found that the process consists of two steps, as shown in Fig. 1.6. First, the separation of thin parts of eutectic Si branches occurs. This step has the greatest effect on the time of the complete spheroidization process and is also affected by the morphology of Si plates. In the second step these separated parts become more rounded with increasing heat treatment time. The effect of solution treatment at 540°C on the 3D morphology and interconnectivity of an AlSi12 alloy is shown in Fig. 1.5.

The spheroidization of eutectic Si between 300°C and 550°C for different heat treatment times was investigated by Röhrig et al. [21]. Unmodified and Na modified Al-Si alloys containing 9-13wt% Si were annealed at 300-550°C for 15min to 38 days. It was found that Si spheroidizes at 550°C within 15min of heat treatment.

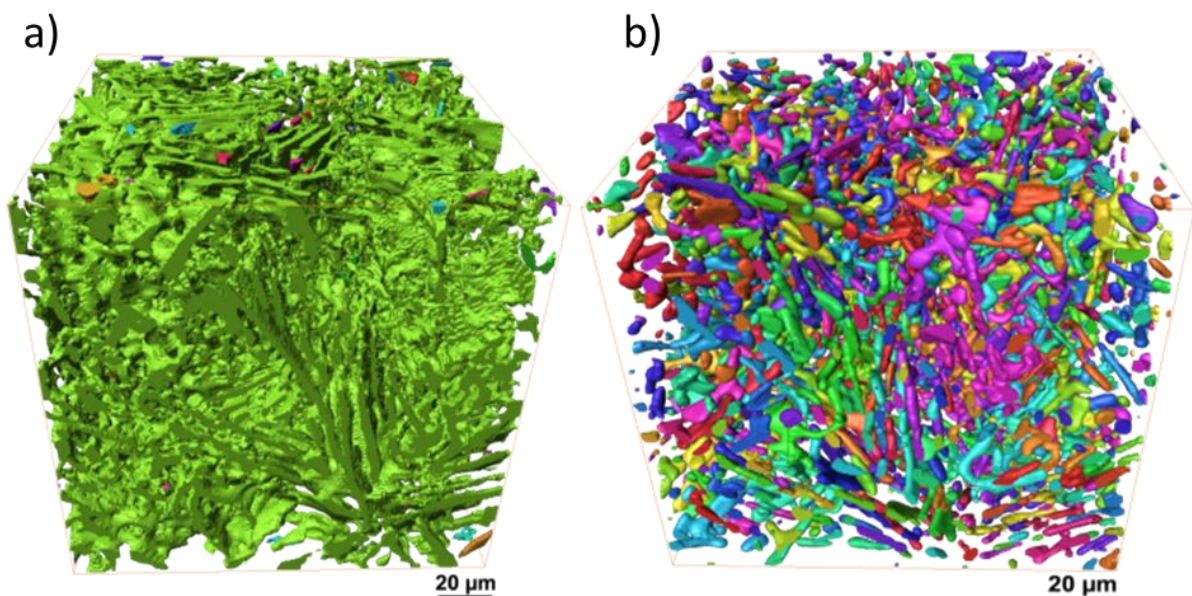


Fig. 1.5: Eutectic Si network reconstructed from synchrotron holotomographies of unmodified AlSi12: a) as-cast condition b) solution treated (540°C/4h) [22].

The morphology of eutectic Si can be platelet-like in unmodified alloys or fibrous coral-like in the case of modified alloys (see section 1.1.1). For the platelet-like morphology, Werner [23] stated that thermal degradation (additional thinning of eutectic Si) takes place at local crystal defects, where the break-up process starts.

These defects can be morphological faults like terminations, kinks and striations of the plates as well as holes and cracks in the plates [23]. On the other hand, modified coral-like eutectic Si, which forms by impurity induced twinning resulting in anisotropic multiple branching of Si at the solid/liquid interface during solidification, spheroidizes faster than unmodified plates [47].

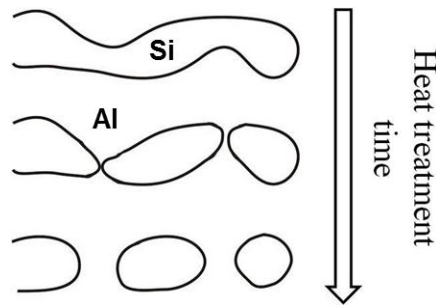


Fig. 1.6: Schematic representation of the spheroidization-process of eutectic Si in Al-Si alloys according to Zhu et al. [20].

1.1.3. Aluminides in Al-Si piston alloys

Due to the addition of Cu, Ni, Mg, Fe and Mn in Al-Si alloys the system becomes more complex, basically because of the formation of multicomponent intermetallic phases. This has been thoroughly investigated in modifications of the Al-Si-Cu-Ni-Fe-Mn-Mg system, which forms the basis for the technological piston alloys, e.g. [24-26]. Fig. 1.7 shows the microstructure of an AlSi13Cu4Ni2MgFe alloy [24].

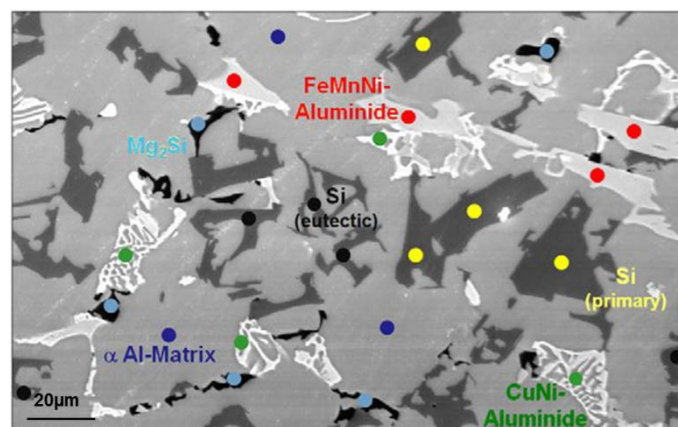


Fig. 1.7: SEM micrograph with qualitatively investigated composition of rigid phases present in an AlSi13Cu4Ni2MgFe alloy [24].

Al₇Cu₄Ni may contain 37 wt% Cu and 18 wt% Ni and may dissolve 2.4 wt% Si and 0.5 wt% Fe [15, 25, 27]. The addition of Fe and Mn in presence of Ni forms Al₉FeNi with up to 4 wt% Si and up to 3.7 wt% Cu [28]. Fe and Mn lead to the formation of α-AlFeMnSi [29,30]. Chen et al. investigated the different aluminides present in an AlSi12.5Cu3.9Ni2.8MgFe alloy by a combination of electron backscattered diffraction

(EBSD) and energy dispersive X-ray spectroscopy (EDX) (Fig. 1.8). The presence of Cu and Mg promotes the formation of $\text{Al}_5\text{Cu}_2\text{Mg}_8\text{Si}_6$ [31]. These phases often form adjacent to one another and are usually interconnected [19, 27, 32-34]. Ni and Cu can combine to form three different AlCuNi phases [19], namely Al_3Ni , $\text{Al}_3(\text{NiCu})_2$ and $\text{Al}_7\text{Cu}_4\text{Ni}$. Al_3Ni may contain up to 31 wt% of Cu and 30 wt% of Ni.

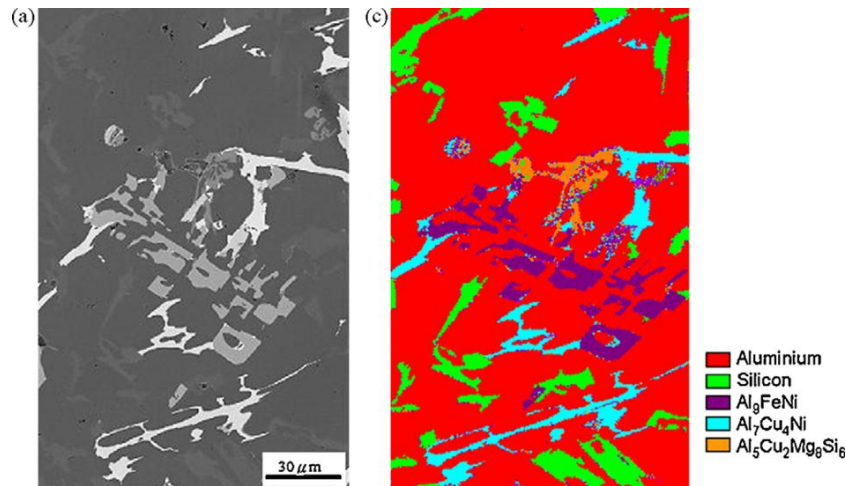


Fig. 1.8: Identified phases by combination of EBSD and EDX mapping of an AlSi12.5Cu3.9Ni2.8MgFe alloy [29].

Asghar et al. [32] investigated the 3D Morphologies and connectivity of different aluminides by synchrotron tomography and serial sectioning of the same sample of an AlSi10Cu5NiFe alloy. The interconnectivity and contiguity of individual aluminides was revealed by combining serial sectioning with EDX analysis (Fig. 1.9).

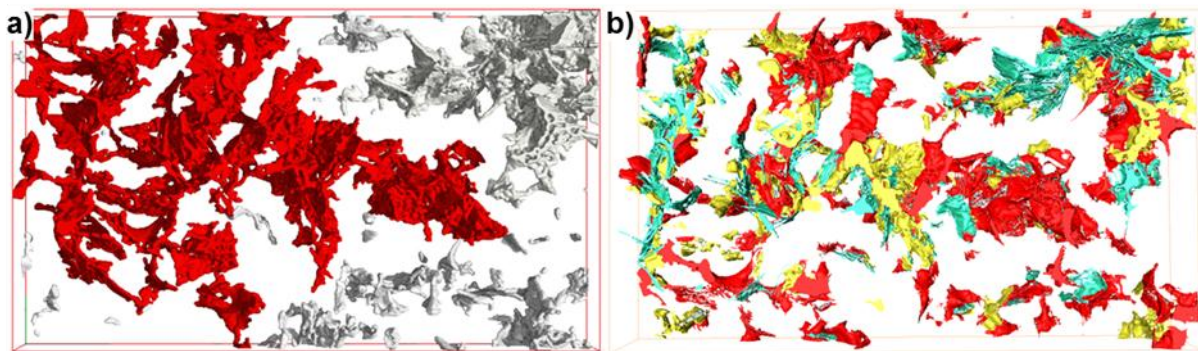


Fig. 1.9: Reconstructed 3D structures in a volume of 291x169x43 μm^3 of an AlSi10Cu5NiFe alloy: a) aluminides with largest intermetallic particle in red revealed by synchrotron tomography b) individual aluminides: Al_2Cu (red), $\text{Al}_7\text{Cu}_4\text{Ni}$ (yellow), Fe-aluminides (cyan) obtained by EDX analysis using serial sectioning of the same sample.

1.1.4. Precipitation strengthening in Al-Si piston alloys

Precipitation strengthening plays a vital role in technological Al-Si alloys. Elements like Cu, Mg and Mn contribute to precipitation strengthening through the formation of age-hardening precipitates $\text{Al}_5\text{Cu}_2\text{Mg}_8\text{Si}_6$, Al_2Cu or Al_2CuMg [25]. However, these precipitates provide a relevant strengthening effect up to $\sim 100^\circ\text{C}$. At higher temperatures Oswald's ripening reduces their strengthening capability. The system Al-Cu-Mn forming $\text{Al}_{20}\text{Cu}_2\text{Mn}_3$ precipitates (Fig. 1.10a) shows higher thermal stability than Al-Cu-(Mg) based precipitates [35]. The systems Al-V-Zr, Al-Sc-Zr and Al-Zr-Ti were suggested for thermally stable nano-sized precipitates based on a composition Al_3M . Al_3Zr (Fig. 1.10) forms during decomposition of the supersaturated solid solution with a metastable cubic L1_2 structure (structurally and chemically analogous to Ni_3Al). Al_3Zr precipitates are shown in Fig. 1.11 for an Al-0.1Zr-0.1Ti alloy aged at 375°C for 1600h [36]. The thermodynamic stable structure of these precipitates is described as tetragonal D0_{23} and their distribution in an Al-0.1Zr (at%) alloy aged at 500°C for 100h is shown in Fig. 1.12. If Zr is accompanied by Ti, V, Sc or Hf the resulting precipitates are considered more stable due to a reduced lattice parameter mismatch between Al_3M precipitates and the α -Al matrix [37].

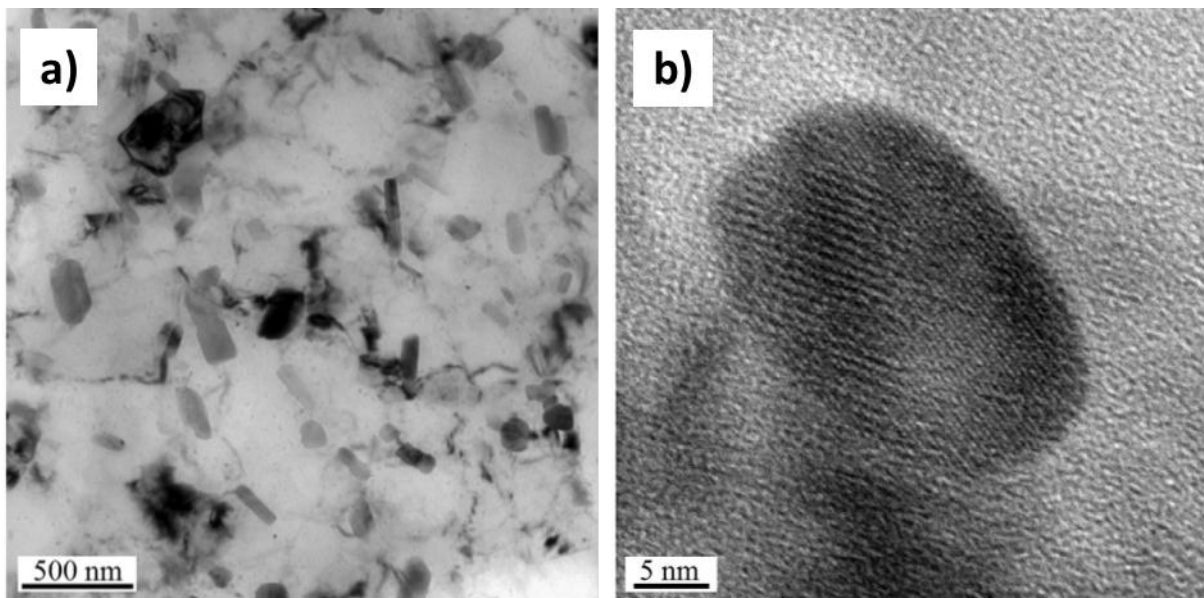


Fig. 1.10: TEM micrographs of a) $\text{Al}_{20}\text{Cu}_2\text{Mn}_3$ dispersoids and b) HR TEM image of Al_3Zr particle with cubic L1_2 structure, both present in an Al-Cu-Mn-Zr-Sc alloy [35].

However, it has been reported that there is no benefit in terms of coarsening resistance of $\text{Al}_3(\text{Zr}_{1-x}\text{Ti}_x)$ as compared with Al_3Zr precipitates during extended isothermal aging at 425°C [38]. One problem of Al_3Zr particles in Al wrought alloys is

their dendritical distribution, visible in Fig. 1.11, which can be overcome by multi-step annealing processes and other alloying additions, including Cu, Mg, Zn, Si, Fe, Mn and Sc [35,36]. The addition of Si reduces the coarsening resistance of precipitates during aging [39]. The magnitude of this effect is determined by the Si concentration. The reason lies in the accelerated diffusion of Zr in the α -Al matrix as it was shown by first-principles calculation by Booth-Morrison et al. [40].

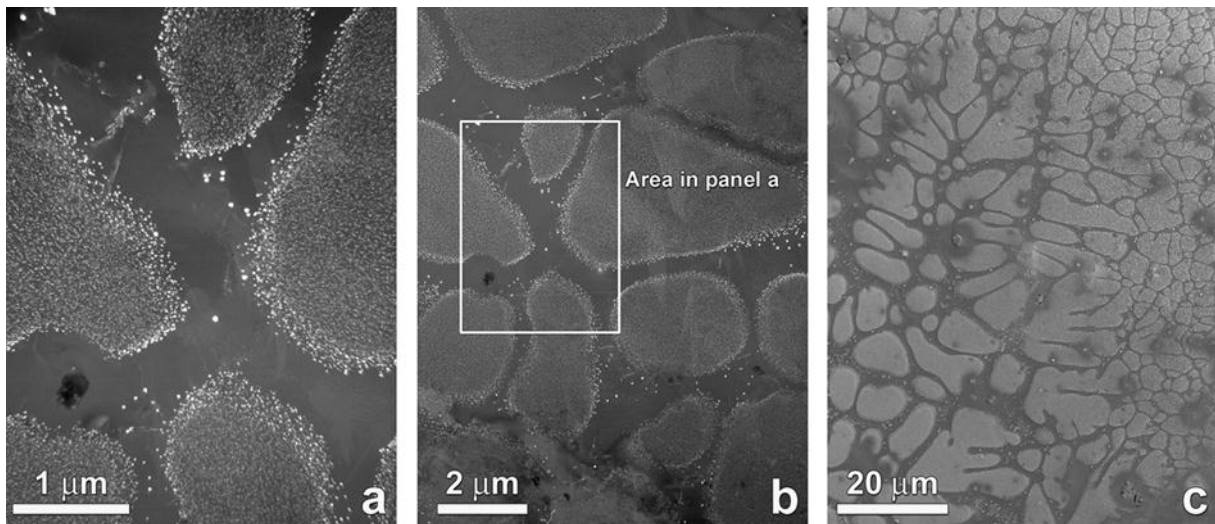


Fig. 1.11: TEM and SEM micrographs of Al-0.1 Zr-0.1 Ti aged at 375°C for 1600 h; a) and b) centered dark-field TEM images showing the dendritic distribution of Al_3Zr ($\text{L}1_2$) precipitates; c) SEM secondary electron image illustrating the dendritic distribution of the precipitates [36].

All these investigations were focused on Al wrought alloys. The casting system Al-Si-Cu-Mg with addition of V, Zr and Ti was investigated recently [41-45]. These investigations concentrated on the mechanical properties of hypoeutectic alloys. The formation, distribution, evolution of precipitates during solution treatment and aging was not studied specifically.

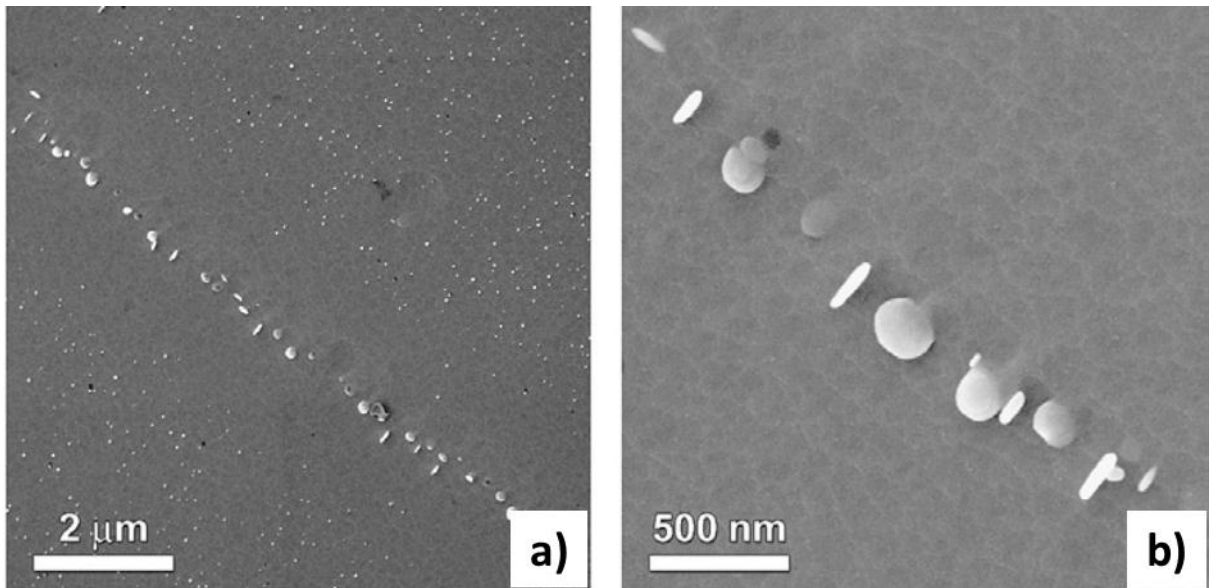


Fig. 1.12: SEM micrographs of disc-shaped Al_3Zr (D_{023}) precipitates in an Al–0.1Zr (at%) alloy aged at 500°C for 100h (after peak aging at 375°C for 100h) [46].

1.2. Mechanical properties of Al-Si piston alloys

One constituent that affects the mechanical properties of eutectic Al-Si alloys is the rigid Si, which is able to carry load depending on its morphology, volume fraction, distribution and interconnectivity [4,22]. Hosch et al. [7] investigated the effect of different Si morphologies on room temperature tensile properties of AlSi12. The fiber-like eutectic Si resulted in an increase of UTS of ~38% at the expense of elongation at fracture.

Requena et al. [22] studied the effect of morphology and interconnectivity of eutectic Si on the compression strength of unmodified AlSi12 at room temperature (Fig. 1.13). The as cast AlSi12 alloy showed ~130% increase in compressive strength compared to an AlSi1.1 alloy equivalent to the matrix in AlSi12. This improvement was due to the presence of interconnected Si lamellae with high aspect ratio. Furthermore, it could be shown that 4h of solution treatment caused ~30% decrease of compressive strength in AlSi12 due to the loss of interconnectivity and spheroidization of eutectic Si. The solution treated AlSi12 still exhibits ~65% higher compressive strength than AlSi1.1. This is caused by the effect of the short-fiber morphology of the disintegrated eutectic Si branches and the presence of strain hardened regions built up during cooling in the α -Al at the Al-Si interface [22]. Ogris [47] investigated theoretically and experimentally the spheroidization process during solution treatment of eutectic Si in a thixoformed A356 alloy. The silicon spheroidization treatment process was a short 3min heat treatment at 540°C . This resulted in higher yield strength, UTS and a 70%

increase of the elongation at fracture at room temperature with respect to the T5 condition. Asghar et al. [34] found that different volume fractions of stable intermetallics led to less or no disconnection of the interpenetrating Si network in near eutectic Al-Si piston alloys with respect to AlSi12, which resulted in higher yield strength at elevated temperatures (Fig. 1.17a).

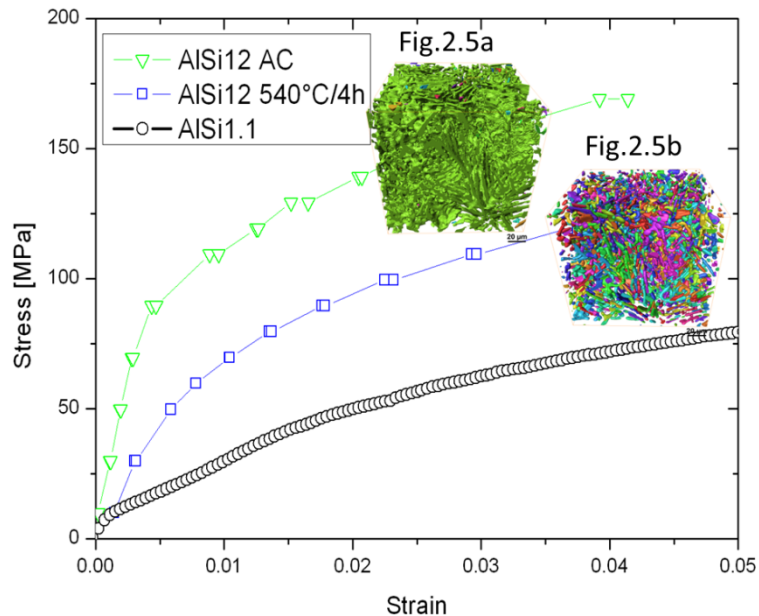


Fig. 1.13: Compressive strength of AlSi12 in as-cast condition and solution treated at 540°C/4h compared with AlSi1.1 [22].

The introduction of short fibers into Al-Si piston alloys was investigated by several researchers [48-52]. In Fig. 1.14 the deep etched microstructure of an AlSi12 alloy reinforced with 20vol% of Al₂O₃ short fibers is shown in the as-cast condition and after 4h solution treatment at 540°C. Metal matrix composites containing Al₂O₃ short fibers and Al-Si alloys show improved strength and creep resistance due to the load carrying capability of the short fibers [50]. This load carrying capability is not guaranteed by the mere addition of short fibers and can be detrimental to the creep resistance [53]. The alloys used as matrices containing ≥ 7 wt% Si enhance the load carrying capacity of the hybrid network of Al₂O₃-Si [50,51]. The contiguity between Si and Al₂O₃ in the hybrid network of an AlSi12 alloy containing 20vol% Al₂O₃ short fibers in as cast condition was retained even after 4h of solution treatment at 540°C although Si spheroidized considerably [52]. The decrease of interconnectivity led to a loss of ~15% in tensile strength at 300°C for an AlSi12/Al₂O₃/20s composite [54]. Furthermore, the anisotropic distribution of Al₂O₃ short fibers (random planar) influence the mechanical properties of the short fiber reinforced Al-Si alloys [54].

Despite the positive effects of short fiber reinforced Al-Si alloys on strength and creep resistance, these composites remain rarely used in automotive industry due to their high production costs and inferior machinability.

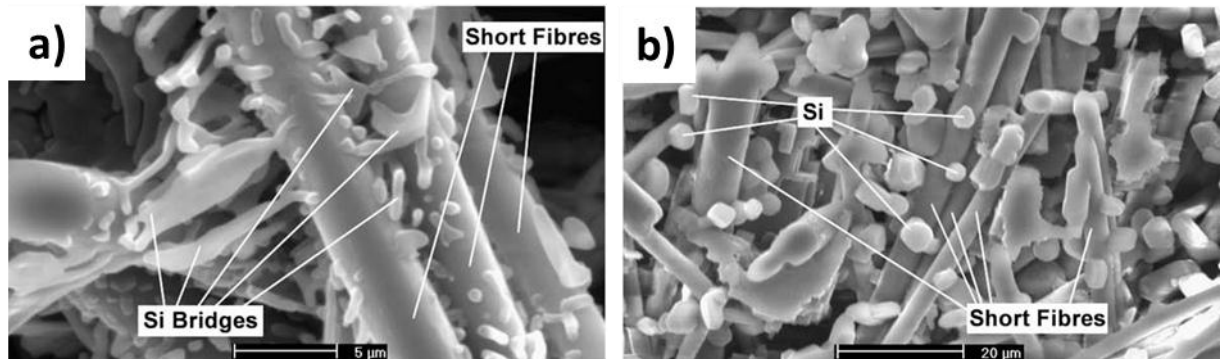


Fig. 1.14: Deep etched microstructure of an AlSi12 alloy reinforced with 20vol% of Al_2O_3 short fibres: a) as-cast condition and b) after 4h at 540°C [52].

Another way to strengthen Al-Si alloys is by the introduction of stiff intermetallics by alloying with transition elements that form aluminides (see section 1.1.3). Chen et al. [55,56] determined the hardness of single aluminides in an Al-Si piston alloy (AlSi14Cu2Ni1.6MgFe in at%) at 25, 200 and 350°C using hot-stage nano-indentation (Fig. 1.15). It was concluded that the formation temperature of an intermetallic phase could be linked to its elastic modulus. The α -AlFeMnSi phase showed hardness similar to Si and was found to be intrinsically brittle with a possibility of cracking. Ni-containing AlCuNi phases ($\text{Al}_7\text{Cu}_4\text{Ni}$ and Al_3Ni) showed high hardness and elastic modulus, whereas $\text{Al}_5\text{Cu}_2\text{Mg}_8\text{Si}_6$ (Q-Phase) and Al_2Cu exhibited inferior hardness and elastic modulus [56]. A study of Al-Si-Ni ternary eutectic related the increase of tensile strength at RT to the presence of Al_3Ni aluminides [57].

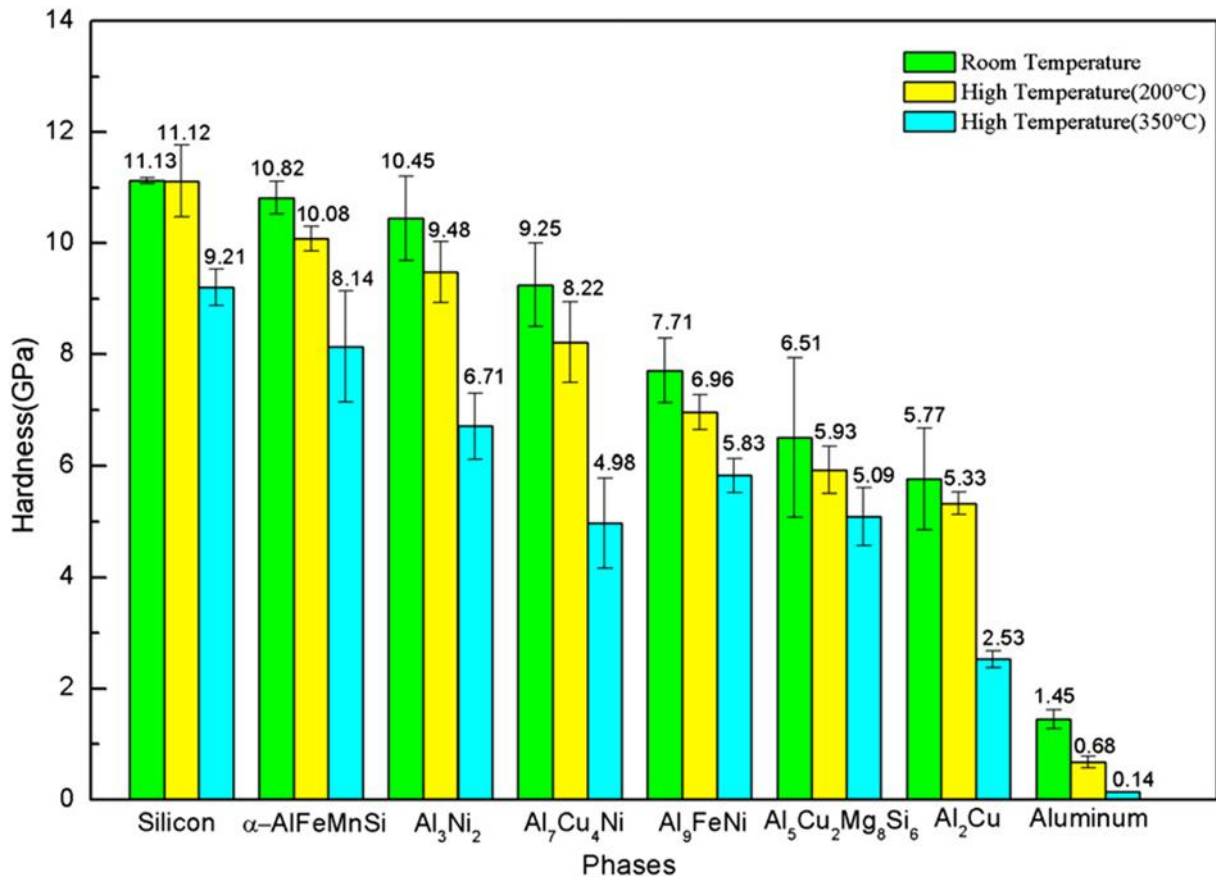


Fig. 1.15: Microhardness at 25, 200 and 350°C of different phases in an AlSi14Cu2Ni1.6MgFe alloy [56].

Asghar et al. [33] investigated the addition of 1.22 wt% Ni and 0.7 wt% of Fe to an AlSi12 alloy. The AlSi12Ni cast alloy behaved like a metal matrix composite consisting of 20vol% of interconnected hybrid reinforcement formed by eutectic Si and Ni + Fe aluminides. This resulted in higher compression strength at RT and 300°C as well as a higher thermal cycling creep resistance in comparison to an AlSi12 alloy. The yield strength of AlSi12Ni at RT was about ~20% higher than AlSi12, while this difference increased to ~60% at 300°C in as cast condition (Fig. 1.16). The thermal cycling creep of AlSi12Ni showed lower minimum strain rate, longer thermal cycling creep life and lower strain to failure than AlSi12 [33]. Stadler et al. [58] investigated the high temperature tensile strength of AlSi7 and AlSi12 with addition of up to 2 wt% Ni. The tensile strength at 250°C of AlSi7 increased ~40% with additions of Ni up to 1 wt%. More than 1 wt% of Ni did not lead to further improvement.

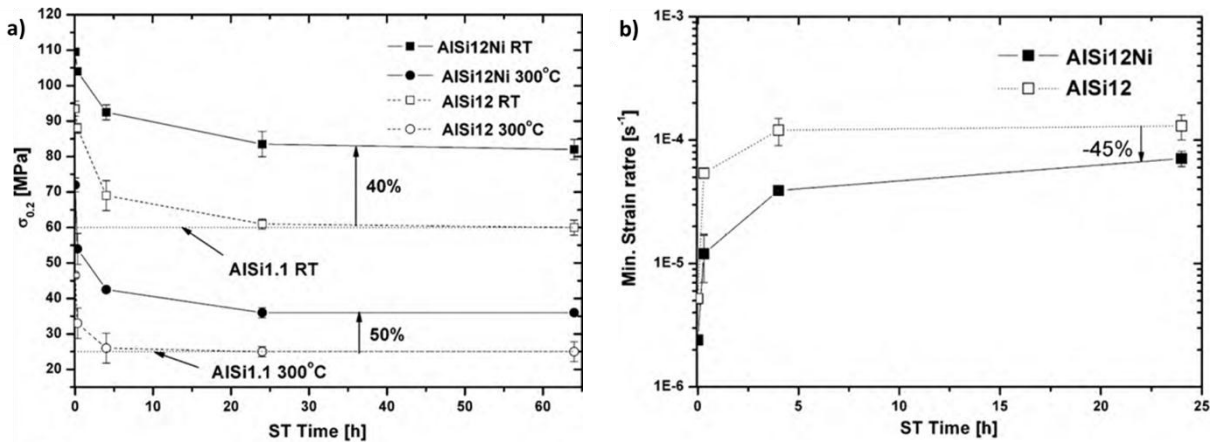


Fig. 1.16: Thermo-mechanical properties of an AISi12Ni alloy compared to AISi12. a) yield strength at RT and 300°C b) minimal strain rate during thermal cycling creep between 50 and 300°C at $\sigma=40\text{MPa}$ [33].

On the other hand, further addition of up to 2 wt% of Ni improved the tensile strength at 250°C of AISi12 for about 30% with respect to the unalloyed AISi12. This increase in high temperature strength is due to the stabilization of contiguity between Al_3Ni and eutectic Si [58].

Besides the addition of Ni the combined effect of Cu and Ni was investigated by several researchers [19,34,59-61]. Asghar et al. [34] investigated the effect of solution heat treatment of AISi10Cu5Ni1-2 alloys and found a correlation between yield strength at 300°C and connectivity of Si, which can be seen in Fig. 1.17. They concluded that the combined effect of Cu and Ni leads to the formation of a complex three dimensional interpenetrating structure containing Si and aluminides that is able to carry load [34]. This resulted in ~16-45% improvement of tensile strength at 300°C with respect to AISi12 [19,34,59-61].

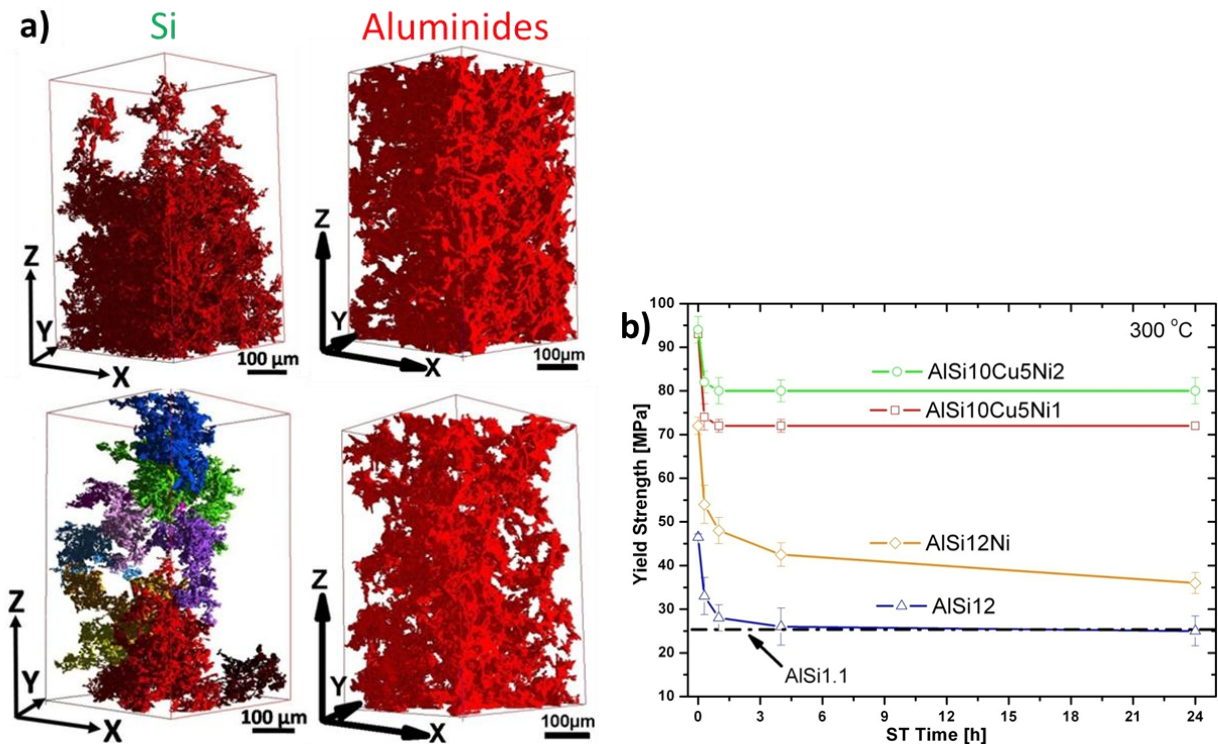


Fig. 1.17: Correlation of architecture and yield strength at 300°C a) rendered volumes of Si and aluminides in AISi10Cu5Ni2 (top) and AISi10Cu5Ni1 (bottom) b) compressive yield strength at 300°C [34].

The strengthening of a cast A354 alloy (AISi9CuMg) with an addition of up to 0.4wt% Zr was investigated in [44,45]. The combined effect of minor additions of Zr, Ti and Ni increased the tensile properties at 300°C. An increase of ~30% in UTS and yield strength with respect to the base A354 alloy (Fig. 1.18) was only found in the as-cast condition at 300°C for additions of 0.2 wt% Zr and 0.2 wt% Ni. Higher Zr and Ni additions led to lower tensile strength at this temperature. This was attributed to the possibility that 0.2 wt% Zr could completely dissolve in the melt at lower temperature in comparison with 0.4 wt% Zr, as the Al-Zr phase diagram indicates [45]. This leads to a higher concentration of Zr-rich precipitates in the 0.2 wt% Zr alloy that improves the strength at high temperature. Unfortunately, the authors do not give an estimation of the experimental scatter of their results that may help to support their claim. After solution treatment at 495°C for 8h reduction of ~16% in the high temperature tensile strength was obtained. This behavior was explained by the fact that the solution treatment at 495°C changes the coherency of Zr-rich nano-particles from L_{12} to the stable $D0_{23}$ [45]. Micro hardness investigations at room temperature after ageing at 500°C from peak-aged condition showed a linear decrease in hardness on a semi-logarithmic scale [46]. Knipling et al. [46] stated that even after aging of an Al-0.1Zr-0.1Ti (at%) alloy at 575°C spheroidal L_{12} precipitates were present and due to the

dendritic distribution of precipitates the transformation at 500°C (for 100h) is extensive along dislocations, although most precipitates still have the metastable L1₂ structure.

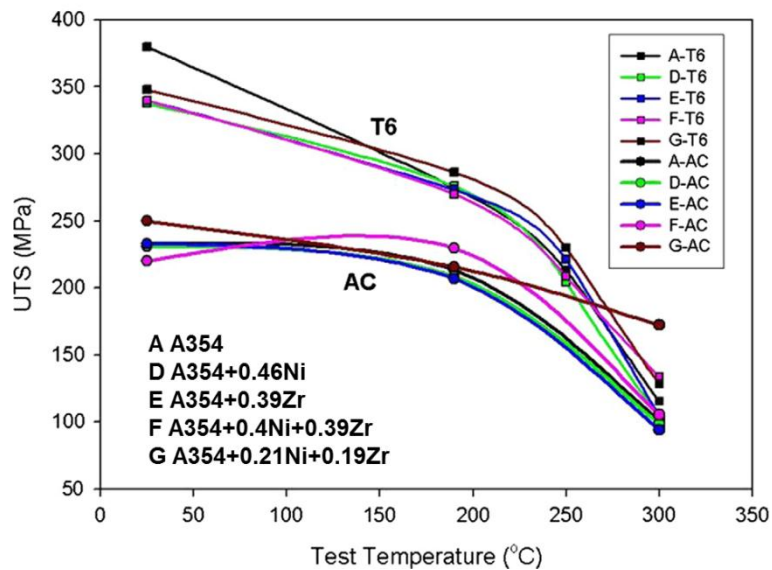


Fig. 1.18: UTS vs testing temperature of A354+minor addition of Ni and/or Zr [45].

Kasprzak et al. investigated the high temperature performance of A319 (AlSi6Cu3.5) and A356 (AlSi7Mg) with addition of 0.2wt% Zr, 0.25wt% V and 0.11wt% Ti [41]. The results indicate that additions of Zr, V and Ti improve the low cycle fatigue strength at room temperature but lower ductility and slightly improve elevated temperature hardness between 150 to 450°C with almost no effect on tensile strength. High temperature exposure at 475°C for 128h of the AlSi7CuMg alloy in T6 condition resulted in improved hardness retention, most likely associated with further precipitation of Zr-rich precipitates [41]. The AlSi7CuMg alloy with 0.2wt% Zr investigated by Elhadari et al. [43] showed higher yield strength and ultimate tensile strength after T6 heat treatment but lower ductility at room temperature compared to A356-T6 (AlSi7Mg) and A319-T6 (AlSi6Cu3.5). A two-step solution heat treatment was performed at 505°C for 0.5h and 525°C for 4.5h, followed by artificial ageing at 150°C for 100h. The tensile fracture in AlSi7CuMg proceeded mainly through the eutectic Si and primary phases, exhibiting intergranular cracking together with some cleavage-like features.

1.3. Tomography

Complex microstructures are in many cases not sufficiently described by two-dimensional (2D) metallography. This is only feasible in the cases where a homogeneous distribution of the microstructural constituents can be assumed. Therefore, adequate characterization requires 3D imaging if no assumptions can be made regarding the internal symmetries of constituents in the microstructure.

1.3.1. Serial sectioning tomography

The principle of serial sectioning, schematically shown in Fig. 1.19, is to perform sequential imaging after stepwise removal of material. A 3D volume is achieved by stacking the 2D images obtained sequentially. The sectioning, destructive in nature, can be applied by mechanical polishing [32, 62-65], while images can be obtained by light optical microscopy. This serial sectioning technique is sometimes termed as light optical tomography (LOT) [64] and can be complemented with additional analytical methods like EDX for identification of phases [32].

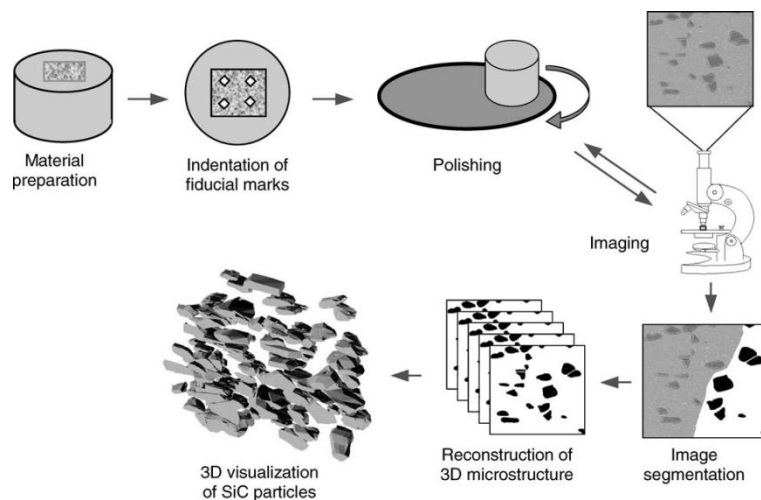


Fig. 1.19: Schematic representation of the light optical tomography technique described by [66].

Another serial sectioning method is the use of FIB which can be combined with other techniques such as EDX and EBSD.

The advantage of serial sectioning is the relatively high resolution, i.e. $\sim 0.3\mu\text{m}$ in case of LOT and even more for FIB-SEM tomography (limited by the resolution of the microscope).

FIB tomography was performed by Lasagni et al. [9] to characterize the 3D microstructure of cast Al-Si alloys. EDX was used to enhance the contrast between

Al and Si. LOT of Al-Si alloys has the advantage of the excellent contrast between Al and Si under the light optical microscope [32]. The clear disadvantage of the serial sectioning techniques is their destructive nature, its time-consuming milling/sectioning process and, in the case of FIB tomography, the relatively small region of interest that can be investigated [67].

1.3.2. X-ray tomography

The complex microstructure of Al-Si based piston alloys (see e.g. Fig. 1.7) requires 3D characterization for their correct description. Tomographic investigations suited for this are different serial sectioning methods [64] or X-ray computed tomography [68,69].

X-ray computed tomography (XCT) can be divided in two techniques, depending on the X-ray source: i) laboratory XCT and ii) synchrotron XCT. They basically differ in the brilliance, coherence and shape of the X-ray beam (Fig. 1.20).

XCT has seen a period of rapid growth over last 15 years with considerable improvements in spatial resolution, brilliance and image reconstruction times [70-,72]. XCT evolved from a purely qualitative method towards a quantitative methodology able to extract materials parameters from 3D images [72]. In terms of brilliance [68] and coherence [72] synchrotron sources are superior to laboratory based XCT. Parallel beam is usually the default technique in synchrotron XCT but cone beam configurations can be achieved using different X-ray focusing optics [68].

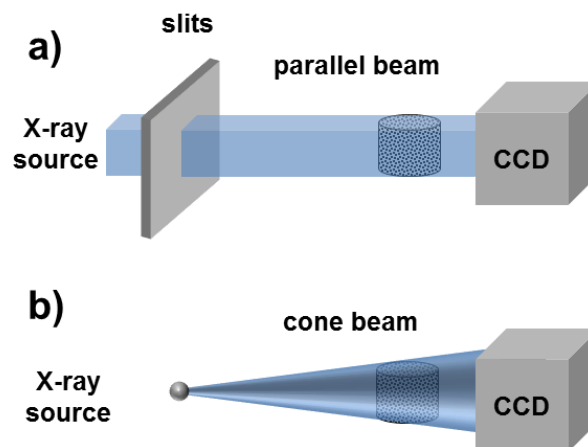


Fig. 1.20: Tomographic setups for a) parallel beam in synchrotron based tomography b) cone beam as example for laboratory XCT.

1.3.2.1. Synchrotron tomography

Synchrotron tomography is a non-destructive technique. The basic principle is the acquisition of X-ray projections (few hundreds to few thousand) with the X-ray beam propagating through a rotating sample. Synchrotron sources provide spatial resolution of $\sim 1\mu\text{m}^3$ for parallel beam configuration and temporal resolution down to $\sim 2\text{ms/projection}$ enabling investigations of microstructure evolution under controlled environmental conditions [72].

- Image contrast mechanisms

For imaging of materials the contrast mechanisms can be described by the X-ray attenuation and the phase shift as the beam passes through the sample. The main contribution to the attenuation of X-rays in the range of 0-300 keV (usually applied at synchrotrons) is provided by the photoelectric effect. The absorption contrast is given by the different attenuation coefficients of the constituent phases in the material. The attenuation can be expressed by the relationship of photometry called Lambert-Beer's law [73]. In piston alloys, higher absorbing phases like $\text{Al}_7\text{Cu}_4\text{Ni}$, Al_3Ni or Al_9FeNi can be distinguished from the $\alpha\text{-Al}$ matrix and Si by absorption contrast [34]. If the attenuation of two phases is very similar, like in the case of Al and Si, it is difficult or impossible to resolve them using absorption contrast. The phase shift of X-rays can be exploited to overcome this obstacle. This is possible through different techniques [72]. The propagation technique and the Bonse-Hart interferometry are the most commonly used for tomographic applications [67]. The propagation technique or in-line contrast exploits the interference of coherent X-rays at interfaces to enhance the visibility of edges and boundaries within an object. Synchrotron sources provide X-rays with high brilliance and transversal coherence especially at long beamlines [72] making them well suited for phase contrast imaging using the propagation technique. This technique was used by Asghar et al. to image Al-Si-piston alloys [32]. The principle of the propagation technique is shown in Fig. 1.21. The sample is placed in a partly coherent X-ray beam while recording the interference image at a distance z [74].

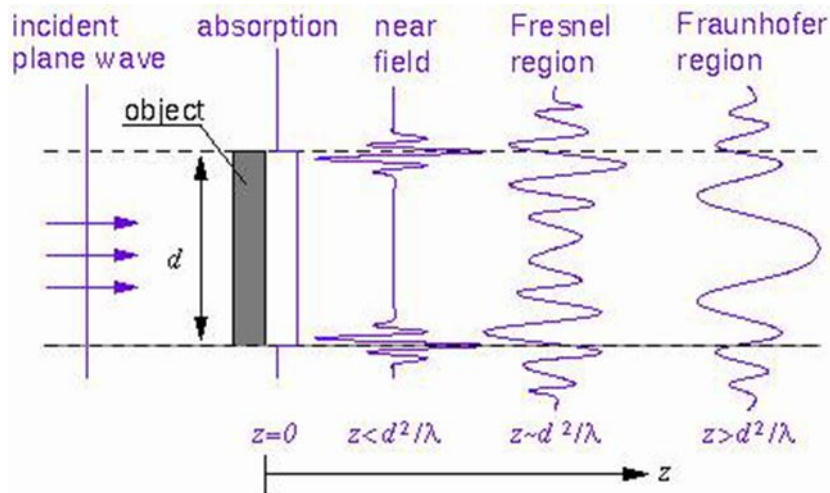


Fig. 1.21: Propagation phase contrast technique [74].

Phase retrieval can be achieved imaging the sample at multiple sample-to-detector distances for which phase contrast intensifies with increasing distance [74,75] (Fig. 1.22).

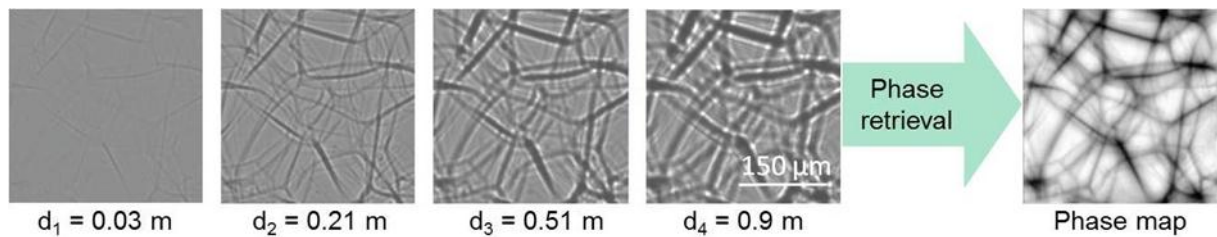


Fig. 1.22: Phase contrast in radiographies of a polymer foam by increasing distance between sample and detector [74].

One distance phase retrieval can also be carried out, as shown by Paganin [76] in combination with an unsharp mask filtering [77]. This solution is less time consuming because it reconstructs the phase of the object from a set of projections collected at a single distance [72]. Different software, e.g. [78], use the Paganin solution. An example is shown in Fig. 1.23 for a paper sample. The one distance phase retrieval technique is not restricted to synchrotron sources but the incident beam of laboratory sources is usually less effective, especially for highly absorbing materials [79].

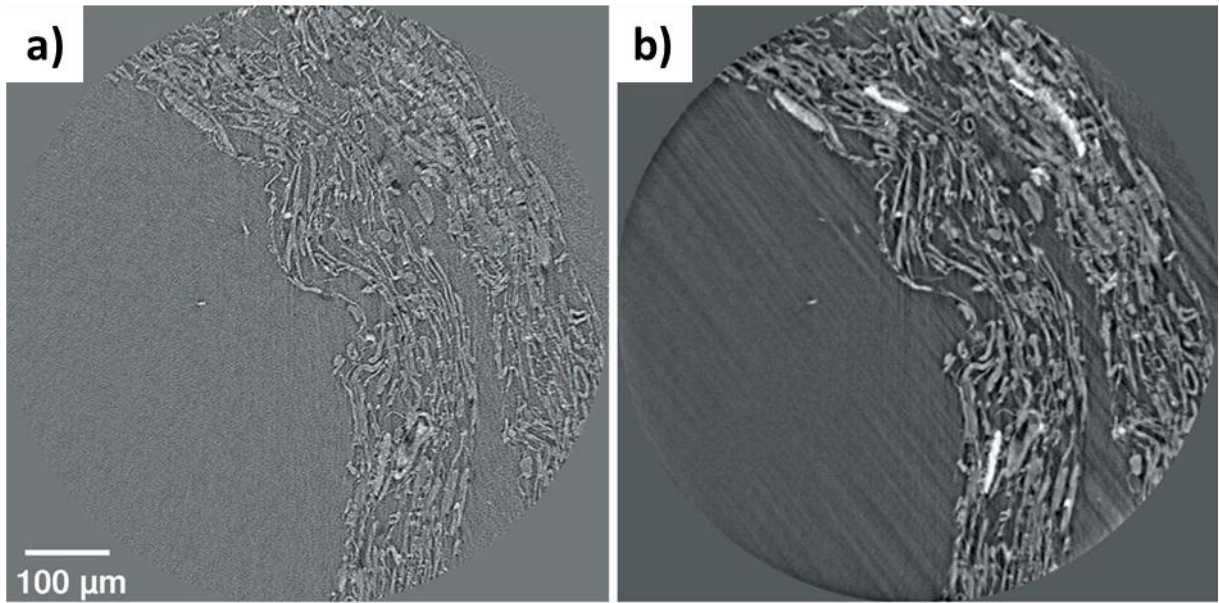


Fig. 1.23: Microstructure of a sample of recycled paper a) standard tomographic reconstruction dominated by X-ray in-line phase contrast b) same slice reconstructed using one distance phase-retrieval [78].

1.4. Hypothesis

Problem

Al-Si based piston alloys can be described as composite materials that exhibit properties analogous to those of short fiber reinforced Al-Si alloys. Due to the internal architecture of Si and aluminides, Al-Si based piston alloys retain high strength even at high temperatures which makes them suited for power train application. The high service temperature and possible solution treatment can change the internal architecture and reduce the high temperature strength attributable to the loss of interconnectivity and spheroidization of Si and aluminides as well as to the coarsening of precipitates. Increasing ductility at room temperature in combination with high temperature strength and thermo-mechanical fatigue resistance is crucial for piston alloy development.

Objectives

The introduction of specific Cu-, Ni-, Fe- and Mg- containing rigid aluminides in cast Al-Si alloys, lead to improved high temperature strength, acceptable ductility at room and high temperatures by retarding surface crack formation. The internal architecture demands 3D imaging techniques to quantify the rigid interpenetrating network. During high temperature exposure such as solution treatment some phases may tend to change their morphology and lead to changes in mechanical properties. This evolution can be followed by X-ray tomography.

Thermo-mechanical tests at room temperature and high temperature are necessary to characterize the behavior of the alloys while this correlates to quantitative investigations of the 3D microstructural evolution at high temperatures of alloys with different Cu-, Ni-, Mg- ratios.

The results are presented as comparative study of alloys investigating the influence of microstructural factors on the mechanical properties.

2. Experimental

2.1. Materials

All materials were produced by gravity die casting. The concentration of main alloying elements is shown in Tab.2.1. The basis of all alloys is the Al-Si system. The first four alloys are variations of alloys used in pistons. The fifth is mainly used for motor blocks or engine parts. This alloy was selected as reference since it presents approximately the same volume fraction of rigid phases as the other alloys but with larger volume fraction of primary Si. The piston alloys were received as complete pistons, as can be seen in Fig. 2.1, in pre-machined condition with 130mm diameter and 135mm height. The piston alloys have a near eutectic Al-Si composition between ~11-13.3wt% Si. The motor block alloy was received as pre-cut parts from a motor block, shown in Fig. 2.1.

Alloy	Si [wt%]	Ni [wt%]	Cu [wt%]	Mg [wt%]	Fe/Mn [wt%]	P [ppm]	Name
AlSi10Cu6Ni2Mg	11	1.8	5.3	0.25	0.34/0.21	25	1062
AlSi12Cu5Ni2Mg	13.3	1.8	4	0.70	0.4/0.22	36	1252
AlSi12Cu4Ni3Mg	13.2	3	4	0.65	0.39/0.2	36	1253
AlSi12Cu5Ni2	12.6	2.13	3.9	0.01	0.46/0.18	36	1252-Mg
AlSi17Cu4Mg	17	-	4	0.5	0.33/0.15	97	1740

Tab.2.1: Main alloying elements of the investigated alloys

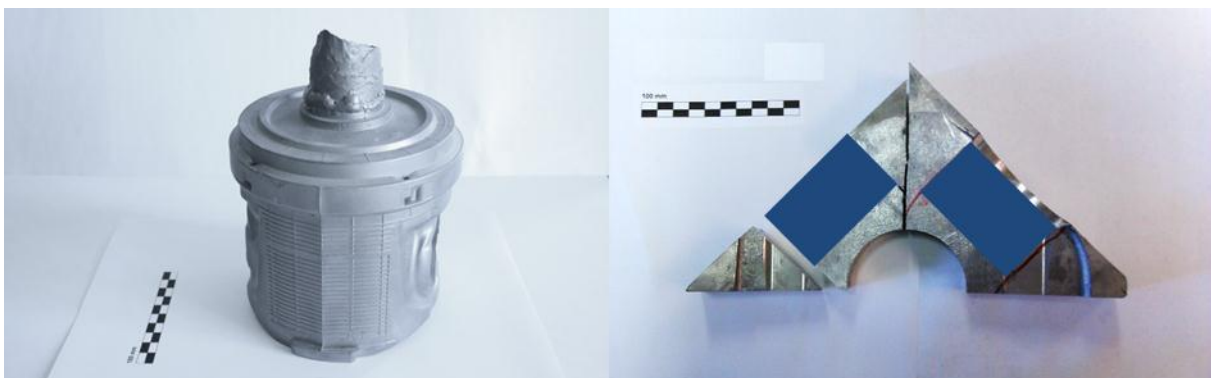


Fig. 2.1: As received piston and part of a pre-cut motor block. The blue marked regions were used for sample preparation (scale bar 100mm).

2.2. Heat treatment

All materials were subjected to the heat treatments presented in Tab. 2.2. The different overaging times were applied to find a stable T7 condition. On the other hand, the 0, 1 and 4h of solution treatment were carried out to investigate the effect on the 3D architecture of the Si-aluminides networks.

	Solution treatment	Ageing treatment	Overaging treatment
Temperature	500°C	230°C	300°C
Time	0,1,4h	5h	0-500h

Tab. 2.2: Table of conducted heat treatments for all alloys

2.3. Experimental methods

2.3.1. Determination of the region of trust

Samples for microstructural and thermo-mechanical investigations must be taken from a microstructurally homogeneous region of the piston. For this, Brinell hardness (HB1/10) maps at the samples with 2mm thickness shown in red in Fig. 2.2 were performed aiming at identifying a region of trust with approximately constant hardness. These 2mm thick samples originated from different depths, namely 2, 12, 17 and 22mm and were tested as function of their position identified according to the numbering shown in Fig. 2.2a). At least five indentations with a distance of 2mm from each other were measured to get statistically relevant hardness values. The Brinell hardness tests were carried out with an EMCO Test M1C-010 device.

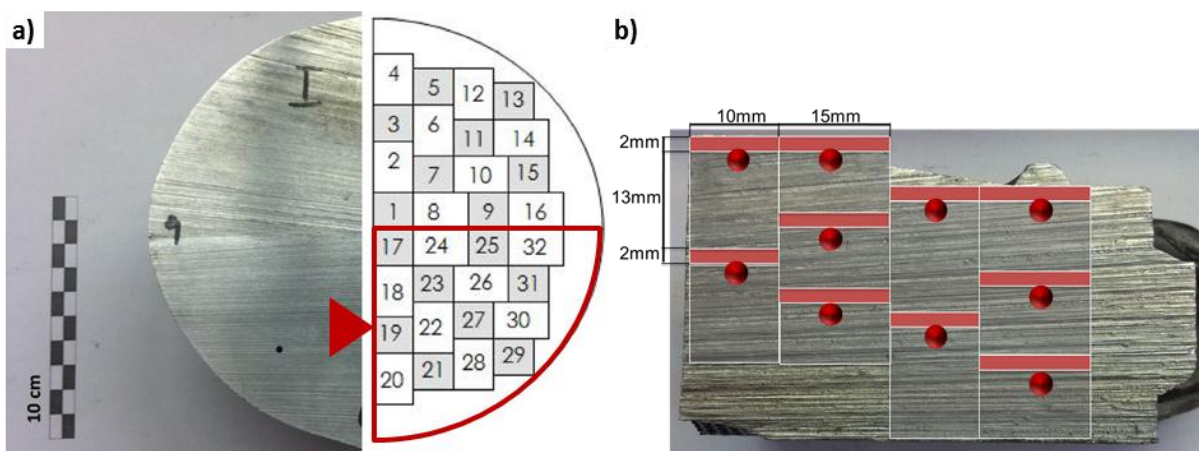


Fig. 2.2: top view (a) and side view (b) of one quarter of a piston with sample arrangement parallel (white in (a)) and perpendicular (gray in (a)) to the surface; spheres correspond to HB1/10 indentation.

2.3.2. Cooling of the piston after solution treatment

Six type K thermocouples were mounted in different positions and depths of a piston (Fig. 2.3) of a piston to determine the cooling rate during quenching from solution treatment temperature. The thermocouples were bonded with conducting paste at the bottom of drilled holes, depicted in Fig. 2.3 in red for 25mm and in blue for 15mm depth. These holes were sealed with two component ceramic glue. The piston was heated up until 500°C was reached at all thermocouple positions.

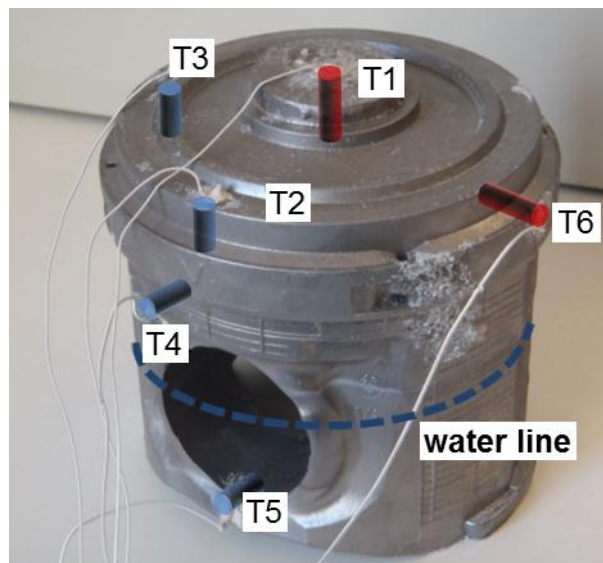


Fig. 2.3: Thermocouples configuration during quenching from solution treatment temperature (500°C). Blue markers correspond to a depth of 15mm, while red ones to a depth of 25mm

The quenching was carried out by submerging the piston in <60°C water up to the marked water line in Fig. 2.3. Data collection with 4 measuring points per second was performed by the data logger switch unit Agilent 34970A with the Benchlink datalogger II software.

2.3.3. Metallography

- Preparation of samples

Samples with a prismatic geometry of 10x10x2mm³ were cut from the piston and embedded in epoxy resin (Fig. 2.2). The grinding and polishing steps are shown in Tab. 2.3. The surface investigated was parallel to the surface of the piston head. Metallographic characterization was carried out with these samples to determine microstructural homogeneity within the piston as it was described in chapter 2.3.1.

polishing agent	grain size	time	force	velocity
SiC Papier+H ₂ O	#500	5 min	15 N	150 r/min
DS+lubricant blue	9 μm	4 min	15 N	300 r/min
DS+lubricant blue	6 μm	4 min	15 N	300 r/min
DS+lubricant blue	3 μm	4 min	15 N	300 r/min
DS+lubricant blue	1 μm	4 min	15 N	300 r/min
OP-S+water	0.04/0.08 μm	2 min	15 N	300 r/min

Tab. 2.3: Workflow of metallographic sample preparation

2.3.4. Light optical microscopy

A light optical microscope Axio imager M2m by Zeiss equipped with a Zeiss Axiocam MRC 5 camera was used for light optical micrography. Microstructural characterization of the alloys was carried out after different solution treatments (0h, 1h and 4h at 500°C) and as function of positions within the piston. The preprocessing of Images was carried out with the software Axio vision MRC 5 version 4.8.2.

2.3.5. Scanning electron microscopy

A FEI Phillips XL30 and a FEI Quanta 200 FEG (field emission gun) scanning electron microscope were used for qualitative analysis of deep etched samples. EDX analysis was carried out to determine elemental distribution in the different phases present in the investigated alloys. Deep etching was performed for 5 min by hydrochloric acid (HCl_{aqua}) with a concentration of 6 mol/l (50:50 concentrated HCl and water).

2.3.6. Light optical tomography

Light optical tomography was performed by two different serial sectioning methods, namely mechanical serial sectioning and ion milling serial sectioning. The light optical microscope mentioned in chapter 2.3.4 was used to acquire micrographs that were aligned, segmented and stacked to evaluate the 3D microstructure of the 1253 alloy after 0h and 4h of solution treatment at 500°C.

2.3.6.1. Mechanical serial sectioning

Mechanical serial sectioning [64] was executed removing material layers with the polishing machine Tegra-force 21 by Struers. For one sectioning step 1 μ m diamond suspension was used for 45-70 seconds. A high surface quality was achieved by using highly diluted OPS suspension for improving image processing and segmentation. Two samples of the 1253 alloy were analyzed in as-cast and after 4h solution treatment at 500°C. The mean depth of material removal for the sample in as-cast condition was 0.9 \pm 0.1 μ m, while a mean depth removal of 1.05 \pm 0.3 μ m was achieved for the 4h solution treated sample (Fig. 2.4). The removed depth was calculated as a function of the diagonal of the Vickers indentations:

Eq. 2.1:

$$\Delta h = \Delta D \cdot \frac{\cos(45^\circ)}{2 \cdot \tan(\frac{136.2^\circ}{2})} \approx \frac{1}{7} \Delta D$$

Δh removed depth

ΔD diagonal change of Vickers indentation between two consecutive sectioning steps

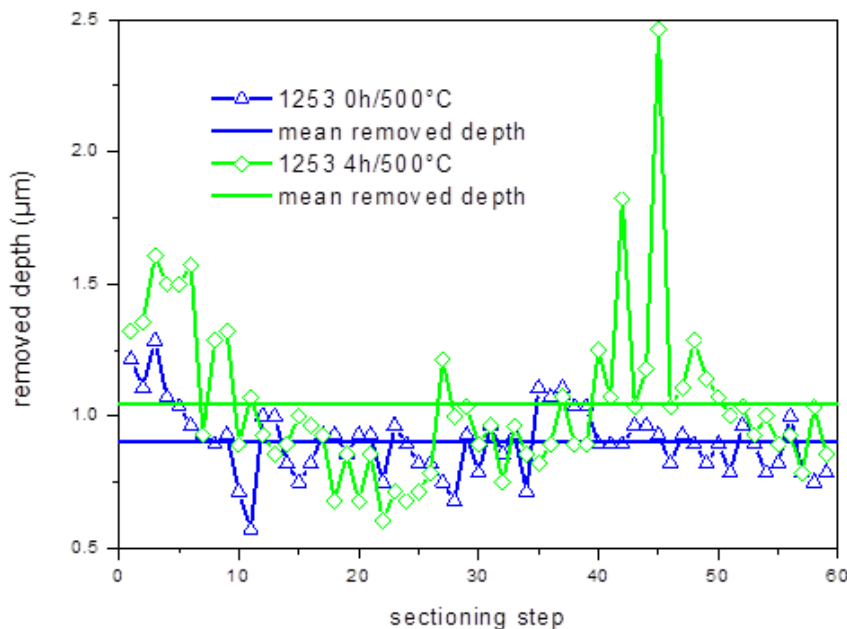


Fig. 2.4: Depth removal during mechanical serial sectioning of the 1253 alloy after 0h and 4h/500°C

The voxel size was $\sim 0.3 \times 0.3 \times 0.9 \mu\text{m}^3$ (0h/500°C) and $\sim 0.3 \times 0.3 \times 1.05 \mu\text{m}^3$ (4h/500°C). The total depth of removed material was $\sim 53.4 \mu\text{m}$ for the 0h/500°C condition and

~61.7 μm for 4h/500 $^{\circ}\text{C}$ (59 removal steps). The investigated volumes were 226x160x53 μm^3 and 226x160x62 μm^3 for 0h/500 $^{\circ}\text{C}$ and 4h/500 $^{\circ}\text{C}$, respectively. The micrographs were acquired with a size of 2584x1936 pixels in xy plane but the visible light and the depth removal in each step limited spatial resolution to ~0.3x0.3x1 μm^3 . The micrographs were stacked and aligned with ImageJ (Plugin StackReg [80]). Segmentation was carried out by hand supported by EDX maps acquired every ten sectioning steps. The elemental distribution was used for qualitative identification of phases.

2.3.6.2. Ion milling serial sectioning

This serial sectioning method was to best of the author's knowledge, performed for the first time in this work. An ion mill device Fishione 1010 was used for serial sectioning of the 1253 alloy in 0h/500 $^{\circ}\text{C}$ to achieve depth resolution of <1 μm . Instead of Vickers indentations for measuring the depth of material removed in each sectioning step, Knoop indentations were used because of their higher length-to-depth ratio, which makes them more sensitive to changes in depth as can be derived from Eq. 2.2.

Eq. 2.2:

$$\Delta h = \Delta D \cdot \frac{1}{2 \cdot \tan\left(\frac{172.5^{\circ}}{2}\right)} \approx \frac{1}{30} \Delta D$$

Δh removed depth

ΔD variation between sectioning steps of the longest diagonal of the Knoop indentation

The indentations were also used to define a region of interest as shown in Fig. 2.5a. The parameters of the ion mill were optimized to yield a good surface quality, a removal depth of ~0.38 μm and prevent the formation of a rough topography owing to heterogeneous removal of distinct microstructural constituents. The balance of the dissimilar removal depths of constituents led to the milling parameters shown in Tab. 2.4. The removal depth achieved is displayed in Fig. 2.6. The total removed depth was ~13.1 μm in 34 steps with a mean sectioning depth of 0.38 \pm 0.18 μm . The voxel size using 1000x magnification in the light optical microscope was

$\sim 0.27 \times 0.27 \times 0.38 \mu\text{m}^3$. The images were stacked, registered and segmented as described in chapter 2.3.6.1. The total investigated volume was $\sim 134 \times 93 \times 13.1 \mu\text{m}^3$

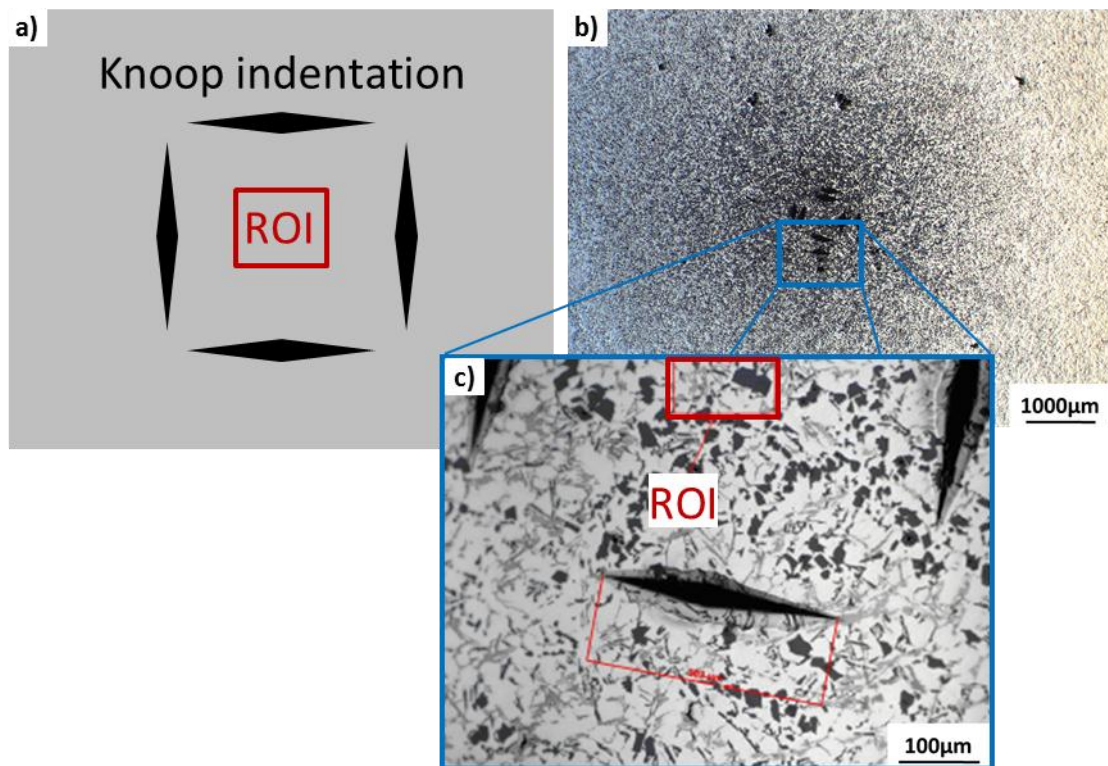


Fig. 2.5: a) Position of Knoop indentations and region of interest b) low magnification overview of sample c) detail showing microstructure and position of region of interest

voltage (kV)	current (mA)	inclination (°)	milling time (min/step)
2.5	8	2	~300

Tab. 2.4: Ion mill parameters used during sectioning

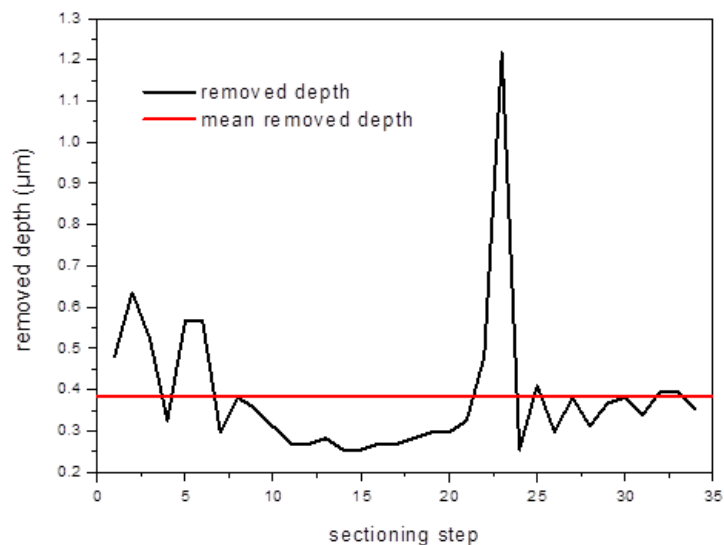


Fig. 2.6: Depth removed by ion milling after consecutive sectioning steps

2.3.7. Synchrotron tomography

The alloys were imaged at the ID19 beamline of the European Synchrotron Radiation Facility (ESRF), with a pink beam with maximum flux at 17.6 keV. The sample to detector distance of 39mm made imaging with absorption and phase contrast possible. One scan consisted of 1000-1500 radiographies. Two different detectors, namely FReLoN [81] and PCO Dimax [82], were used. Alloys 1062, 1252, 1740 and 1252-Mg were imaged by the FReLoN camera with a voxel size of $(0.28\mu\text{m})^3$ and an exposure time of 0.1s per projection. The same sample of each alloy was imaged in as-received (0h/500°C) condition and after 1h and 4h of solution treatment at 500°C. The scanned volume was cylindrical with 0.6mm in diameter and 0.6mm height. The size of the quantified volume was $\sim 420 \times 420 \times 500 \mu\text{m}^3$ in the case of 1062, 1252, 1252-Mg and 1740 alloy. The 1253 alloy was imaged by the PCO camera with a voxel size of $(0.55\mu\text{m})^3$ and exposure time of 5ms per projection. The size of the quantified volume was $\sim 650 \times 650 \times 1000 \mu\text{m}^3$ for the 1253 alloy. Two different scintillators were used, namely a Eu-doped Ga-Gd-Garnet (GGG Eu) and a Tb-doped Lu-Oxyorthosilicate (LSO Tb4.8) [83]. Fig. 2.7 shows a schematic layout of the setup used at the ID19 beamline.

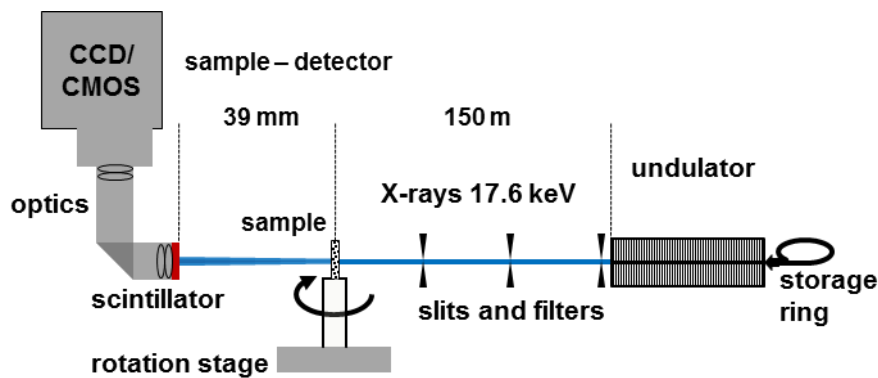


Fig. 2.7: Schematic layout of the setup at the ID19 beamline of the ESRF

2.3.7.1. Reconstruction, segmentation and image processing

Reconstruction of tomographic scans was carried out with a filtered backprojection algorithm applying additional CCD-filtering (median filter to correct spikes) and sinogram-filtering [84] (filtering sinograms with a high-pass filter to correct for ring artefacts) at the ESRF. The main challenge was to optimize the segmentability of all phases.

The reconstruction with filtered backprojection provided satisfying results for highly absorbing phases, as representatively shown in Fig. 2.8a. The primary and eutectic

Si, revealed by phase contrast, showed poor contrast with respect to the Al-matrix (Fig. 2.8d). This hindered a confident segmentation of Si.

One-distance phase retrieval with the approach proposed by Paganin [76] was implemented as an alternative solution. First, reconstruction was carried out after filtering with a δ/β ratio of 200, corresponding to Si (Fig. 2.9).

The δ/β ratio describes the relation between refraction and absorption of X-rays. The refractive index decrement (δ) represents the phase shift and β , directly proportional to the attenuation coefficient, represents the absorption (amplitude change) of the X-ray passing through the material.

However, the segmentation of Si proved to be difficult because the one-distance phase retrieval strongly blurred the highly absorbing aluminides. This led to contrast gradients at the interfaces between high and low absorbing constituents, as can be seen in Fig. 2.8b. Applying an unsharp mask filtering as described by Sanchez et al. [77], was also not satisfactory in terms of segmentability of phases.

The one-distance phase retrieval by ANKA Phase [78], an application for filtering of projections available as plugin for Fiji/ImageJ, was used as a second possible preprocessing route. The additional image restoration implemented in ANKA phase, described by Andrews et al. [85], did not solve the segmentability by global grey-value thresholding but improved the segmentation by hand. The result of filtering with $\delta/\beta=50$, corresponding to the mean value of aluminides, can be seen in Fig. 2.8c. This pre-processing route showed improvement in identifying Si (Fig. 2.8f). None of the mentioned pre-processing routes made a complete segmentation of low absorbing phases by global threshold possible.

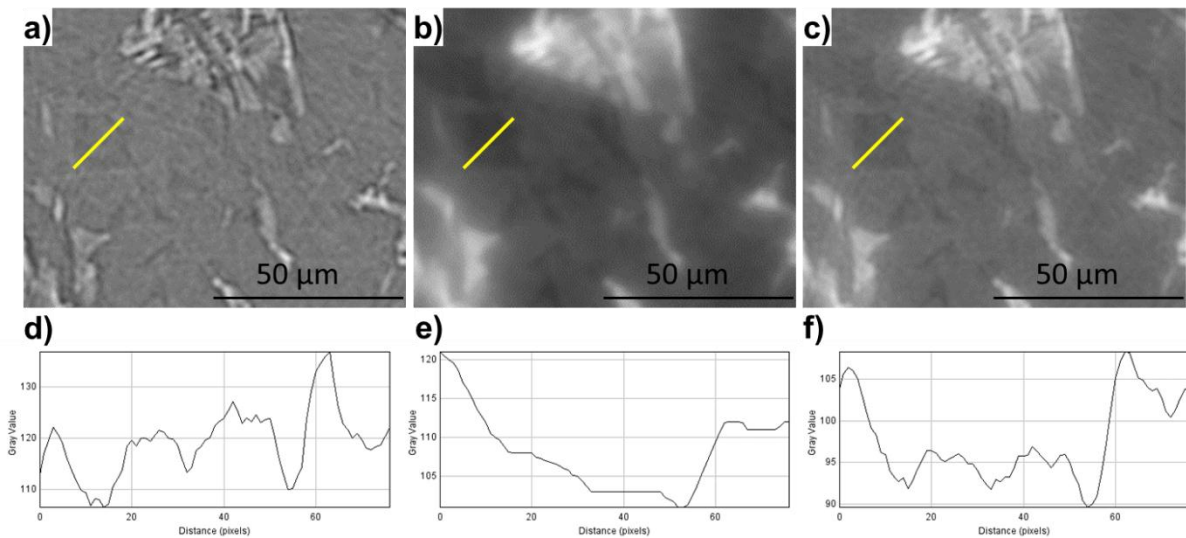


Fig. 2.8: Portions of slices reconstructed after different pre-processing approaches a) standard reconstruction by filtered backprojection b) one-distance phase retrieval reconstruction with $\delta/\beta=200$, corresponding to Si (at 17.6keV) c) one-distance phase retrieval with $\delta/\beta=50$, corresponding to aluminides (~mean value of Al_9FeNi , Al_2Cu and $\text{Al}_7\text{Cu}_4\text{Ni}$) + stabilization with ANKA Phase [78] in the 1252 alloy.

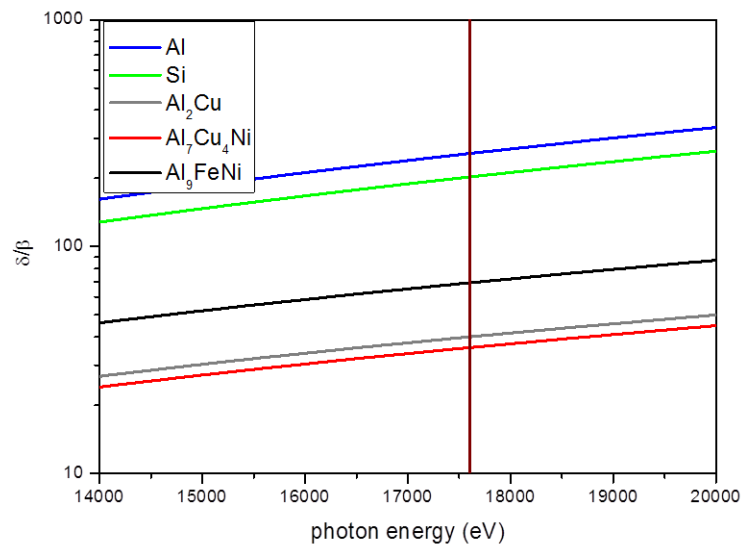


Fig. 2.9: δ/β ratio as a function of photon energy (17600eV photon energy marks the energy during tomography) [86].

The preprocessing and image processing were carried out with Fiji/ImageJ 1.48, Avizo fire 7 and 8. A detailed flow chart of image processing is shown in Fig. 2.10.

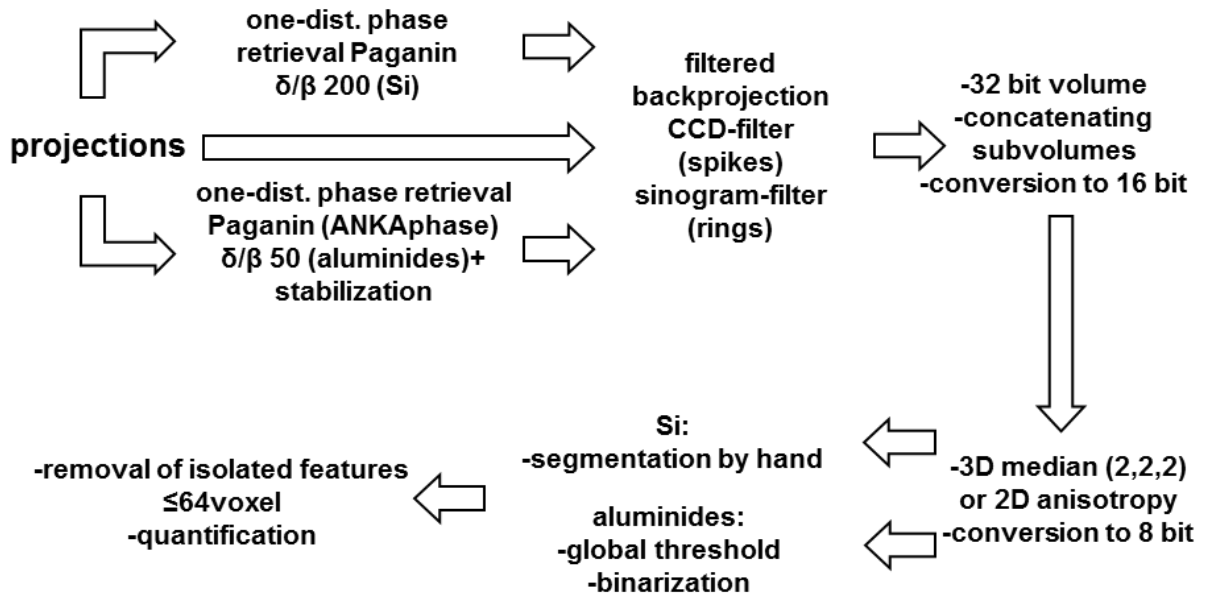


Fig. 2.10: Flow chart of volume reconstruction and image processing

2.3.7.2. Morphological analysis

The principal curvatures are defined as the maximum and minimum curvatures of a surface in a point where all curves have the same tangent vector [87] (Fig. 2.11). This can be seen as normal curvatures of a tangent plane intersecting in a point of the surface. Mean (Germain-) and total (Gaussian-) curvatures were calculated using Avizo (version 7 and 8) to describe the surface morphology of aluminides and Si. These curvatures are derived from the two principal curvatures, $\frac{1}{r_{min}}$ and $\frac{1}{r_{max}}$, as can be seen in Eq. 2.3 and Eq. 2.4, where r_{min} and r_{max} correspond to the minimum and maximum curvature radii of the surface in a point.

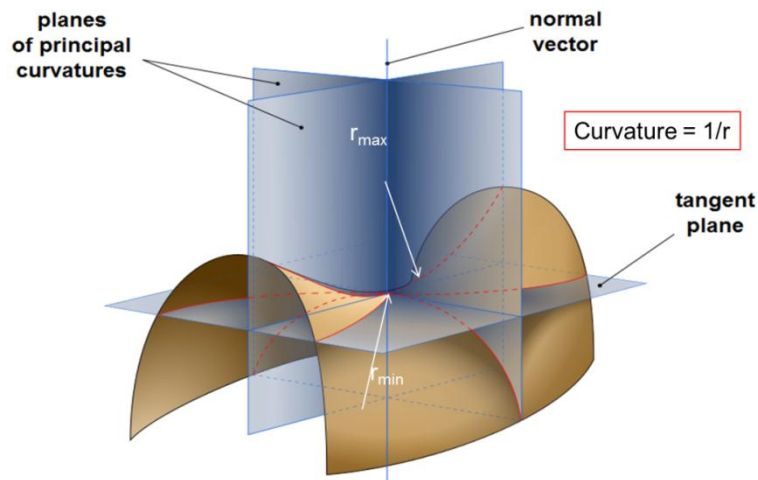


Fig. 2.11: Description of principal curvatures on a surface in the three dimensional space [87].

Eq. 2.3:

$$\textit{Gaussian curvature} = \frac{1}{r_{min}} \times \frac{1}{r_{max}}$$

Eq. 2.4:

$$\textit{mean curvature} = \frac{\left(\frac{1}{r_{min}} + \frac{1}{r_{max}}\right)}{2}$$

The computation of these curvatures is based on a discrete triangular surface. The algorithm works by approximating the surface locally by a quadric form. The mean and Gaussian curvatures were calculated separately from the rendered surface of segmented constituents. After saving these curvatures in a text file and combining them into one file with two rows 100k values were randomly chosen from datasets of >100M values. The randomly chosen values correspond to the mean and Gaussian curvatures of one specific point on the surface of the rendered phase. Absolute zeroes for Gaussian and mean curvatures were ignored in the selection process to avoid effects of the flat borders of the investigated volumes.

2.3.8. Hardness tests

Brinell hardness tests HB(1/10) were performed with an EMCO Test M1C-010 device. Samples of the investigated alloys were tested after 0h and 1h of solution treatment at 500°C with subsequent ageing at 300°C for up to 500h to determine a stable T7 condition. The samples were water quenched after ageing treatment at 300°C and stored in liquid N₂ to avoid natural ageing prior to the Brinell hardness tests.

2.3.9. Nanohardness of matrix

Nanoindentations were carried out with a TI-750 device by Hysitron to determine the hardness of the matrix of the alloys after 0h and 1h of solution treatment at 500°C with subsequent overaging for 100h at 300°C. A Berkovich indenter was used with a maximum applied force of 3000µN. The loading cycle is shown in Fig. 2.12. At least 30 indentations (3 groups of 10) were performed to get a statistically relevant hardness value.

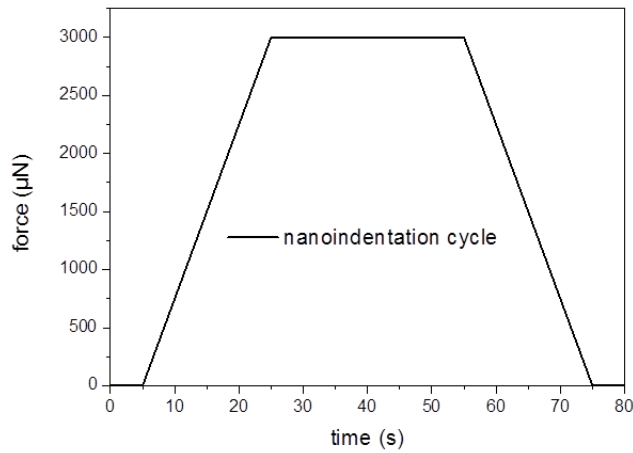


Fig. 2.12: Loading cycle applied during nanoindentation

2.3.10. Thermo-mechanical tests

2.3.10.1. Compression tests

Compression tests were carried out in a Dil-805D Bähr dilatometer equipped with a deformation unit. Temperature was controlled by a type K thermocouple welded on the center of the sample.

Cylindric samples with 10 ± 0.1 mm length and 5 ± 0.1 mm diameter were used for compression tests at RT, 300°C and 380°C. The investigated heat treatment conditions for all alloys are shown in Tab. 2.5.

- Strain rate: $1.1 \times 10^{-3} \text{ s}^{-1}$
- total Deformation: 3-4 mm, $\epsilon = 0.3$ (RT), $\epsilon = 0.4$ (300°C/380°C)

	solution treatment	ageing treatment	overageing treatment
Temperature	500°C	230°C	300°C
time/duration	0/1h/4h	5h	100h

Tab. 2.5: Heat treatments applied for thermo-mechanical tests

2.3.10.2. Tensile tests

Tensile tests were carried out at 300°C and 380°C in a Gleeble-1500. The samples were machined according to the geometry shown in Fig. 2.13. The pre-forms of samples were cut from the determined region of trust (chapter 2.3.1). The

2.3.10.4. Young's modulus

The determination of the Young's modulus between RT and 380°C was necessary to evaluate the data obtained during thermo-mechanical fatigue experiments. For this dynamic mechanical analysis was carried out in a G2 device by RSA. Three point bending was operated with 1N of pre-force, 0.02% strain by 1Hz. The support jaws had a distance of 25mm. Constant heating rate of 5K/min was applied. Samples were 30mm±0.2 in length, 10mm±0.1 in width and of 1.2mm±0.01 thickness.

2.3.10.5. Thermo-mechanical fatigue

Thermo-mechanical fatigue tests were performed using a Gleeble-1500 for all investigated alloys in the conditions shown in Tab. 2.6. The geometry was the same as for the high temperature tensile tests (Fig. 2.13). Two types of temperature cycles were applied with constant load. The heating and cooling rate was 12.5K/s and a dwell time of 3s was applied at minimum and maximum temperature. Therefore, one thermal cycle lasted 46s for a temperature variation between 50-300°C and 58.8s in case of a variation between 50-380°C. The temperature profiles are presented in Fig. 2.15.

alloy	ST time 500°C [h]	overaging time at 300°C [h]	temperature range	load [MPa]
1062	0/1/4	100	50-300°C	50(0.5xRp _{0.2} ^{300°C})
			50-380°C	35(0.5xRp _{0.2} ^{380°C})
1252	0/1/4	100	50-300°C	50(0.5xRp _{0.2} ^{300°C})
			50-380°C	35(0.5xRp _{0.2} ^{380°C})
1740	0/1/4	100	50-300°C	50(0.5xRp _{0.2} ^{300°C})
			50-380°C	35(0.5xRp _{0.2} ^{380°C})
1253	0/1/4	100	50-300°C	50(0.5xRp _{0.2} ^{300°C})
			50-380°C	35(0.5xRp _{0.2} ^{380°C})
1252-Mg	0/1/4	100	50-300°C	50(0.5xRp _{0.2} ^{300°C})
			50-380°C	35(0.5xRp _{0.2} ^{380°C})

Tab. 2.6: Investigated alloys, initial conditions and test parameters used for thermo-mechanical fatigue experiments

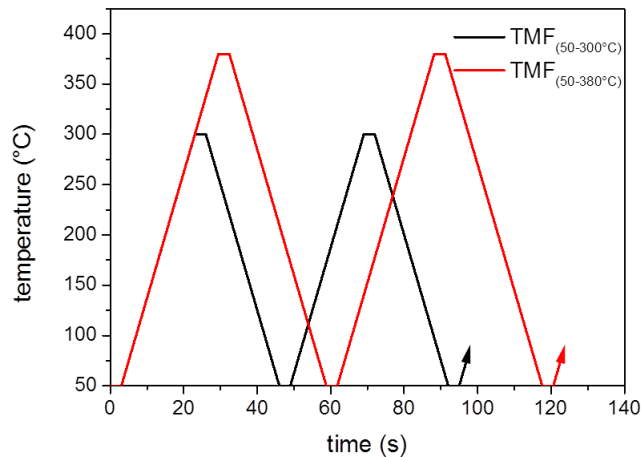


Fig. 2.15: Temperature cycles at constant load applied for the thermo-mechanical fatigue tests

The total elongation measured during a thermo-mechanical fatigue test (ϵ_{TMF}) can be divided in three parts: i) the thermal elongation produced by the change of temperature (ϵ_{cte}), ii) the elongation due to the decrease of elastic properties (Young's modulus) with increasing temperature ($\epsilon_{\Delta E}$) and iii) the effective plastic elongation or remaining plastic elongation (ϵ_{pl}). In Eq. 2.5 the relations between these contributions and the total elongation are shown. The elongation caused by thermal expansion was calculated as described in Eq. 2.6. The elongation due to the decrease of Young's modulus was calculated as shown in Eq. 2.7. To calculate the resulting plastic strain the coefficient of thermal expansion CTE (α) and the Young's modulus were measured as a function of temperature as described in chapters 2.3.10.3 and 2.3.10.4.

Eq. 2.5:

$$\epsilon_{pl} = \epsilon_{TMF} - \epsilon_{cte} - \epsilon_{\Delta E}$$

ϵ_{TMF} strain measured during the thermo-mechanical fatigue test (total relative elongation).

Eq. 2.6: Elongation caused by the thermal expansion during temperature cycling

$$\epsilon_{cte} = \alpha \cdot \Delta T$$

Eq. 2.7: Elongation due to the variation of Young's modulus during thermal cycling

$$\epsilon_{\Delta E} = \sigma \left(\frac{1}{E_{(T)}} - \frac{1}{E_{50^{\circ}\text{C}}} \right)$$

σ =applied load

$E_{50^{\circ}\text{C}}$ =Young's modulus at 50°C

$E_{(T)}$ =Young's modulus at Temperature T

3. Results

3.1. Cooling of the pistons after solution treatment

The temperature evolution during water quenching of the piston after solution treatment at 500°C was measured as function of time and position to determine the actual cooling rate. Fig. 3.1 shows the cooling curves obtained. The thermocouples T1, T2, T3 and T6 exhibited a cooling rate of ~3K/s between 500°C and 250°C. The cooling rate of T4 was ~6K/s in the same temperature range. The results show that the cooling rate in all parts of the piston head, from where all samples for further investigations were taken, is between 3-6K/s.

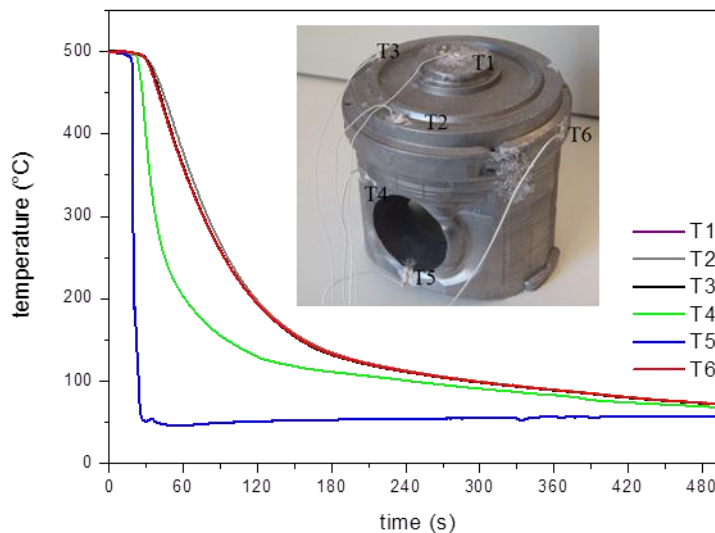


Fig. 3.1: Cooling curves during water quenching of the piston after solution treatment at 500°C.

3.2. Region of trust

Fig. 3.2 shows color-coded Brinell hardness maps obtained at different depths from the top surface of a piston of the 1062 alloy in as-cast condition. It can be seen that the hardness is higher in the vicinity of the surface and becomes more homogeneous at depths between 12 and 22mm. Therefore, the region of trust for obtaining samples for further investigations was chosen as depicted in Fig. 3.3.

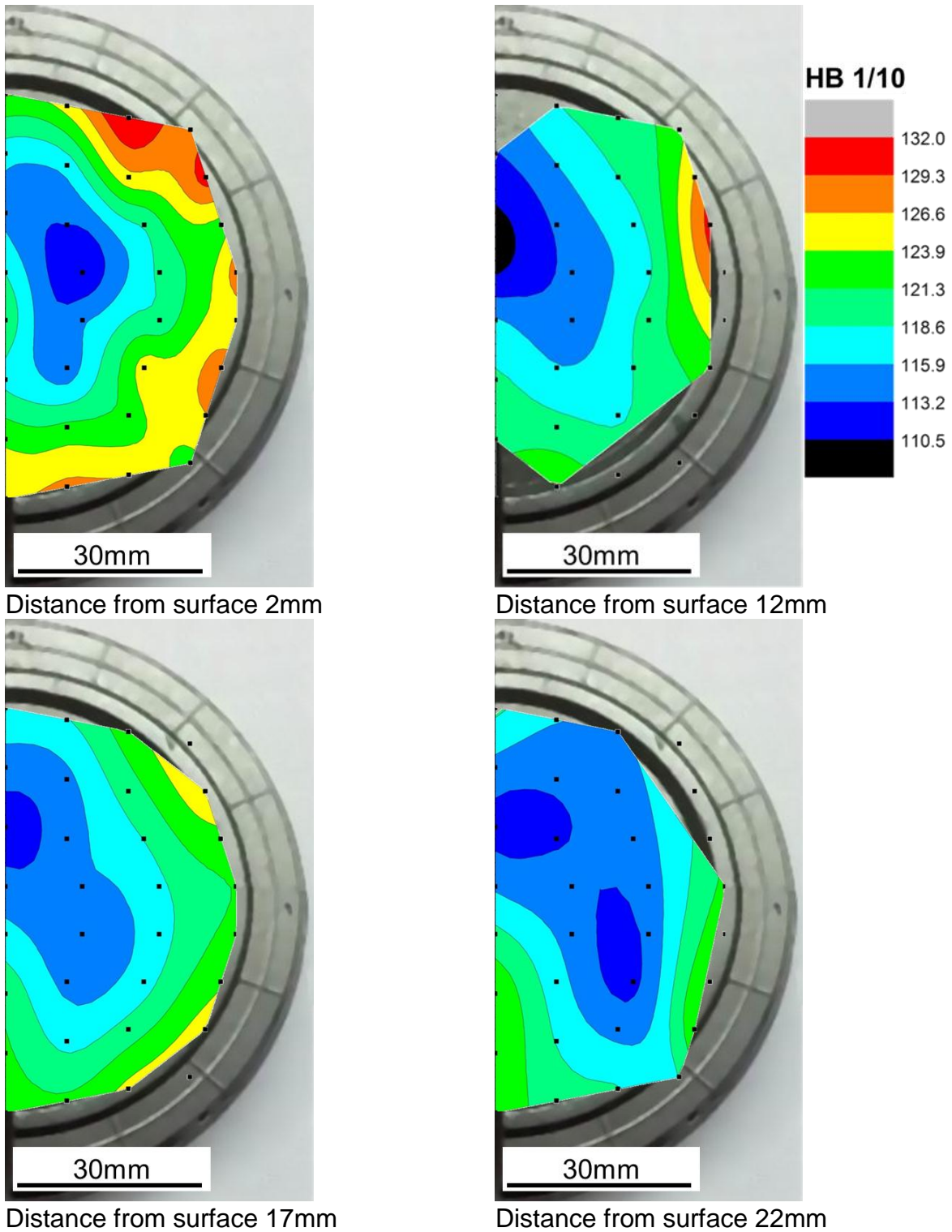


Fig. 3.2: Brinell hardness maps at different depths from the top of the surface of a piston of the 1062 alloy in as cast condition.



Fig. 3.3: Region of trust chosen taking into account the Brinell hardness maps.

3.3. Light optical microscopy

3.3.1. Effect of solution treatment time

Samples of all alloys taken from the region of trust (Fig. 3.3) were solution treated at 500°C and prepared for metallographic investigations. The alloys 1062, 1252, 1253 and 1252-Mg show microstructures formed by primary Si, eutectic Si and several aluminides embedded in the α -Al matrix (Fig. 3.4 to Fig. 3.7). Fig. 3.4 displays the 1062 alloy after 0h (a, b), 1h (c, d) and 4h (e, f) at 500°C. Slight spheroidization of primary and eutectic Si can be observed after 1h and 4h. The degree of spheroidization seems to increase with solution treatment time. The same trend can be observed for the alloys 1252 (Fig. 3.5), 1253 (Fig. 3.6) and 1252-Mg (Fig. 3.7). Fig. 3.8 shows the results for the 1740 alloy. Spheroidization of primary and eutectic Si is more pronounced than for the other alloys. Furthermore, some aluminides also seem to spheroidize during solution treatment.

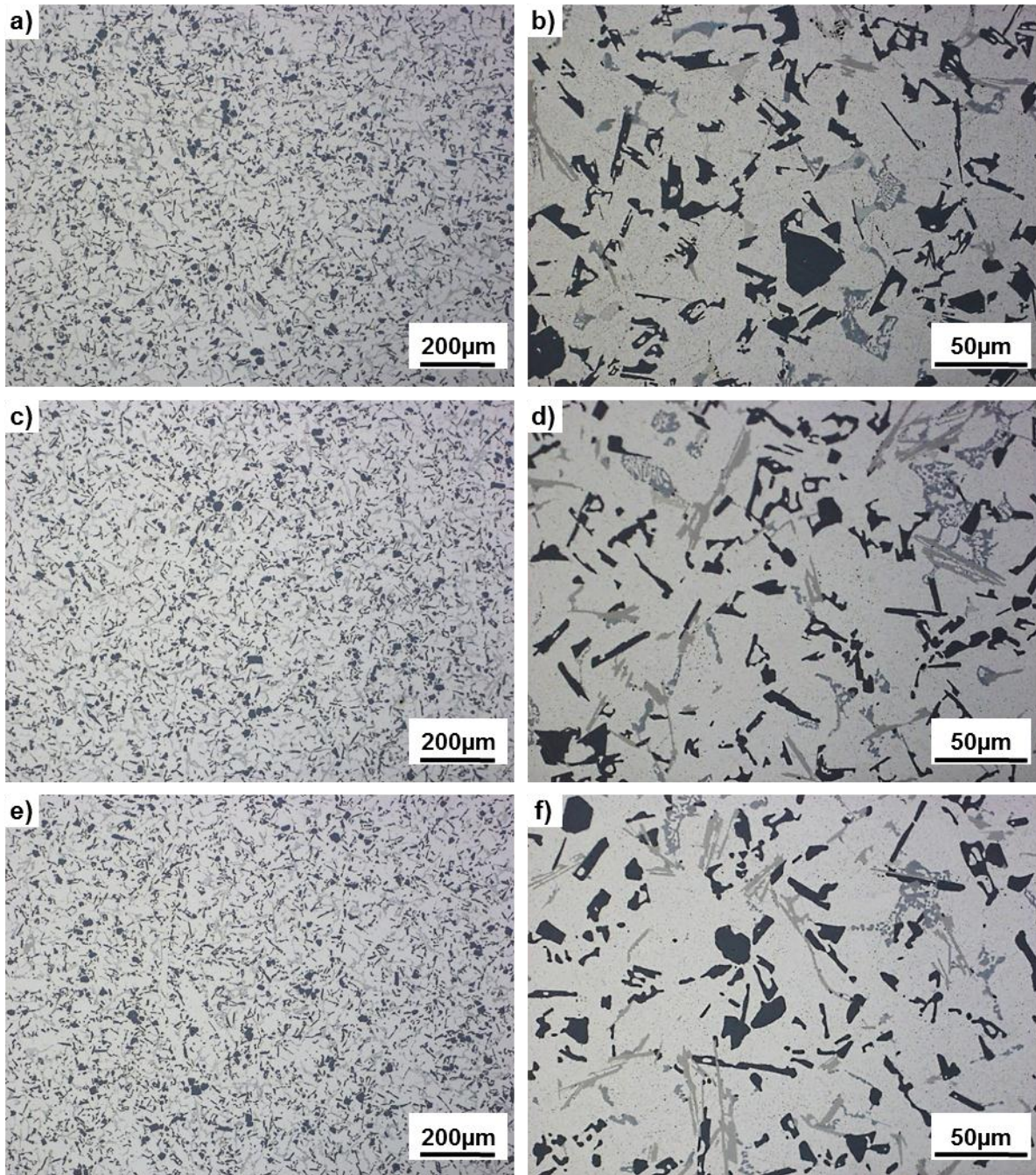


Fig. 3.4: Light optical micrographs of the 1062 alloy after solution treatment at 500°C: a), b) 0h, c), d) 1h, e), f) 4h.

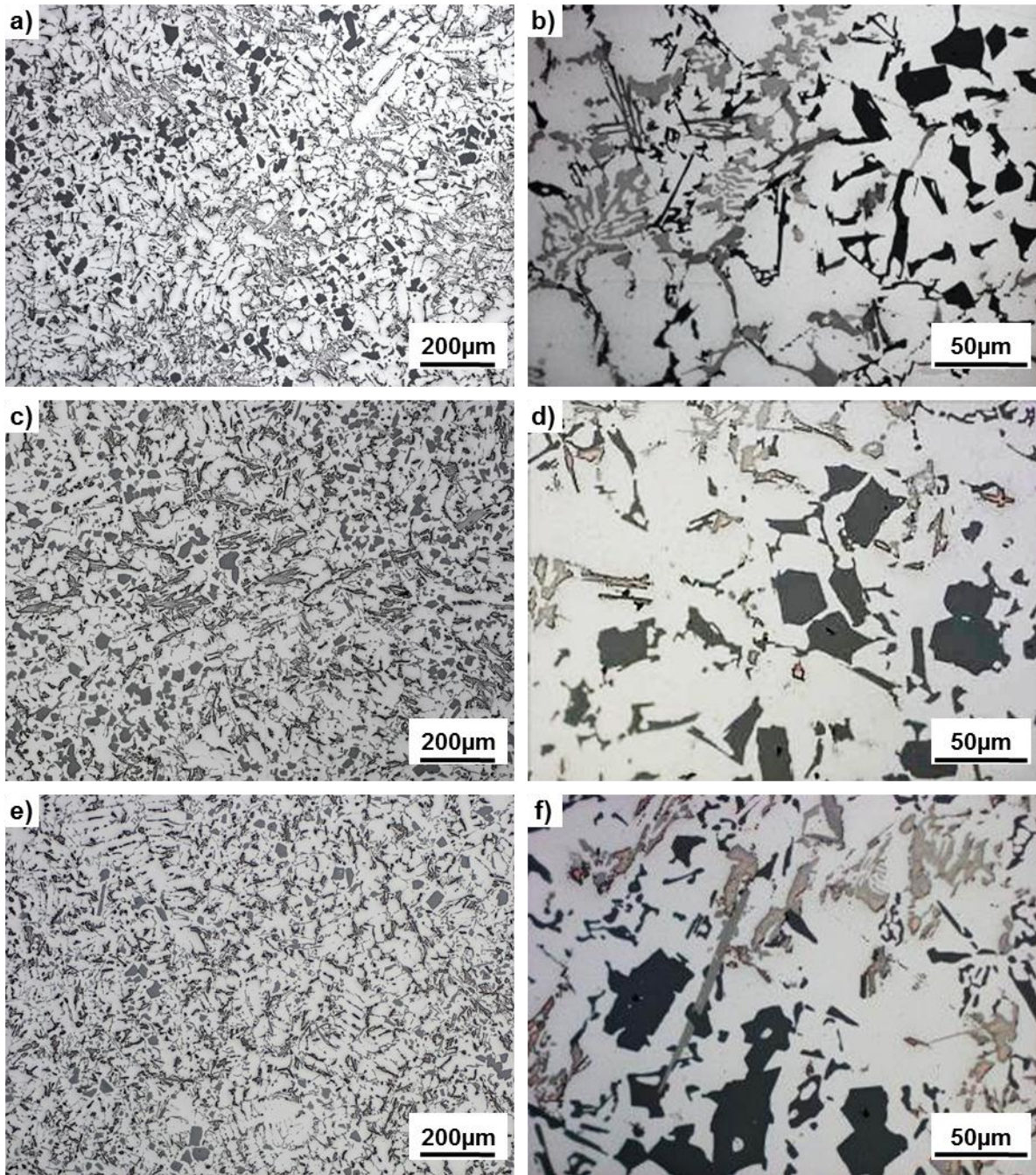


Fig. 3.5: Light optical micrographs of the 1252 alloy after solution treatment at 500°C: a), b) 0h, c), d) 1h, e), f) 4h.

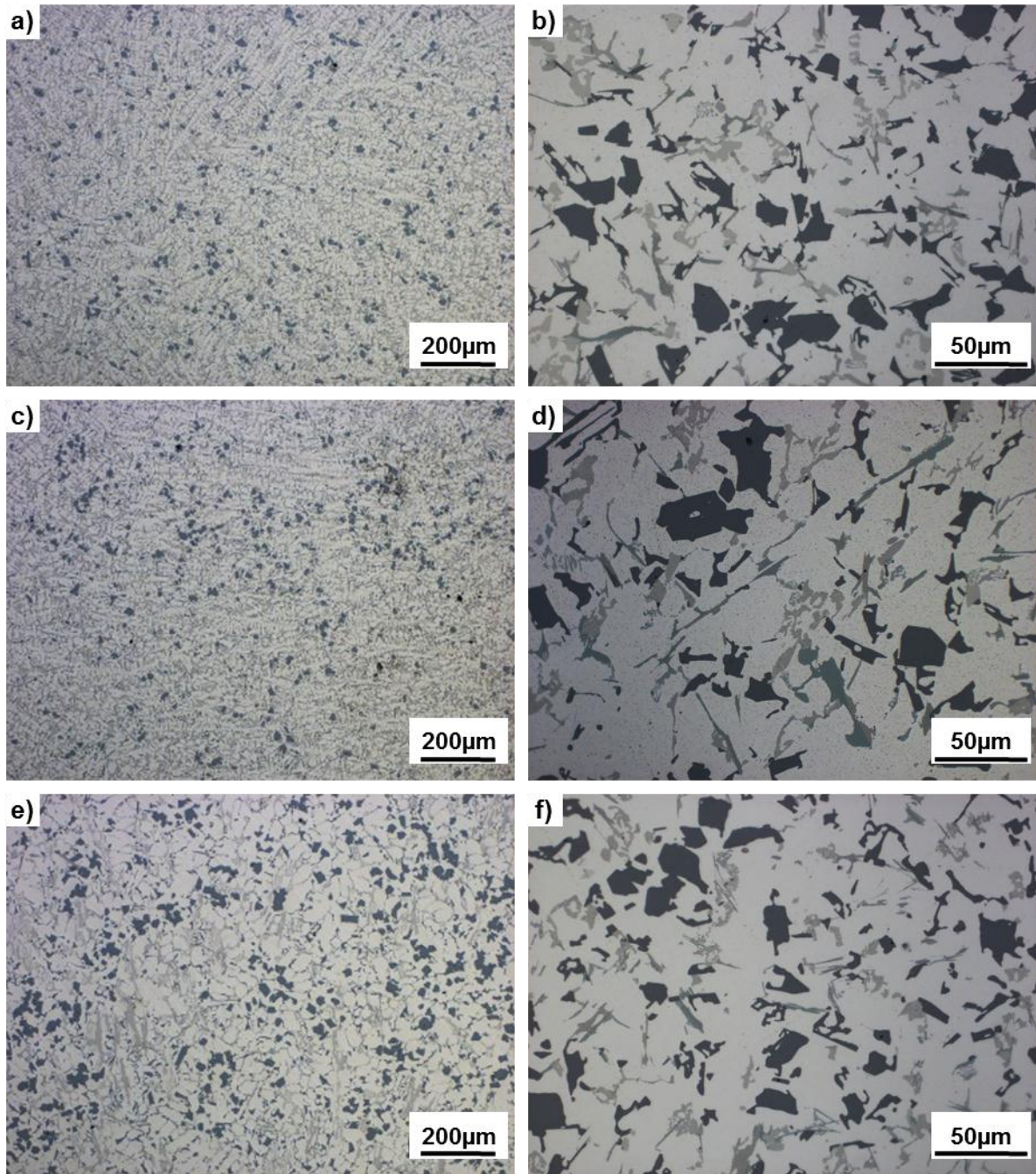


Fig. 3.6: Light optical micrographs of the 1253 alloy after solution treatment at 500°C: a), b) 0h, c), d) 1h, e), f) 4h.

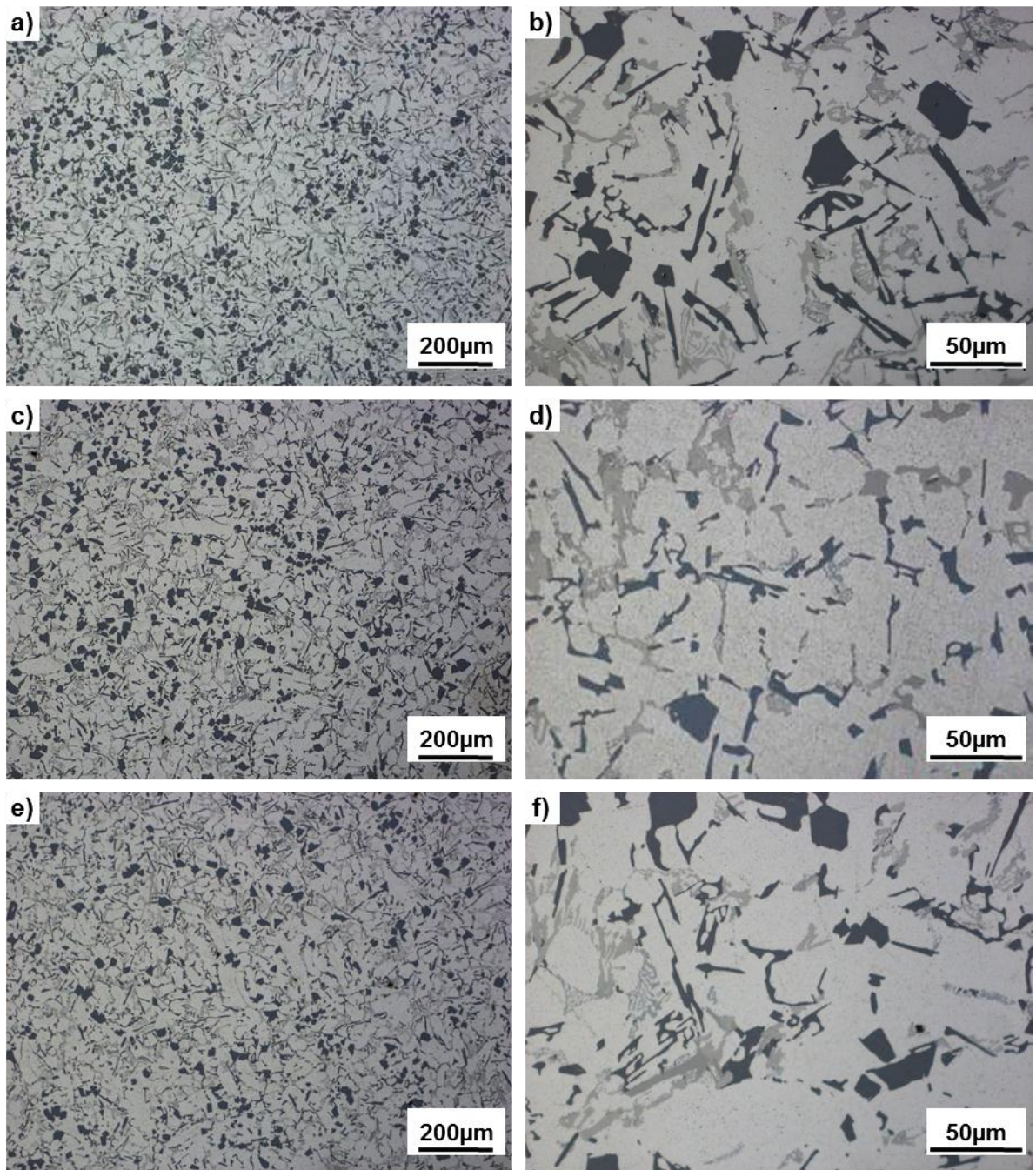


Fig. 3.7: Light optical micrographs of the 1252-Mg alloy after solution treatment at 500°C: a), b) 0h, c), d) 1h, e), f) 4h.

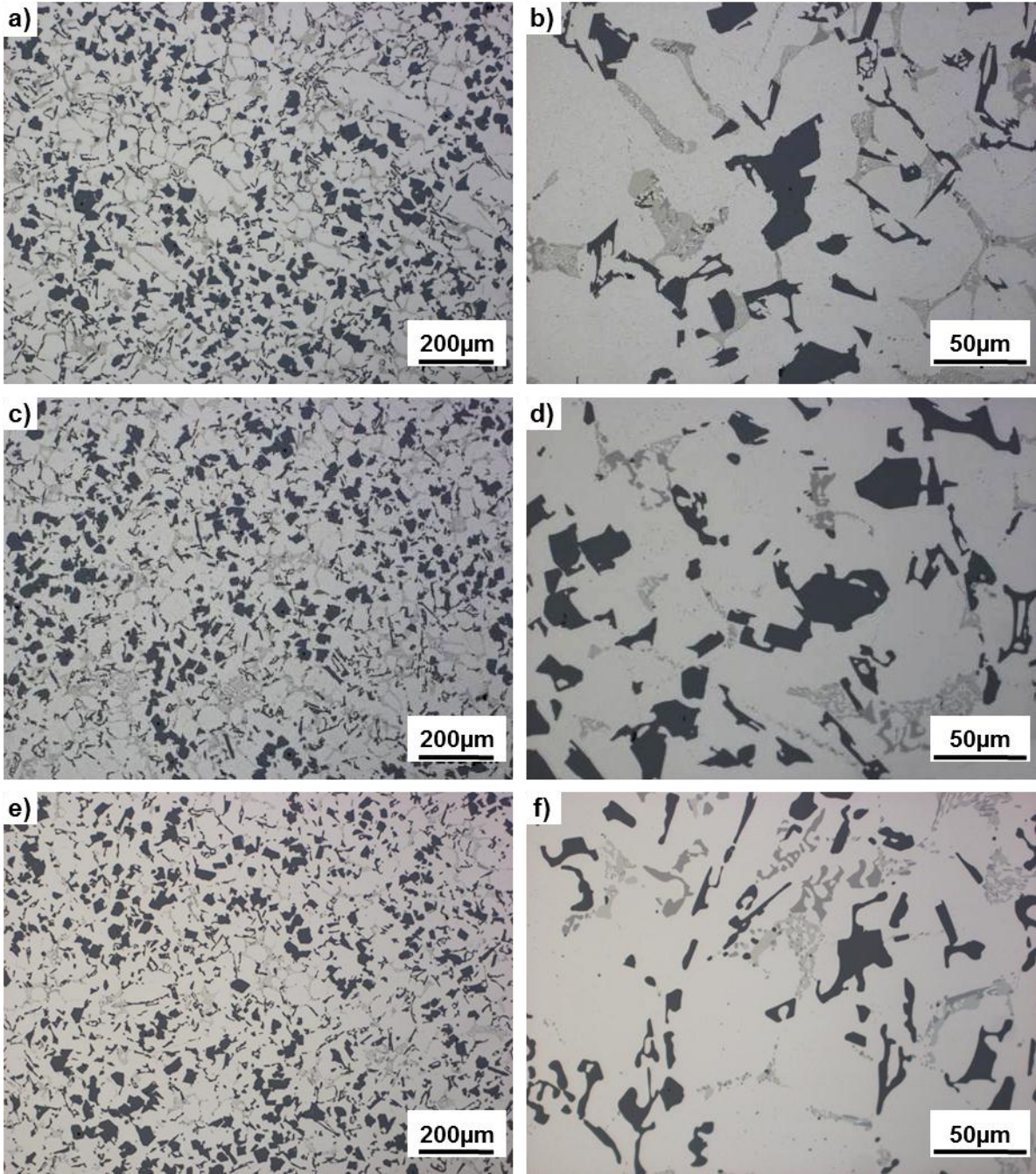


Fig. 3.8: Light optical micrographs of the 1740 alloy after solution treatment at 500°C: a), b) 0h, c), d) 1h, e), f) 4h.

3.4. SEM

3.4.1. Effect of solution treatment time

The interconnectivity of Si and its contiguity with the different aluminides can be observed qualitatively in the micrographs of deep etched samples shown in Fig. 3.9, Fig. 3.10 and Fig. 3.11 for the 1062, 1252 and 1740 alloys, respectively. Backscattered electron (BSE) micrographs are shown next to secondary electron (SE) micrographs to distinguish Si and aluminides. The network of Si and Aluminides remains highly interconnected even after 4h at 500°C.

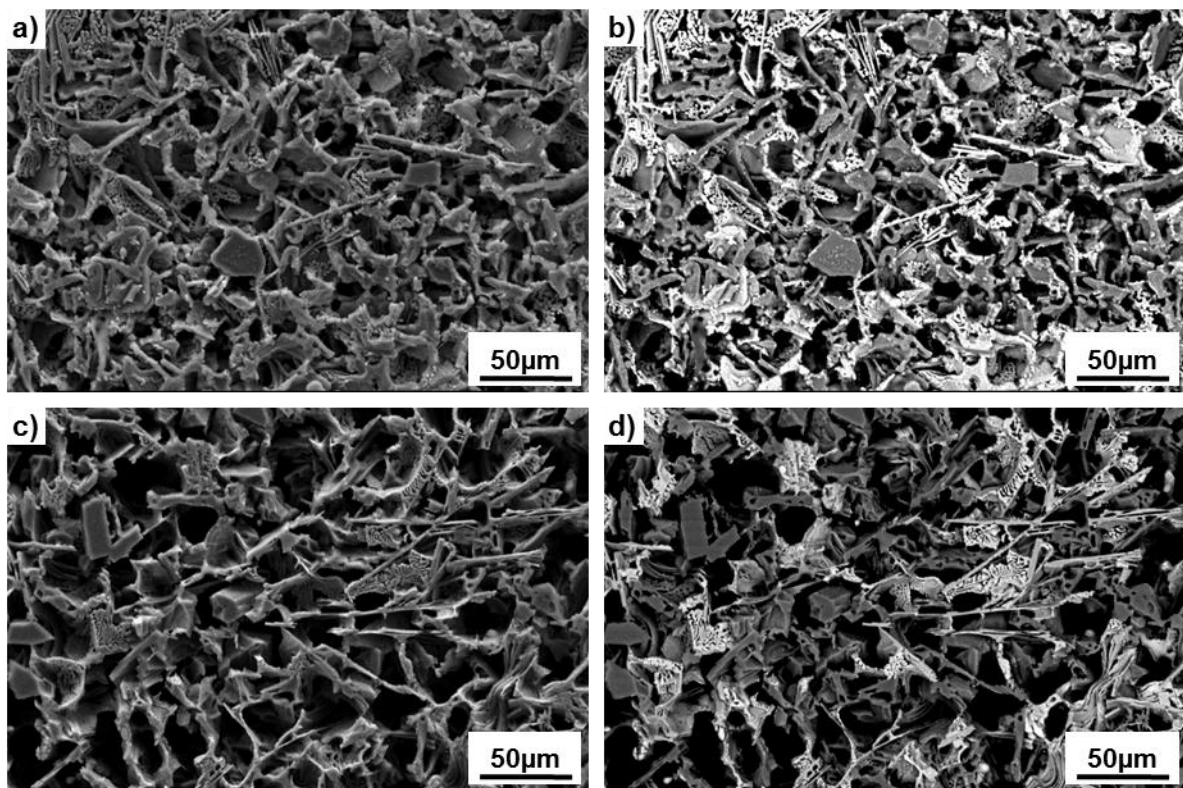


Fig. 3.9: SE (a,c) and BSE (b,d) micrographs of the deep etched 1062 alloy after 0h (a,b) and 4h (c,d) at 500°C.

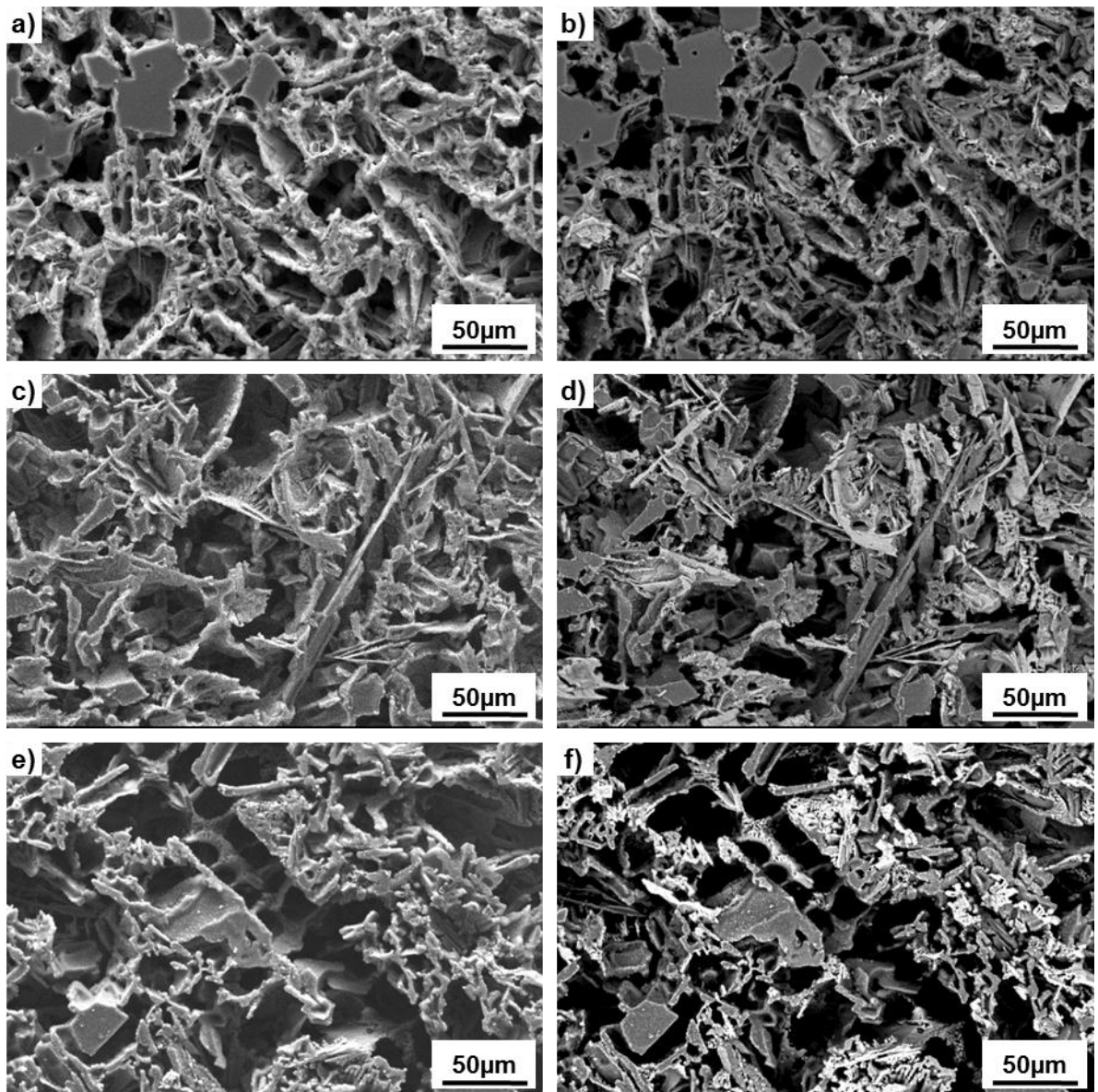


Fig. 3.10: SE (a,c,e) and BSE (b,d,f) micrographs of the deep etched 1252 alloy after 0h (a,b), 1h (c,d) and 4h at 500°C (e,f).

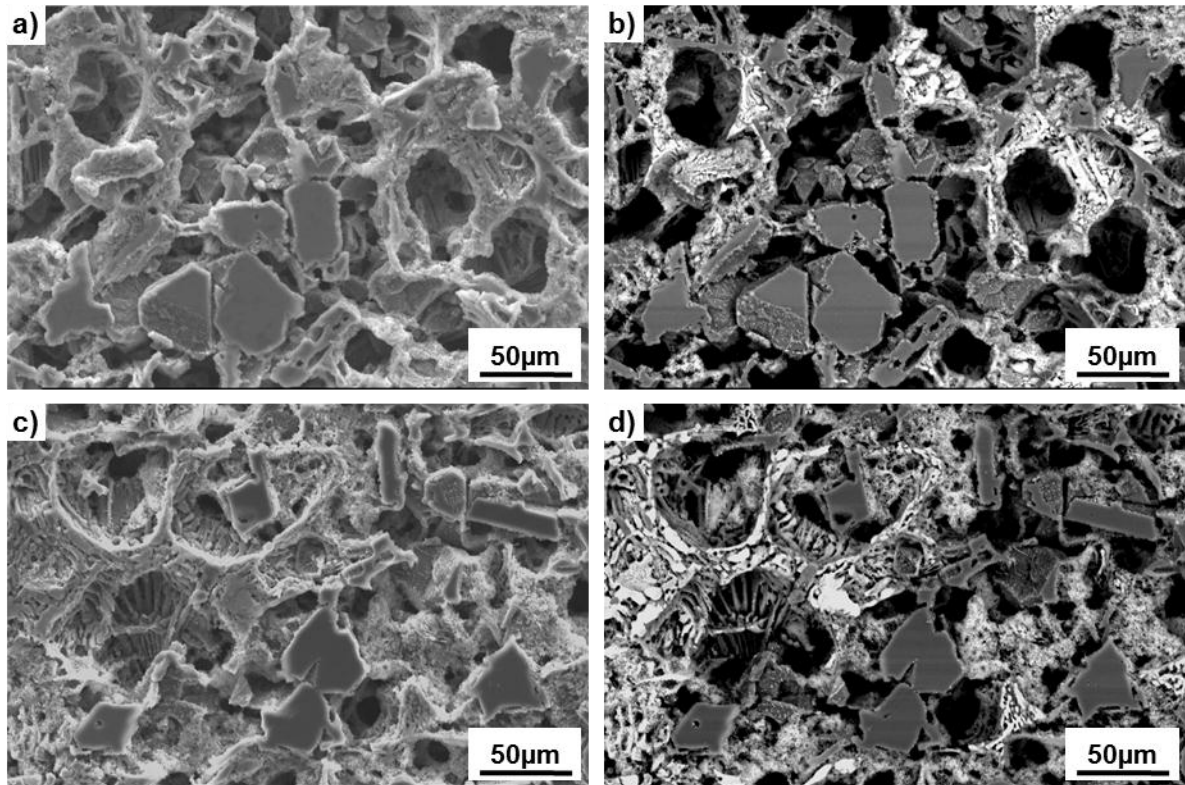


Fig. 3.11: SE (a,c) and BSE (b,d) micrographs of the deep etched 1740 alloy after 0h (a,b) and 4h at 500°C (c,d).

3.4.2. Effect of ageing time at 300°C

The size of precipitates in the α -Al matrix after overaging heat treatment during 100h at 300°C was analyzed qualitatively for all alloys by means of scanning electron microscopy. Fig. 3.12 shows BSE micrographs of the 1062 and 1740 alloys. After 100h at 300°C AlCu(Mg) and $Al_{20}Cu_2Mn_3$ precipitates in the 1062 alloy have a size of ~300-600nm (Fig. 3.12a,b). All alloys showed similar precipitation sizes as the 1062 alloy after overaging. The number and size of precipitates revealed by SEM in the 1062 alloy remains fairly constant with respect to 0h/500°C+100h/300°C after solution treatment at 4h/500°C with subsequent overaging for 100h at 300°C (Fig. 3.12a and Fig. 3.12b). In the case of the 1740 alloy the amount of precipitates revealed by SEM increases with respect to 0h/500°C+100h/300°C after solution treatment at 4h/500°C and subsequent overaging (Fig. 3.12c and Fig. 3.12d).

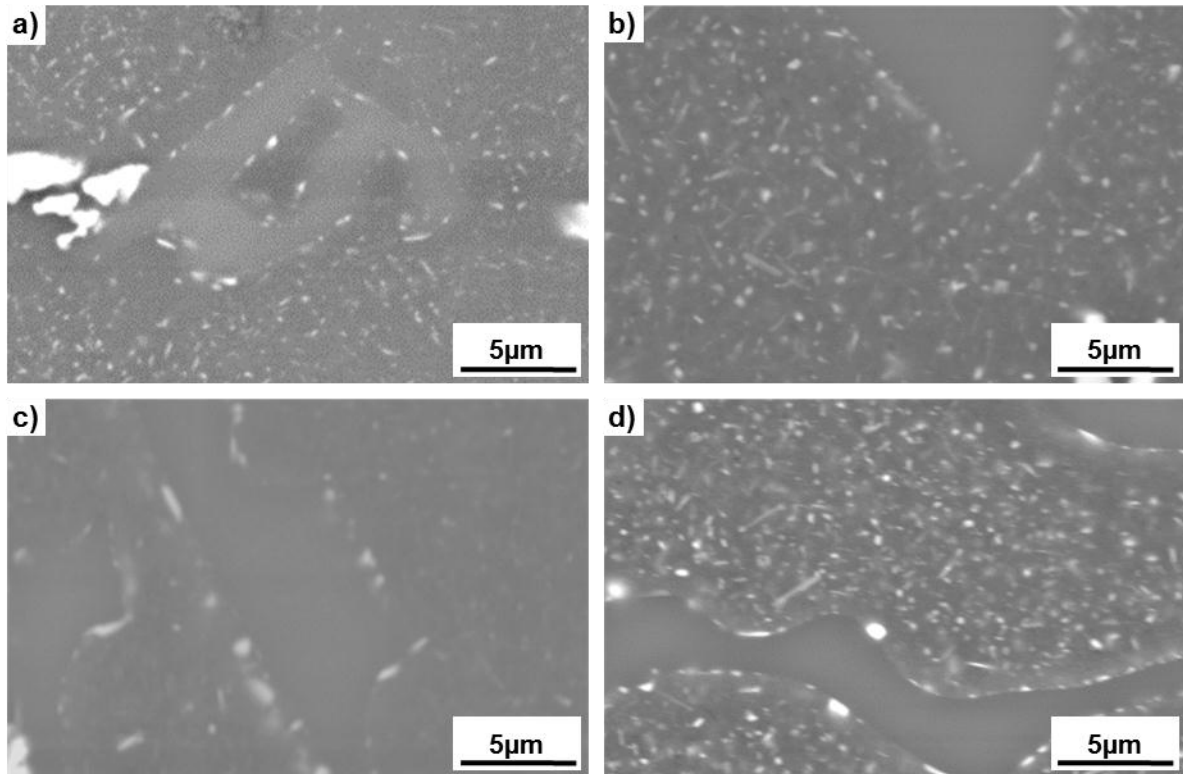


Fig. 3.12: BSE micrographs of the 1062 piston alloy after a) 0h/500°C and b) 4h/500°C and of the 1740 after c) 0h/500°C and d) 4h/500°C. Both alloys were overaged for 100h/300°C.

3.4.3. Element mapping

The elements present in each phase were determined by EDX mapping for all investigated alloys.

The following possible intermetallic phases were identified:

- a) Phase containing Al, Cu and Ni, with higher amount of Cu, most probably γ -phase ($\text{Al}_7\text{Cu}_4\text{Ni}$) [28,31]. This phase was found in the 1062, 1252, 1253 and 1252-Mg alloys (Fig. 3.13, Fig. 3.14, Fig. 3.15 and Fig. 3.16).
- b) Aluminides containing Mg, Cu and Si. This corresponds to the Q-phase ($\text{Al}_4\text{Cu}_2\text{Mg}_8\text{Si}_7$) [31,34]. Present in the 1062, 1252, 1253 and 1740 alloys (Fig. 3.13, Fig. 3.14, Fig. 3.15 and Fig. 3.17).
- c) Aluminides containing Al, Cu and Ni with a ratio of Cu:Ni ~ 1 , described as δ -phase (Al_3CuNi) [25,31]. Present in the 1252, 1253 and 1252-Mg alloy. The presence of small amounts of Zr was also observed in this phase (Fig. 3.14, Fig. 3.15 and Fig. 3.16).
- d) Primary aluminides containing solely Al and Cu, which correspond to θ -phase (Al_2Cu) [31] were only found in the 1740 alloy (Fig. 3.17).

However, the formation of primary Al_2Cu aluminides in Ni containing alloys is possible [25,28,31,34]

- e) Aluminides containing Al, Fe, Mn, Ni and Cu. This corresponds to the T-phase (Al_9FeNi) with dissolved Cu and Mn [25,31]. Present in the 1062, 1252, 1253 and 1252-Mg alloys.(Fig. 3.13, Fig. 3.14, Fig. 3.15 and Fig. 3.16)
- f) Phase containing Al, Fe, Mn, Ni, Cu and Si. This phase was identified by EDX in a previous study [34]. It was suggested to correspond to a modification of the $\text{Al}_{15}(\text{Me})_3\text{Si}_2$ phase. Present in all alloys with varying content of Me= Fe, Mn, Ni, Cu. These aluminides additionally dissolve in the case of the 1252, 1253 and 1252-Mg alloys relatively high amounts (~1at%) of V, Ti and/or Zr. This was determined by EDX point analysis of the identified phases (Fig. 3.13- Fig. 3.17).

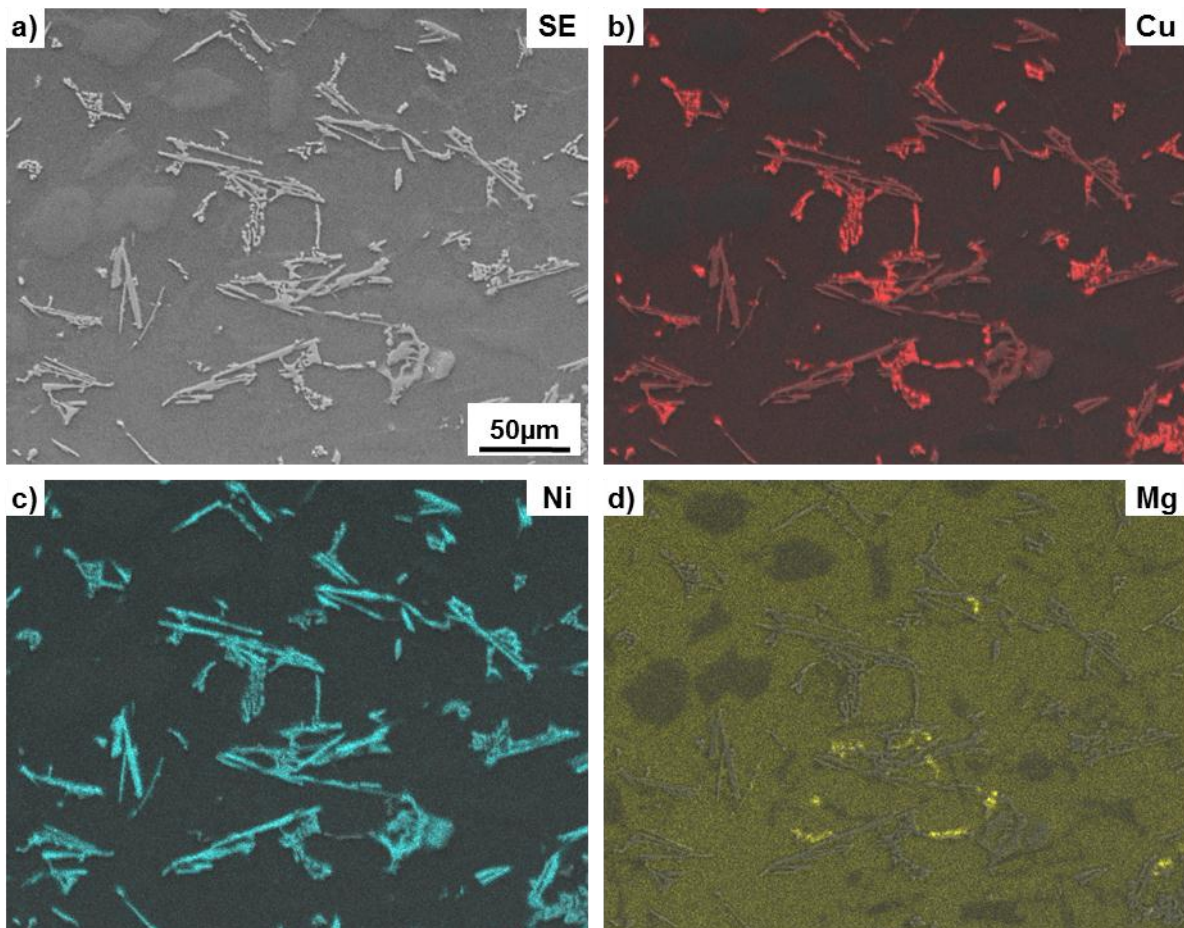


Fig. 3.13: Elemental mapping of the 1062 alloy in 0h/500°C condition.

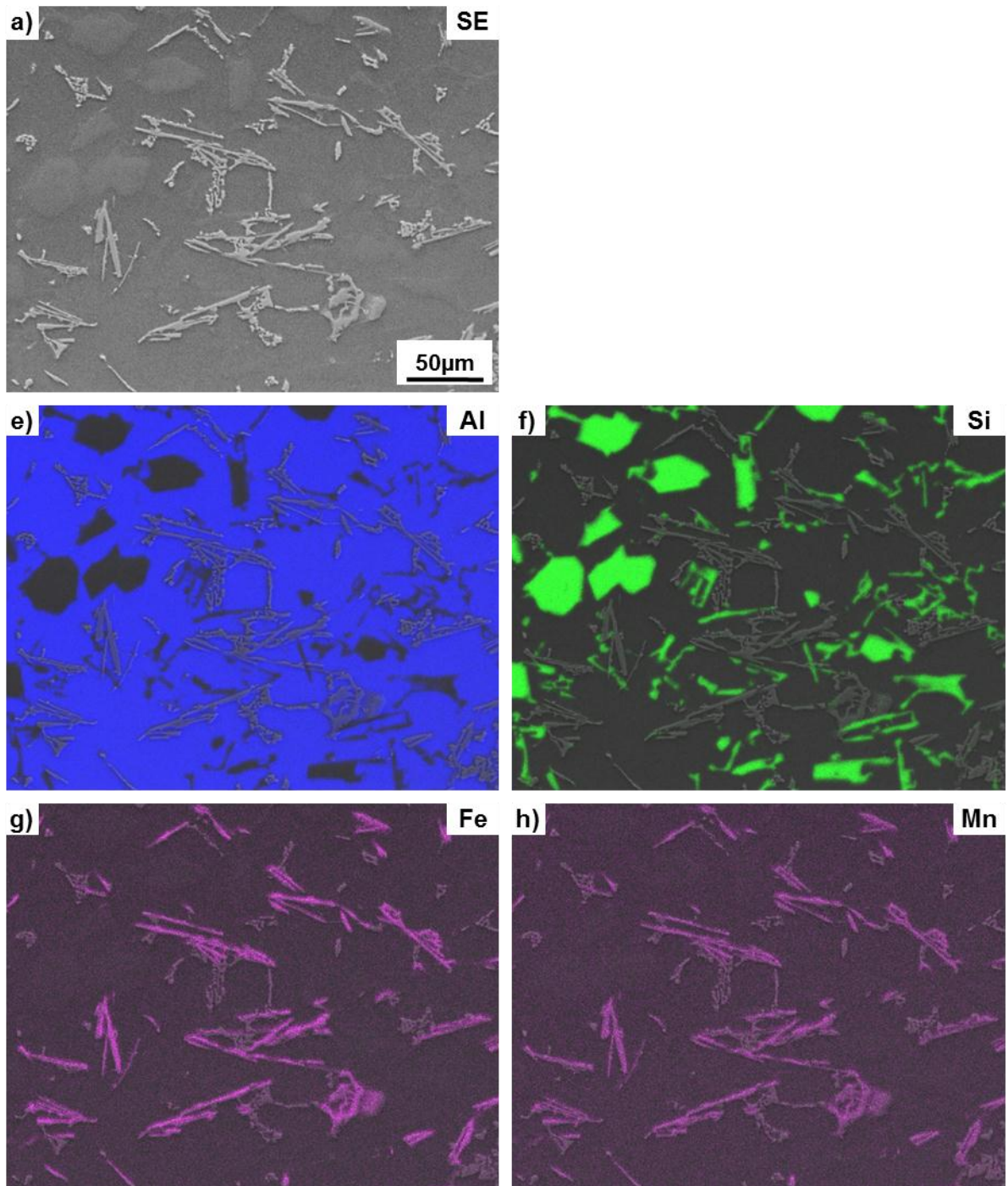


Fig. 3.13 continued: Elemental distribution of Fe and Mn in the 1062 alloy in 0h/500°C condition.

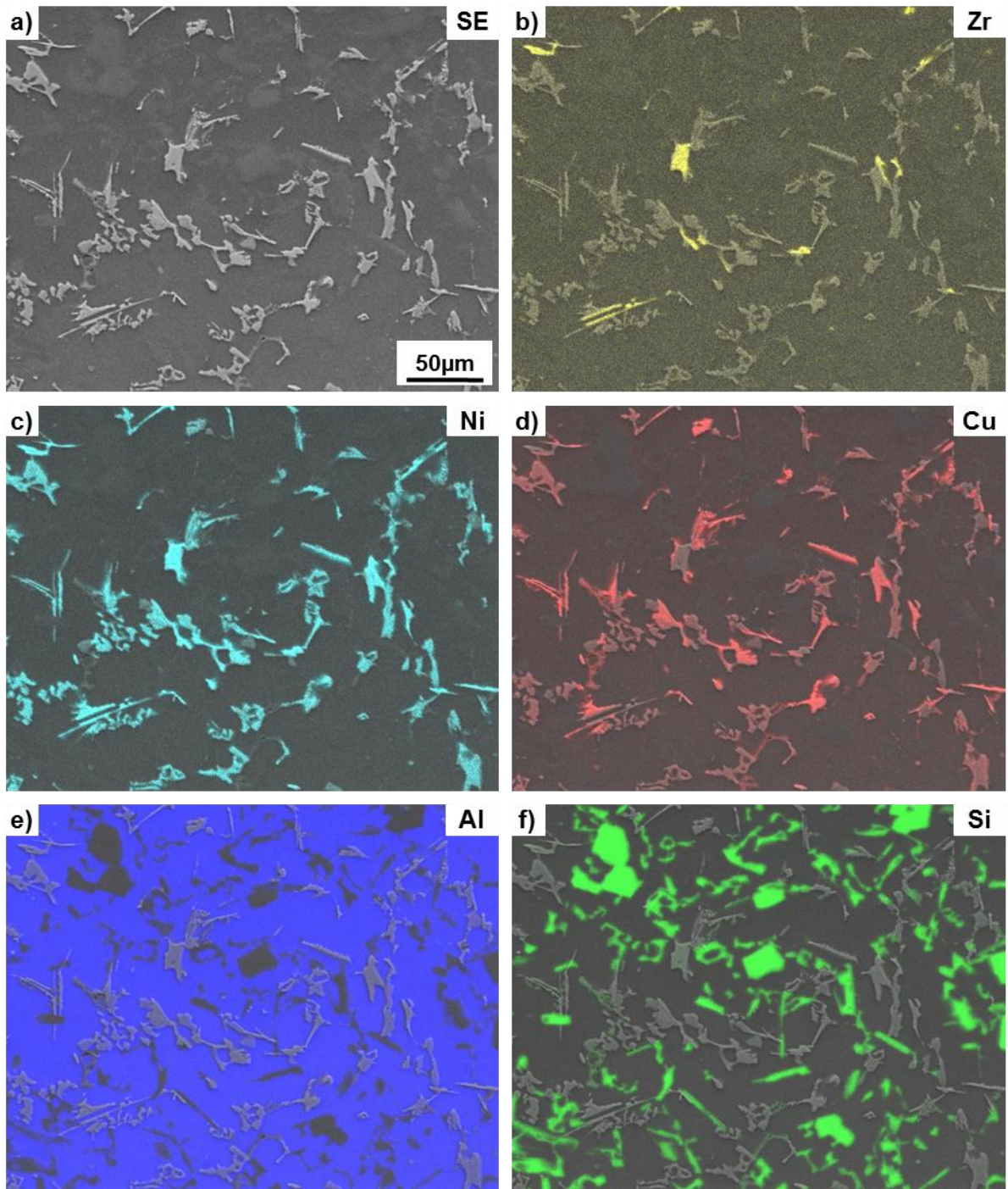


Fig. 3.14: Elemental mapping of the 1252 alloy in 0h/500°C condition.

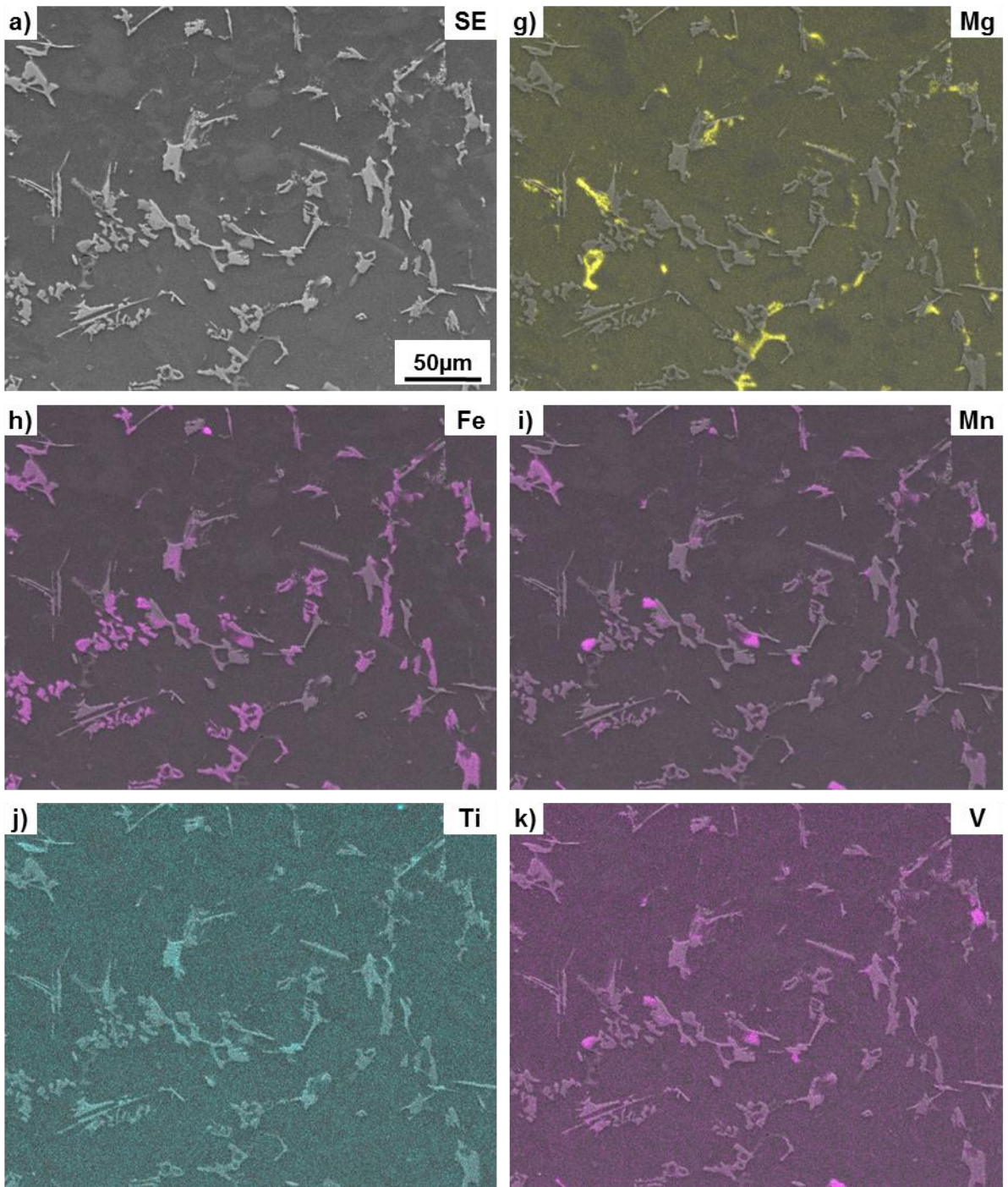


Fig. 3.14 continued: Elemental mapping of the 1252 alloy in 0h/500°C condition.

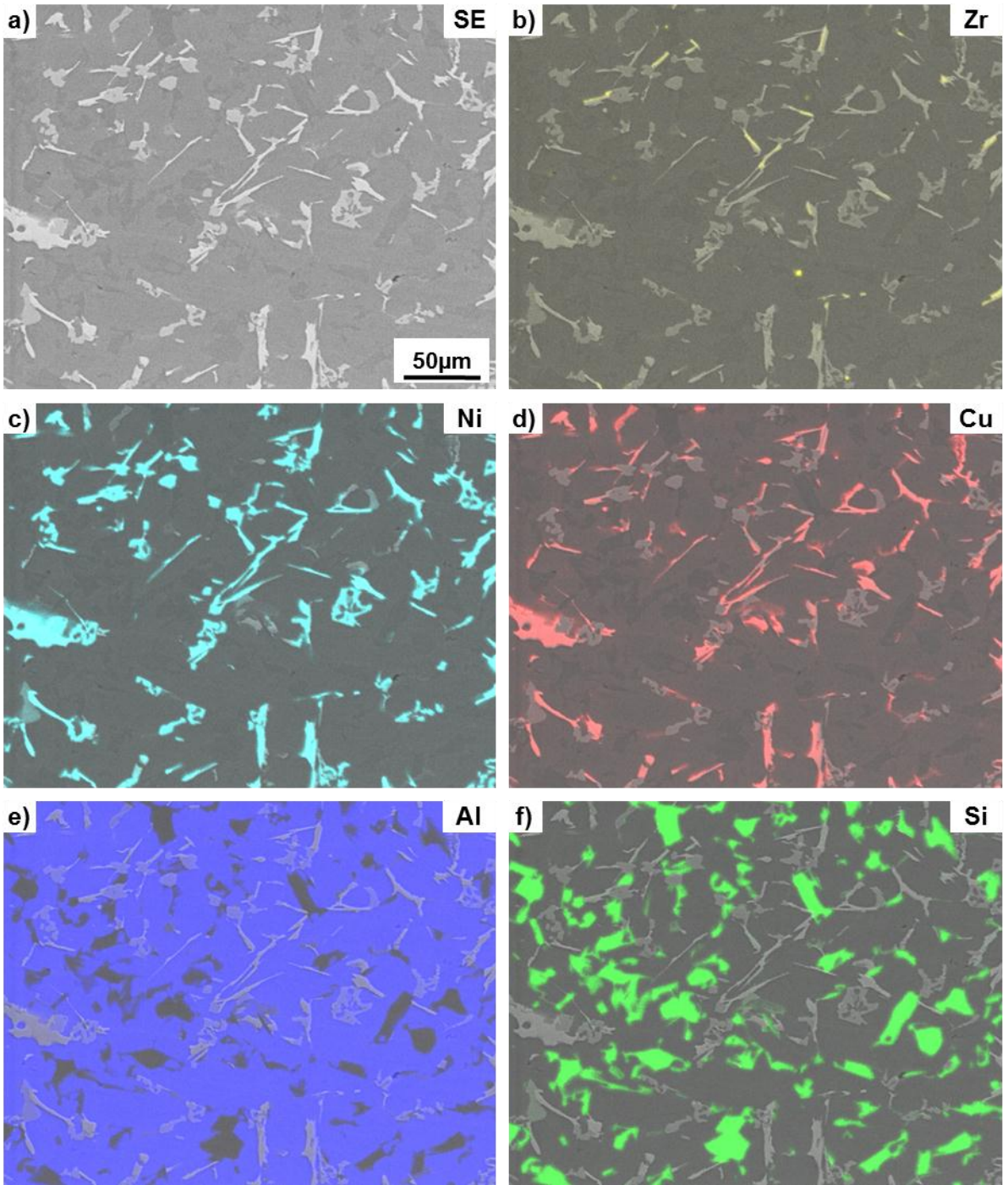


Fig. 3.15: Element mapping of the 1253 alloy in 0h/500°C condition.

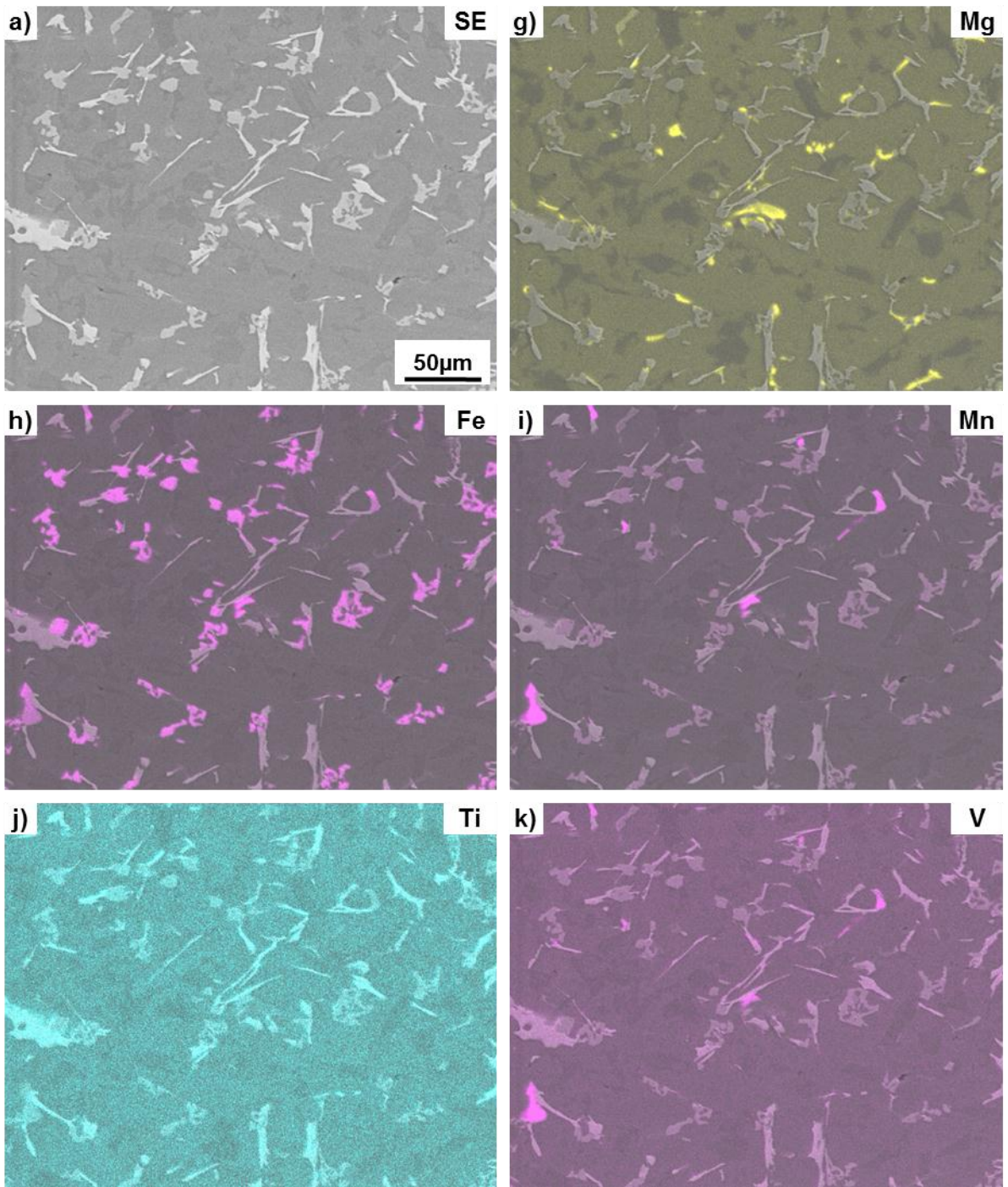


Fig. 3.15 continued: Element mapping of the 1253 alloy in 0h/500°C condition.

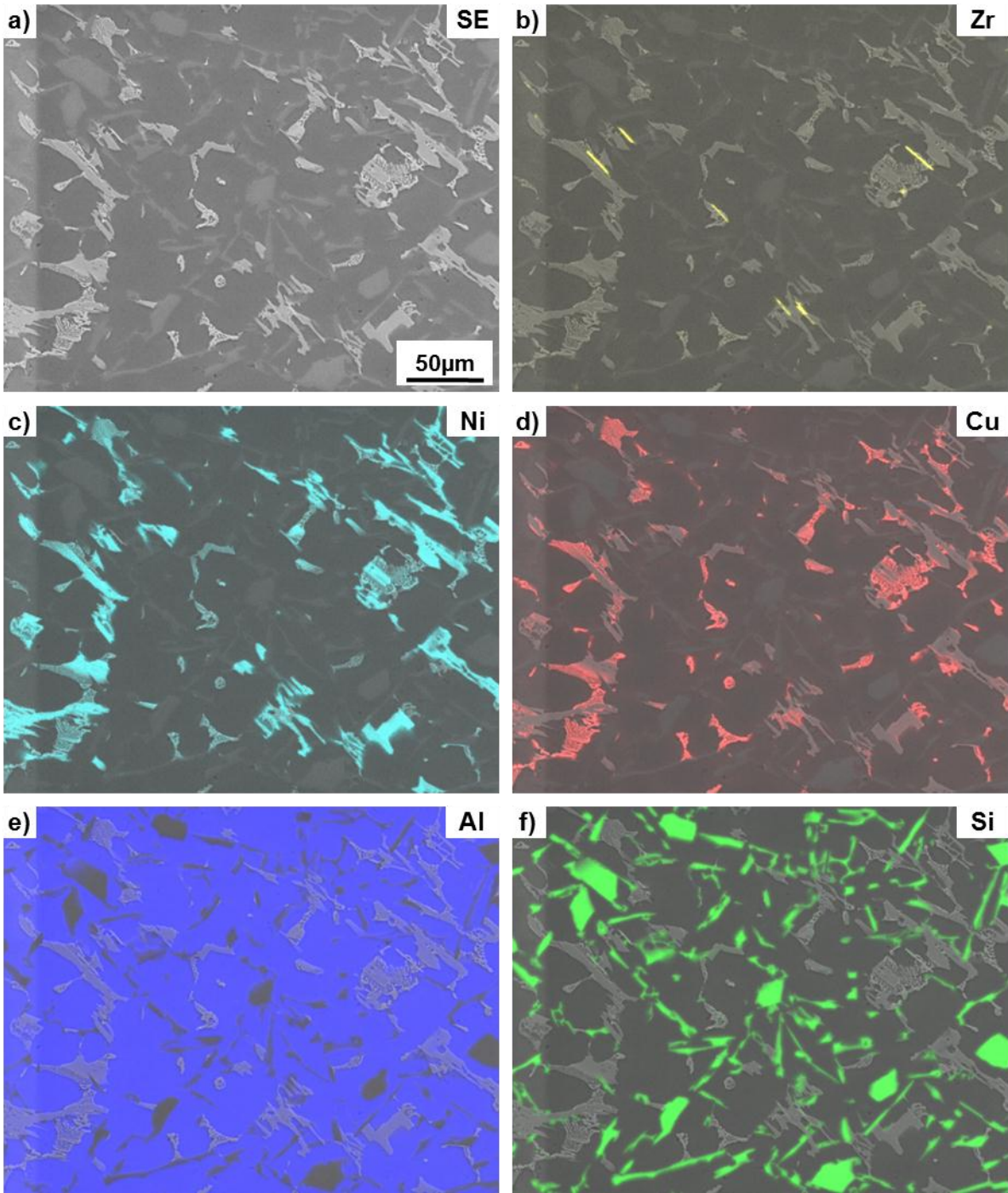


Fig. 3.16: Element mapping of the 1252-Mg alloy in 0h/500°C condition.

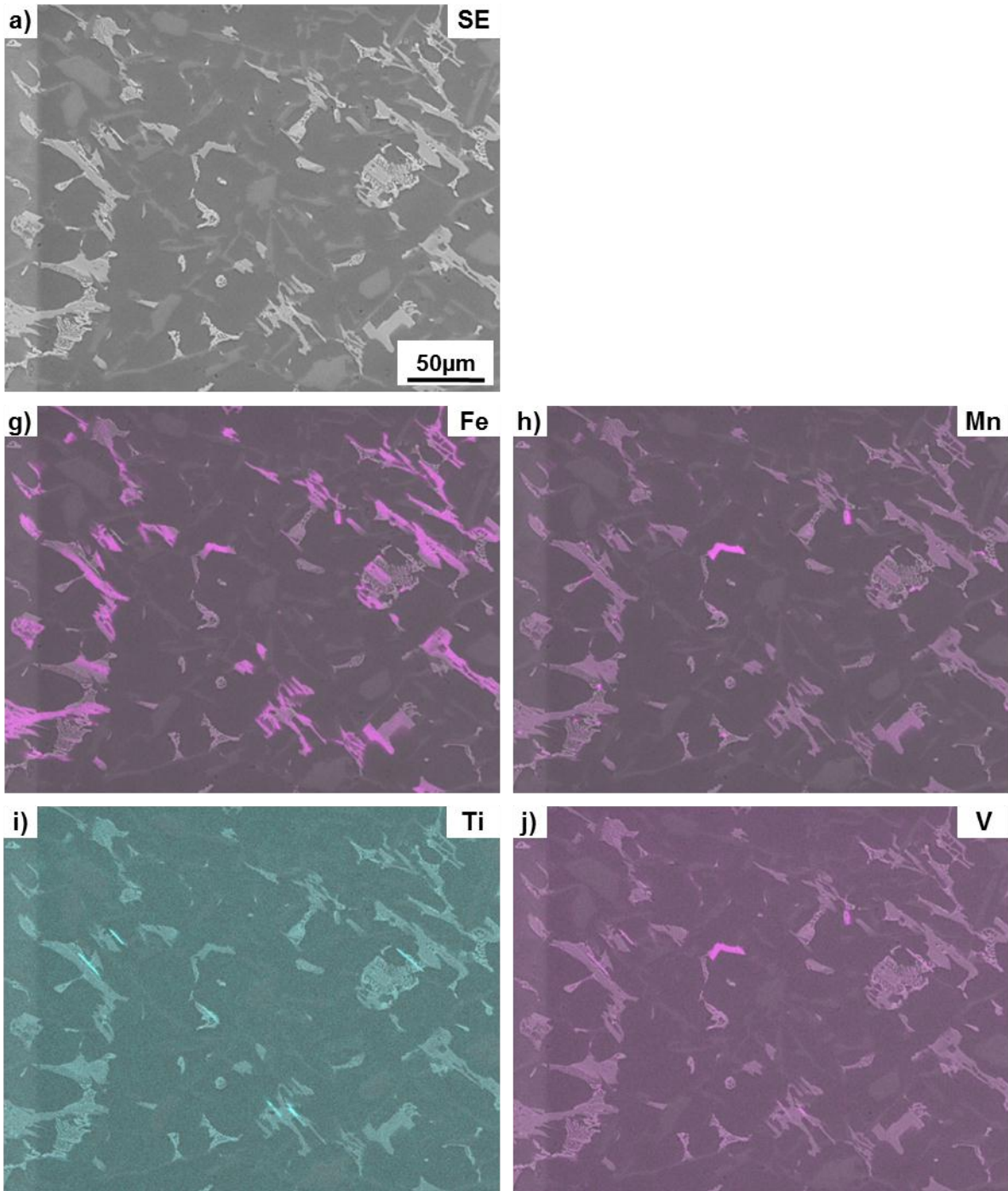


Fig. 3.16 continued: Element mapping of the 1252-Mg alloy in 0h/500°C condition.

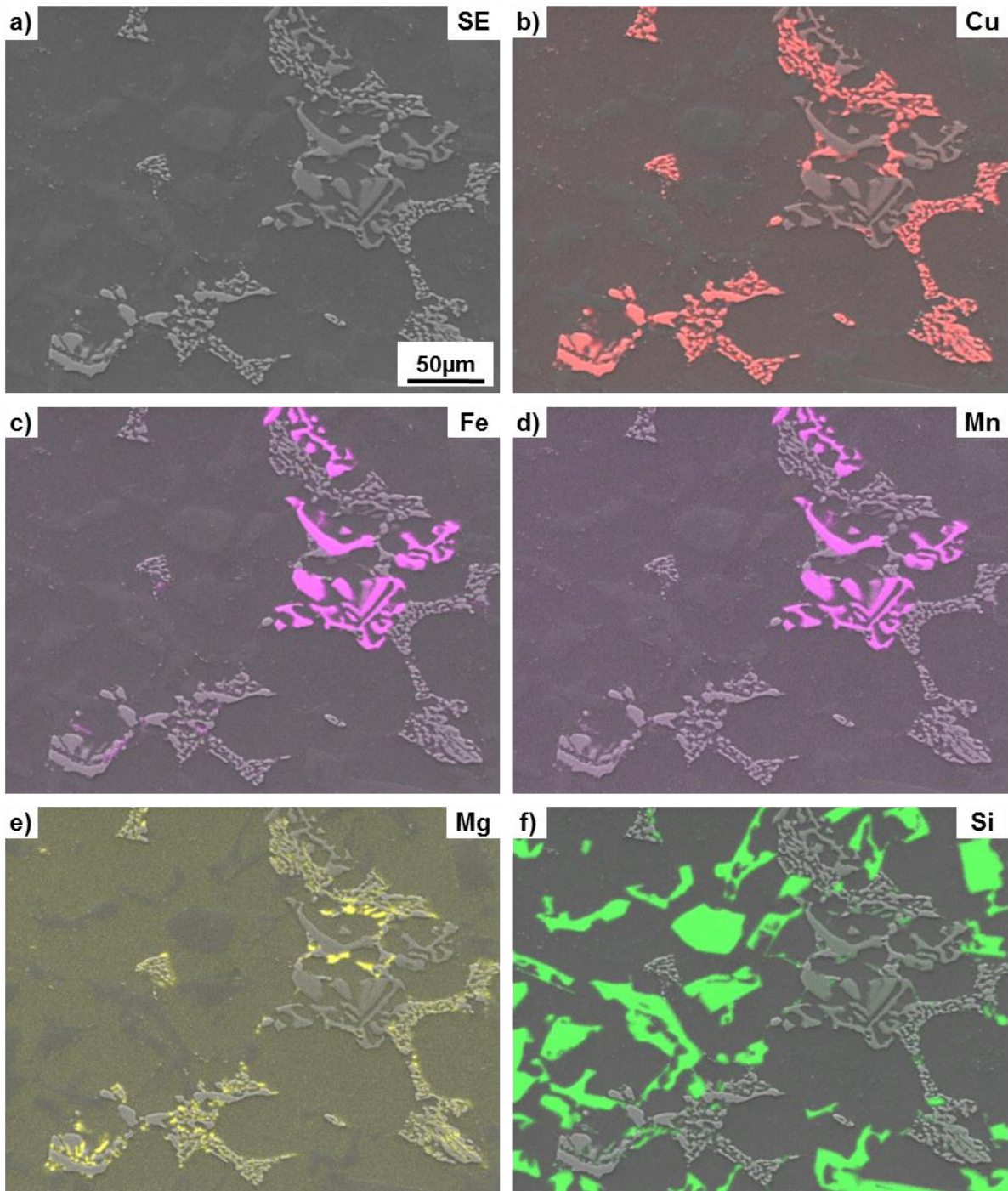


Fig. 3.17: Element mapping of the 1740 alloy in 0h/500°C condition.

3.5. Light optical tomography

3.5.1. Mechanical serial sectioning

The alloy 1253 was investigated by mechanical serial sectioning in 0h/500°C and with 4h/500°C condition. The nominal voxel size in both cases was $0.1 \times 0.1 \times 1 \mu\text{m}^3$ but due to use of LOM with an objective (500x total magnification, numerical aperture 0.8, approximate wave length 500nm) the resulting spatial resolution is estimated as $\sim 0.3 \times 0.3 \times 1 \mu\text{m}^3$. 3D rendered volumes of $226 \times 160 \times 60 \mu\text{m}^3$ are shown in Fig. 3.18 for

the 1253 alloy without solution treatment. Similar 3D rendered volumes with the same size are shown in Fig. 3.19 for the 1253 alloy after 4h of solution treatment at 500°C. The α -Al matrix is transparent in all figures. Fig. 3.18a) and Fig. 3.19a) show the segmented 3D networks of Si for each condition. The volume fraction of Si in the investigated volumes is ~13.6vol% and ~12.6vol% for the 0h/500°C and 4h/500°C conditions, respectively.

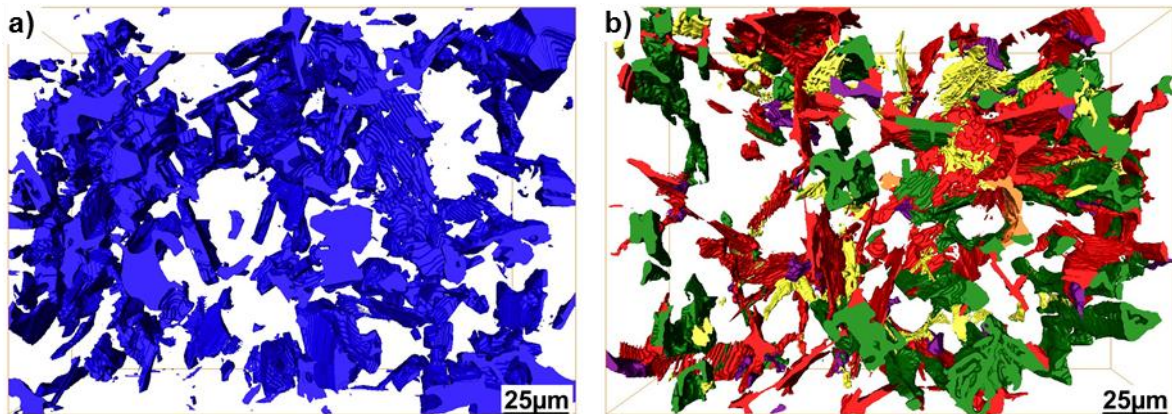


Fig. 3.18: Reconstructed volume of mechanical serial sectioning of 1253 0h/500°C.

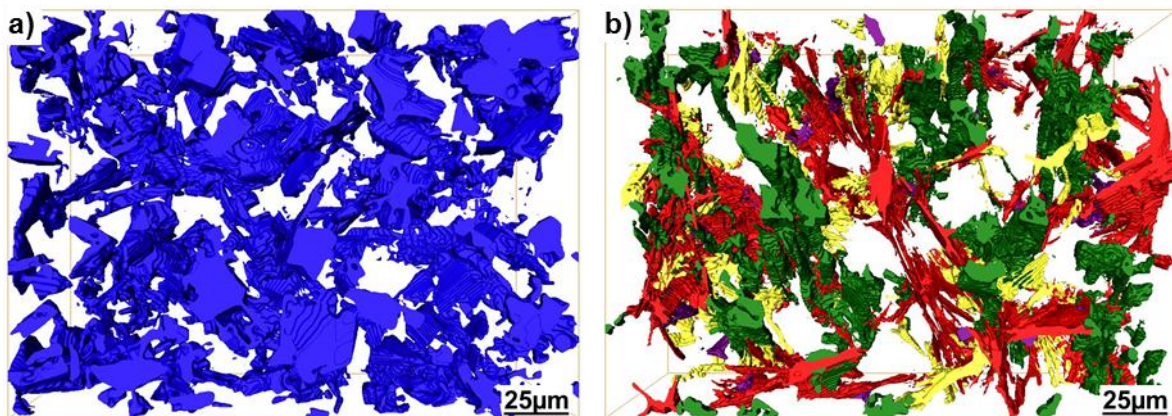


Fig. 3.19: Reconstructed volume of mechanical serial sectioning of 1253 4h/500°C.

color	elements by EDX	possible phases
blue	Si	Si
red	Al, Cu, Ni	Al_7Cu_4Ni
orange	Al, Ni, Cu, Zr	$Al_3(NiCu)_2$ or $Al_3Ni_2(Cu)$
green	Al, Fe, Ni	Al_9FeNi
yellow	Al, Cu, Mg, Si	Q-phase $Al_5Cu_2Mg_8Si_6$
magenta	Al, Si, Mn, Fe, Cu, Ni,	$Al_{15}(Me)_3Si_2$

Tab. 3.1: Color coded constituents with identified elements and possible phases obtained by mechanical serial sectioning and ion milling serial sectioning of the 1253 alloy.

On the other hand, the hybrid 3D networks formed by several intermetallic phases are shown in Fig. 3.18b) and Fig. 3.19b) for the 0h/500°C and 4h/500°C conditions, respectively. Different colors represent phases qualitatively identified by EDX (Tab.

3.1). The volume fraction of aluminides in the investigated volumes is ~6.7vol% and ~5.2vol% for the 0h/500°C and 4h/500°C conditions, respectively. It is impossible from these destructive investigations to infer whether this decrease in volume fraction of intermetallic phases is due to a heterogeneous distribution of these phases or a consequence of a dissolution process.

3.5.2. Ion milling serial sectioning

Serial sectioning by ion milling showed a more detailed picture of the microstructure owing to the higher magnification used for the light optical microscope and the smaller removed depth by sectioning, namely ~0.38 μm . The total amount of removed material was 13.1 μm in depth. The voxel size is ~0.27x0.27x0.38 μm^3 . The resulting investigated volume of 1253 0h/500°C was 134x93x13.1 μm^3 . It can be seen in Fig. 3.20 that aluminides are connected to Si and with each other. The green colored aluminides (AlFeNi) corresponding to the Al₉FeNi phase with additional Cu (Tab. 3.1) share the biggest interface with Si in the investigated volume.

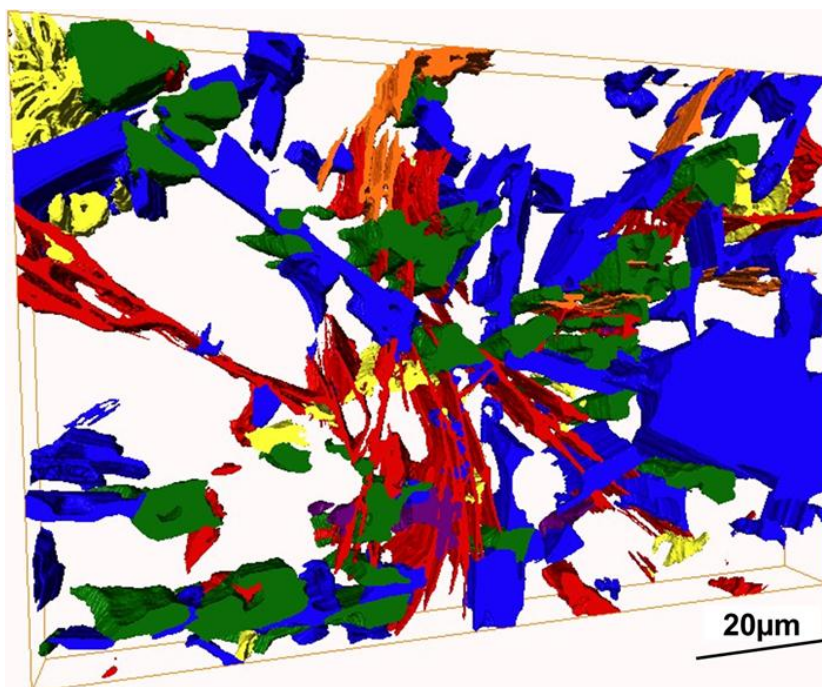


Fig. 3.20: Rendered volume of 1253 0h/500°C obtained by ion mill serial sectioning.

3.6. Synchrotron X-ray micro-computed tomography (S μ CT)

3.6.1. Volume fraction, interconnectivity and Euler number of aluminides

The evolution of volume fraction of aluminides after solution treatment is shown in Fig. 3.21 for all alloys. All alloys except 1253 were investigated using one sample solution treated for 0h/1h/4h at 500°C (shown in Fig. 3.21 with a continuous line and filled symbols). The alloy 1253 was investigated with a different sample at each solution treatment stage (marked by a dash-dotted line and unfilled symbols in Fig. 3.21). The error bars were calculated choosing ± 2 gray values (8bit) of the best fitted global threshold. The investigated volumes of the alloys 1062, 1252, 1252-Mg and 1740 had a size of $\sim 400 \times 400 \times 500 \mu\text{m}^3$ ($\sim 0.08 \text{mm}^3$). The volumes of the 1253 alloy had a size of $\sim 650 \times 650 \times 1000 \mu\text{m}^3$ ($\sim 0.42 \pm 0.04 \text{mm}^3$).

The piston alloys 1062, 1252, 1253 and 1252-Mg form aluminides that are thermally stable in terms of volume fraction. Thus, the volume fractions of aluminides is $\sim 9.5 \pm 1 \text{vol}\%$ for 1252, 1062 and 1252-Mg, $\sim 12 \pm 1 \text{vol}\%$ for 1253 for all studied conditions. The initial volume fraction of aluminides in the 1740 alloy is $5.7 \pm 0.8 \text{vol}\%$ and decreases to $4 \pm 0.05 \text{vol}\%$ after 4h solution treatment.

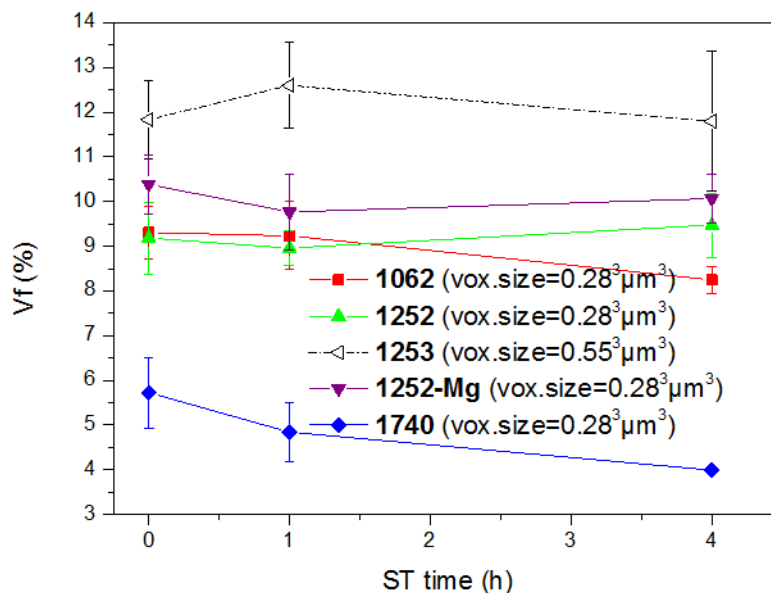


Fig. 3.21: Evolution of the volume fraction of aluminides as function of solution treatment (ST) time at 500°C.

The interconnectivity of aluminides in the 1740 alloy shows a significant decrease from $89 \pm 3\%$ to $70 \pm 4\%$ after 1h/500°C, as it is shown in Fig. 3.22. On the other hand,

all piston alloys show that also the interconnectivity of aluminides remains practically constant, i.e. 95-98%, after 4h of solution treatment.

Despite of the global stability of the networks of aluminides in the piston alloys in terms of volume fraction and interconnectivity some local changes were found in the 1252 (Fig. 3.23 and Fig. 3.25) and the 1062 alloys (Fig. 3.24). Local dissolution of phases was observed less frequently in the 1062 alloy and affected eutectic-like morphologies (Fig. 3.24 a,c). In the case of 1252 alloy dissolution of highly absorbing aluminides and low absorbing Mg₂Si or Q-Phase (Fig. 3.26) was observed in the tomographies after 1h/500°C of solution treatment. No further changes were observed after 4h of exposure at 500°C. The grey value in the case of the low absorbing phase was slightly different from Si and needed to be segmented by hand. The effect of this dissolution is minor on interconnectivity because of high crosslinking of the aluminides and Si network but changes locally the contiguity and connections between phases.

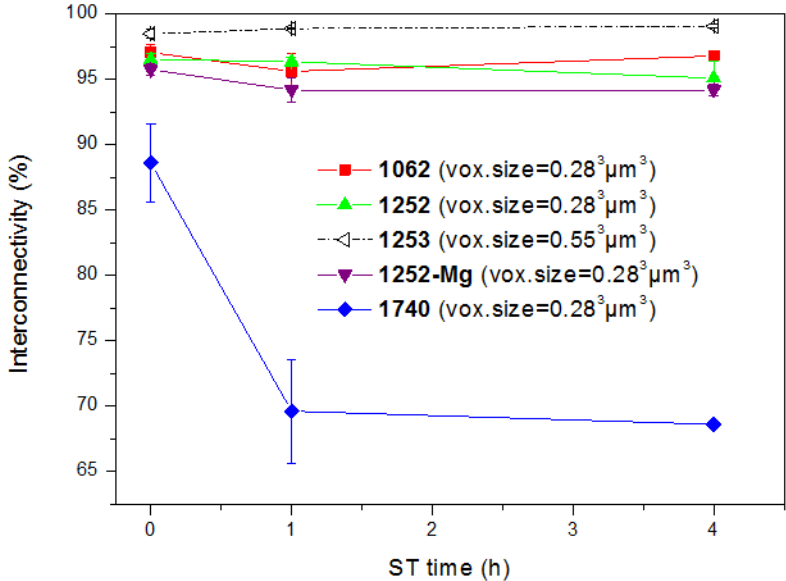


Fig. 3.22: Evolution of the interconnectivity of aluminides as a function of solution treatment time at 500°C.

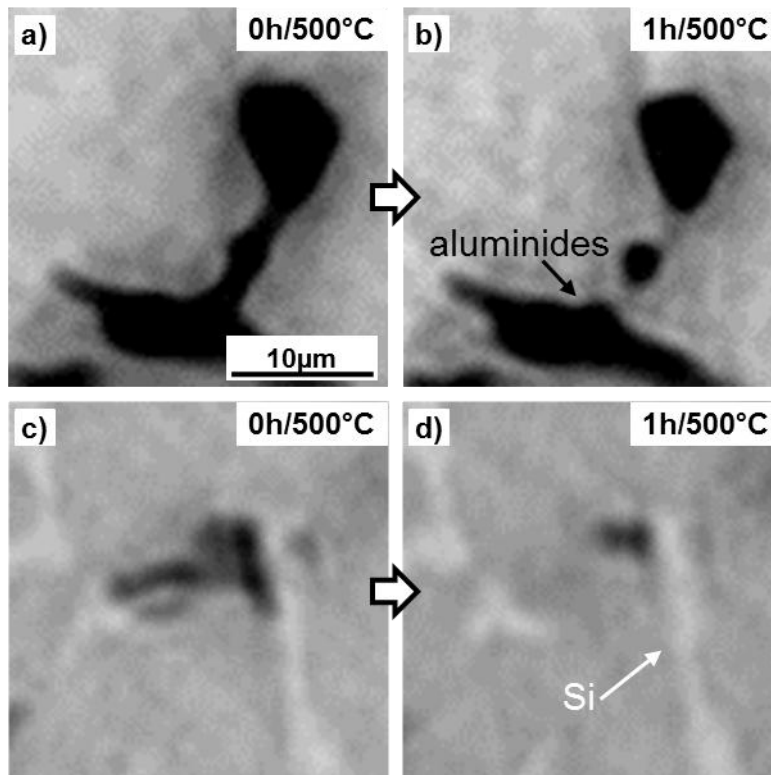


Fig. 3.23: 2D slices of the alloy 1252 after (a,c) 0h/500°C and (b,d) 1h/500°C.

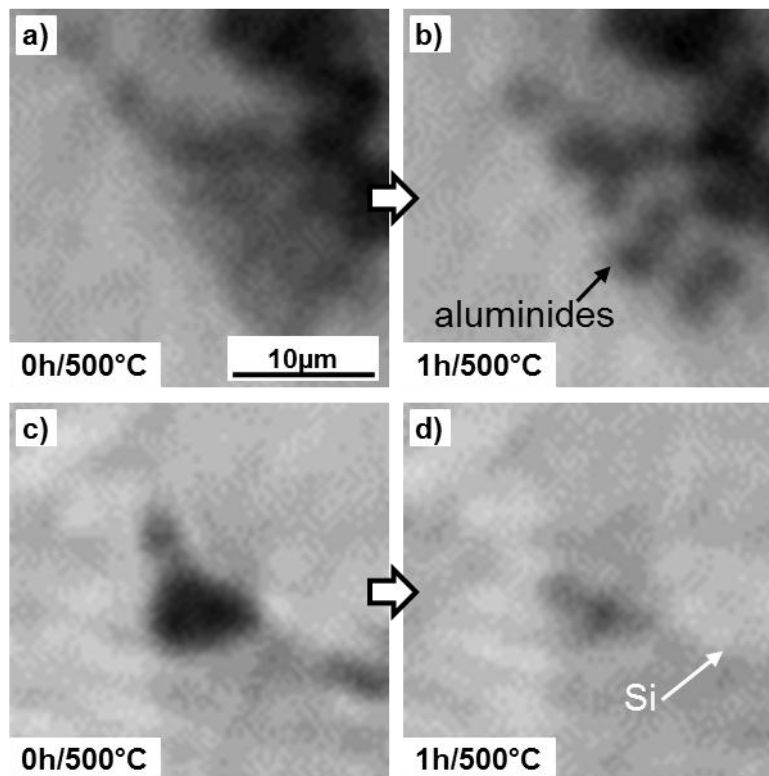


Fig. 3.24: 2D slices of the alloy 1062 after (a,c) 0h/500°C and (b,d) 1h/500°C.

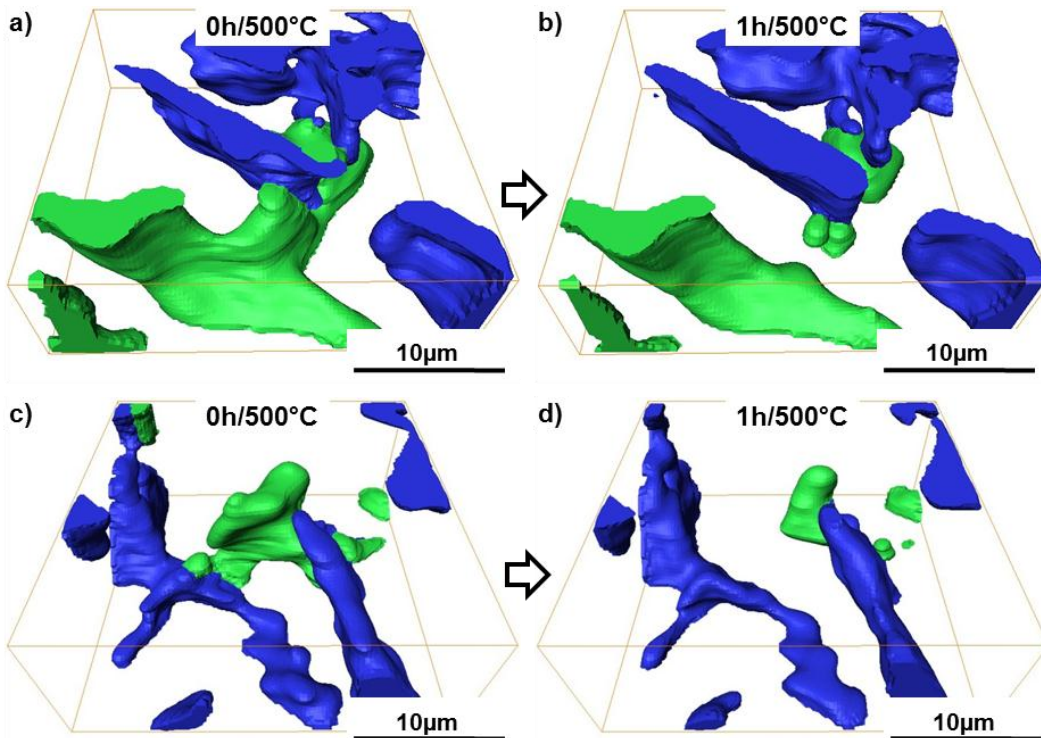


Fig. 3.25: Local dissolution of intermetallic phases in the 1252 alloy after (a,c) 0h/500°C and (b,d) 1h/500°C. Blue corresponds to Si, green indicates aluminides.

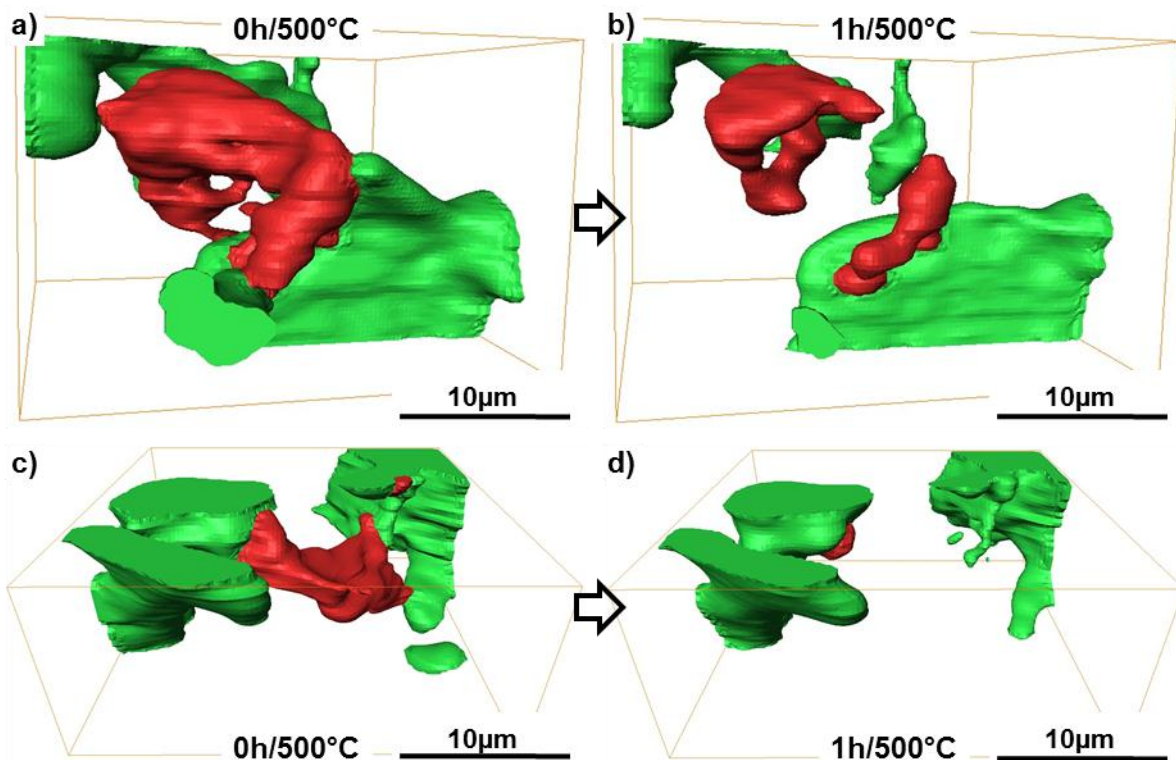


Fig. 3.26: Detail on partial dissolution of Mg_2Si or Q-phase in the 1252 alloy (a, c) 0h/500°C and (b, d) 1h/500°C. Red corresponds to Mg_2Si or Q-phase, green indicates other intermetallics (aluminides).

The specific Euler number, χ_v , was calculated as a function of solution treatment time (Fig. 3.27). The specific Euler number, i.e. the Euler number divided by the volume

fraction of the phase considered, was chosen due to differing volume fractions of aluminides in the 1740 alloy. Furthermore, only the specific Euler number of the largest particle within the investigated volume was evaluated because small disconnected regions may have misleading influence on the results.

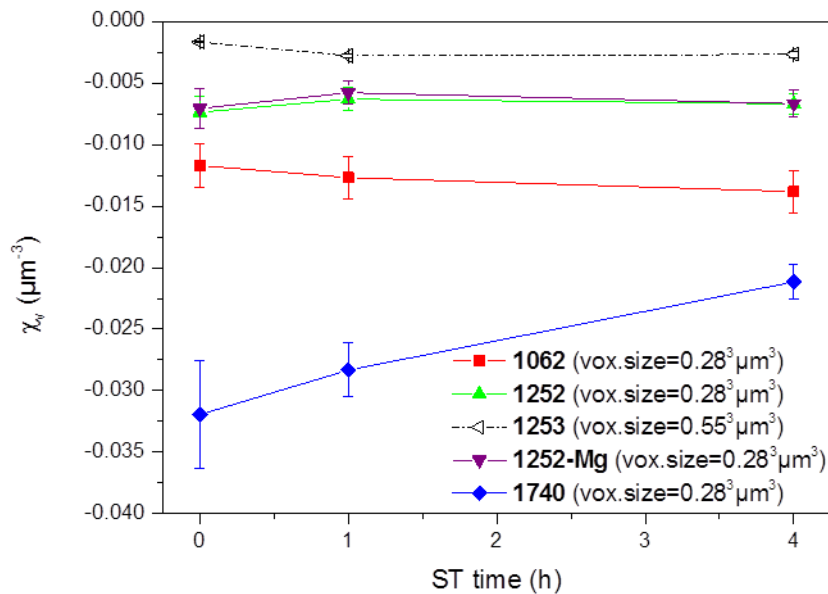


Fig. 3.27: Evolution of the specific Euler number of the largest particle of aluminides as a function of solution treatment time at 500°C.

3.6.2. Euler number of eutectic and primary silicon

In Fig. 3.28a) the evolution of the Euler number, χ , of eutectic and primary silicon is shown as a function of solution treatment time at 500°C for the 1062, 1252 and 1740 alloys. Also the specific Euler number, χ_v , was calculated (Fig. 3.28b). The investigated regions have a size of $(56\mu\text{m})^3$. The Si needed to be segmented by hand due to insufficient contrast between silicon and aluminium in the tomographies. It can be seen in Fig. 3.28a) that the Si Euler number for the 1062, 1252 and 1740 alloys decreases after 1h/500°C of solution treatment and remains constant for the 4h/500°C condition. In Fig. 3.28b) this decrease is less pronounced for the 1740 alloy. The 1252 alloy has the same volume fraction of silicon as the 1253 and 1252-Mg alloy. Therefore, the evolution of Euler number of the 1252 alloy is expected to be similar to that of the 1253 and 1252-Mg alloy.

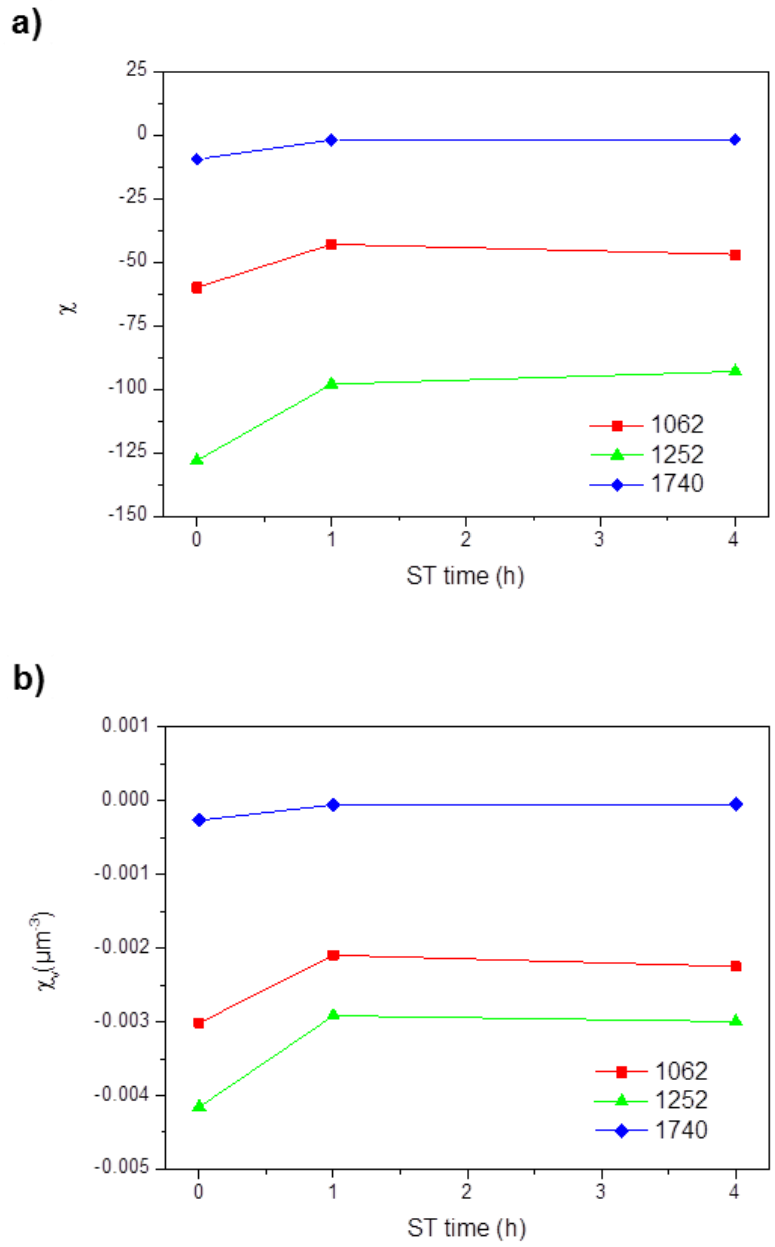


Fig. 3.28: Evolution of Euler numbers of eutectic and primary silicon as a function of solution treatment time at 500°C: a) χ =Euler number b) χ_v =specific Euler number.

3.6.3. Morphology of aluminides

The morphological stability of aluminides is described by a distribution histogram of Gaussian and mean curvatures. The different morphologies, i.e. saddle-, pit- or spheroid-like are shown in the corresponding quadrants of Fig. 3.29. The results for the alloy 1062 are shown in Fig. 3.29 - Fig. 3.31 for 0h, 1h and 4h at 500°C. The surface curvature distributions were calculated for the same volumes as for the determination of volume fraction, interconnectivity and Euler number. Corresponding 3D rendered sub-volumes $(56\mu\text{m})^3$ within the investigated region of interest are shown for the different solution treatment times in Fig. 3.32 with the Gaussian curvature as surface color map.

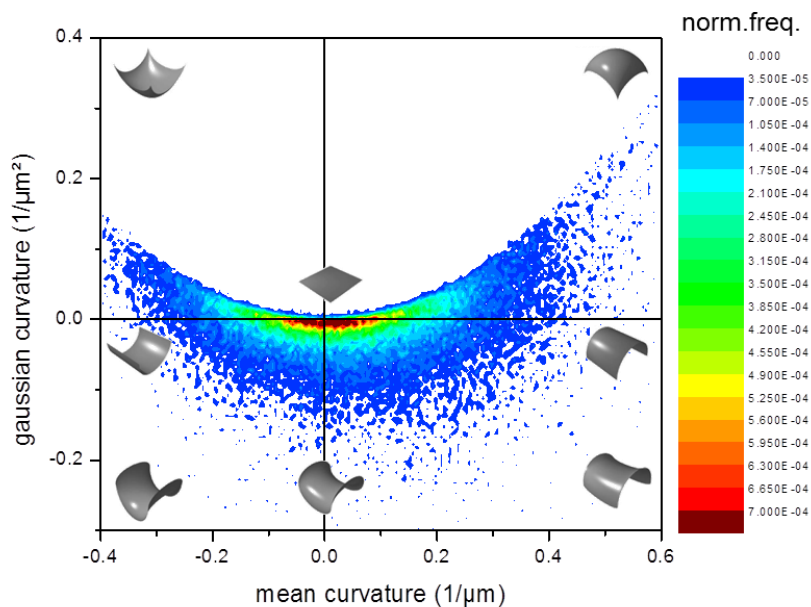


Fig. 3.29: Aluminides surface curvature distribution in the 1062 alloy after 0h/500°C.

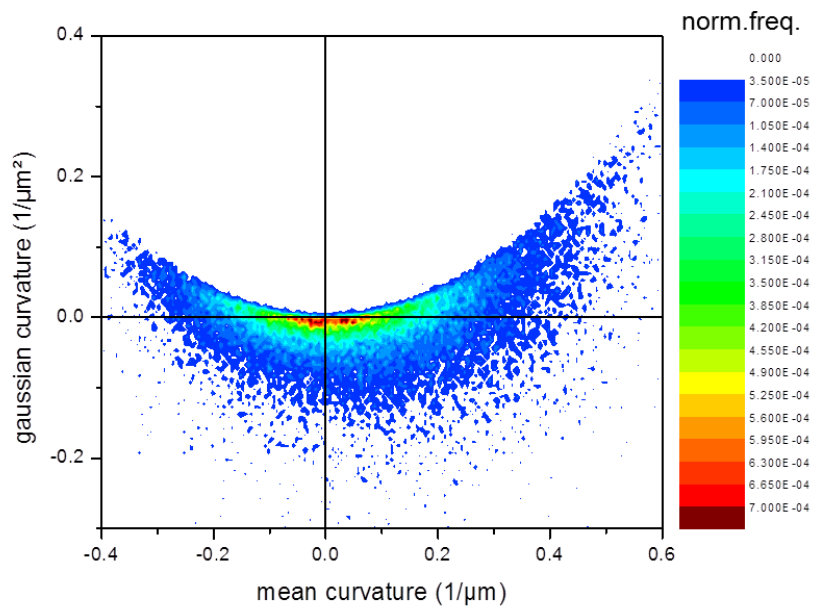


Fig. 3.30: Aluminides surface curvature distribution in the 1062 alloy after 1h/500°C.

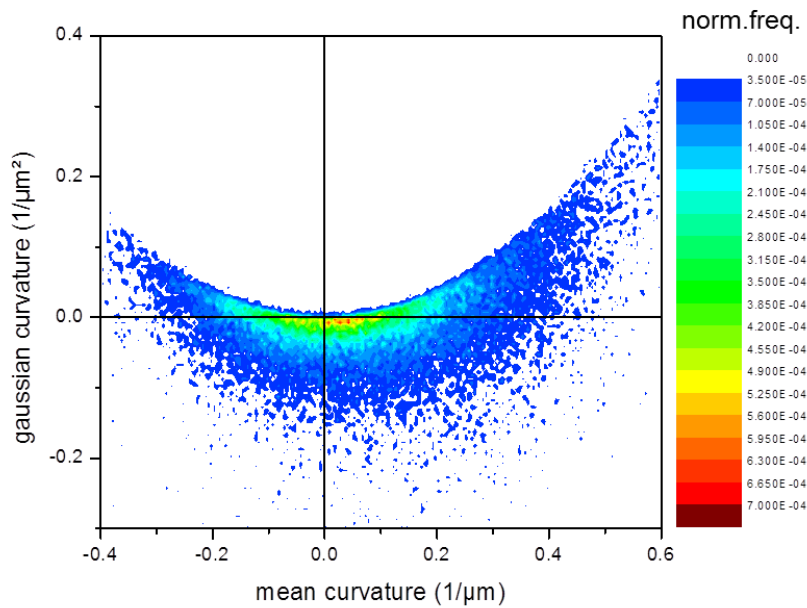


Fig. 3.31: Aluminides surface curvature distribution in the 1062 alloy after 4h/500°C.

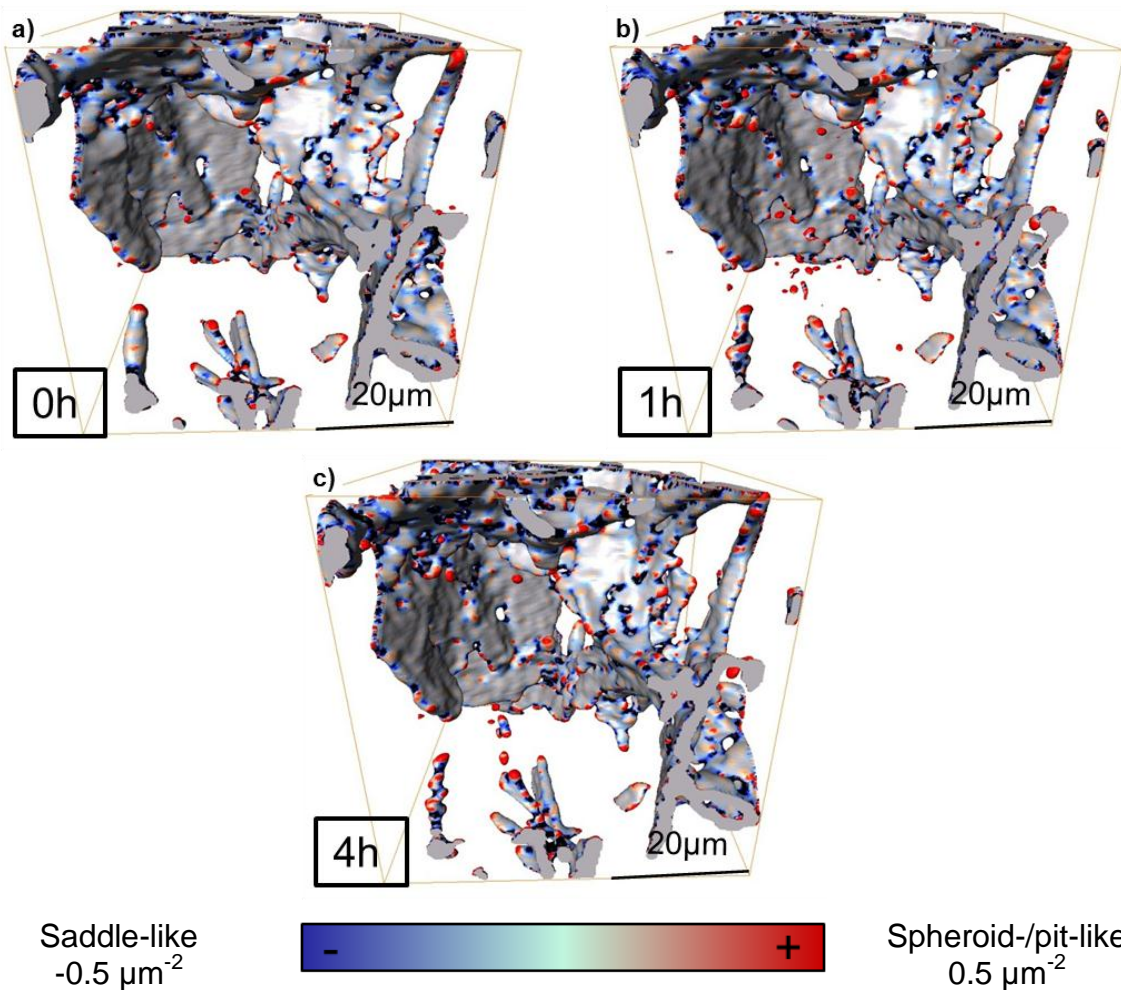


Fig. 3.32: Gaussian curvatures of aluminides in the 1062 alloy in a volume of (56 μm)³: a) 0h/500°C, b) 1h/500°C and c) 4h/500°C. Voxel size=(0.28μm)³

Visible changes in the aluminides network in the 1062 alloy during solution treatment are a slight increase of spheroid-like regions with large curvatures (positive-positive quadrant) and a decrease in the number of flat regions. A direct comparison of the 0h/1h/4h/500°C conditions is shown in Fig. 3.33. Fig. 3.33a) shows the aluminides surface curvature distribution for normalized frequency >3.5E-5 (see scales in Fig. 3.29-Fig. 3.31). Fig. 3.33b) shows the aluminides surface curvature distribution for normalized frequency >3.5E-4.

Analogue to the 1062 alloy the curvature distribution of aluminides in the alloy 1252 is shown in Fig. 3.34, Fig. 3.35 and Fig. 3.36 for 0h/1h/4h/500°C, respectively. 3D rendered volumes of the same region (56μm)³ after 0h/1h/4h/500°C are displayed in Fig. 3.37 with Gaussian curvature as surface color.

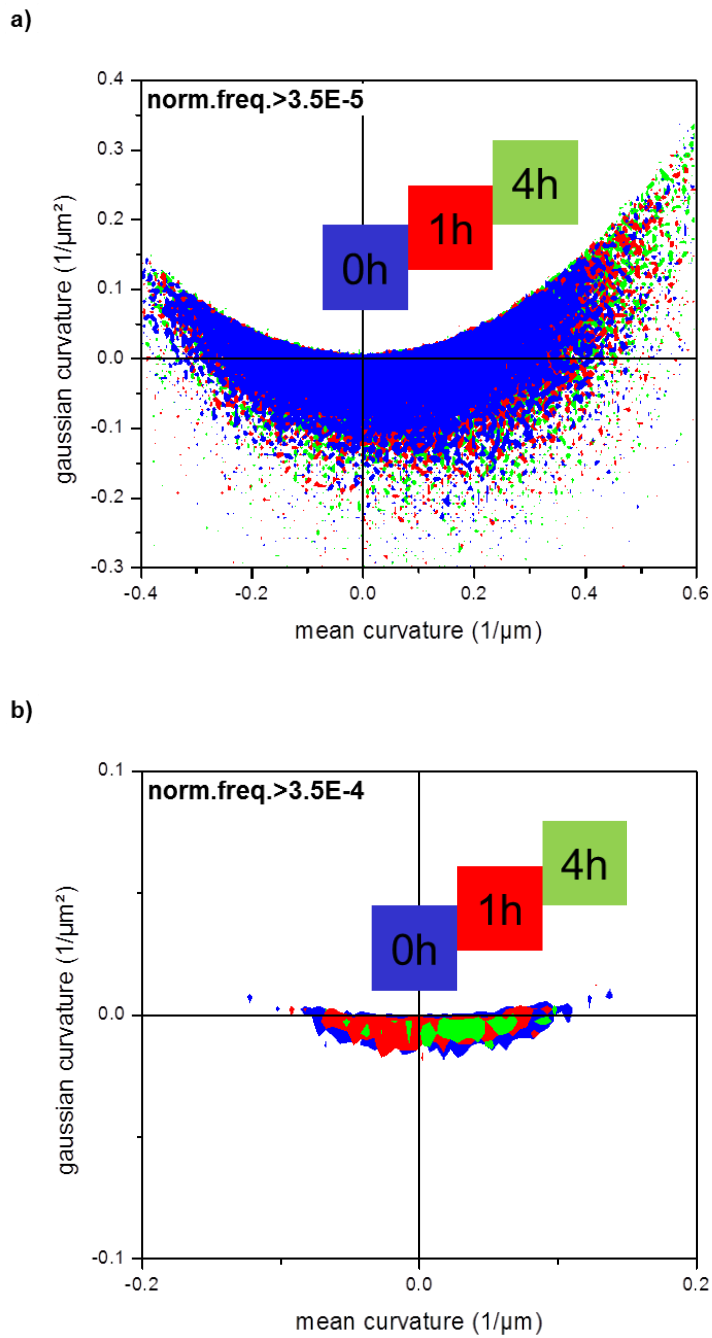


Fig. 3.33: Comparison of the surface curvature distribution of aluminides in the 1062 alloy after 0h/1h/4h/500°C: a) norm.freq. >3.5E-5 b) norm.freq. >3.5E-4.

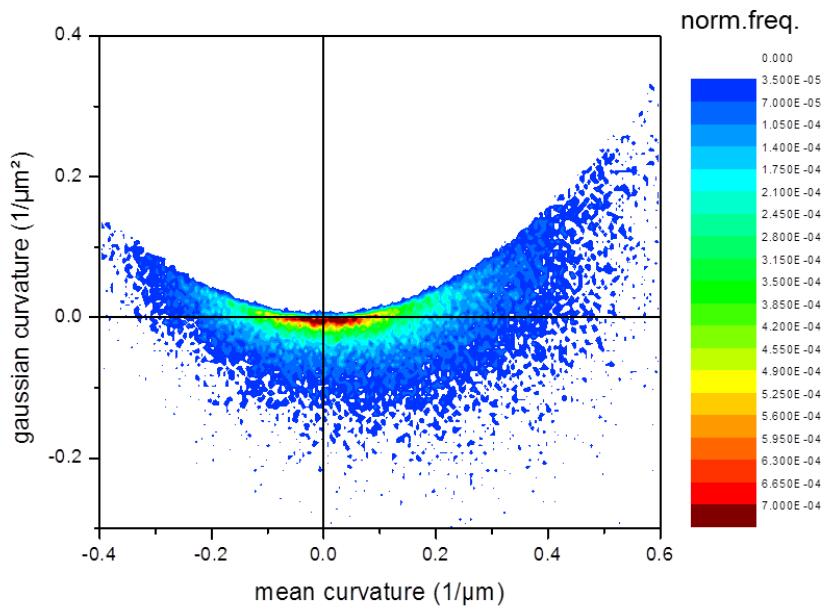


Fig. 3.34: Aluminides surface curvature distribution in the 1252 alloy after 0h/500°C.

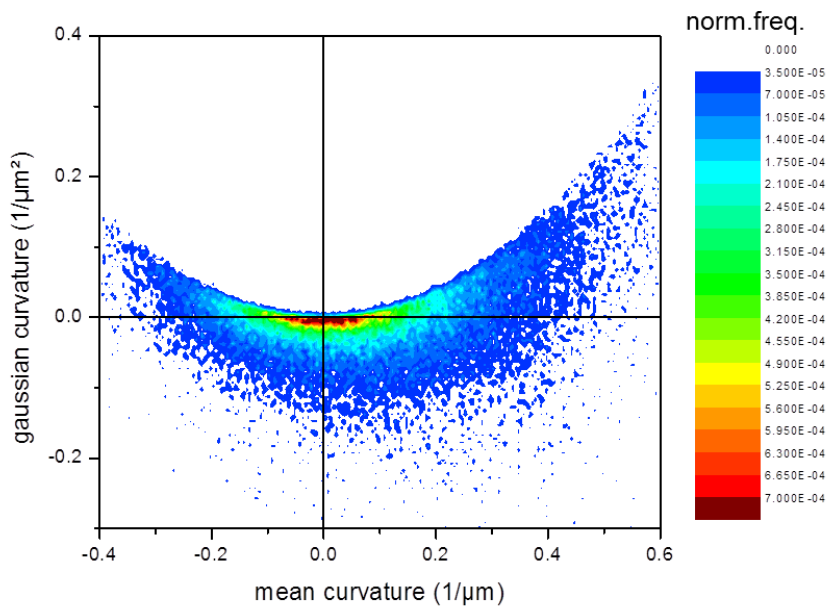


Fig. 3.35: Surface curvature distribution in the 1252 alloy after 1h/500°C.

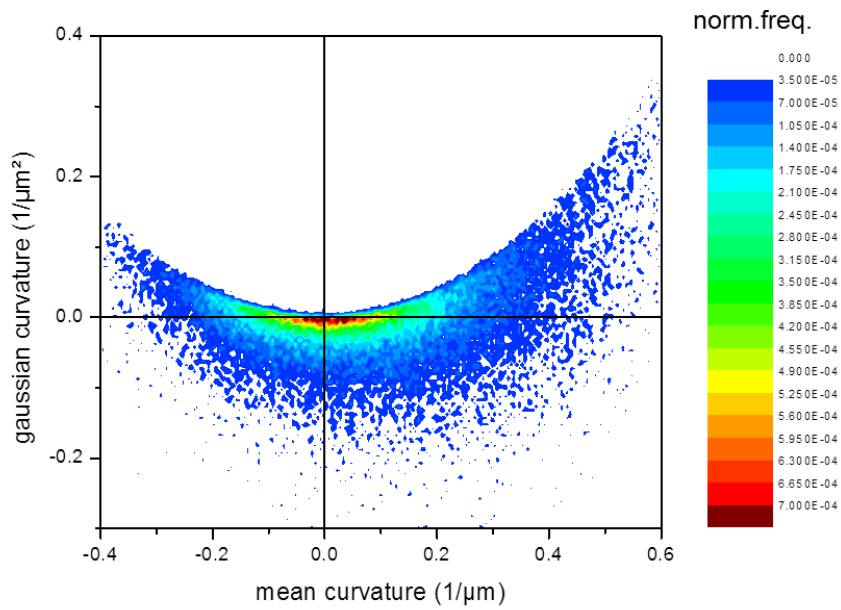


Fig. 3.36: Surface curvature distribution in the 1252 alloy after 4h/500°C.

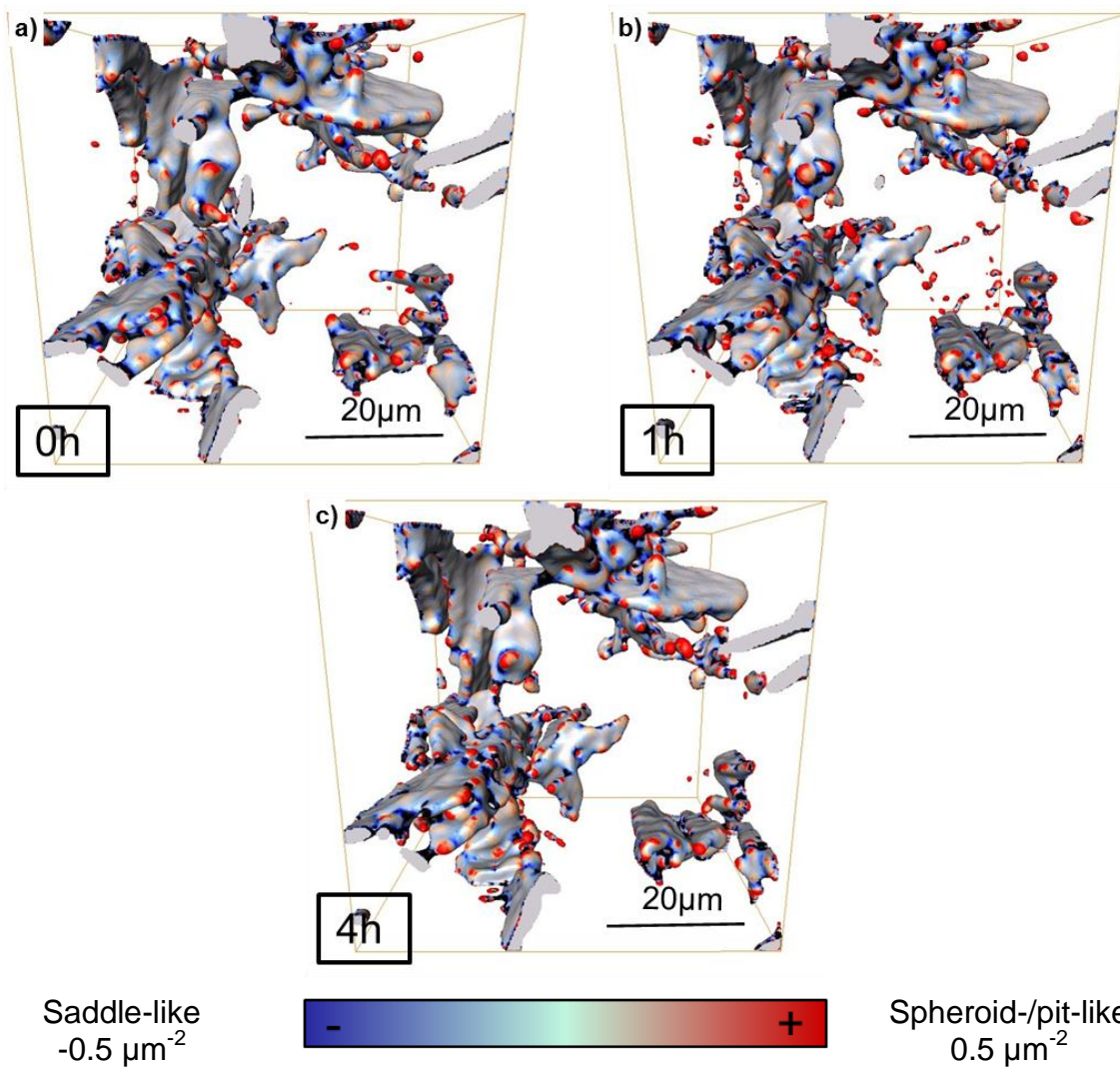


Fig. 3.37: Gaussian curvatures of aluminides in the 1252 alloy in a volume of $(56 \mu\text{m})^3$: a) 0h/500°C, b) 1h/500°C and c) 4h/500°C. Voxel size= $(0.28\mu\text{m})^3$

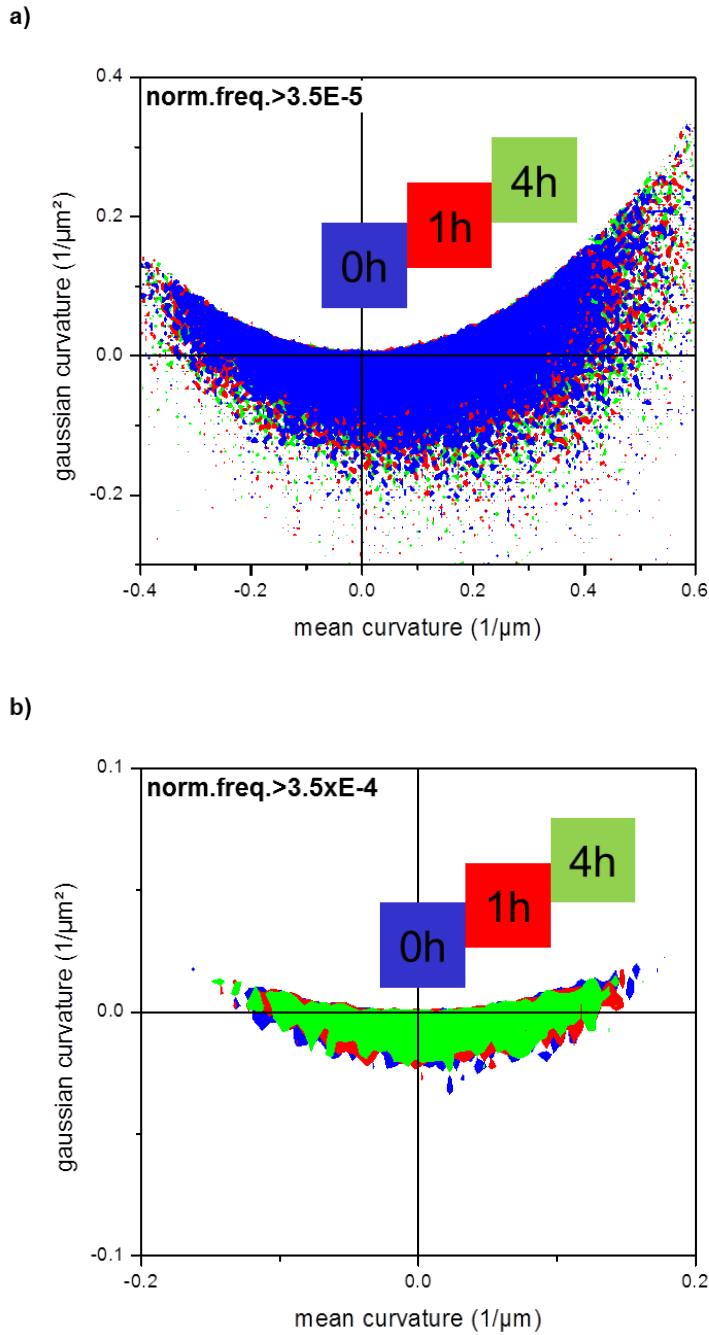


Fig. 3.38: Comparison of the surface curvature distribution of aluminides in the 1252 alloy after 0h/1h/4h at 500°C: a) norm.freq. >3.5E-5 b) norm.freq. >3.5E-4.

No perceptible changes are observed in the surface curvature distribution of aluminides in the 1252 alloy as a function of solution treatment time. In Fig. 3.38 the aluminides surface curvature distribution of the 1252 alloy is shown after 0h/1h/4h/500°C. Fig. 3.38a) shows all the values for normalized frequency >3.5E-5 analogue to Fig. 3.33a). Fig. 3.38b) shows the normalized frequency range >3.5E-4.

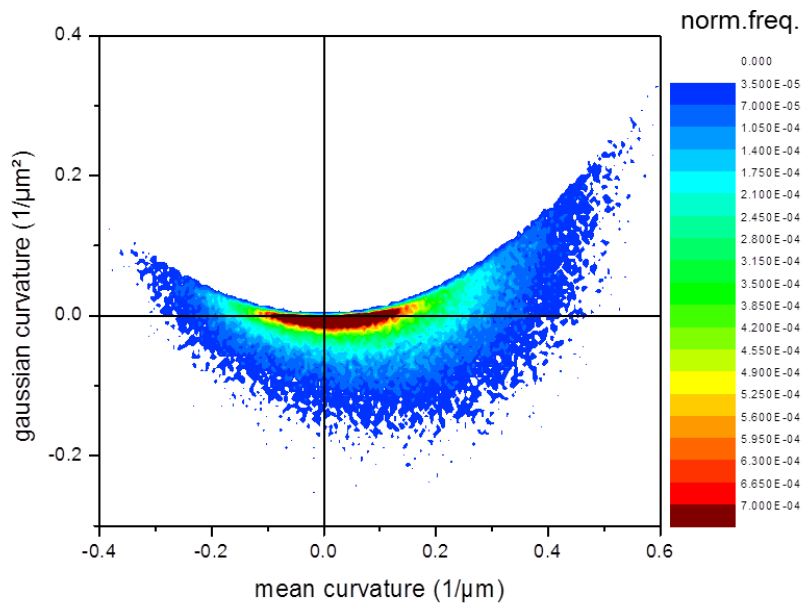


Fig. 3.39: Aluminides surface curvature distribution in the 1253 alloy after 0h/500°C.

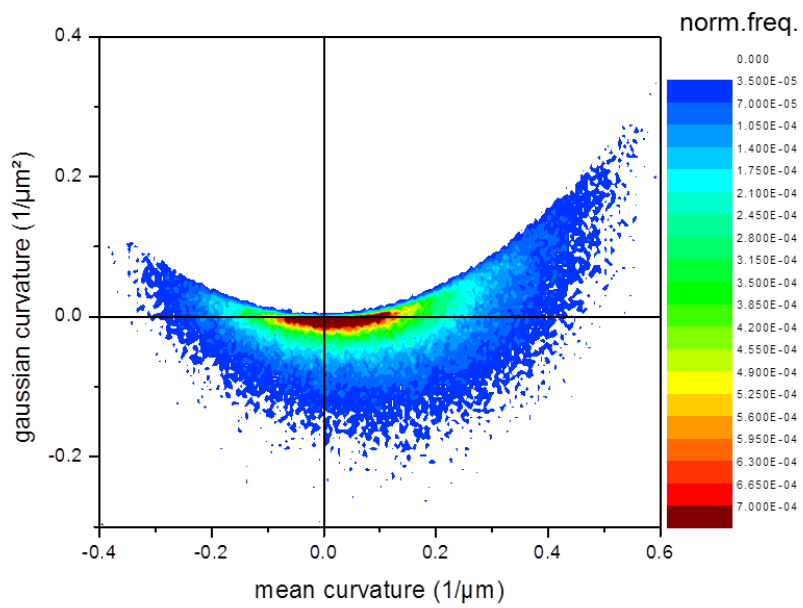


Fig. 3.40: Aluminides surface curvature distribution in the 1253 alloy after 1h/500°C.

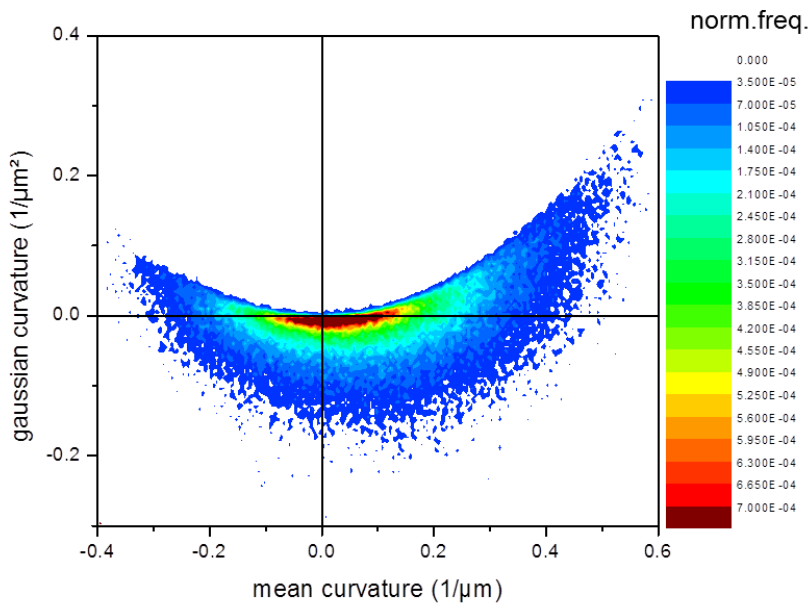


Fig. 3.41: Aluminides surface curvature distribution in the 1253 alloy after 4h/500°C.

The aluminides surface curvature distribution of the 1253 alloy is shown in Fig. 3.39, Fig. 3.40 and Fig. 3.41 for 0h/1h/4h at 500°C, respectively. There are no significant changes in distribution of the aluminides surface curvature. The comparison of the three conditions 0h/1h/4h at 500°C shows no changes after solution treatment (Fig. 3.42). In Fig. 3.42a) all values for normalized frequency $>3.5E-5$ are presented.

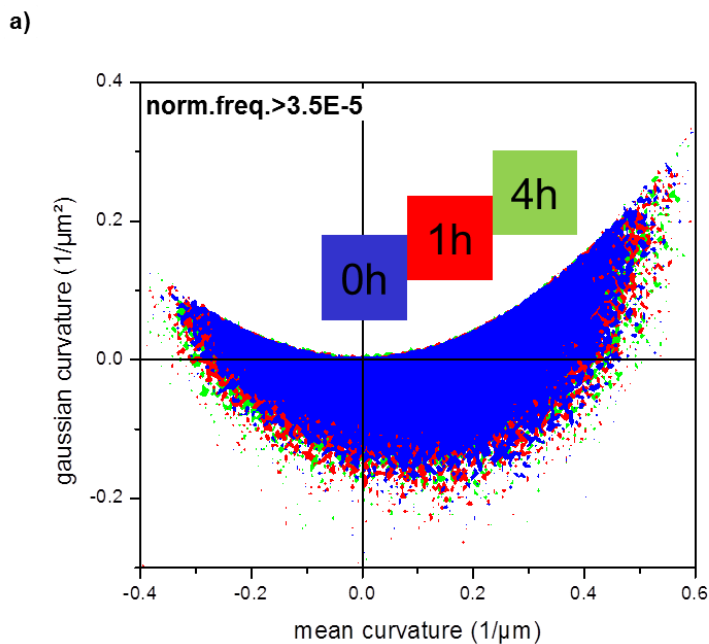


Fig. 3.42: Comparison of the surface curvature distribution of aluminides in the 1253 alloy after 0h/1h/4h at 500°C: a) norm.freq. $>3.5E-5$ b) norm.freq. $>3.5E-4$.

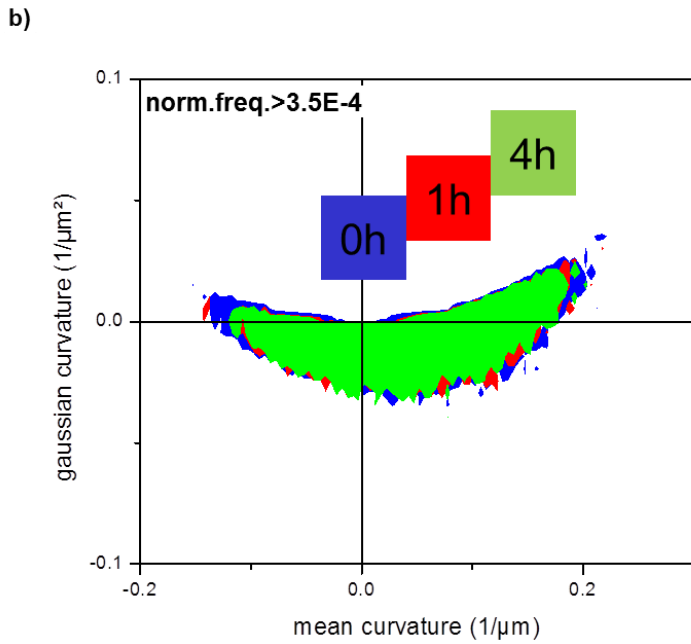


Fig. 3.42 continued: Comparison of the surface curvature distribution of aluminides in the 1253 alloy after 0h/1h/4h at 500°C: a) norm.freq. >3.5E-5 b) norm.freq. >3.5E-4.

In Fig. 3.42b) the flattest regions corresponding to normalized frequency values >3.5E-4 are shown.

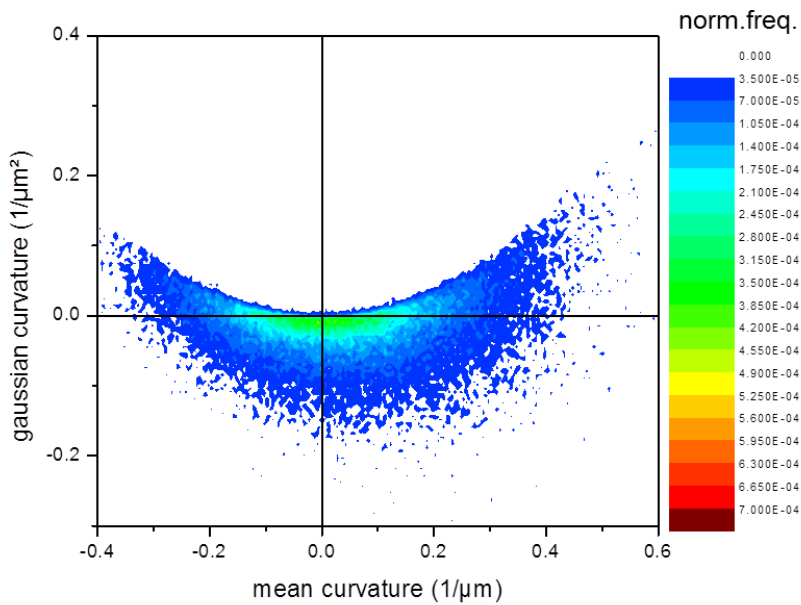


Fig. 3.43: Aluminides surface curvature distribution in the 1252-Mg alloy after 0h/500°C

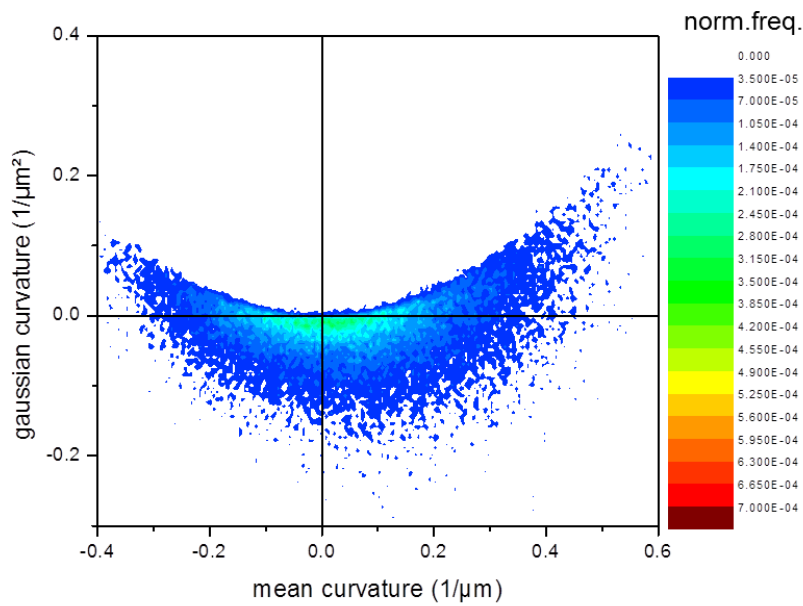


Fig. 3.44: Aluminides surface curvature distribution in the 1252-Mg alloy after 1h/500°C

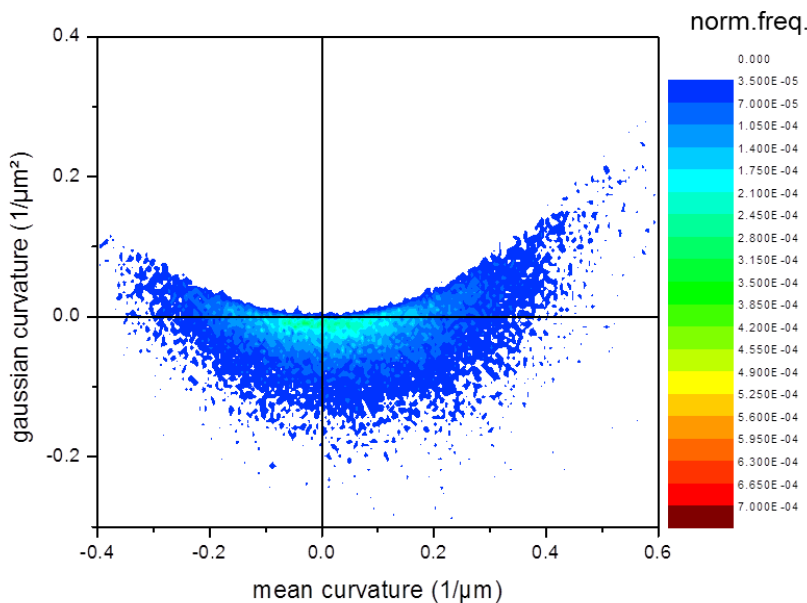


Fig. 3.45: Aluminides surface curvature distribution in the 1252-Mg alloy after 4h/500°C

The aluminides surface curvature distribution of the 1252-Mg alloy is shown in Fig. 3.43, Fig. 3.44 and Fig. 3.45 for 0h/1h/4h500°C, respectively. 3D rendered volumes of the same region $(56\mu\text{m})^3$ after 0h/1h/4h at 500°C are shown in Fig. 3.46 with Gaussian curvature as a surface color.

There are small perceptible changes in the distribution of surface curvatures. In Fig. 3.47a) values for normalized frequency $>3.5\text{E-}5$ are presented. In Fig. 3.47b) the flat regions corresponding to the normalized frequency $>2.1\text{E-}4$ are shown. The

spheroidization of aluminides is not detectable but the distribution at the flat regions close to (0,0) tends to broaden with solution treatment time, which was not seen in the 1252 and 1253 alloys. The comparison of the three conditions 0h/1h/4h at 500°C shows this change after solution treatment (Fig. 3.47b).

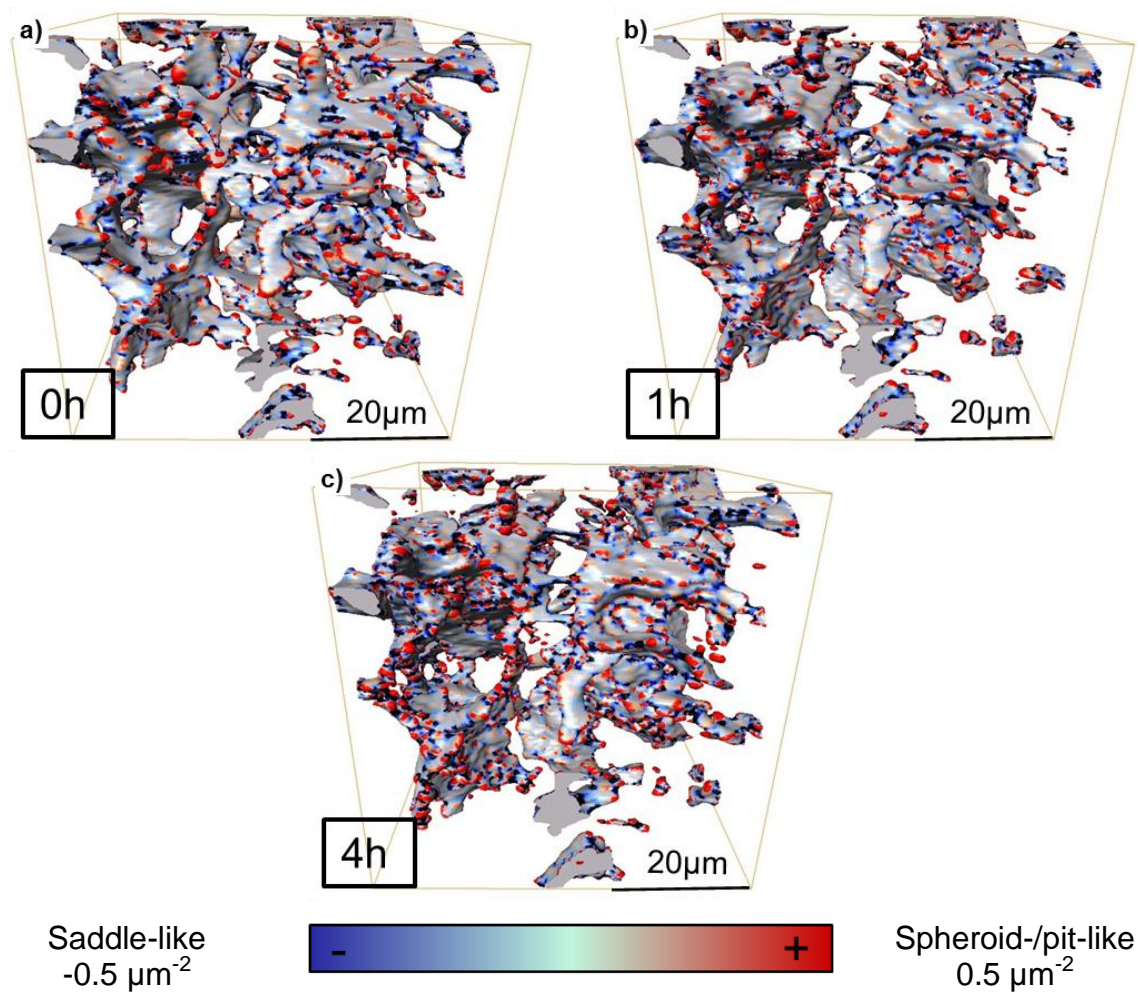


Fig. 3.46: Gaussian curvatures of aluminides in the 1252-Mg alloy in a volume of $(56 \mu\text{m})^3$: a) 0h/500°C, b) 1h/500°C and c) 4h/500°C. Voxel size= $(0.28 \mu\text{m})^3$

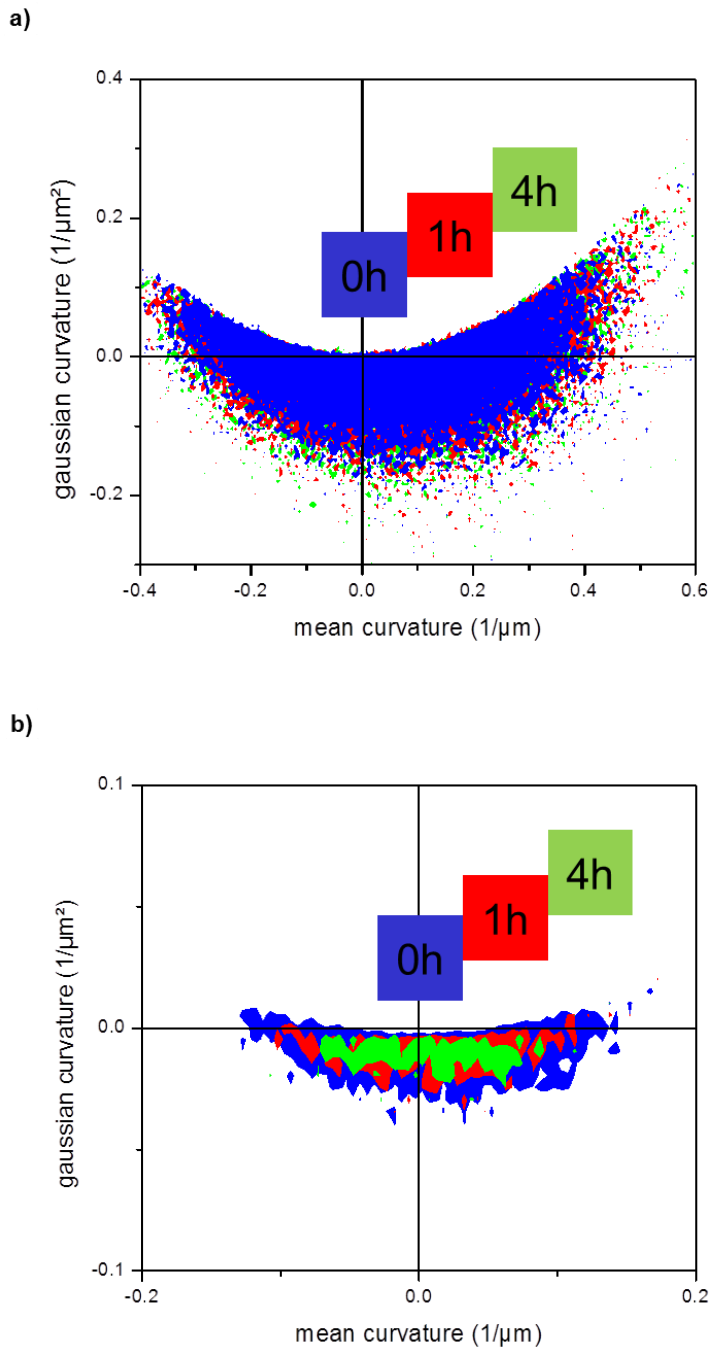


Fig. 3.47: Comparison of the surface curvature distribution of aluminides in the 1252-Mg alloy after 0h/1h/4h at 500°C: a) norm.freq. $>3.5\text{E-}5$ b) norm.freq. $>2.1\text{E-}4$.

Fig. 3.48, Fig. 3.49 and Fig. 3.50 show the curvature of aluminides in the 1740 alloy after 0h/1h/4h of solution treatment at 500°C, respectively. The alloy 1740 shows broader distribution of Gaussian and mean curvatures than the piston alloys. Change of interconnectivity and volume fraction of aluminides is shown in the 3D rendered volumes in Fig. 3.51 with additional Gaussian curvature color scale. The comparison between solution treated conditions 0h/1h/4h at 500°C displayed in Fig. 3.52 shows an evolution towards spheroid-like morphologies and some broadening of the surface

curvature distribution towards negative Gaussian curvatures. In Fig. 3.52a) the surface curvature distribution of aluminides is shown for normalized frequency $>3.5E-5$. In Fig. 3.52b) the distribution for normalized frequency $>1.2E-4$ are shown. This value was chosen because the maximum normalized frequency is $\sim 3E-4$.

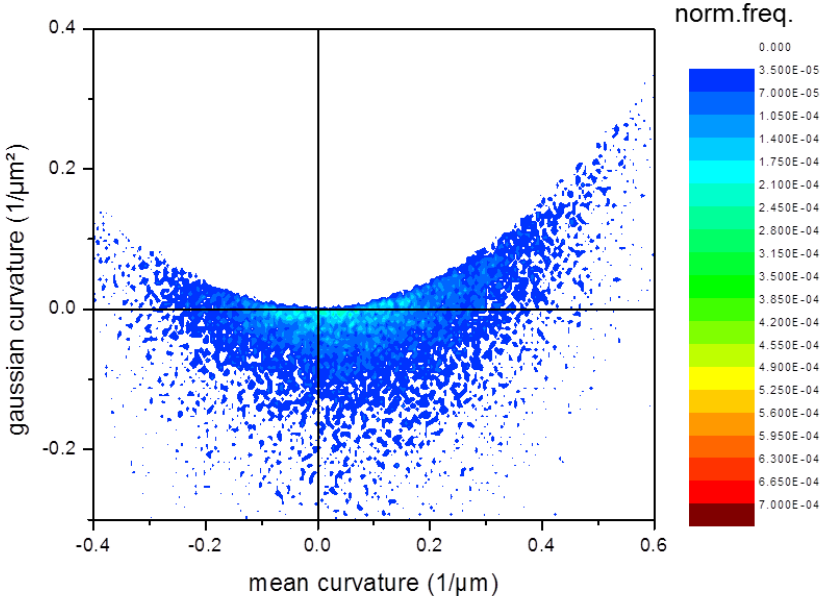


Fig. 3.48: Aluminides surface curvature distribution in the 1740 alloy after 0h/500°C.

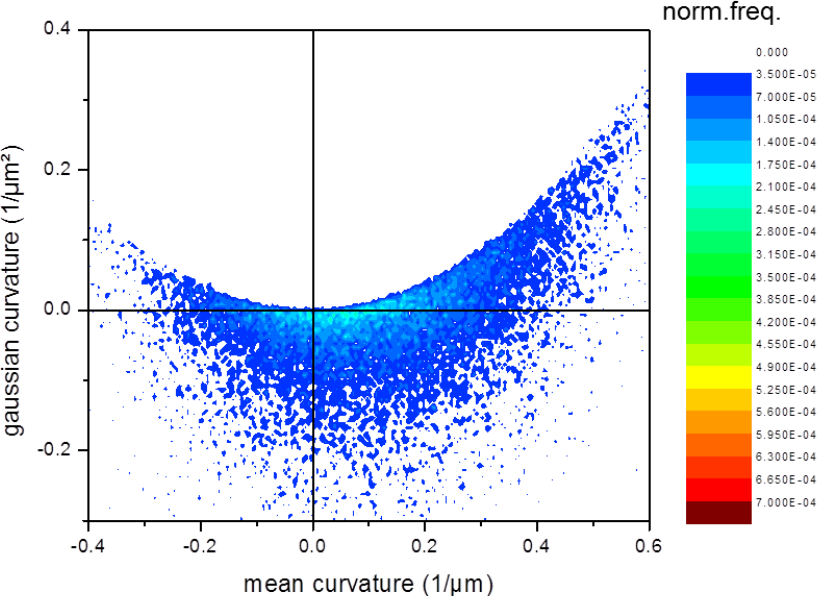


Fig. 3.49: Aluminides surface curvature distribution in the 1740 alloy after 1h/500°C.

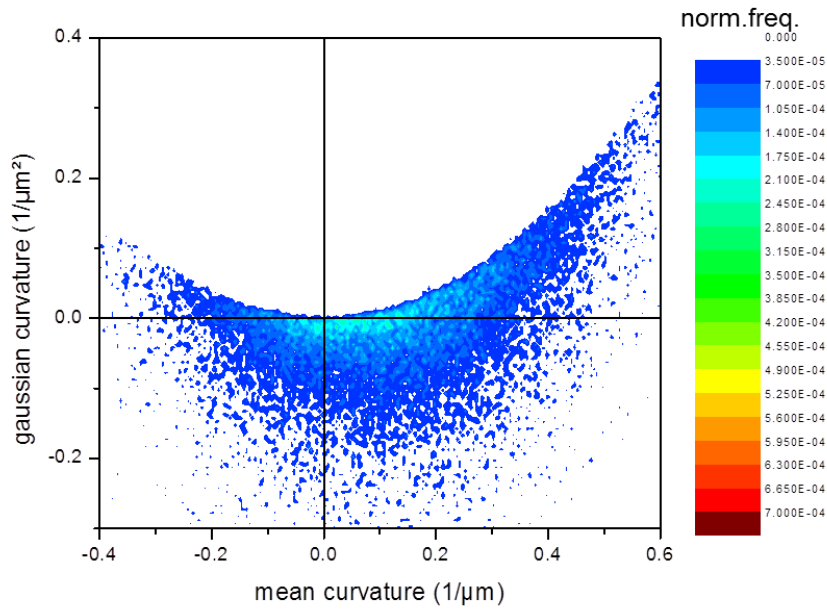


Fig. 3.50: Aluminides surface curvature distribution in the 1740 alloy after 4h/500°C.

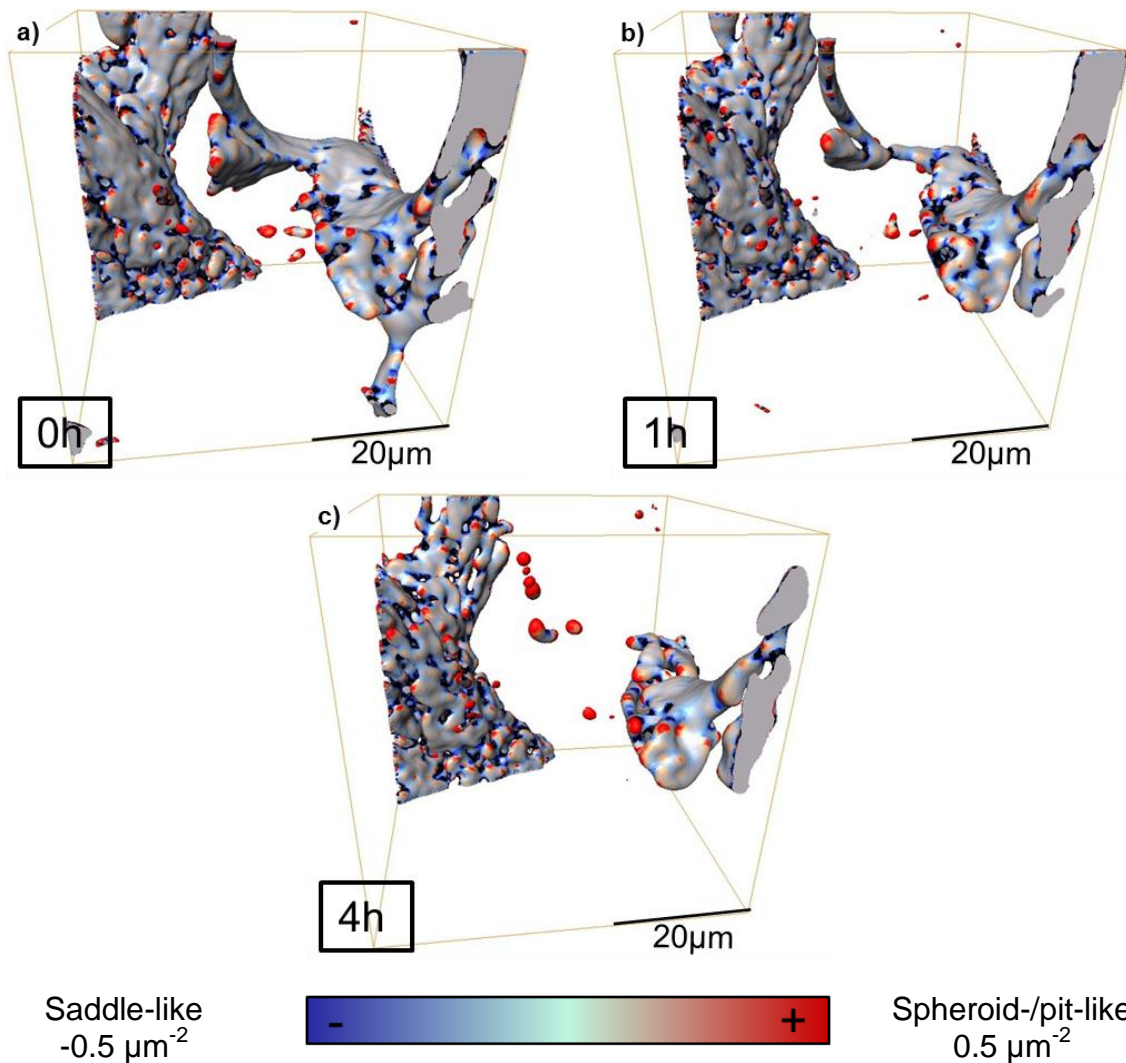


Fig. 3.51: Gaussian curvatures of Aluminides in the 1740 alloy in a volume of $(56 \mu\text{m})^3$: a) 0h/500°C, b) 1h/500°C and c) 4h/500°C. Voxel size= $(0.28 \mu\text{m})^3$

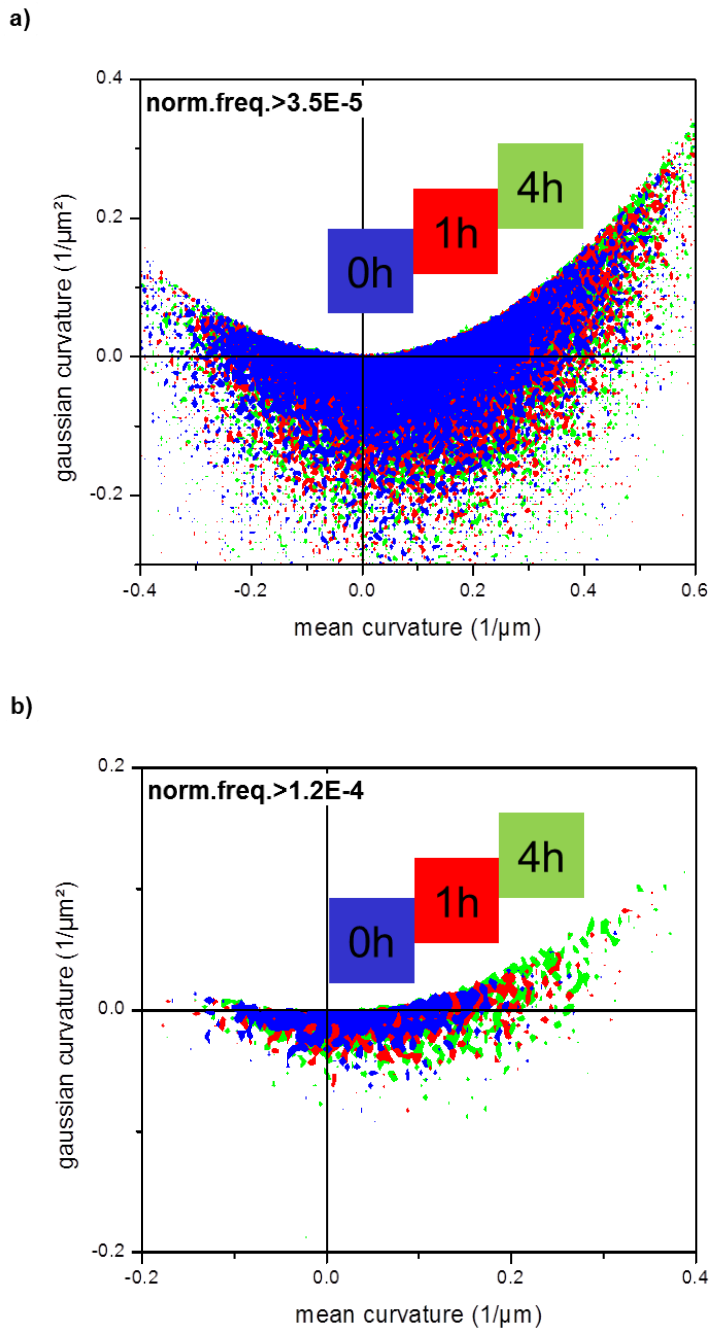


Fig. 3.52: Comparison of the surface curvature distribution of aluminides in the 1252 alloy after 0h/1h/4h at 500°C: a) norm.freq. >3.5E-5 b) norm.freq. >1.2E-4.

3.6.3.1. Morphology of Silicon

The evolution of the morphology of eutectic and primary Si in the 1062 alloy is depicted in Fig. 3.53 to Fig. 3.55 as mean and Gaussian curvature distribution of the same investigated volume after 0h, 1h and 4h at 500°C, respectively. It can be seen that spheroid regions with larger curvatures tend to form after 1h of 500°C as reflected by the higher frequency in the right upper corner of the positive-positive quadrant. This can be clearly observed in the overlapped graphs in Fig. 3.56. 3D

rendered volumes of the hand segmented silicon with Gaussian curvature as color scale is shown in Fig. 3.57.

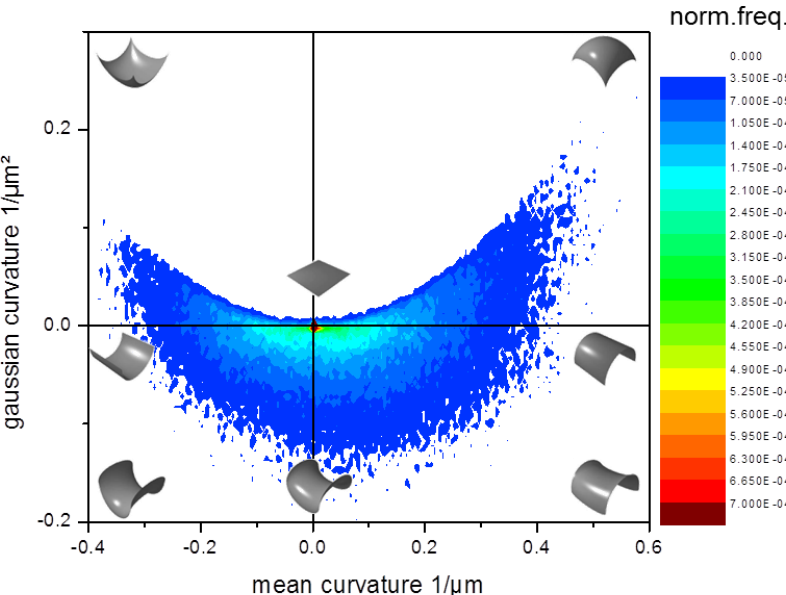


Fig. 3.53: Surface curvature distribution of silicon in the 1062 alloy after 0h/500°C.

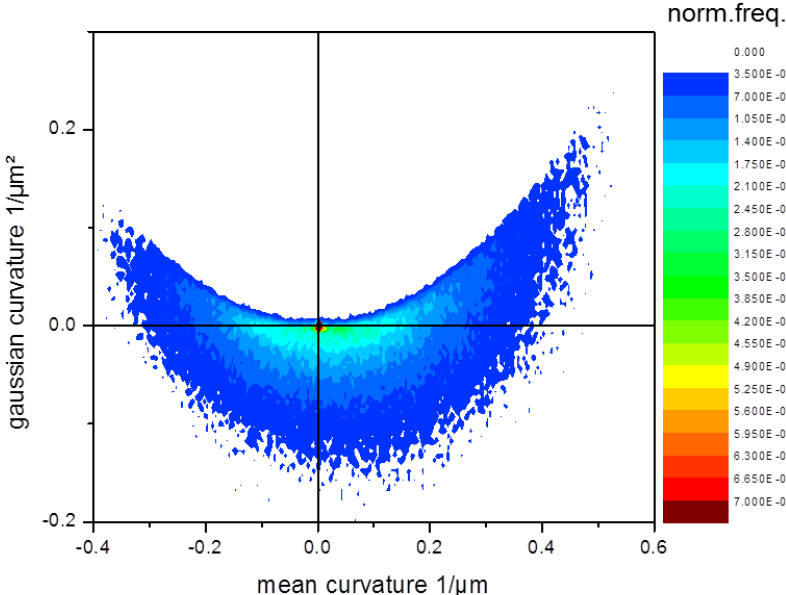


Fig. 3.54: Surface curvature distribution of silicon in the 1062 alloy after 1h/500°C.

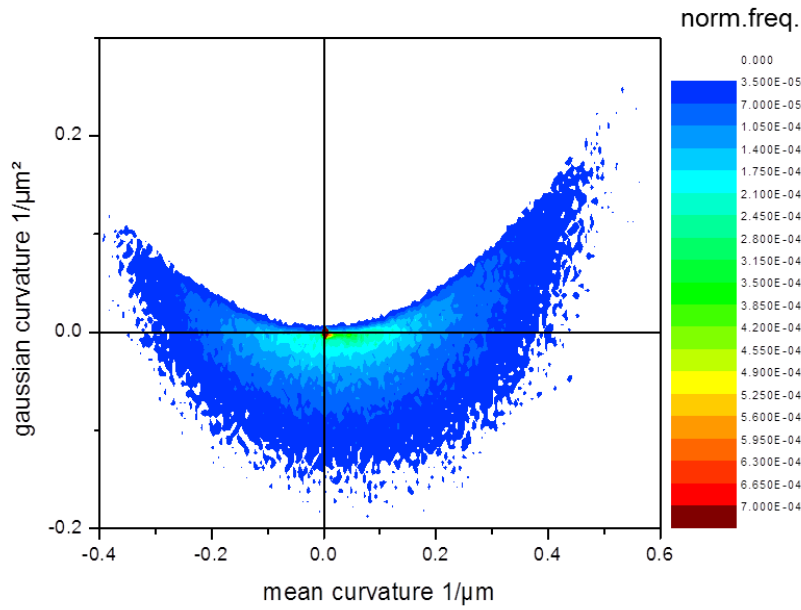


Fig. 3.55: Surface curvature distribution of silicon in the 1062 alloy after 4h/500°C.

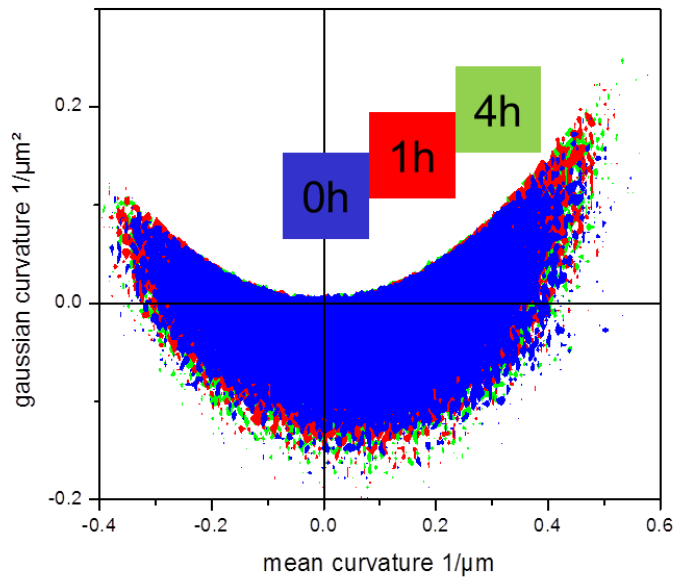


Fig. 3.56: Spheroidization of silicon in the same region of interest of the 1062 alloy after 0h/1h/4h at 500°C. Norm.freq>3.5E-5.

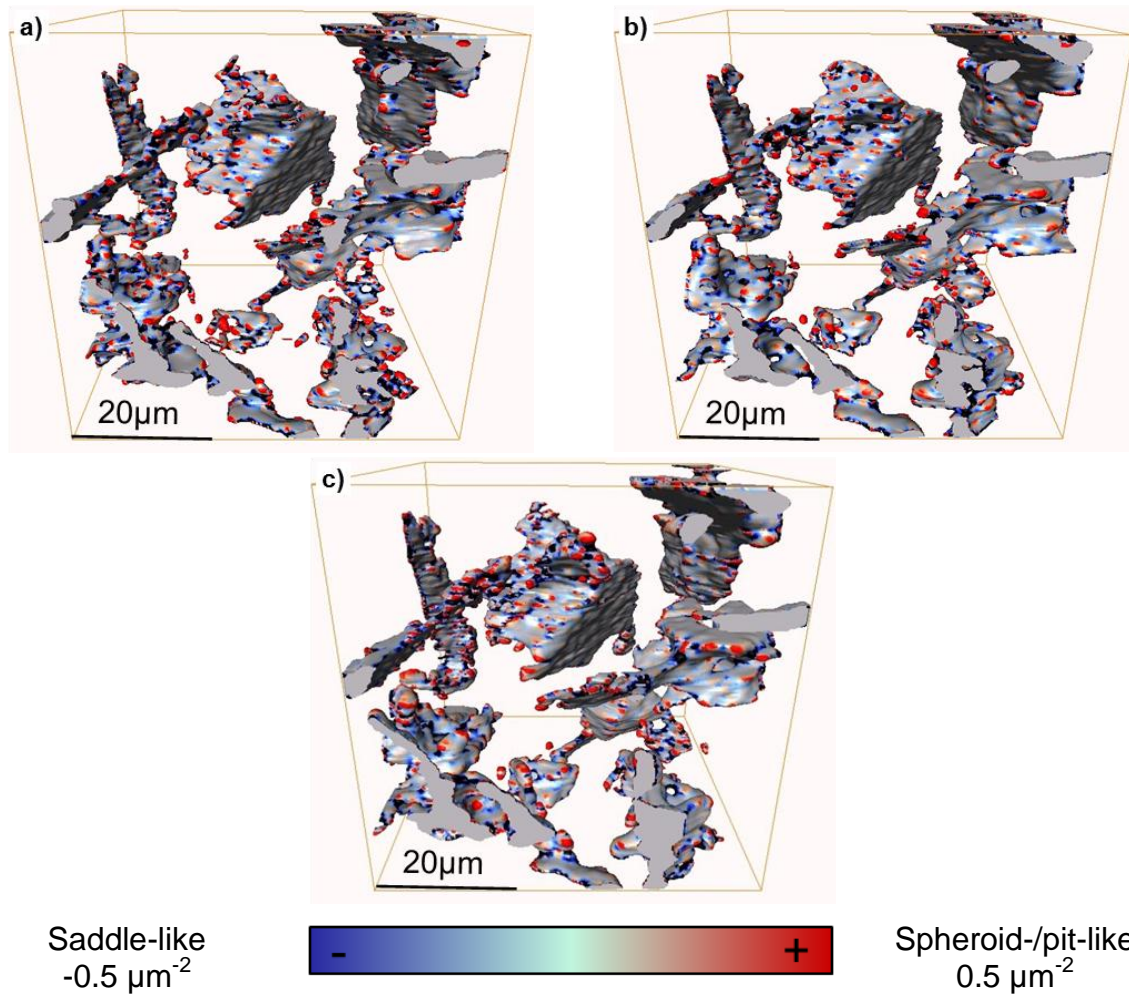


Fig. 3.57: Gauss curvatures of Si in the 1062 alloy for a volume of 56x56x56 μm^3 : a) 0h/500°C, b) 1h/500°C and c) 4h/500°C.

The evolution of the morphology of eutectic and primary Si in the 1252 alloy is depicted in Fig. 3.58 to Fig. 3.60 as Gaussian and mean curvature distribution graphs after 0h, 1h and 4h at 500°C, respectively. It can be seen that spheroid regions with larger curvature tend to form after 4h at 500°C as reflected by the higher frequency in the right upper corner of the positive-positive quadrant. This can be clearly observed in the overlapped graphs in Fig. 3.61. The morphological changes in the silicon in the 1252 alloy are clearer than in the 1062 alloy (Fig. 3.56). Here, also a slight increase of pit-like regions can be seen after 4h of solution treatment.

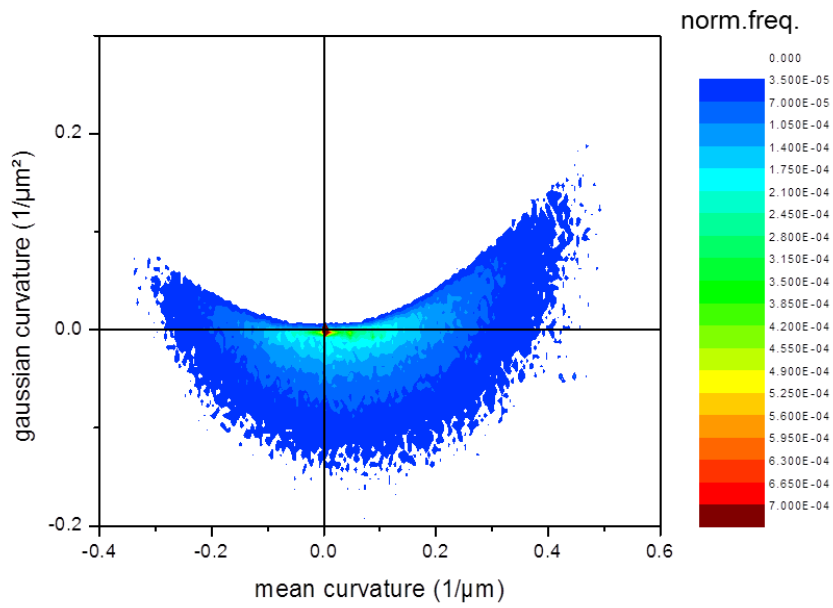


Fig. 3.58: Surface curvature distribution of silicon in the 1252 alloy after 0h/500°C.

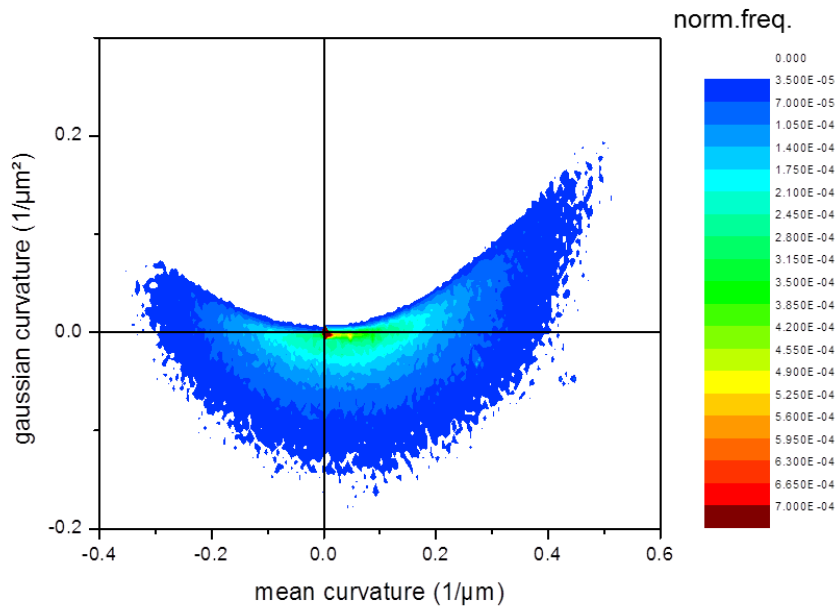


Fig. 3.59: Surface curvature distribution of silicon in the 1252 alloy after 1h/500°C.

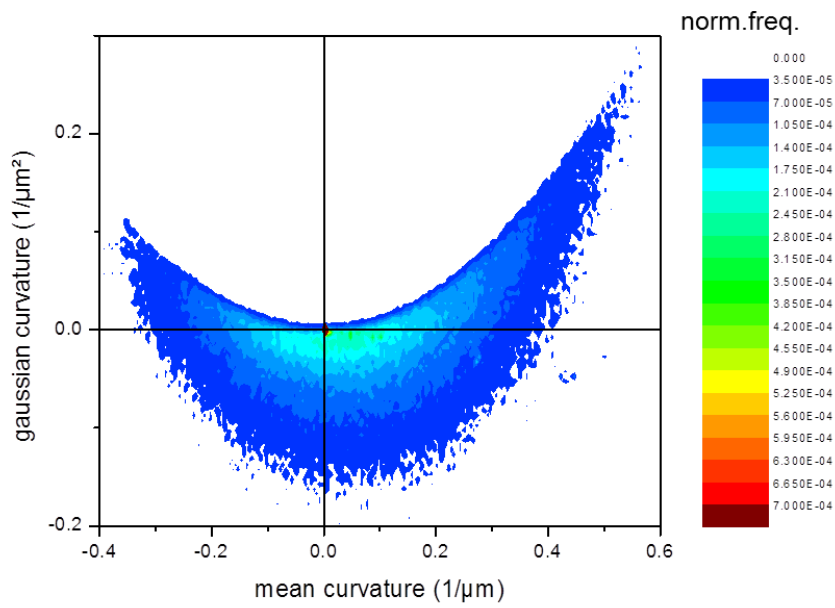


Fig. 3.60: Surface curvature distribution of silicon in the 1252 alloy after 4h/500°C.

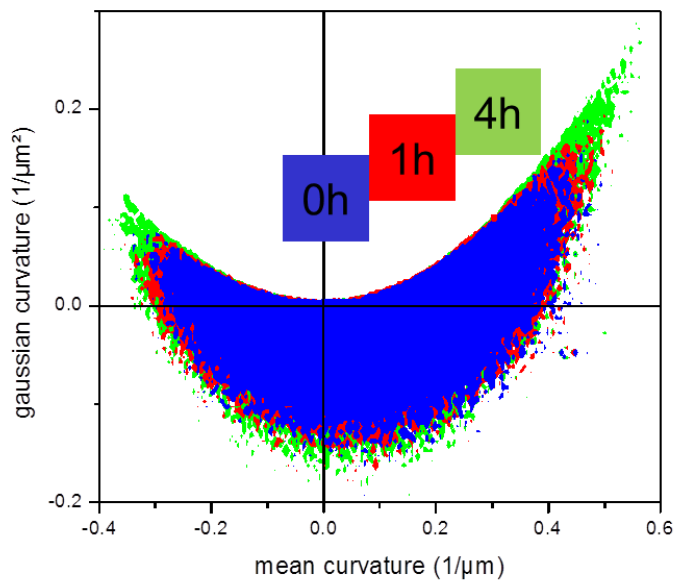


Fig. 3.61: Spheroidization of silicon in the same region of interest of the 1252 alloy after 0h/1h/4h at 500°C. Norm.freq>3.5E-5.

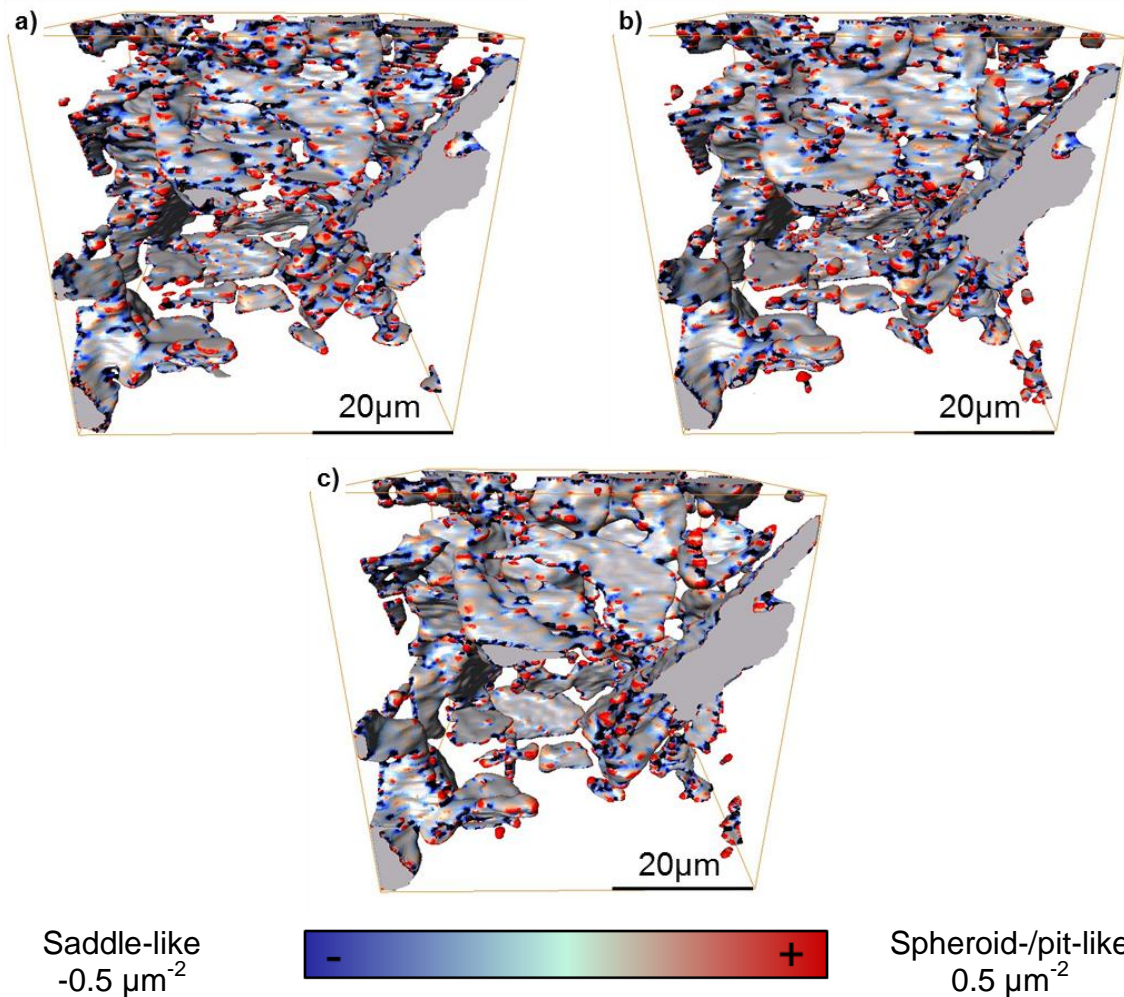


Fig. 3.62: Gauss curvatures of Si in the 1252 alloy in a volume of $56 \times 56 \times 56 \mu\text{m}^3$: a) 0h/500°C, b) 1h/500°C and c) 4h/500°C.

The evolution of the morphology of eutectic and primary Si in the 1740 alloy is shown in Fig. 3.63 to Fig. 3.65 as Gaussian and mean curvature distributions after 0h, 1h and 4h at 500°C, respectively. 3D rendered volumes are shown in 0h/1h/4h/500°C conditions with Gaussian surface curvature color scale in Fig. 3.67. Analogue to the 1062 alloy it can be seen that more spheroid regions with larger curvatures tend to form after 1h at 500°C as reflected by the higher frequency in the right upper corner of the positive-positive quadrant. This can be observed in the overlapped graphs in Fig. 3.66. There is also a higher amount of flat regions (Fig. 3.63 to Fig. 3.65) owing to the higher amount of blocky primary silicon in the 1740 alloy.

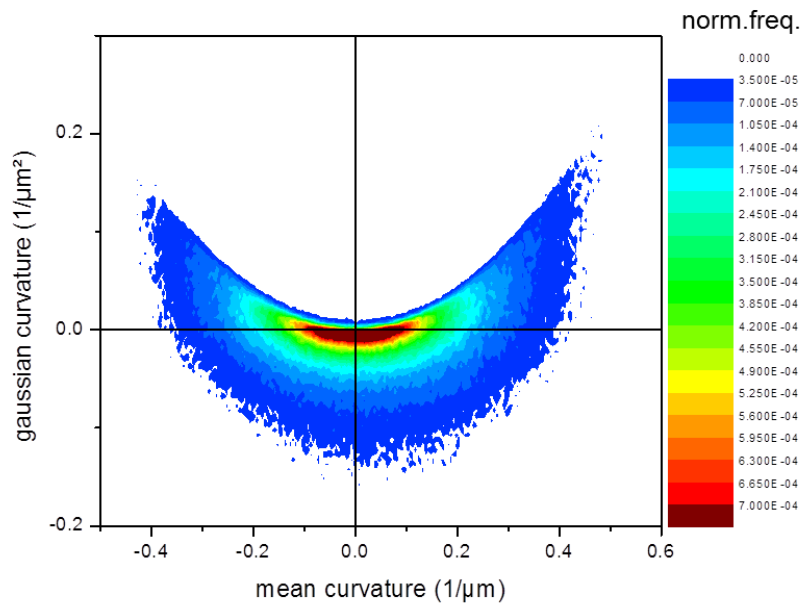


Fig. 3.63: Surface curvature distribution of silicon in the 1740 alloy in 0h/500°C.

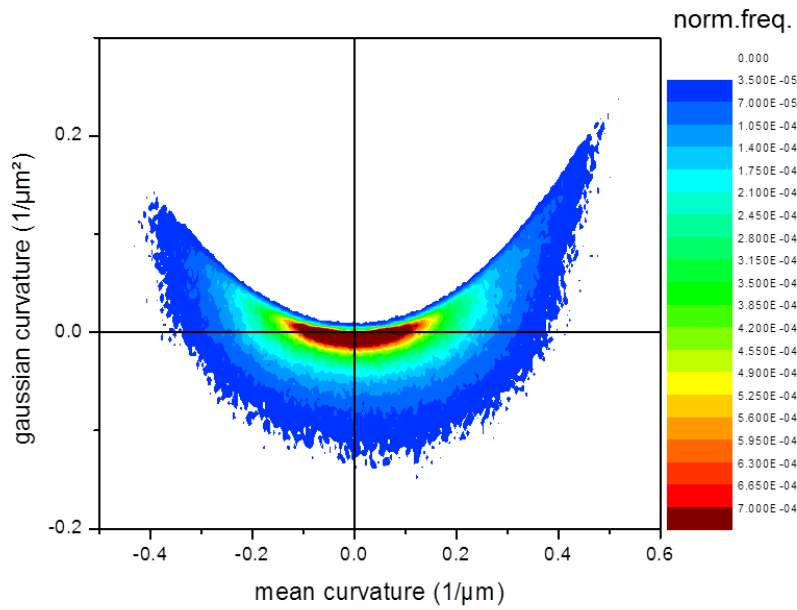


Fig. 3.64: Surface curvature distribution of silicon in the 1740 alloy in 1h/500°C.

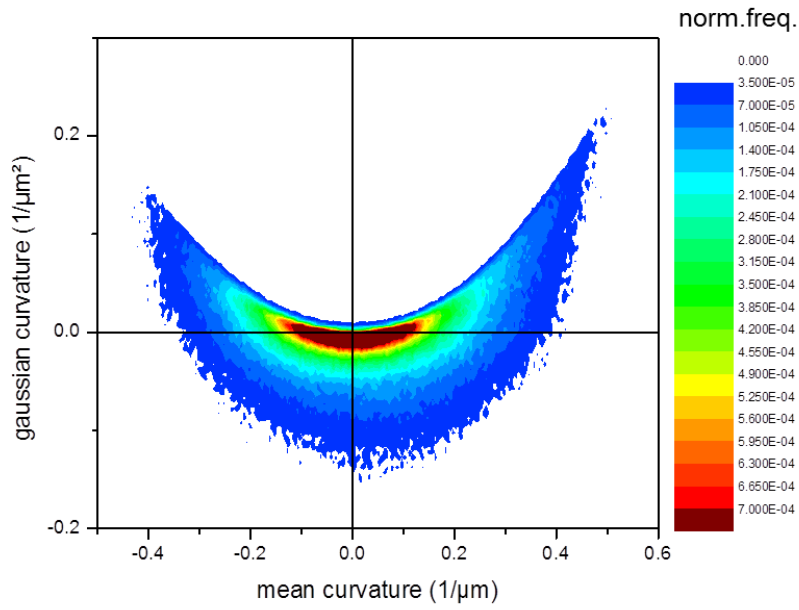


Fig. 3.65: Surface curvature distribution of silicon in the 1740 alloy in 4h/500°C.

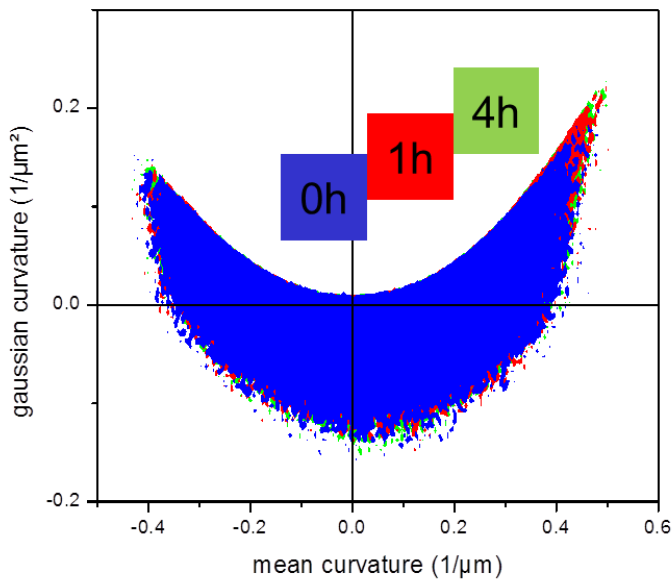


Fig. 3.66: Spheroidization of silicon in the same region of interest of the 1740 alloy after 0h/1h/4h at 500°C.

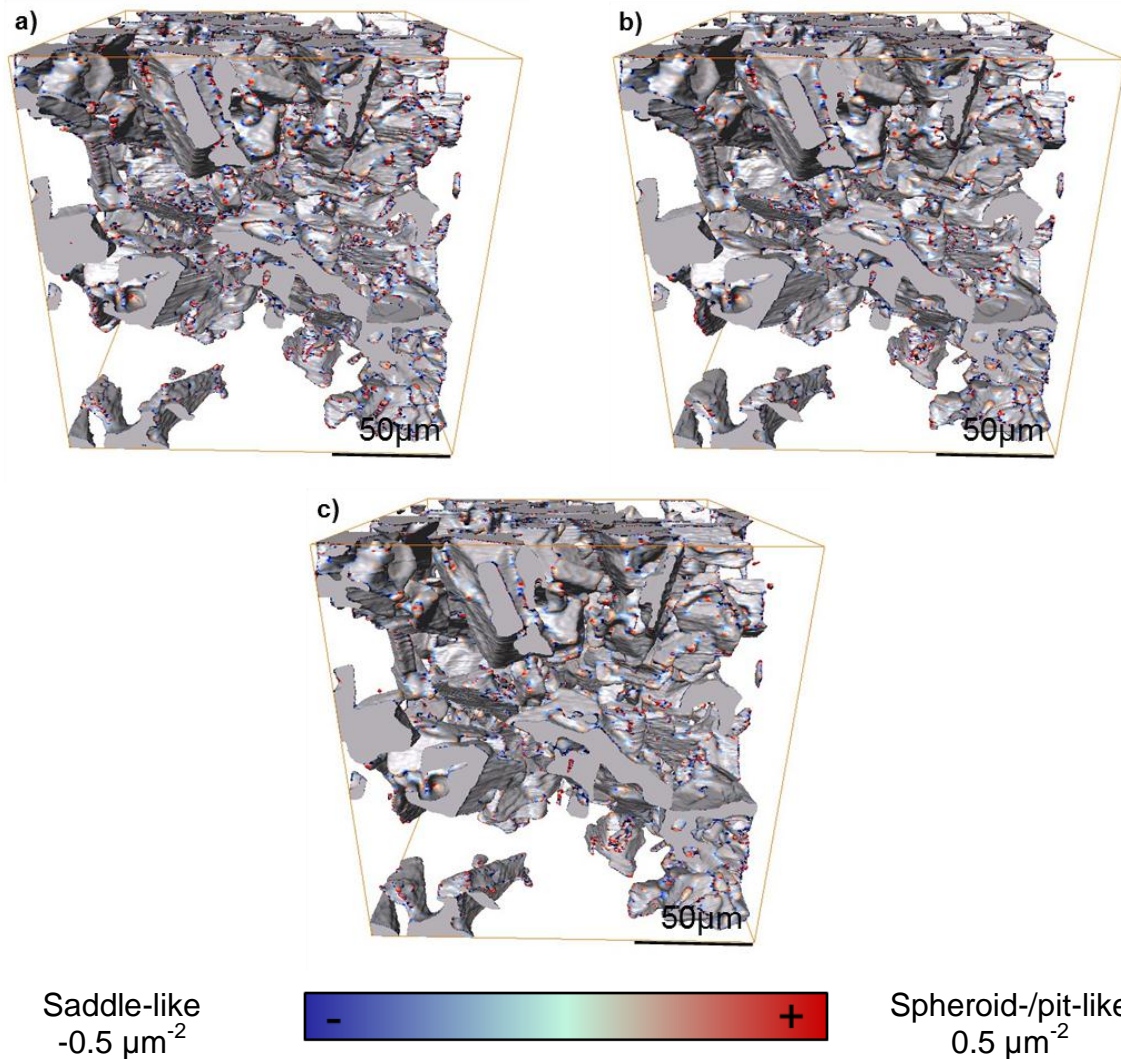


Fig. 3.67: Gauss curvatures of Si in the 1740 alloy in a volume of 651x600x600 μm^3 : a) 0h/500°C, b) 1h/500°C and c) 4h/500°C.

3.7. Hardness evolution during ageing

Brinell hardness HB1/10 was performed for all alloys to determine their overageing behavior at 300°C. Two initial conditions were considered, namely no solution treatment (0h/500°C) and 1h solution treatment at 500°C (1h/500°C). The results obtained are shown in Fig. 3.68 to Fig. 3.72. Both initial conditions show nearly identical evolution for the cases of the 1062 and 1740 alloys (Fig. 3.68 and Fig. 3.72). A stable condition is reached after 100h at 300°C for all alloys. This stable condition is used to define the T7 heat treatment in this work.

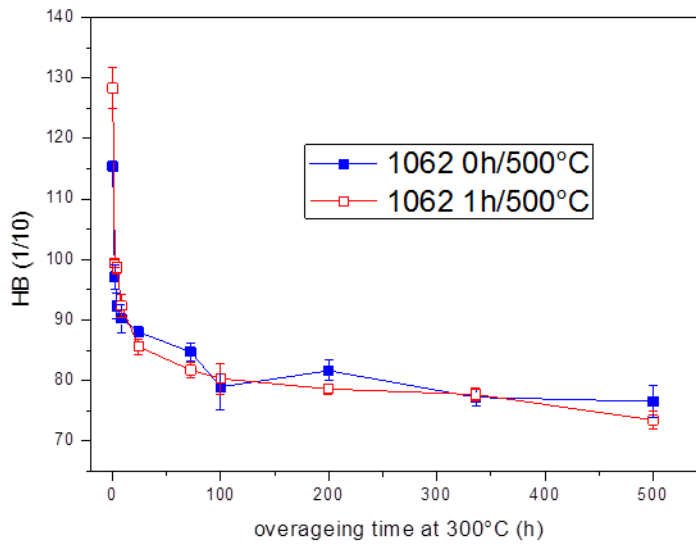


Fig. 3.68: Brinell hardness evolution for the 1062 alloy after exposure at 300°C.

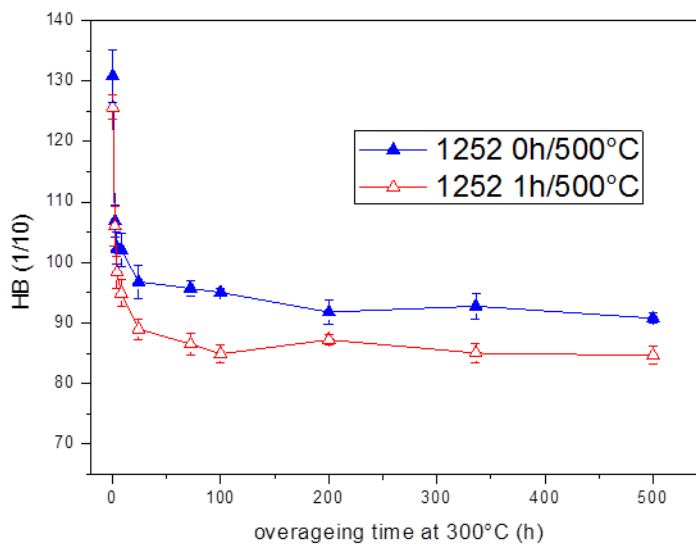


Fig. 3.69: Brinell hardness evolution for the 1252 alloy after exposure at 300°C.

On the other hand, the alloys 1252, 1253 and 1252-Mg showed different hardness evolution between the initial conditions. After 5-10h of exposure at 300°C the hardness curves detach from each other resulting in a higher hardness for the 0/500°C condition than for 1h/500°C after 500h at 300°C.

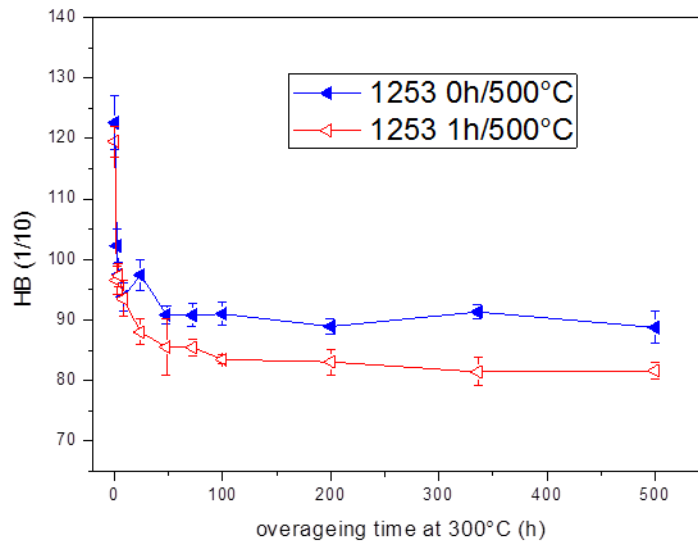


Fig. 3.70: Brinell hardness evolution for the 1253 alloy after exposure at 300°C.

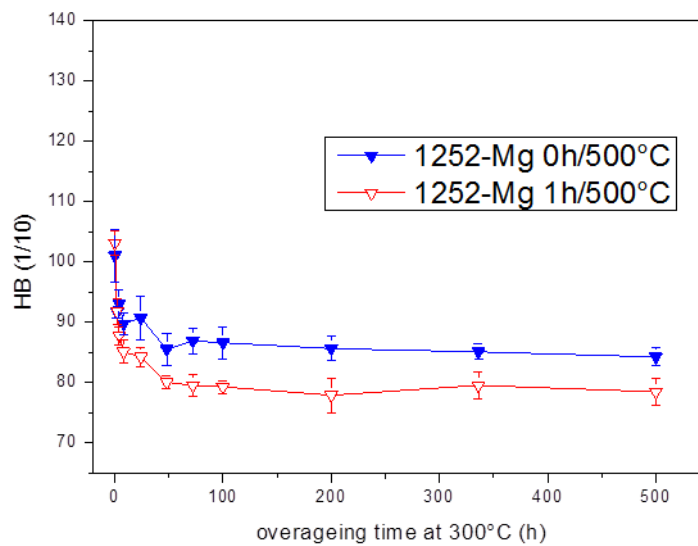


Fig. 3.71: Brinell hardness evolution for the 1252-Mg alloy after exposure at 300°C.

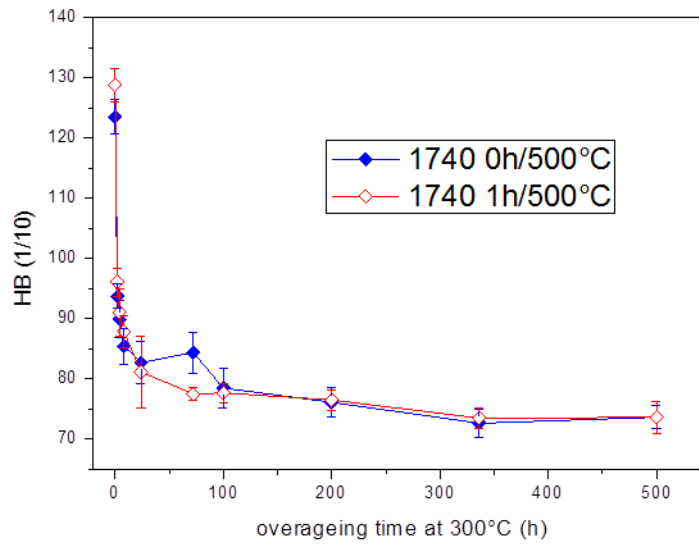


Fig. 3.72: Brinell hardness evolution for the 1740 alloy after exposure at 300°C.

3.8. Hardness of matrix

The hardness of the matrix was investigated by nanoindentation to determine if the differences in HB 1/10 observed between the 0h/500°C and 1h/500°C initial conditions during overageing of the 1252, 1253 and 1252-Mg alloys (Fig. 3.69-Fig. 3.71) are a consequence of the precipitation condition of the matrix. The results (Tab. 3.2) show that the hardness of the matrix is practically the same for the 0h/500°C and 1h/500°C conditions. Only the 1253 alloy shows a slight increase after 1h/500°C+100h/300°C.

	0h/500°C+100h/300°C H[GPa]	1h/500°C+100h/300°C H[GPa]
1062	1.01±0.04	0.96±0.02
1252	0.84±0.02	0.91±0.03
1253	0.78±0.02	0.88±0.03
1252-Mg	0.77±0.1	0.74±0.04

Tab. 3.2: Hardness measured of the matrix of the piston alloys measured by nanoindentation.

3.9. Thermo-mechanical tests

3.9.1. Compression tests

Characteristic true stress/true strain curves obtained during the compression tests at RT, 300°C and 380°C are shown in Fig. 3.73 for the 1252-Mg alloy. Similar strain hardening/softening behaviors were observed for the corresponding conditions and test temperature of the other alloys.

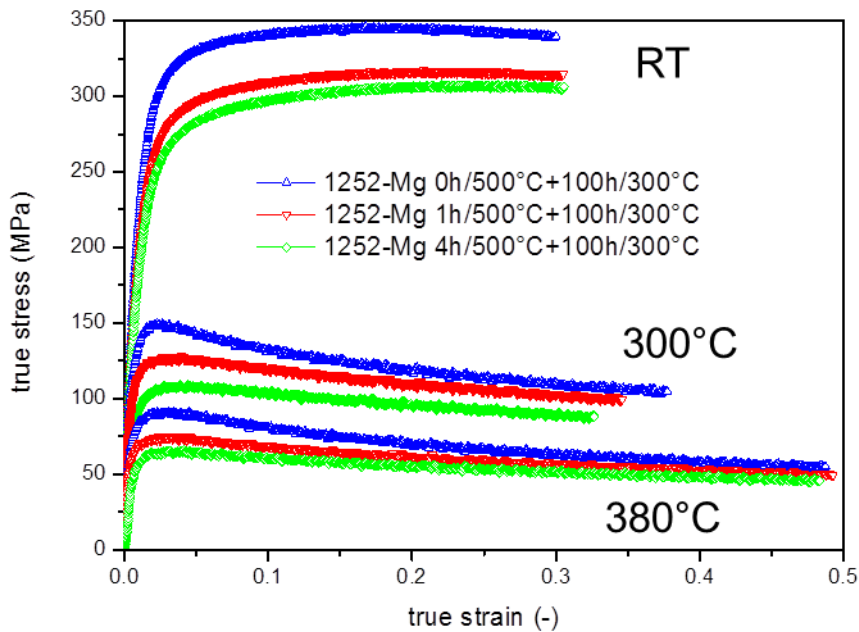


Fig. 3.73: Representative compressive stress strain curves obtained for the 1252-Mg alloy after 0h, 1h and 4h solution treatment at 500°C and consecutive overaging during 100h at 300°C.

The compression strength is shown in Fig. 3.74 a) to c) as a function of solution treatment time (ST time) for each testing temperature and for all investigated alloys in T7 condition. At room temperature the alloys 1062 and 1740 exhibit an increase of compressive strength after 1h/500°C, from $290\pm 10\text{MPa}$ and $283\pm 10\text{MPa}$ to $318\pm 5\text{MPa}$ and $300\pm 5\text{MPa}$, respectively. The alloys 1252, 1252-Mg and 1253 in 0h/500°C condition show similar compressive strength, i.e. at room temperature $333\pm 5\text{MPa}$, $341\pm 6\text{MPa}$ and $332\pm 5\text{MPa}$, respectively. The compressive strength decreases slightly for these alloys after, 1h at 500°C i.e. $325\pm 5\text{MPa}$, $317\pm 0.1\text{MPa}$ and $327\pm 5\text{MPa}$, respectively. A further strength decrease of about 3-5% is observed at room temperature for all alloys after 4h solution treatment.

Similar trends are observed for all alloys at 300°C and 380°C. The highest compressive strength is observed in the 0h/500°C condition. Then the strength decreases after 1h of solution treatment and remains practically constant for the 4h/500°C conditions, except for the 1252-Mg alloy which exhibits a further strength decrease at both temperatures. Also the 1252 alloy shows a slight decrease between 1h and 4h at 500°C for the tests carried out at 300°C. The 1740 alloy shows the lowest strength among all studied alloys for the homologous solution treatment conditions. At 300°C the 1252, 1252-Mg and 1253 alloys show similar strength for

the 0h and 1h/500°C conditions but only 1253 is able to maintain a stable strength after 4h solution treatment ($\sigma_{\max}=126\pm 2\text{MPa}$). At 380°C, the alloys can be ordered in the following sequence in terms of increasing strength: 1740, 1062, 1252 ~ 1252-Mg, 1253.

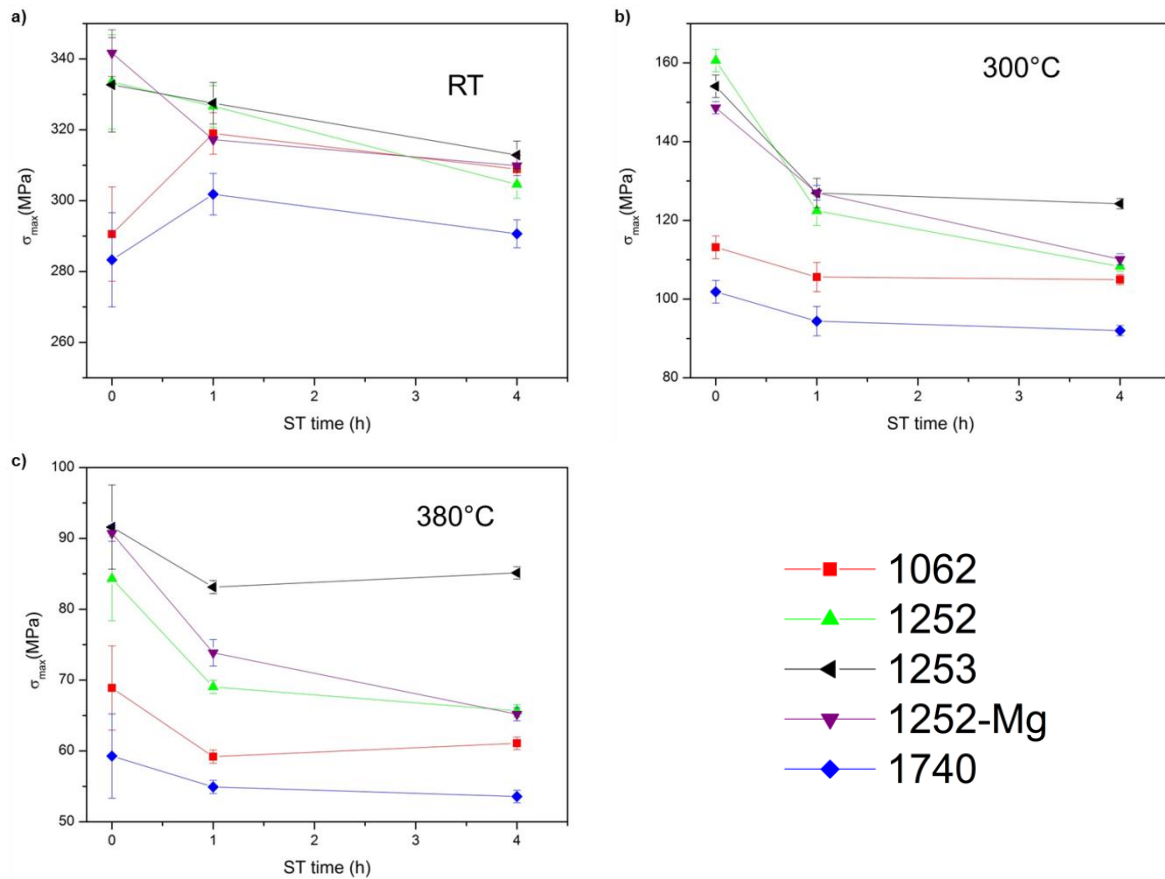


Fig. 3.74: Compressive strength (σ_{\max}) at RT, 300°C and 380°C for all investigated alloys as a function of solution treatment time (ST) at 500°C. All alloys were overaged during 100h at 300°C prior to the tests.

The compressive yield strength, $\sigma_{0.2}$, is shown in Fig. 3.75a) to c) as a function of solution treatment time for each testing temperature and for all investigated alloys with subsequent overaging for 100h at 300°C. At room temperature all alloys exhibit a decrease in compressive yield strength after 1h at 500°C. Further solution treatment up to 4h shows a slight decrease of $\sigma_{0.2}$ for all alloys, except for the 1062 alloy which exhibits an increase of ~15% between 1h and 4h at 500°C of solution treatment. Although this seems surprising two samples showed this result with a small variance. At 300°C and 380°C similar trends for $\sigma_{0.2}$ than for σ_{\max} are observed for all alloys and conditions. Analogue to the behavior of σ_{\max} , $\sigma_{0.2}$ of the 1253 alloy maintains stable after 4h of solution treatment ($\sigma_{0.2}=96\pm 0.1\text{MPa}$). At 380°C, the alloys

can be ordered in the following sequence in terms of increasing strength: 1740, 1062, 1252 ~ 1252-Mg, 1253.

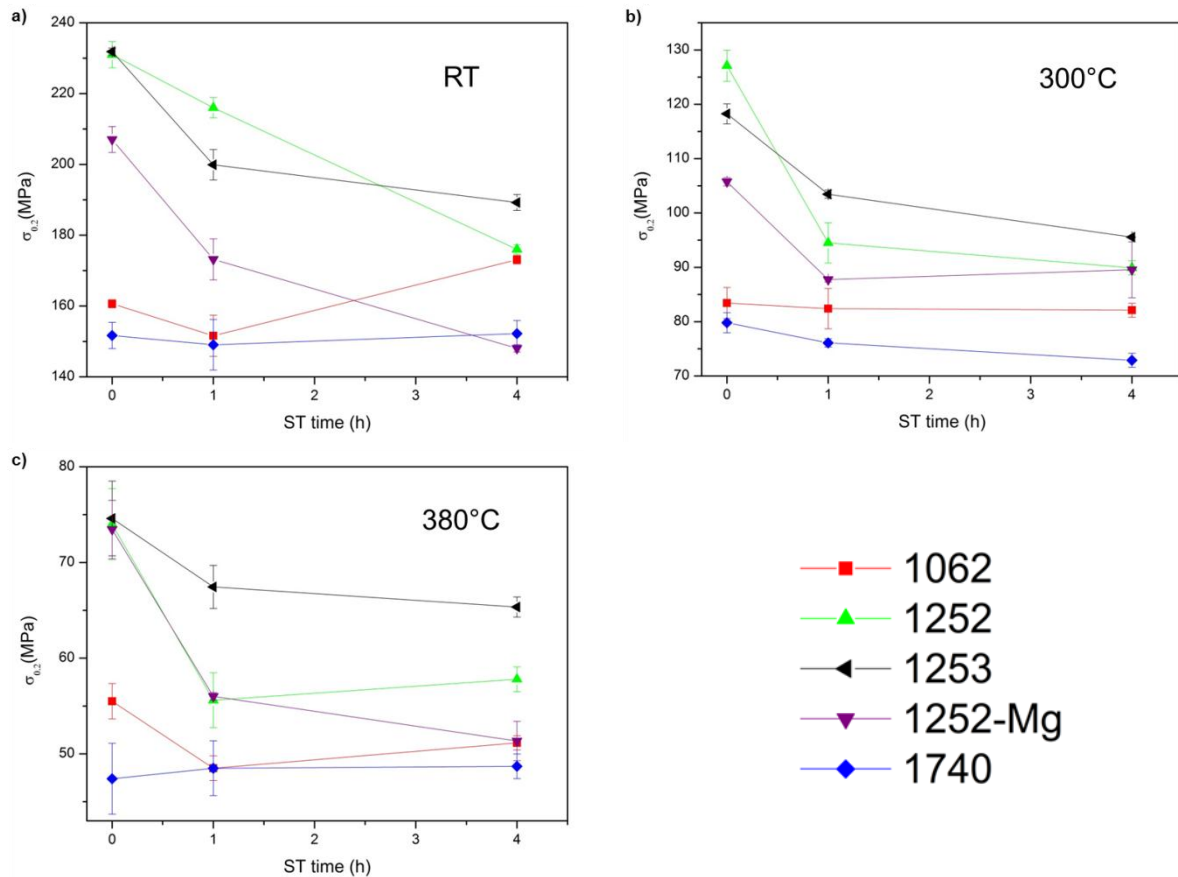


Fig. 3.75: Compressive yield strength ($\sigma_{0.2}$) at RT, 300°C and 380°C for all investigated alloys as a function of solution treatment time (ST) at 500°C. All alloys were overaged during 100h at 300°C prior to the tests.

3.9.2. Tensile tests

Characteristic results of high temperature tensile tests at 300°C and 380°C for the 1252-Mg alloy are shown in Fig. 3.76 after 0h/1h/4h at 500°C and subsequent overaging at 300°C during 100h. The ultimate tensile strength (σ_{max}), yield strength ($\sigma_{0.2}$) and elongation at fracture (A) at 300°C are displayed as a function of solution treatment time for all investigated alloys in Fig. 3.77, Fig. 3.78 and Fig. 3.79, respectively.

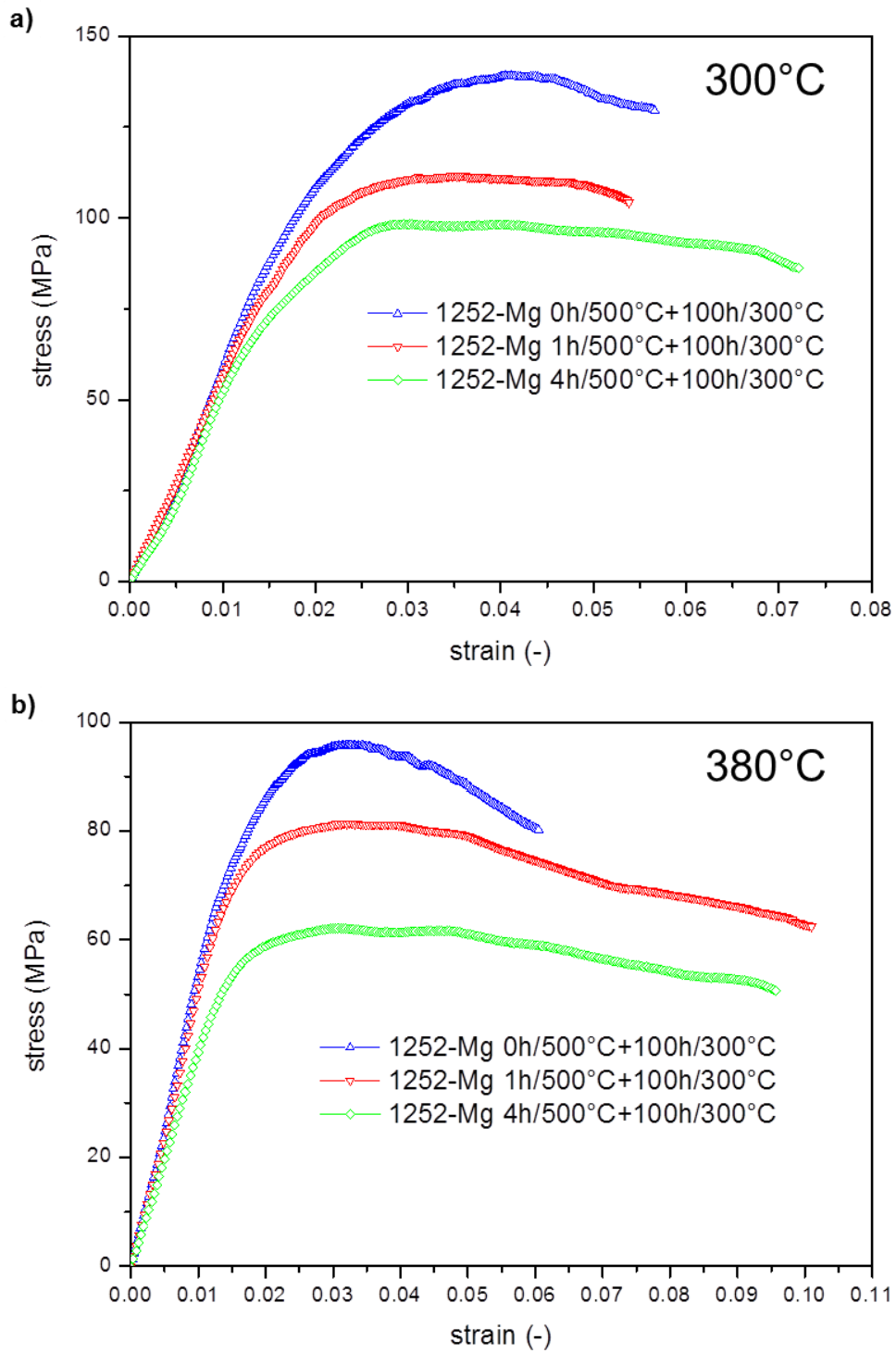


Fig. 3.76: Characteristic stress strain curves obtained during the tensile tests of the 1252-Mg alloy in 0h/1h/4h/500°C solution treated condition and subsequent overaging at 300°C: a) 300°C b) 380°C.

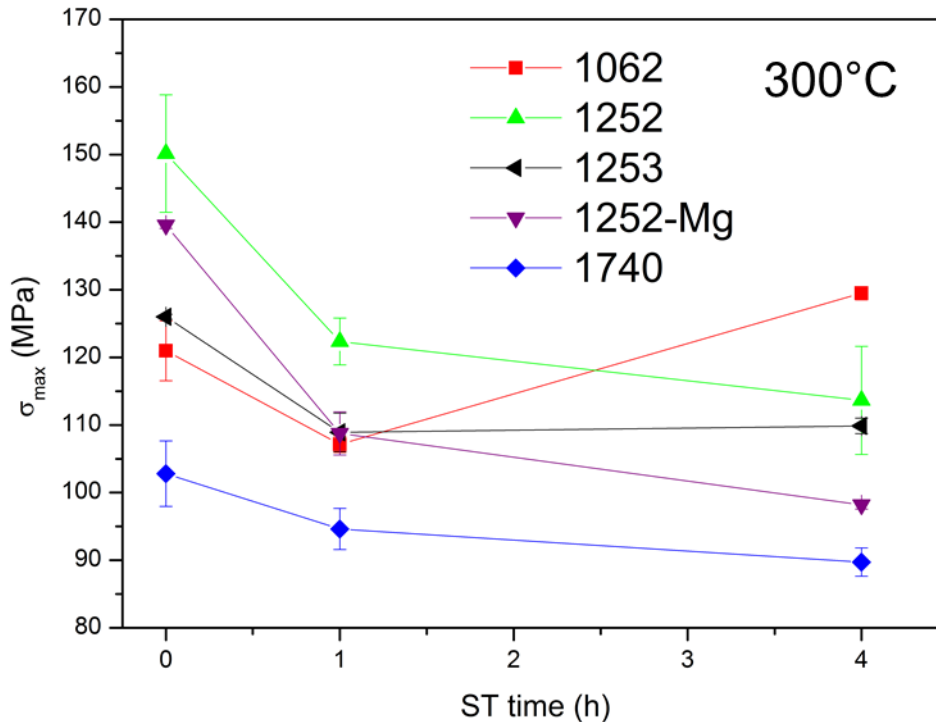


Fig. 3.77: σ_{\max} at 300°C as a function of solution treatment time at 500°C. All the alloys were subjected to overaging at 300°C for 100h.

In Fig. 3.77 the alloys 1252 and 1252-Mg show a decrease of σ_{\max} of ~20% after 1h at 500°C. Further solution treatment results in more but moderate ~7% additional loss of UTS. The alloys 1253 and 1062 show a lower decrease of <15% after 1h at 500°C. After 4h at 500°C the 1253 alloy keeps a constant σ_{\max} . The alloy 1062 shows an increase of σ_{\max} of about 20% between 1h and 4h at 500°C, confirmed with 4 samples. On the other hand, the 1740 alloy displays a total 15% decrease of σ_{\max} after 4h solution treatment. The 1740 alloy shows a lower σ_{\max} than the other alloys for all studied conditions.

The yield strength ($\sigma_{0.2}$) at 300°C (Fig. 3.78) shows an evolution similar to σ_{\max} . The alloys 1252 and 1252-Mg show the strongest $\sigma_{0.2}$ decrease after 1h at 500°C. The 1062 alloy shows an increase of yield strength after 4h at 500°C. $\sigma_{0.2}$ of the 1253 alloy decreases after 1h at 500°C and remains constant after 4h at 500°C.

The elongation at fracture (A) (Fig. 3.79) shows in general higher values for all alloys after solution treatment. The 1062 alloy shows a local maximum of elongation at fracture after 1h at 500°C. The alloys 1252-Mg and 1062 exhibit highest elongations at fracture of up to 5-6%.

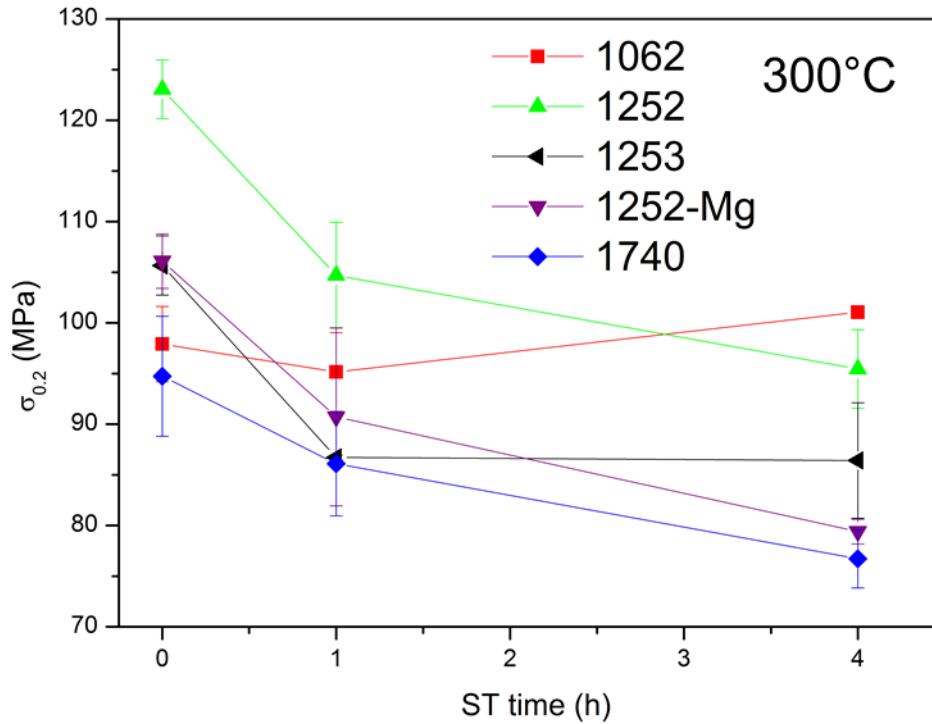


Fig. 3.78: Yield strength at 300°C as a function of solution treatment time at 500°C. All the alloys were subjected to overaging at 300°C for 100h.

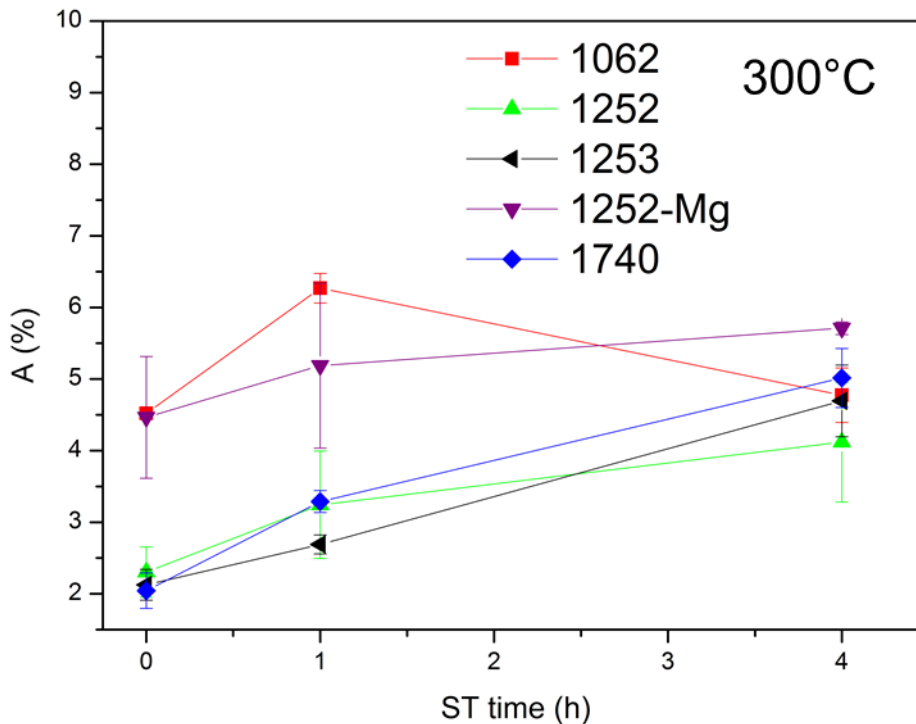


Fig. 3.79: elongation at fracture at 300°C as a function of solution treatment time at 500°C. All the alloys were subjected to overaging at 300°C for 100h.

σ_{max} at 380°C after 1h at 500°C in Fig. 3.80 shows for all alloys a decrease of ~20%. The highest σ_{max} for 1h at 500°C are achieved by 1252, 1252-Mg and 1253. Further solution treatment leads to a σ_{max} decrease of ~7% for 1252 and 1252-Mg. The alloys 1253, 1062 and 1740 remain constant after 4h at 500°C.

The evolution of yield strength at 380°C (Fig. 3.81) shows a decrease of $\sigma_{0.2}$ for all alloys after 1h at 500°C. The alloys 1252 and 1253 show minor changes comparing 1h/500°C and 4h/500°C. The alloy 1740 has the lowest $\sigma_{0.2}$ independent of all the studied alloys and conditions.

The alloys that show highest σ_{max} and $\sigma_{0.2}$ also exhibit lowest elongation at fracture (Fig. 3.82).

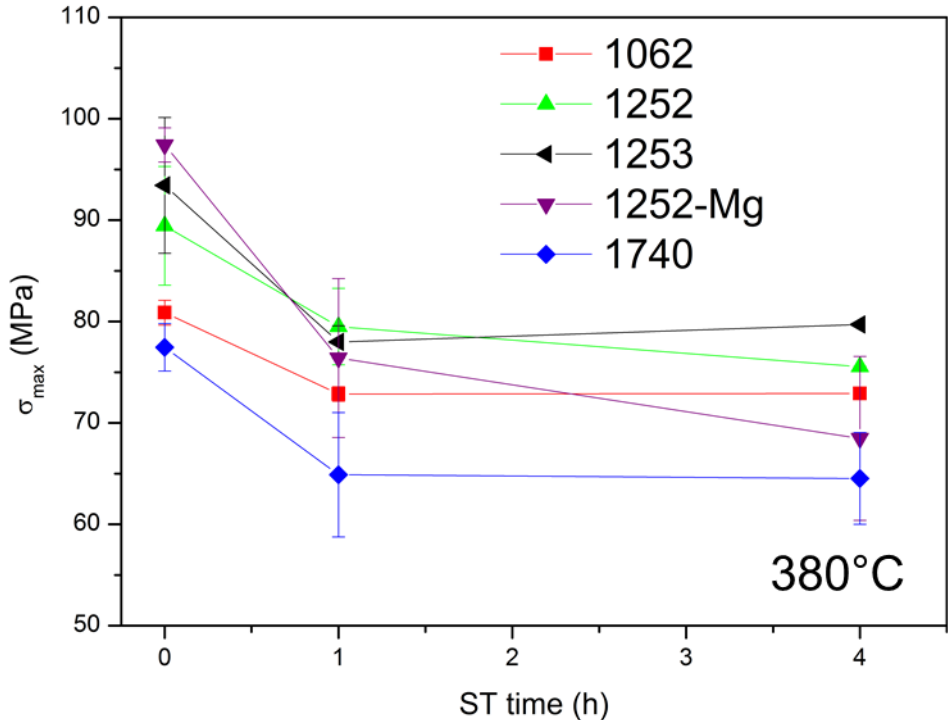


Fig. 3.80: UTS at 380°C after solution treatment at 500°C and overaging at 300°C for 100h.

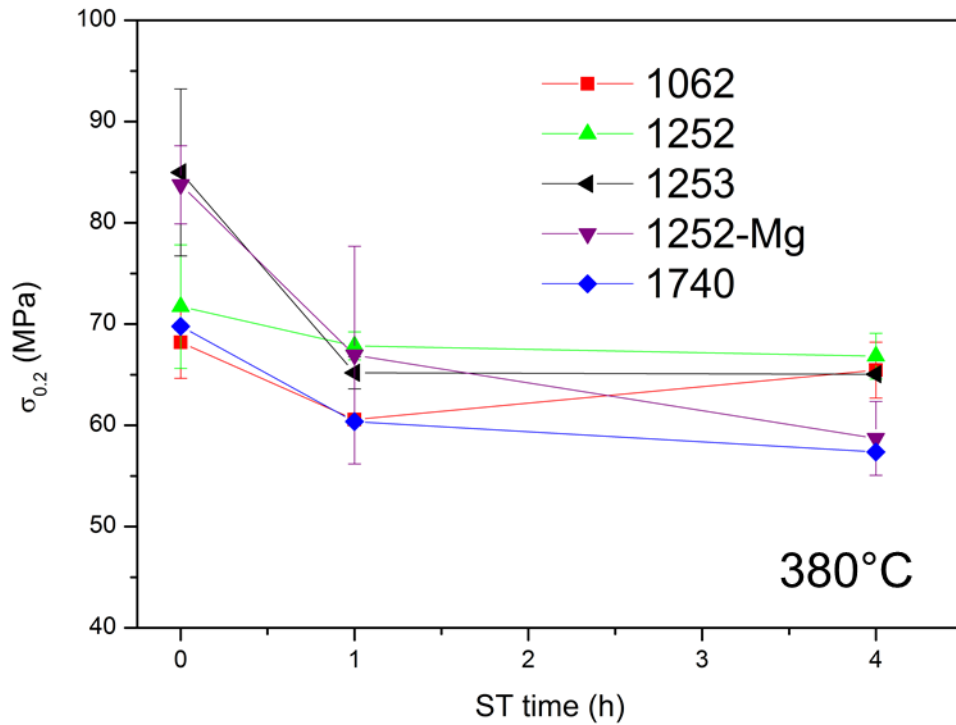


Fig. 3.81: Yield strength at 380°C after solution treatment at 500°C and overaging at 300°C for 100h.

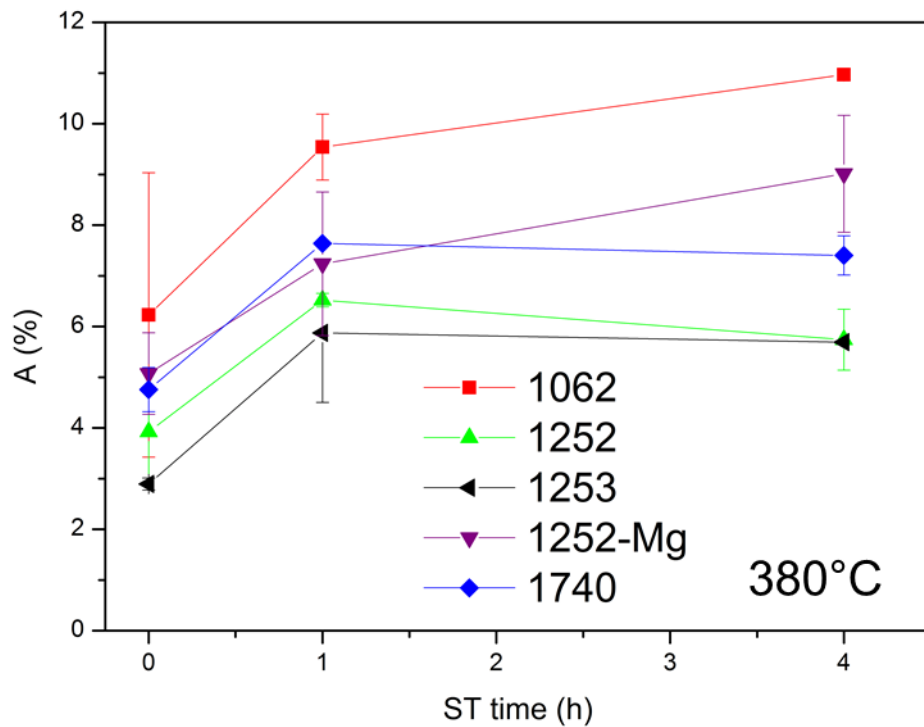


Fig. 3.82: Elongation at fracture measured at 380°C after solution treatment at 500°C and overaging at 300°C for 100h.

3.9.3. Thermo-mechanical fatigue

3.9.3.1. Coefficient of thermal expansion and dynamic mechanical analysis

The CTE of the piston alloys is shown as a function of temperature in Fig. 3.83. Due to the similar evolution of the CTE for the different alloys an average was calculated. This average was fitted with a linear function between 50°C and 300°C (see Fig. 3.83). The linear fit was used to calculate the fraction of strain contributed by the thermal expansion during thermal cycling of the specimen, see Eq. 2.6 in section 2.3.10.5.

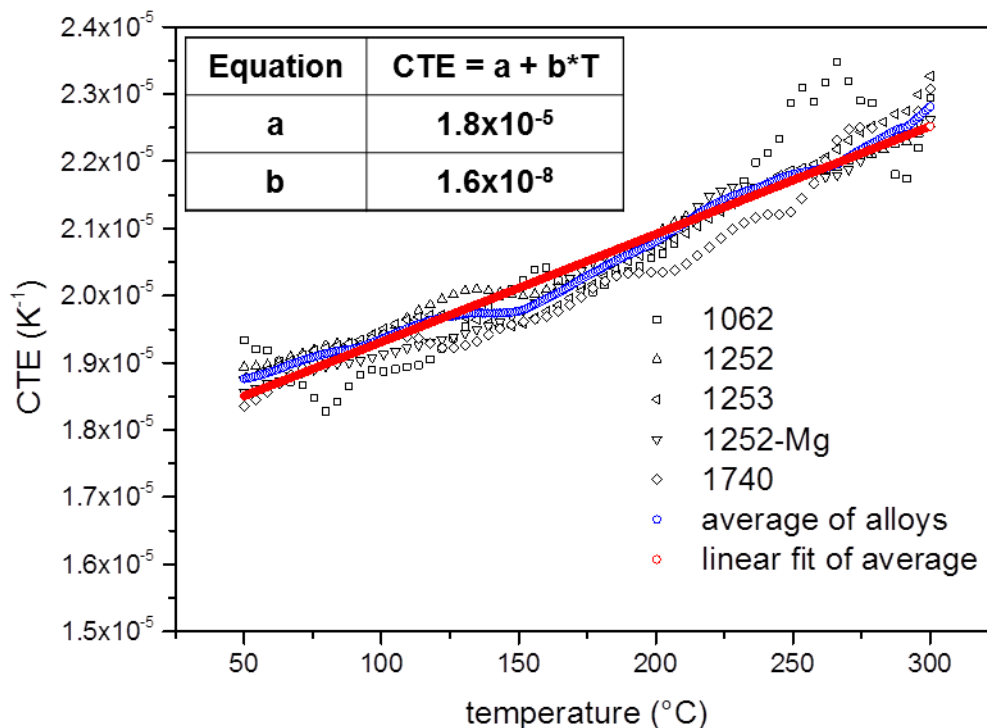


Fig. 3.83: Coefficient of thermal expansion as a function of temperature approximated as linear fit with resulting equation.

Eq. 3.1: Linear fit to calculate the coefficient of thermal as a function of temperature

$$CTE(T) [K^{-1}] = 1.8x10^{-5} + 1.6x10^{-8} \cdot T$$

The evolution of the Young's modulus of the alloys 1740, 1253 and 1252-Mg is presented in Fig. 3.84 as a function of temperature. The corresponding evolution of the loss module is shown in Fig. 3.85. Due to similarity of the Young's modulus of all alloys within the experimental precision of ± 4 GPa an average was calculated between 50 to 300°C.

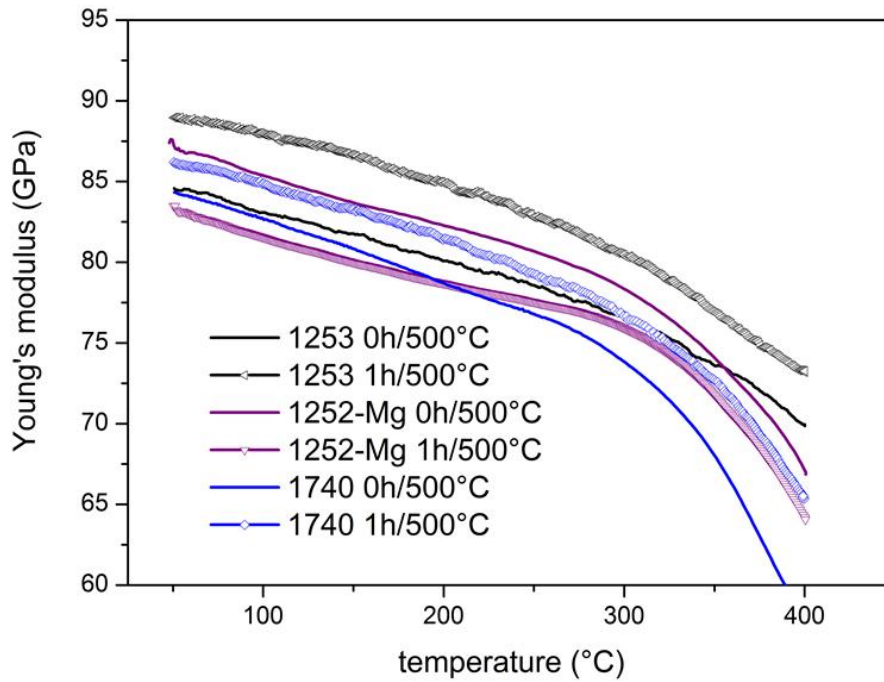


Fig. 3.84: Young's modulus of the 1740, 1253 and 1252-Mg alloys as a function of temperature obtained by dynamic mechanical analysis.

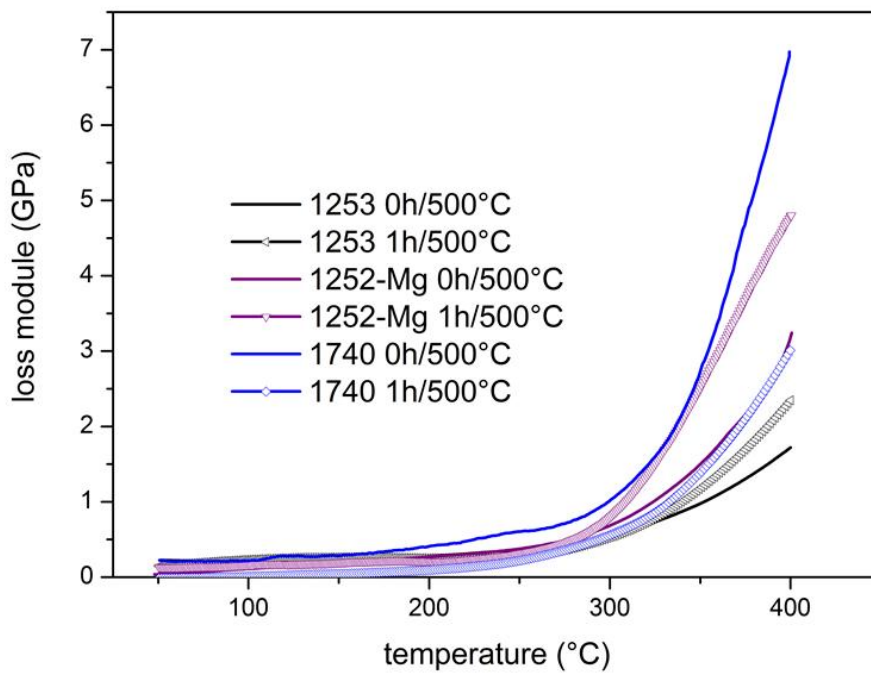


Fig. 3.85: Loss module of the 1740, 1253 and 1252-Mg alloys as a function of temperature.

The linear equation to calculate the Young's modulus as a function of temperature is given in Eq. 3.2.

Eq. 3.2: Linear fit to calculate the Young's modulus at a given temperature

$$E(T)[GPa] = 87 - 3.2 \times 10^{-2} \cdot T$$

This linear fit was used to calculate the influence of Young's modulus during thermo-mechanical fatigue using Eq. 2.7 in section 2.3.10.5. This fit was extrapolated to determine the Young's modulus between 300°C and 380°C.

3.9.3.2. Thermo-mechanic fatigue

3.9.3.2.1. $\Delta T=50-300^\circ\text{C}$, $\sigma=50\text{MPa}$

Plastic strain, ε , (a) and strain rate, $\dot{\varepsilon}$, (b) as a function of time, t , as well as $\dot{\varepsilon}$ as a function of ε (c) obtained during the TMF tests between 50 and 300°C at $\sigma=50\text{MPa}$ are shown in Fig. 3.86 to Fig. 3.90 for the 1062, 1252, 1253, 1252-Mg and 1740 alloys. All alloys show a significant decrease in thermo-mechanical fatigue resistance in terms of cycles to failure and minimum strain rate after 1h of solution treatment at 500°C.

Fig. 3.91 shows a comparison of the relationship between solution treatment time and minimum strain rate ($\dot{\varepsilon}_{min}$) for all investigated alloys. The 1252, 1253 and 1252-Mg alloys in 0h/500°C condition show the lowest $\dot{\varepsilon}_{min}$, i.e. $\sim 2.0 \times 10^{-7} \text{ s}^{-1}$, $\sim 2.5 \times 10^{-7} \text{ s}^{-1}$ and $\sim 2.8 \times 10^{-7} \text{ s}^{-1}$, respectively. The 1062 and 1740 alloys in the same condition exhibit significantly higher $\dot{\varepsilon}_{min}$, i.e. $\sim 8.3 \times 10^{-7} \text{ s}^{-1}$ and $\sim 5.2 \times 10^{-6} \text{ s}^{-1}$.

The cycles to failure are shown in Fig. 3.92 for all alloys and solution treatment conditions. The alloys that exhibit the lowest $\dot{\varepsilon}_{min}$ at 0h/500°C also show the highest number of cycles to failure. This parameter is reduced after solution treatment. The minimum strain rates of the strongest alloys, namely 1252, 1253 and 1252-Mg, are reduced to $\sim 1.2 \times 10^{-6} \text{ s}^{-1}$, $\sim 2.0 \times 10^{-6} \text{ s}^{-1}$ and $\sim 3.4 \times 10^{-6} \text{ s}^{-1}$, respectively. The cycles to failure are decreased to $\sim 1/3$ for 1252 and $\sim 1/4$ for 1252-Mg after 1h/500°C. Further solution treatment up to 4h/500°C does not show a strong impact on $\dot{\varepsilon}_{min}$ and cycles to failure.

The elongation at fracture, A , is shown in Fig. 3.93 for all alloys and solution treatment conditions. Increase of A with solution treatment time is perceptible for all alloys except 1062 and 1740, for which nearly constant elongation at fracture in all solution treatment conditions can be observed.

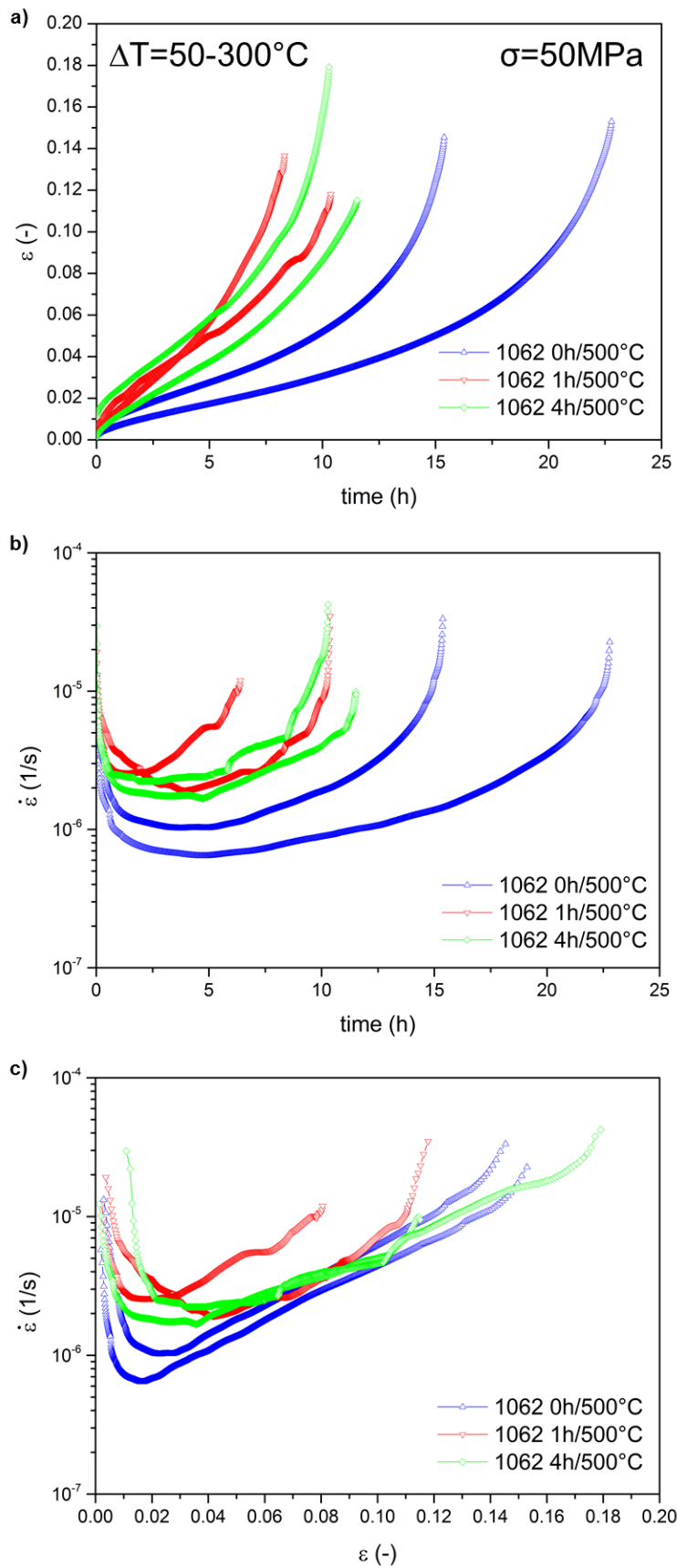


Fig. 3.86: Thermo-mechanical fatigue behavior between 50 and 300°C at an applied stress of 50MPa for the 1062 alloy a) ε vs. t b) $\dot{\varepsilon}$ vs. t c) $\dot{\varepsilon}$ vs. ε .

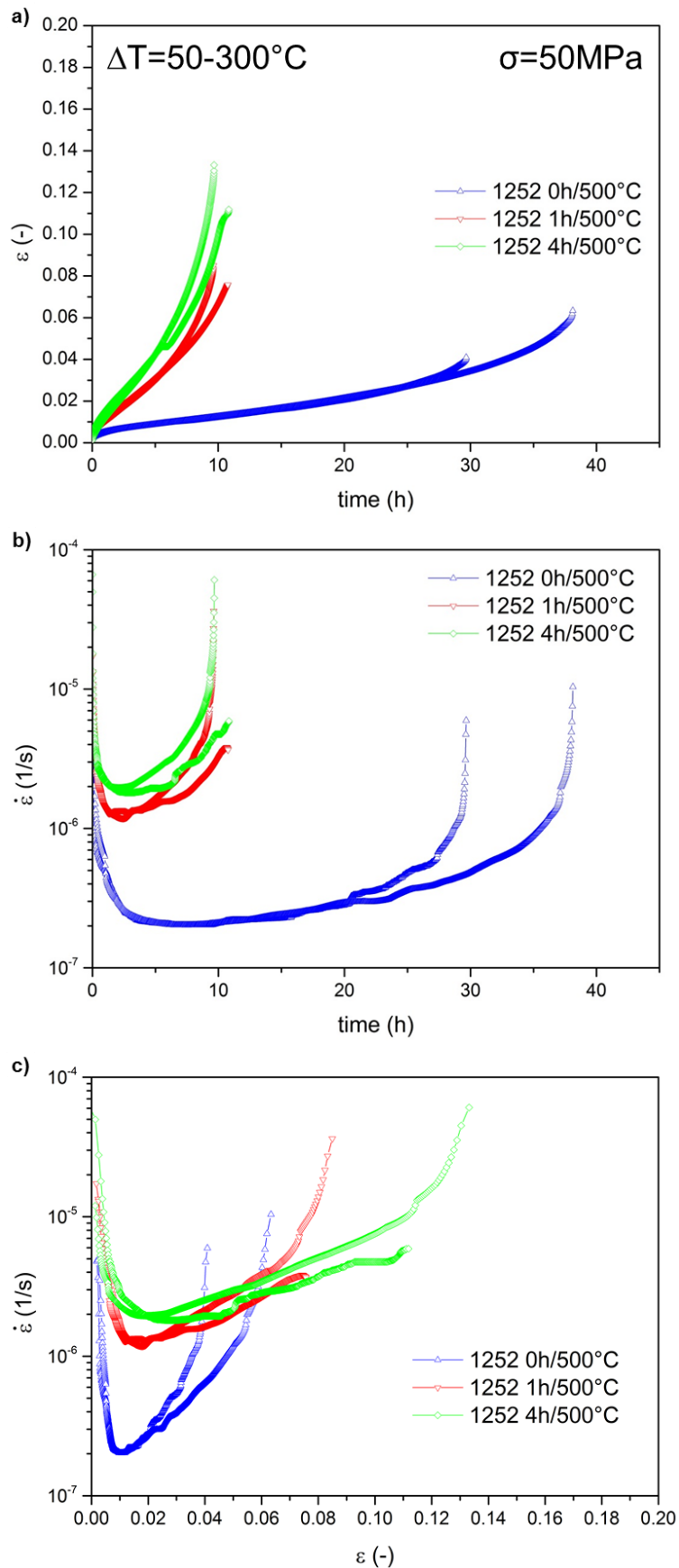


Fig. 3.87: Thermo-mechanical fatigue behavior between 50 and 300°C at an applied stress of 50MPa for the 1252 alloy a) ε vs. t b) $\dot{\varepsilon}$ vs. t c) $\dot{\varepsilon}$ vs. ε .

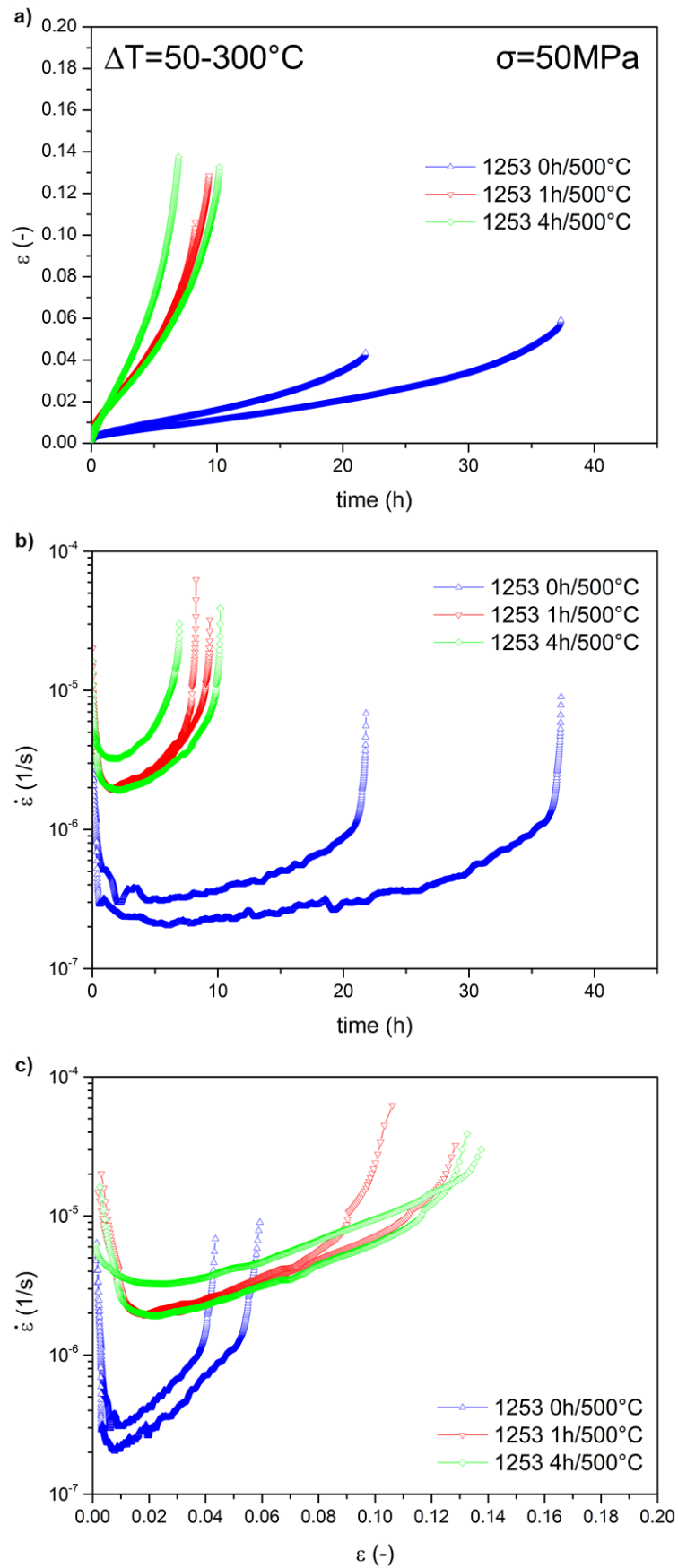


Fig. 3.88: Thermo-mechanical fatigue behavior between 50 and 300°C at an applied stress of 50MPa for the 1253 alloy a) ε vs. t b) $\dot{\varepsilon}$ vs. t c) $\dot{\varepsilon}$ vs. ε .

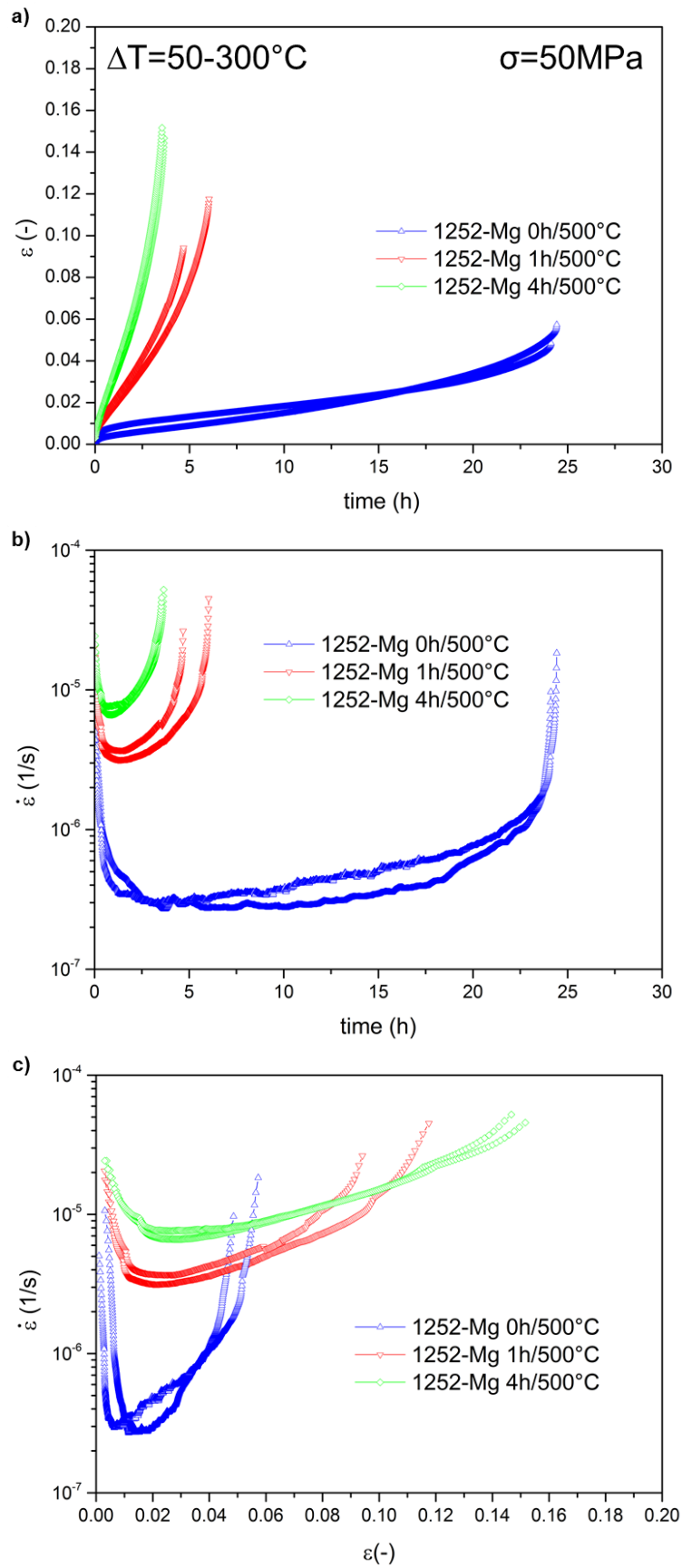


Fig. 3.89: Thermo-mechanical fatigue behavior between 50 and 300°C at an applied stress of 50MPa for the 1252-Mg alloy a) ε vs. t b) $\dot{\varepsilon}$ vs. t c) $\dot{\varepsilon}$ vs. ε .

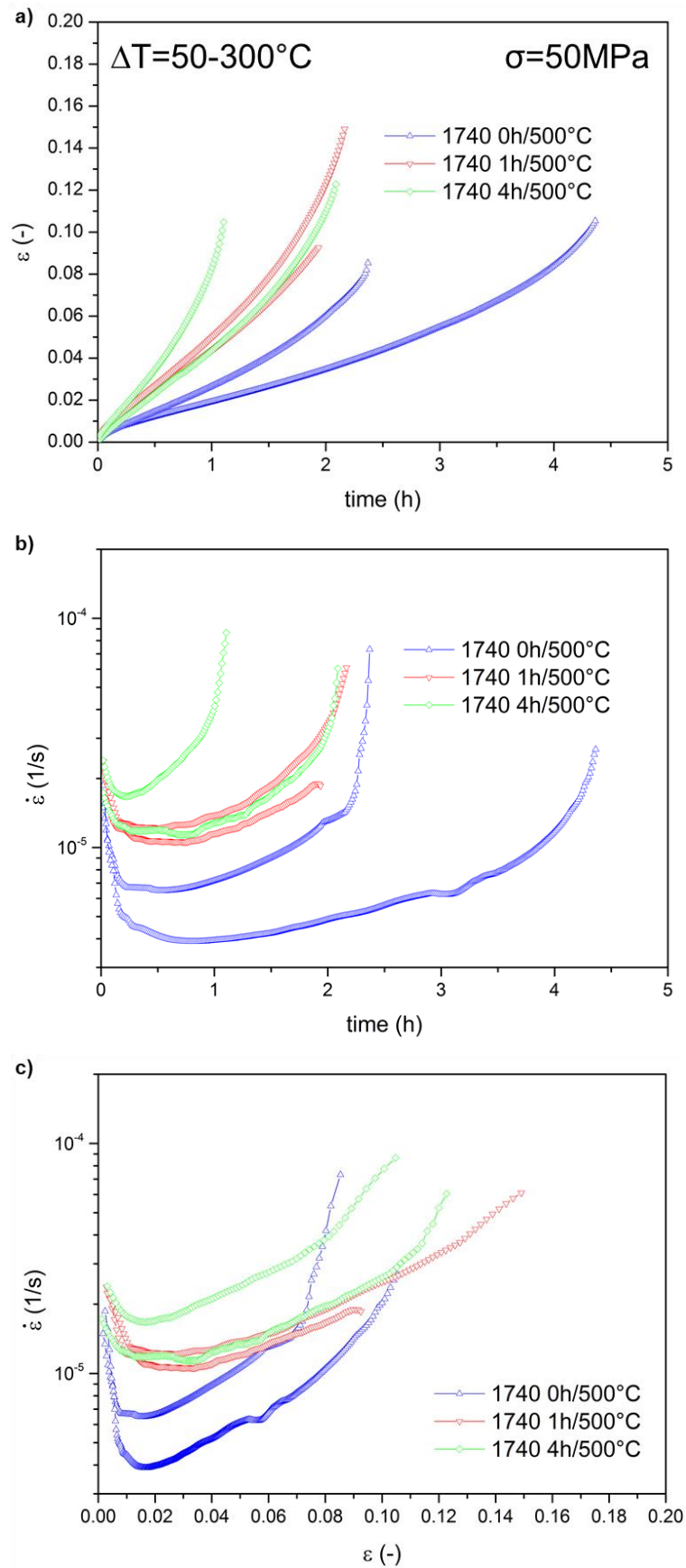


Fig. 3.90: Thermo-mechanical fatigue behavior between 50 and 300°C at an applied stress of 50MPa for the 1740 alloy a) ε vs. t b) $\dot{\varepsilon}$ vs. t c) $\dot{\varepsilon}$ vs. ε .

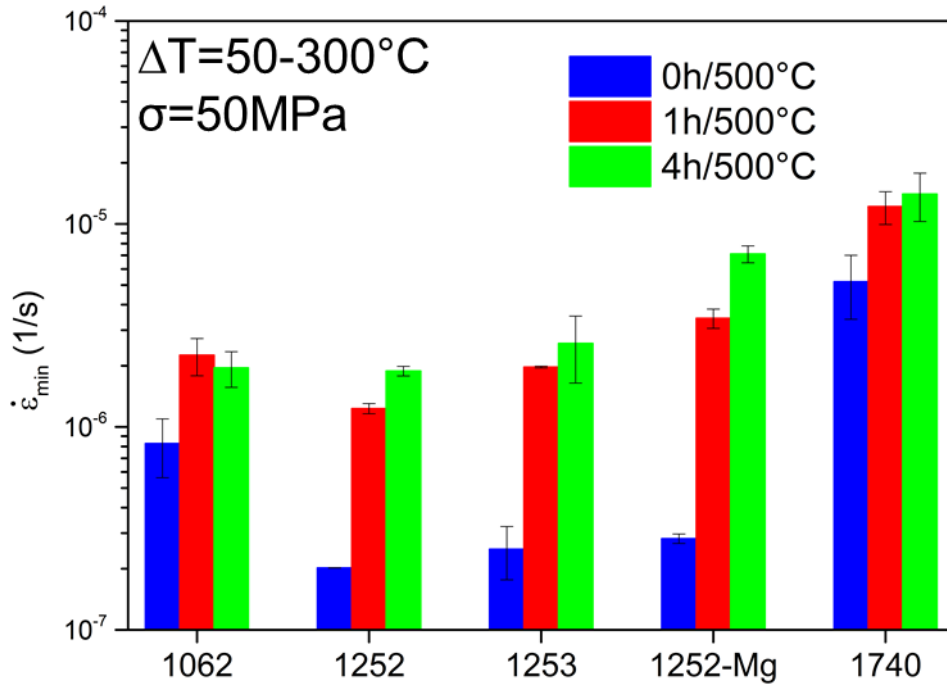


Fig. 3.91: Minimum strain rates ($\dot{\epsilon}_{min}$) for the TMF tests with $\Delta T=50-300^{\circ}\text{C}$, $\sigma=50\text{MPa}$.

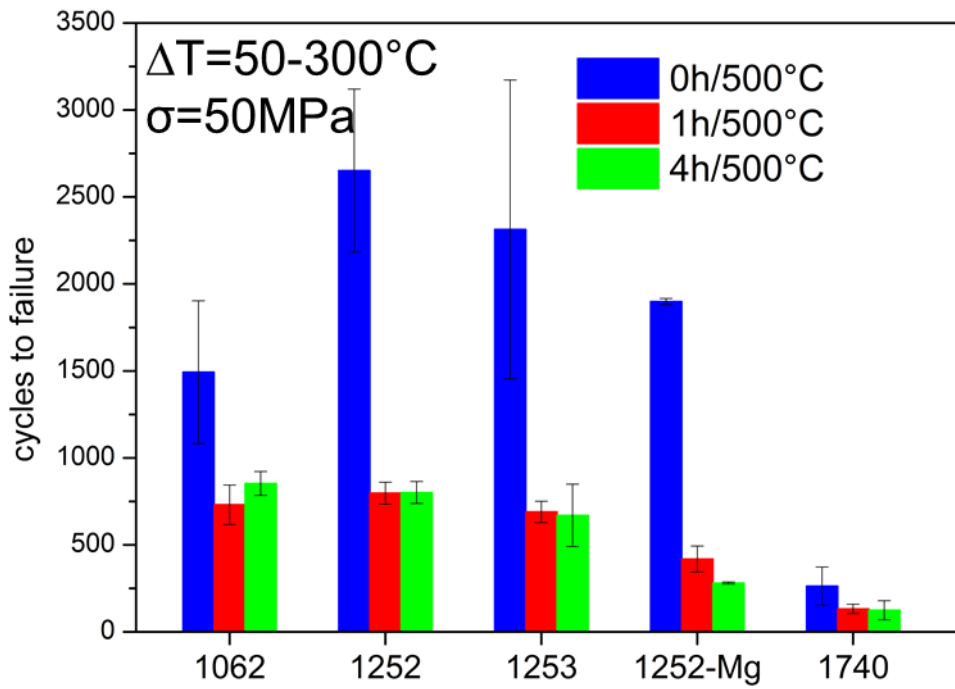


Fig. 3.92: Cycles to failure for the TMF tests with $\Delta T=50-300^{\circ}\text{C}$, $\sigma=50\text{MPa}$.

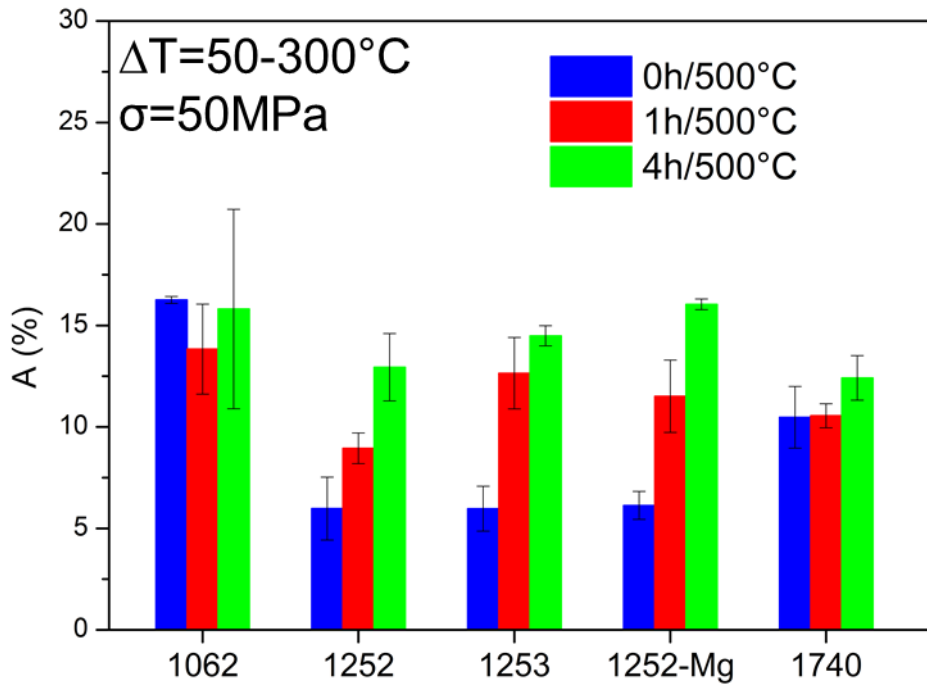


Fig. 3.93: Elongation at fracture for the TMF tests with, $\Delta T=50-300^{\circ}\text{C}$, $\sigma=50\text{MPa}$.

3.9.3.2.2. $\Delta T=50-380^{\circ}\text{C}$, $\sigma=35\text{MPa}$

Analogue to the thermo-mechanical fatigue tests between $50-300^{\circ}\text{C}$ Fig. 3.94-Fig. 3.98 show ε (a) and $\dot{\varepsilon}$ (b) as a function of t as well as $\dot{\varepsilon}$ as a function of ε (c) for the 1062, 1252, 1253, 1252-Mg and 1740 alloys during thermal cycling between $50-380^{\circ}\text{C}$ and $\sigma=35\text{MPa}$. Although the behavior in terms of effect of solution treatment time is comparable to the tests with $\Delta T=50-300^{\circ}\text{C}$ the loss of thermo-mechanical fatigue resistance in terms of $\dot{\varepsilon}_{min}$ and cycles to failure is more significant.

The minimum strain rate of all alloys is presented in Fig. 3.99. The relative increase of $\dot{\varepsilon}_{min}$ for the alloys 1252, 1253 and 1252-Mg after 1h/500°C is not as pronounced as for $\Delta T=50-300^{\circ}$. Analogue to $\Delta T=50-300^{\circ}\text{C}$ thermo-mechanical fatigue with $\Delta T=50-380^{\circ}\text{C}$ does not show a significant impact on $\dot{\varepsilon}_{min}$ upon further solution treatment up to 4h/500°C.

The largest numbers of cycles to failure (Fig. 3.100) are achieved by the 1252 and, 1253 alloys. 1740 shows inferior performance and also no influence of solution treatment on cycles to failure. The alloys 1252, 1253 and 1252-Mg reveal in Fig. 3.101 an influence of solution treatment on the elongation at fracture. On the other hand, the 1062 and 1740 alloys exhibit little influence of solution treatment on the elongation at fracture. These alloys are already more ductile than the others at 0h/500°C.

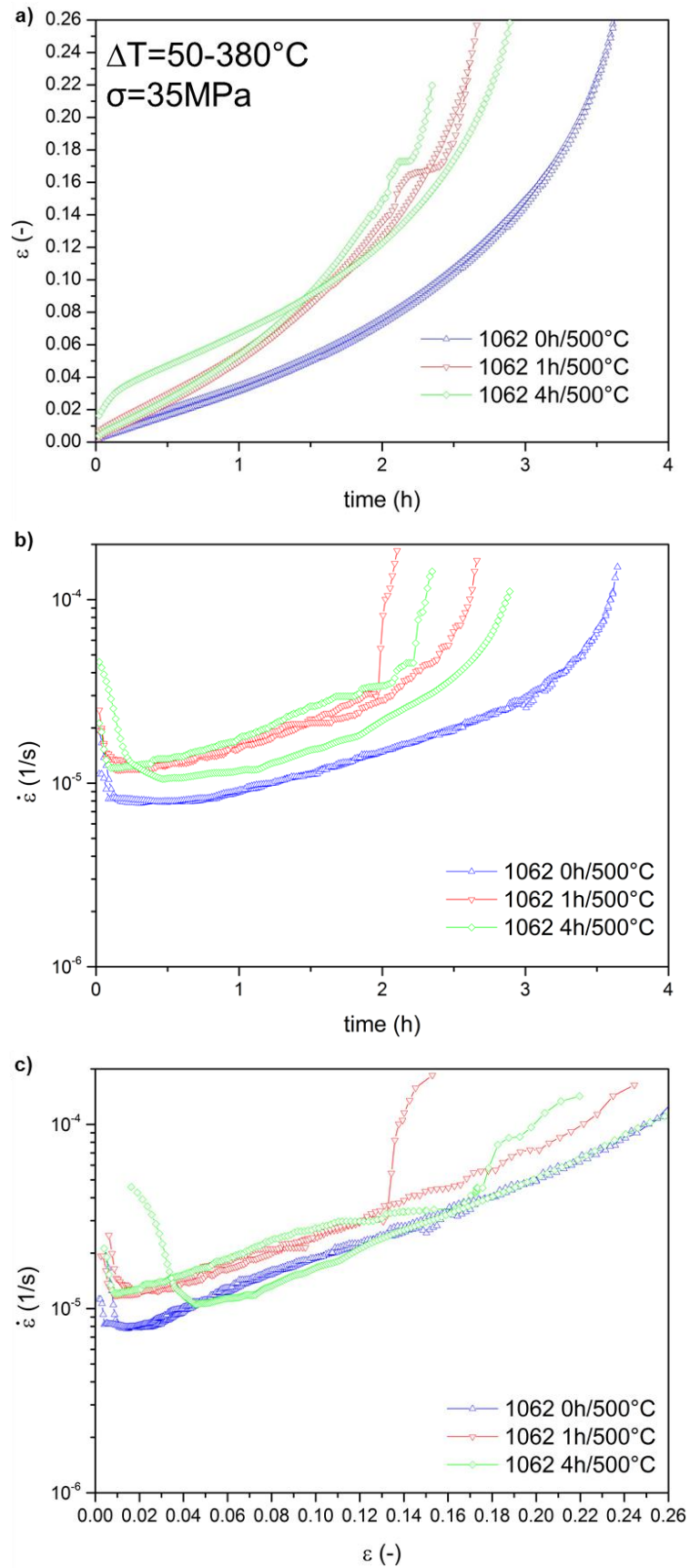


Fig. 3.94: Thermo-mechanical fatigue behavior between 50 and 380°C at an applied stress of 35MPa for the 1062 alloy a) ε vs. t b) $\dot{\varepsilon}$ vs. t c) $\dot{\varepsilon}$ vs. ε .

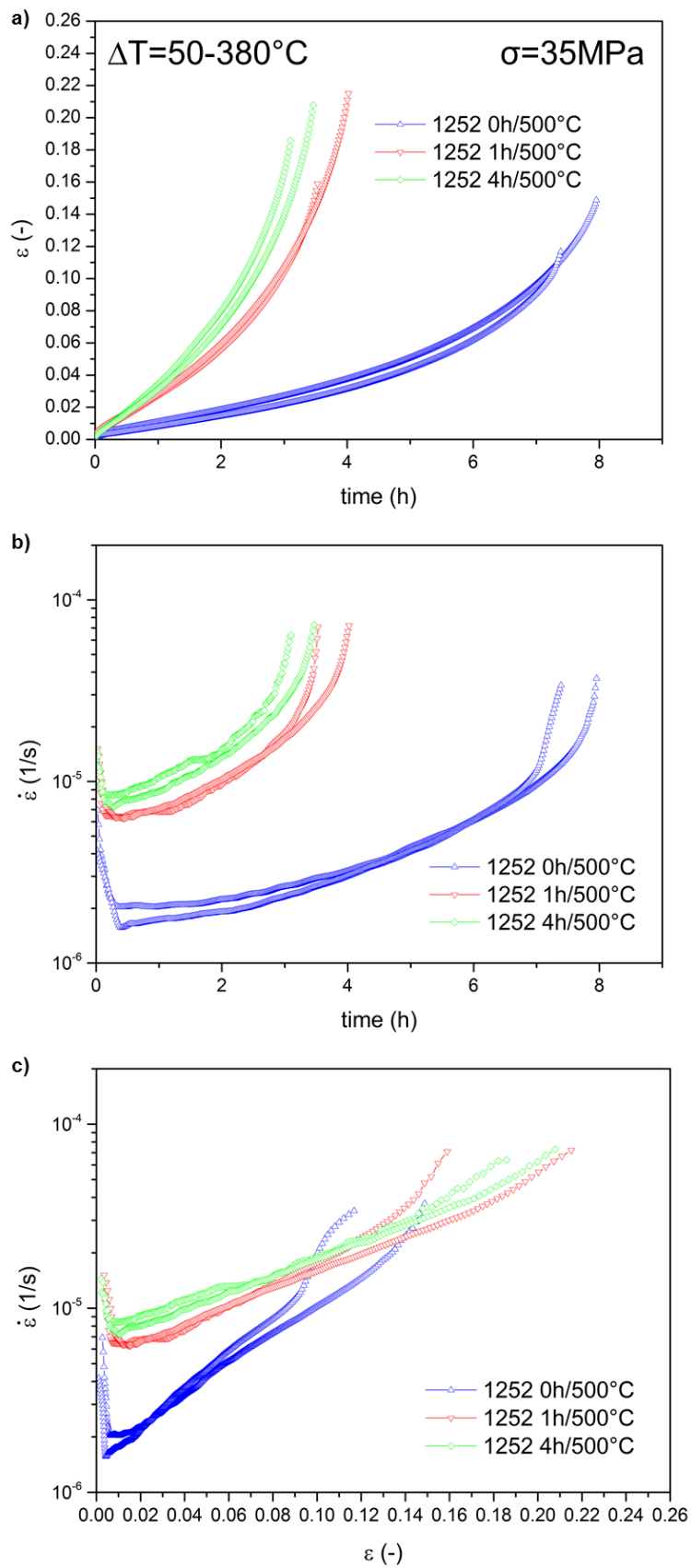


Fig. 3.95: Thermo-mechanical fatigue behavior between 50 and 380°C at an applied stress of 35MPa for the 1252 alloy a) ε vs. t b) $\dot{\varepsilon}$ vs. t c) $\dot{\varepsilon}$ vs. ε .

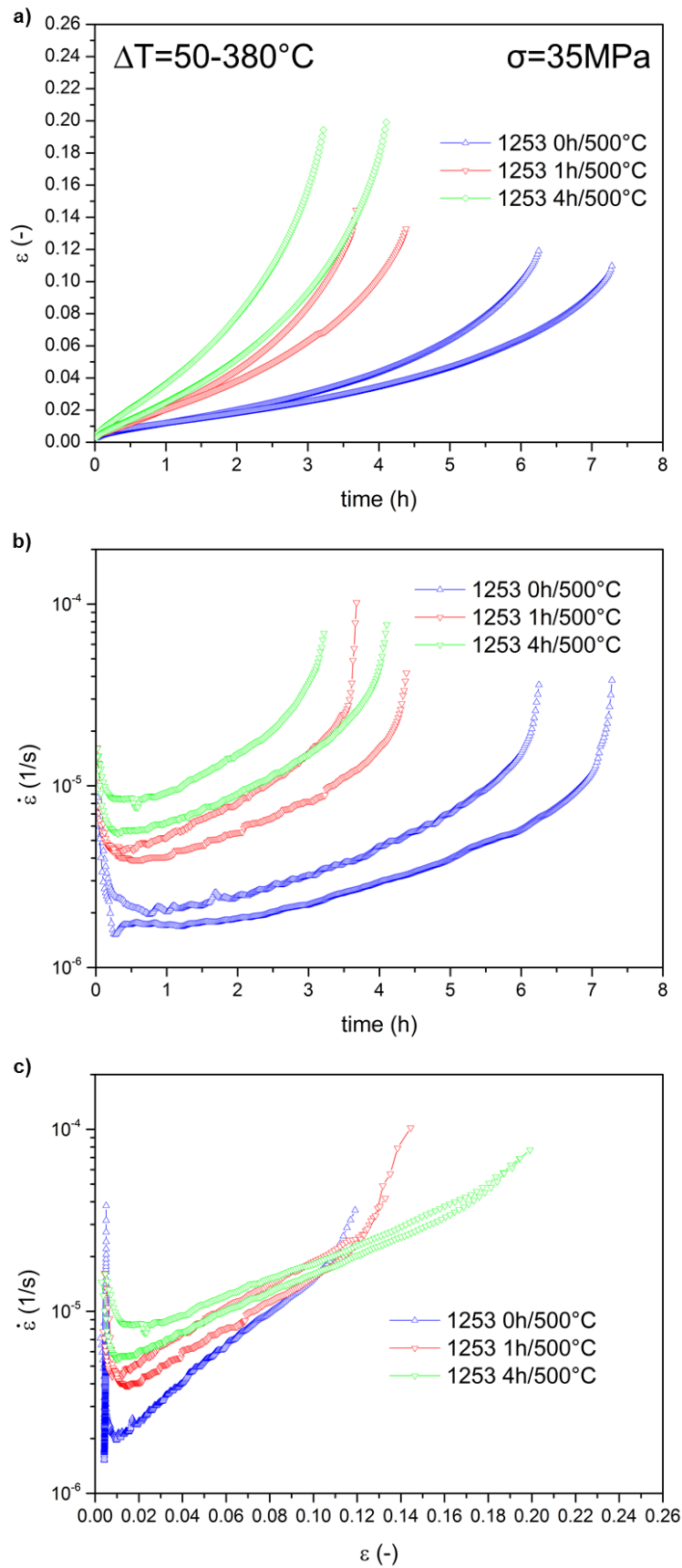


Fig. 3.96: Thermo-mechanical fatigue behavior between 50 and 380°C at an applied stress of 35MPa for the 1253 alloy a) ε vs. t b) $\dot{\varepsilon}$ vs. t c) $\dot{\varepsilon}$ vs. ε .

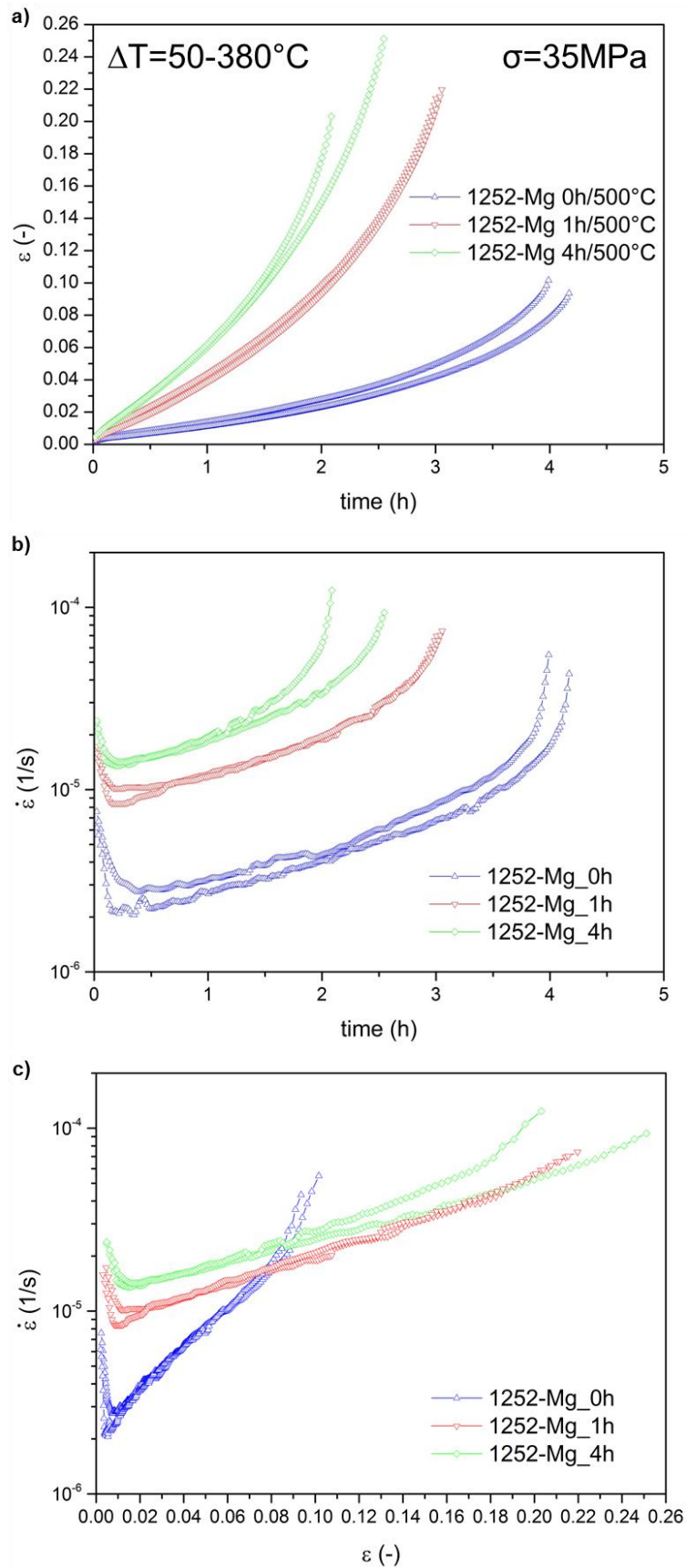


Fig. 3.97: Thermo-mechanical fatigue behavior between 50 and 380°C at an applied stress of 35MPa for the 1252-Mg alloy a) ϵ vs. t b) $\dot{\epsilon}$ vs. t c) $\dot{\epsilon}$ vs. ϵ .

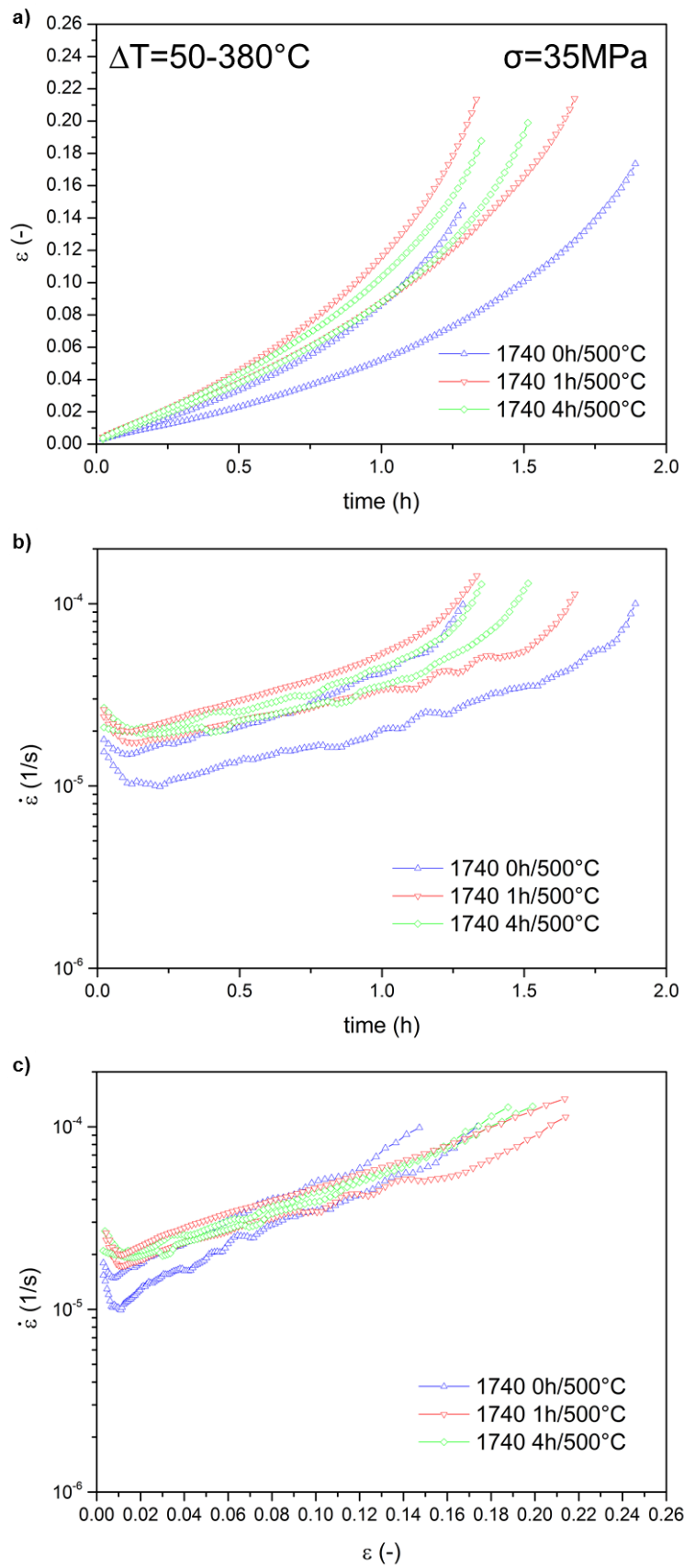


Fig. 3.98: Thermo-mechanical fatigue behavior between 50 and 380°C at an applied stress of 35MPa for the 1740 alloy a) ε vs. t b) $\dot{\varepsilon}$ vs. t c) $\dot{\varepsilon}$ vs. ε .

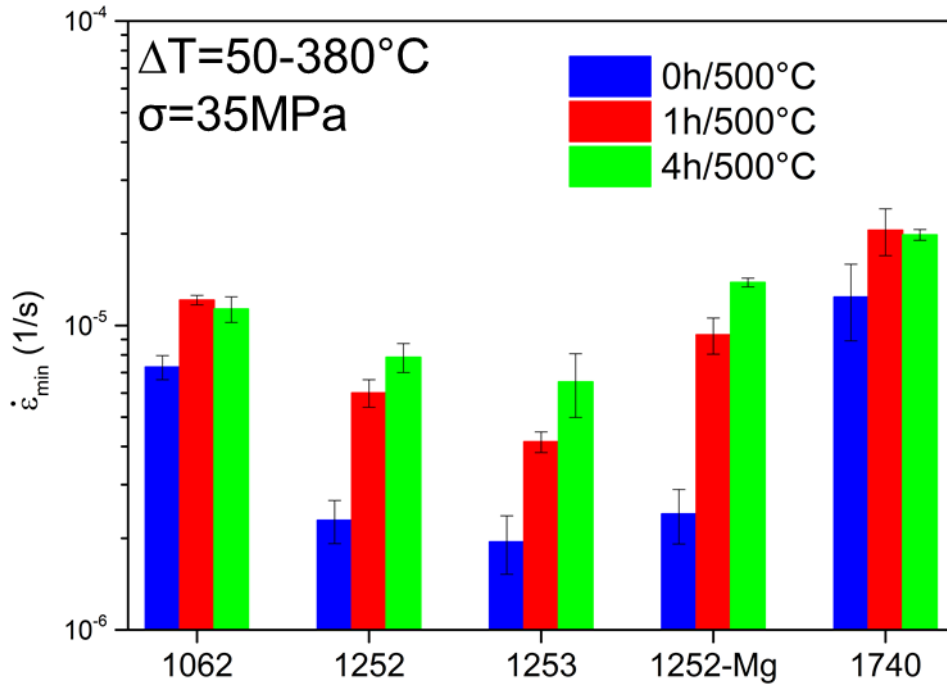


Fig. 3.99: Minimum strain rates ($\dot{\epsilon}_{min}$) for the TMF tests with $\Delta T=50-380^{\circ}\text{C}$, $\sigma=35\text{MPa}$.

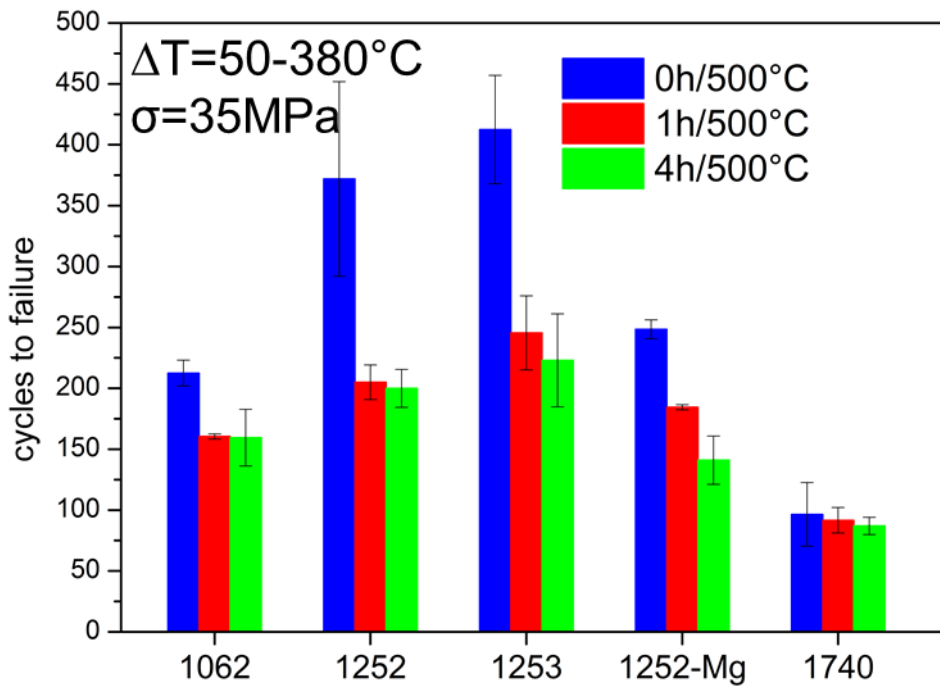


Fig. 3.100: Cycles to failure for the TMF tests with $\Delta T=50-380^{\circ}\text{C}$, $\sigma=35\text{MPa}$.

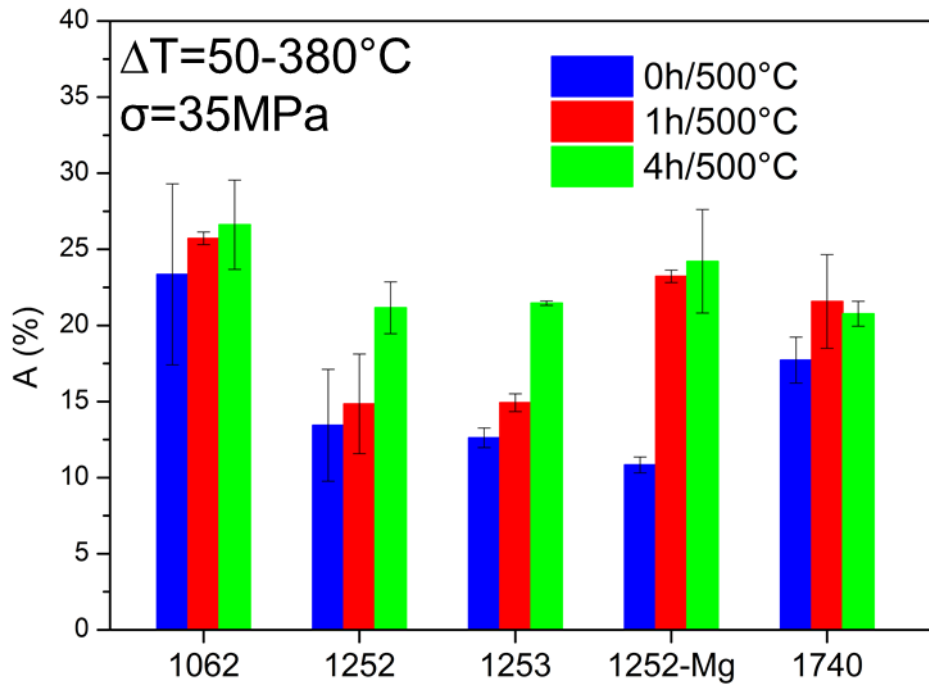


Fig. 3.101: Elongation at fracture for the TMF tests with $\Delta T = 50-380^{\circ}\text{C}$, $\sigma = 35\text{MPa}$.

4. Discussion of results

4.1. Evolution of the microstructure during solution treatment

4.1.1. Qualitative changes of the rigid networks

Microstructural changes during solution treatment of Al-Si alloys were investigated extensively throughout the years. Especially, the evolution of eutectic silicon in Al-Si alloys was studied thoroughly. In most cases 2D investigations were used to describe microstructural changes. These qualitative studies showed that the spheroidization of silicon may occur within minutes [21, 47]. The light optical micrographs in Fig. 3.4-Fig. 3.8 showed some spheroidization of eutectic and primary silicon in all alloys after 1h of solution treatment at 500°C. The shape of the aluminides in the 1062, 1252, 1253 and 1252-Mg alloys are more stable than in the 1740 alloy after 1h of solution treatment.

Deep etching revealed that the network formed by Si and aluminides remains highly interconnected even after 4h of solution treatment (Fig. 3.9-Fig. 3.11). The morphology of the eutectic silicon is flake-like and the primary silicon shows only small particle sizes with diameter ~25µm. These features are controlled by the addition of P [16]. Sr or other modifying elements are not added to the alloys because fine fiber-like silicon structures tend to disconnect and spheroidize faster [47]. However, spheroidization of silicon after 1h and 4h of solution treatment was perceptible in the deep etched SE or BSE micrographs shown in Fig. 3.9-Fig. 3.11 for the 1062, 1252 and 1740 alloys, respectively.

The identification of intermetallic phases in the alloys, obtained by EDX mapping and correlation with the literature showed that despite the variation of alloying elements (Ni/Cu ratio and Mg content) qualitatively the same phases were present. The volume fraction of certain aluminides changed correspondingly with the chemical composition. The 1253 alloy showed, due to the higher Ni content, larger volume fractions of Ni-rich phases than the 1252 and 1252-Mg alloys. The Q-phase, $\text{Al}_4\text{Cu}_2\text{Mg}_8\text{Si}_7$, which is probably one of the phases which show partial dissolution in the 1252 alloy (Fig. 3.26), cannot form in 1252-Mg. Asghar et al. [34] investigated two near eutectic Al-Si alloys with differing volume fraction of aluminides and found that these interpenetrating networks of aluminides are responsible for retaining interconnectivity of the silicon network after solution treatment.

4.1.2. Changes in the network of aluminides

The changes in the network of aluminides occurring during solution treatment are discussed in terms of the evolution of the volume fraction, interconnectivity and specific Euler number.

The results are summarized in Tab. 4.1. The volume fraction of aluminides in the 1062, 1252 and 1252-Mg alloys remains constant at $\sim 9.5 \pm 1 \text{ vol\%}$, analog to the 1253 alloy at $\sim 12 \pm 1 \text{ vol\%}$, after solution treatment. Asghar et al. [34] investigated an AlSi10Cu5Ni1 and an AlSi10Cu5Ni2 with a volume fraction of aluminides $\sim 8.5 \pm 1 \text{ vol\%}$ and $\sim 13 \pm 1 \text{ vol\%}$, respectively. Also here the volume fraction of aluminides remained constant with solution treatment at 500°C . In the case of the 1740 alloy the volume fraction is not stable and decreases from $5.7 \pm 0.8 \text{ vol\%}$ to $4 \pm 0.05 \text{ vol\%}$. Therefore, the stability of the volume fraction of aluminides can be related to the concentration of Ni in the alloy, analog to the results shown by [34,58].


Besides the volume fraction there are significant changes in the interconnectivity of aluminides in the 1740 alloy. Fig. 3.22 and Tab. 4.1 show that the reduction of this parameter is more significant in the first hour of solution treatment and remains practically constant afterwards. The reduction of interconnectivity of aluminides in the AlSi10Cu5Ni1 alloy investigated by Asghar et al. was also in this order of magnitude [34]. This loss of interconnectivity in the 1740 alloy can be related to the dissolution of an intermetallic phase with a coral-like shape depicted in Fig. 3.51. This corresponds to the Al_2Cu phase identified by EDX analysis (Fig. 3.17).


The network of aluminides in the 1062, 1252, 1253 and 1252-Mg alloys do not show any interconnectivity changes and remain highly interconnected after 4h of solution treatment at 500°C , i.e. 95-98%. Nevertheless, local connectivity changes occur in these alloys during solution treatment (Fig. 3.23-Fig. 3.26) without significant influence on the size of the largest particle, i.e. interconnectivity.

The evolution of the specific Euler number, χ_v , of the 1252 and 1252-Mg alloy (Fig. 3.27) show an increase of $\sim 10\%$, i.e. from $\sim 7 \times 10^{-3} \mu\text{m}^{-3}$ after 0h at 500°C to $\sim 6 \times 10^{-3} \mu\text{m}^{-3}$ after 1h at 500°C . This can be related to the loss of connections in the network of aluminides as it was shown in Fig. 3.25.

alloy	Interconnectivity			vol.fraction			χ_v (of largest particle)			curvatures			observed behavior		
	%			%			μm^{-3}								
	0h	1h	4h	0h	1h	4h	0h	1h	4h	0h	1h	4h	0h	1h	4h
1062	97.0±0.6	95.6±0.8	96.8±0.3	9.3±0.6	9.3±0.8	8.3±0.3	-1.2x10 ⁻²	-1.3x10⁻²	-1.4x10⁻²	slight spheroid.			homogenous		
	≈	≈		≈	≈	≈		↓ -9%	↓ -17%	distr.broadening			dissolution		
1252	96.5±0.5	96.3±0.3	95.0±1.3	9.2±0.8	9.0±0.4	9.5±0.7	-7.4x10 ⁻³	-6.3x10⁻³	-6.7x10⁻³	constant			local		
	≈	≈		≈	≈	≈		↑ +15%	↓ -6%	constant			dissolution		
1253	98.5±0.3	98.9±0.1	99.0±0.2	11.8±0.9	12.6±1.0	11.8±1.5	-1.6x10 ^{-3*}	-2.8x10 ^{-3*}	-2.6x10 ^{-3*}	constant			constant		
	≈	≈		≈	≈	≈		≈	≈	shape constant			shape constant		
1252-Mg	95.7±0.5	94.2±0.9	94.2±0.6	10.4±0.7	9.8±0.9	10.0±0.6	-7.0x10 ⁻³	-5.8x10⁻³	-6.7x10⁻³	distr.broadening			distr.broadening		
	≈	≈		≈	≈	≈		↑ +17%	↓ -15%						
1740	88.6±3	69.6±4.0	68.6±0.1	5.7±0.8	4.8±0.6	4.0±0.04	-3.2x10 ⁻²	-2.8x10⁻²	-2.1x10⁻²	distr.broadening			local+global		
		↓ -21%	≈ -2%		↓ -16%	↓ -17%		↑ +13%	↑ +25%	distr.broadening			dissolution		

* Different samples

 Values showing an increase

 Values showing a decrease

 Values which remain constant

Tab. 4.1: Evolution during solution treatment at 500°C of different parameters of the aluminides network in the investigated alloys

The 1740 alloy exhibits a ~10% increase of χ_v of the aluminides after 1h of solution treatment, which indicates a decrease of connections within the network. Furthermore, the 1740 alloy has a specific Euler number of -0.032, which is significantly lower than for the piston alloys. This can be explained by the fibrous coral-like morphology of the aluminides (Al_2Cu) present in the 1740 alloy, which forms additional connections leading to more negative specific Euler numbers.

4.1.3. Changes in the network of eutectic and primary silicon

The evolution of the silicon network in Al-Si alloys during solution treatment was described by Zhu et al. as a two-step process [20]. First, the separation of thin parts of eutectic branches reduces the interconnectivity of the silicon network. These separations occurred in Sr-modified Al-Si alloys after shorter exposure time than in unmodified Al-Si alloys [21,47]. The investigated alloys are all unmodified but have low amounts of P to induce small sizes of the primary silicon particles. The disintegration of the eutectic Si network during solution treatment of unmodified Al-Si alloys was investigated three-dimensionally by Lasagni et al. using FIB-tomography [9]. The connecting nodes between Si branches in unmodified Al-Si alloys showed sizes of $\sim 1\text{-}4\mu\text{m}^2$, which should be at least partially resolvable in the regions of interest investigated in this work by synchrotron tomography (voxel size of $(0.28)^3\mu\text{m}^3$). To resolve the Si and Al sufficient contrast between these phases is necessary, which in the case of the investigated alloys was locally not always fulfilled. Therefore, it can be expected that the separations of Si branches are even more numerous than observed. However, it was found that the global connectivity of the silicon network is constant during solution treatment although some connections tend to separate (Fig. 3.62). The Euler number and the specific Euler number as a function of solution treatment time was calculated for the Si network in the 1062, 1252 and 1740 alloys. This evolution shows an increase of the Euler numbers after 1h of solution treatment, which indicates a loss of connections within the silicon network (Tab. 4.2). After further solution treatment the Euler number remains constant indicating a stable Si network after 1h at 500°C.

alloy	Interconnectivity			vol.fraction			X_v			Curvatures		
	%			%			μm^{-3}			0h	1h	4h
1062	0h	1h	4h	0h	1h	4h	0h	1h	4h	0h	1h	4h
	34.2	34.2	33.1	11.6	11.9	12.4	-3.0×10^{-3}	-2.0×10^{-3}	-2.3×10^{-3}	slight spheroid.		
	≈	≈		≈	≈		↑	+33%	≈			
1252	0h	1h	4h	0h	1h	4h	0h	1h	4h	0h	1h	4h
	91.9	91.6	92.2	17.7	19.3	17.9	-4.2×10^{-3}	-2.9×10^{-3}	-3.0×10^{-3}	slight spheroid.		
	≈	≈		≈	≈		↑	+31%	≈			
1740	0h	1h	4h	0h	1h	4h	0h	1h	4h	0h	1h	4h
	88.7	87.9	87.9	20.7	21.4	21.9	-2.7×10^{-4}	-5.3×10^{-5}	-4.5×10^{-5}	slight spheroid.		
	≈	≈		≈	≈		↑	+80%	↑	+15%		

■ Values showing an increase

■ Values showing a decrease

■ Values which remain constant

Tab. 4.2: Evolution during solution treatment at 500°C of different parameters of the Si network in the investigated alloys

4.1.4. Changes in the hybrid network formed by silicon and aluminides

Based on the results of the behavior of the silicon and the aluminides network in Fig. 3.27 and Fig. 3.28 and the large contiguity between them a combined analysis of both networks is presented in Fig. 4.1. The evolution of the hybrid network expressed by the changes of the Euler number, χ , and the specific Euler number, χ_v , is related to the loss of connections within the individual silicon and aluminides network [88,89,90] but also to the loss of connections between them. The interface between aluminides and silicon in the 1062 and 1252 alloy remains fairly constant after solution treatment (Tab. 4.3). The interface between aluminides and silicon in the 1740 alloy however is significantly reduced after 1h and 4h of solution treatment at 500°C to 50% and 25% (Fig. 4.2) with regards to the 0h/500°C condition, respectively. This indicates that contiguity between phases is related to the global stability of aluminides as shown by Asghar et al. [34].

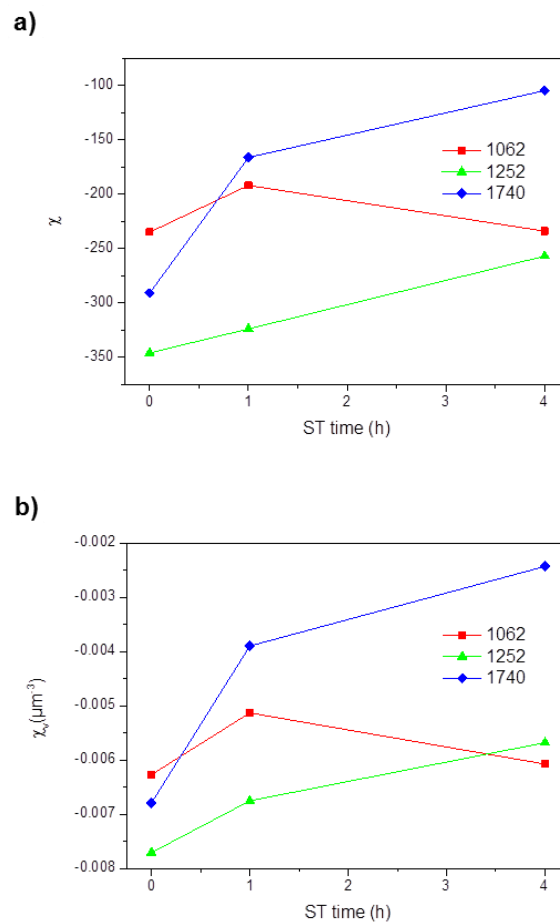


Fig. 4.1: Evolution of Euler numbers of the combined hybrid network of aluminides and silicon as a function of solution treatment time at 500°C: a) χ =Euler number b) χ_v =specific Euler number.

alloy	interconnectivity			vol.fraction			X_v			specific interface (contiguity)		
	%			%			μm^{-3}			μm^{-1}		
	0h	1h	4h	0h	1h	4h	0h	1h	4h	0h	1h	4h
1062	99.5	98.0	99.7	21.4	21.4	22.0	-6.3×10^{-3}	-5.1×10^{-3} ↑ +19%	-6.1×10^{-3} ↑ +3%	5.0×10^{-2}	4.7×10^{-2}	5.0×10^{-2}
	≈	≈		≈	≈					≈	≈	≈
1252	98.6	98.6	98.9	25.4	27.2	25.6	-7.7×10^{-3}	-6.8×10^{-3} ↑ +12%	-5.9×10^{-3} ↑ +24%	2.4×10^{-2}	3.2×10^{-2}	2.8×10^{-2}
	≈	≈		≈	≈					≈	≈	≈
1740	88.7	87.9	87.9	24.4	24.3	24.5	-6.8×10^{-3}	-3.9×10^{-3} ↑ +42%	-2.4×10^{-3} ↑ +65%	5.1×10^{-3}	2.7×10^{-3} ↓ +42%	1.3×10^{-3} ↓ +75%
	≈	≈		≈	≈							

■ Values showing an increase

■ Values showing a decrease

■ Values which remain constant

Tab. 4.3: Evolution during solution treatment at 500°C of different parameters of the hybrid Si-aluminides network in the investigated alloys

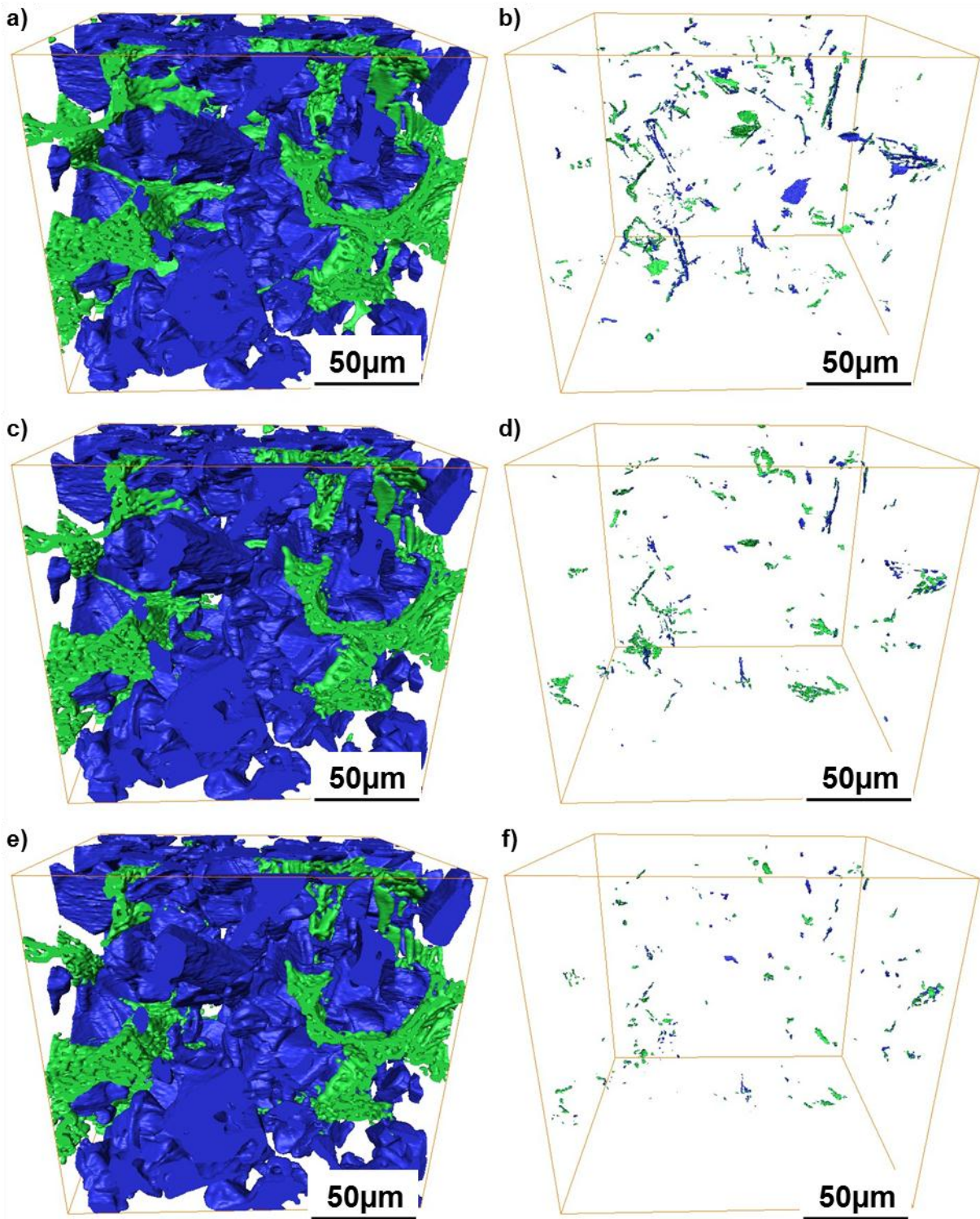


Fig. 4.2: Segmented aluminides and silicon and their interface in the 1740 alloy after 0h/1h/4h at 500°C: a)+b) 0h/500°C c)+d) 1h/500°C e)+f) 4h/500°C. Blue corresponds to the side of the interface facing the Si, while green is the side of the interface facing the aluminides

4.2. Thermo-mechanical properties correlated with internal architecture

The first characterization of mechanical behavior presented was the determination of homogeneity within the piston and the evolution of Brinell hardness during solution treatment at 500°C and overaging at 300°C. The Brinell hardness shows (Fig. 3.68-Fig. 3.72) that the near eutectic alloys (1252, 1253 and 1252-Mg) have a significant decrease in Brinell hardness after 1h of solution treatment and subsequent overaging up to 500h. This decrease alone could have originated from coarsening of various types of precipitates embedded in the α -Al matrix [27,35-39]. Therefore, nano indentations were carried out to investigate the strength of the matrix of the piston alloys individually (Tab. 3.2). The results showed that the matrix precipitates are not responsible for the characteristic loss of Brinell hardness since the hardness of the matrix remains constant after solution treatment (section 3.8). Precipitates like Al_3Zr can be transformed from the cubic L1_2 to the D0_{23} structure by isothermal aging at 425°C [38], particularly in the presence of Si (Si >0.05at%) [39]. In the case of this structural change, leading to less effective precipitation strengthening, the resulting hardness of nano indentations should show a decrease similar to the Brinell hardness, which is not the case for the piston alloys. This rules out the matrix strength as a responsible parameter for the decrease in strength observed after 1h of solution treatment, while emphasizes the importance of the evolution of the 3D architecture of rigid networks.

The relationship between 3D architecture of the alloy and mechanical properties can be analyzed based on the changes of the networks of silicon and aluminides. Silva et al. [91] investigated theoretically the effect of connectivity, expressed by the change of the Euler number in a non-periodic 2D microstructure, on the mechanical properties by removing connections randomly. The calculated strength of the model material decreased more than 35% after removal of 10% of the connections. Furthermore, the strengthening effect of interconnected Si networks in Al-Si alloys was shown by Requena et al. [22]. The importance of stable aluminides for the thermo-mechanical properties after solution treatment was proved by Asghar et al. [34]. The networks of aluminides and the silicon network form together an interpenetrating hybrid network which affects the conservation of interconnectivity and morphological stability of the phases after solution treatment.

Fig. 4.3 shows the interrelation between tensile proof strength, $\sigma_{0.2}$, at 300 and 380°C, volume fraction of aluminides, $V_{\text{aluminides}}$, and solution treatment time in the

investigated alloys. It can be seen that only the 1740 alloy shows a possible dependence of strength with $Vf_{\text{aluminides}}$. Furthermore, the range of volume fraction of aluminides in the piston alloys, i.e. ~8-13vol%, does not seem to affect the strength of the alloys since $\sigma_{0.2}$ changes with solution treatment time independently of $Vf_{\text{aluminides}}$.

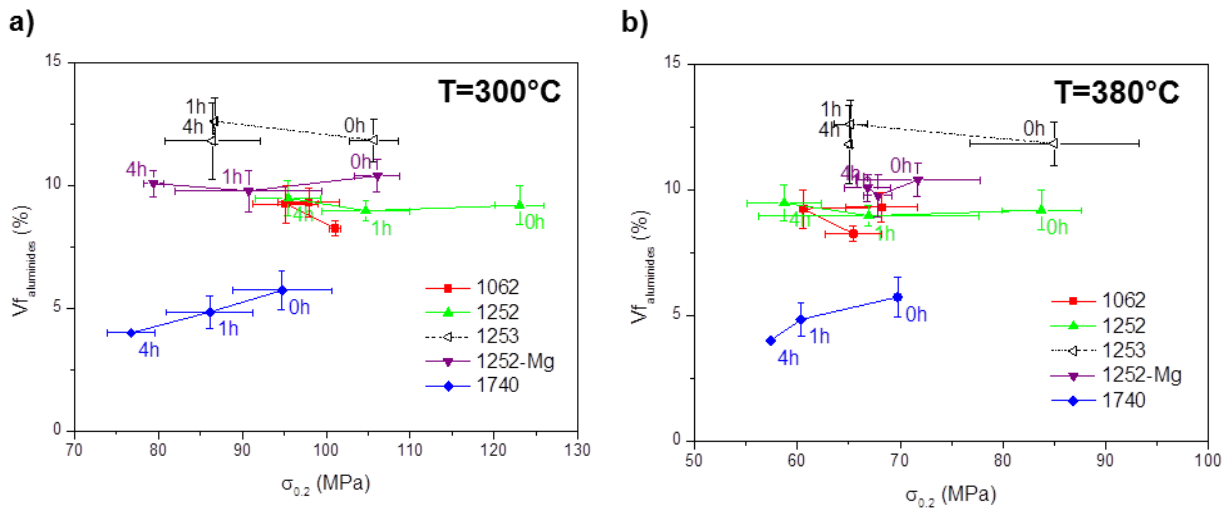


Fig. 4.3: Interrelation between tensile proof strength, $\sigma_{0.2}$, volume fraction of aluminides, $Vf_{\text{aluminides}}$, and solution treatment time at 500°C: a) 300°C, b) 380°C.

The investigated near eutectic alloys 1252, 1253 and 1252-Mg have a stable network of aluminides in terms of volume fraction and interconnectivity (Fig. 4.1). The morphology of the aluminides network derived from the surface curvature distribution is stable after 1h and 4h of solution treatment at 500°C. The contiguity area between the silicon and aluminides is retained after solution treatment in the case of the near eutectic 1252 and 1062 alloys (Tab. 4.3). The results show that morphology and contiguity area of silicon and aluminides are less related to the changes of thermo-mechanical properties after solution treatment.

However, the Euler number of the combined hybrid network changes during solution treatment (Fig. 4.1 and Tab. 4.3). In Fig. 4.4 the loss of connections within the hybrid network, expressed by changes of the specific Euler number, χ_v , indicates that this is a relevant parameter that directly influences the changes of observed thermo-mechanical properties ($\sigma_{0.2}$, $\dot{\epsilon}_{min}$ and cycles to failure) in the first hour of solution treatment for the 1252 piston alloy. In this time, χ_v increases from -7.7×10^{-3} to -6.8×10^{-3} provoking a significant decrease in strength and thermo-mechanical fatigue resistance of the alloy. Between 1h and 4h of solution treatment, there is a further increase of χ_v but does not influence considerably $\sigma_{0.2}$ or thermo-mechanical fatigue resistance. Similarly, the 1062 alloy already has a χ_v 6.3×10^{-3} μm in the 0h condition

that results in thermo-mechanical parameters close to the ones of the 1252 alloy in solution treated condition. This indicates that, for the piston alloys $\chi_v < \sim 7 \times 10^{-3}$ is necessary to produce a strength increase ($\sigma_{0.2}$ and TMF resistance) in comparison to the stabilized alloys after 1h of solution treatment at 500°C. On the other hand, the evolution of strength of the 1740 alloy with solution treatment time is a combination of the changes in the volume fraction of aluminides (Fig. 4.3), the loss of connections within the hybrid Si-aluminides network and by the spheroidization of Si and aluminides.

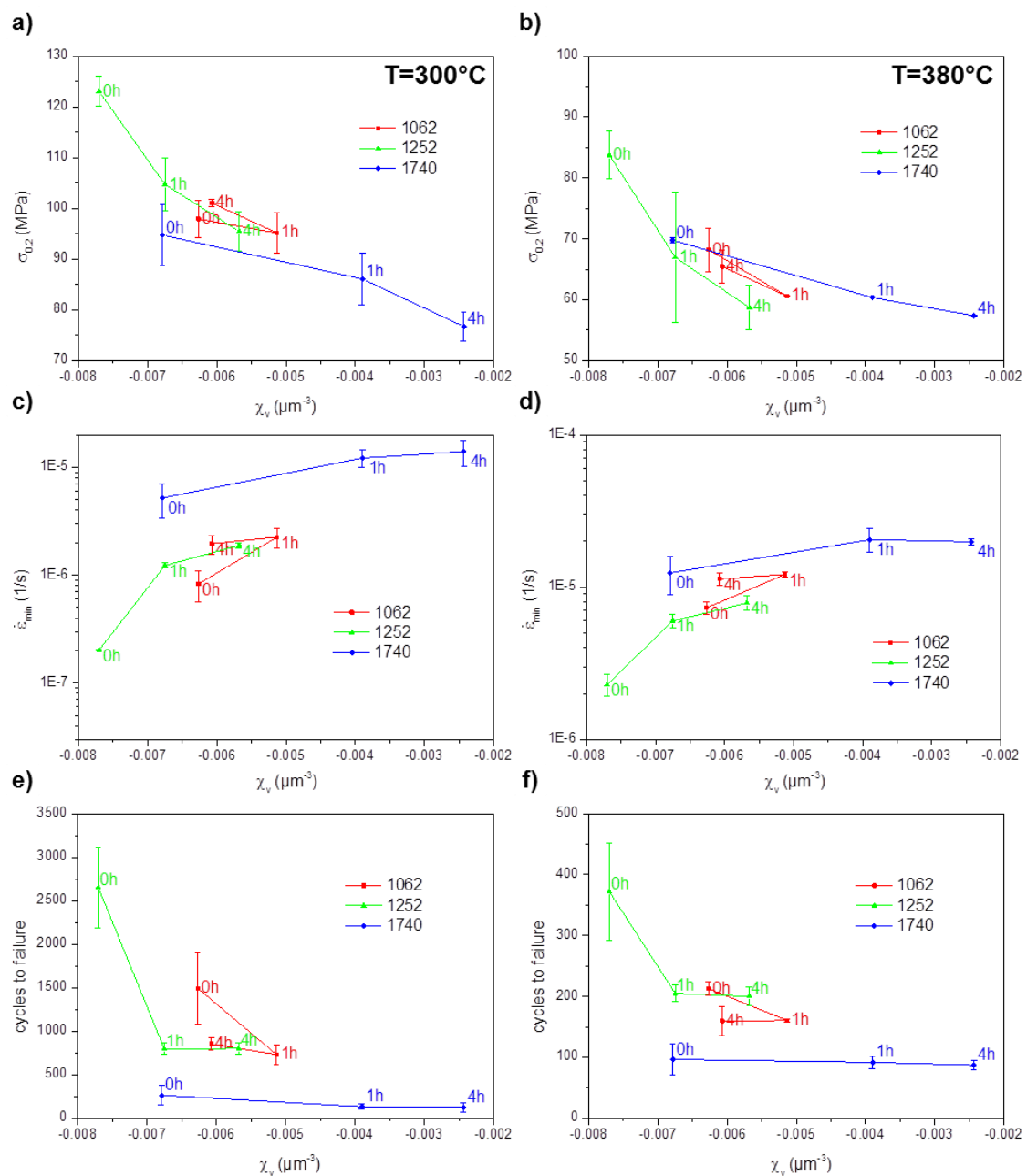


Fig. 4.4: Comparison of mechanical properties as a function of χ_v =specific Euler number of the hybrid network of Si and aluminides: a) $\sigma_{0.2}$ vs. χ_v b) $\dot{\epsilon}_{min}$ vs. χ_v c) cycles to failure vs. χ_v .

5. Conclusions

5.1. Experimental imaging methods

- A 3D serial sectioning method based on the removal of material layers using ion milling was developed. Material removal was controlled using Knoop indentations around the pre-selected region of interest. Voxel sizes of $0.27 \times 0.27 \times 0.38 \mu\text{m}^3$ ($2.98 \times 10^{-2} \mu\text{m}^3$) with a precision of $\pm 0.18 \mu\text{m}$ in z direction were obtained after aligning successive light optical micrographs. Combination with EDX analysis of the region of interest every 10 slices ($\sim 3.8 \mu\text{m}$) was applied to identify the different intermetallic phases and thus reveal their contiguity.
- Synchrotron microtomography was used to study the 3D microstructure of the alloys. Phase contrast allowed resolving primary Si particles and eutectic Si branches $> 1 \mu\text{m}$. A one-distance phase retrieval procedure was applied to improve image quality and further segmentation of the microstructural components. The presence of highly absorbing intermetallics next to eutectic and primary Si results in local contrast variations that hindered a full automatic image segmentation.

5.2. Evolution of the microstructure during solution treatment

The investigated alloys consist of an interconnected hybrid network of Si and aluminides that undergo the following changes during solution treatment at 500°C :

- The morphology of the eutectic silicon is flake-like, while the primary silicon shows particle sizes with diameter $< 25 \mu\text{m}$.
- Light optical micrographs show slight spheroidization of eutectic and primary silicon in all alloys after 1h of solution treatment.
- Qualitative, the shape of the aluminides observed by light optical microscopy of the 1062, 1252, 1253 and 1252-Mg alloys is more stable than in the hypereutectic 1740 reference alloy.
- Deep etching revealed that the hybrid network formed by eutectic Si and aluminides remains highly interconnected after 4h of solution treatment at 500°C .

The following primary intermetallic phases were identified by EDX mapping and correlation with the literature:

- $\text{Al}_7\text{Cu}_4\text{Ni}$ (γ -phase) in the 1062, 1252, 1253 and 1252-Mg alloys.
- $\text{Al}_4\text{Cu}_2\text{Mg}_8\text{Si}_7$ (Q-phase) in the 1062, 1252, 1253 and 1740 alloys. This phase and/or Mg_2Si are the low absorbing phases which show partial dissolution in the 1252 alloy during the first hour of solution treatment as revealed by synchrotron tomography.
- Al_3CuNi (δ -phase) Cu:Ni ratio~1, with some Zr in the 1252, 1253 and 1252-Mg alloys.
- Al_2Cu (θ -phase) in the 1740 alloy.
- Al_9FeNi in the 1062, 1252, 1253 and 1252-Mg alloys
- $\text{Al}_{15}(\text{Me})_3\text{Si}_2$ (Me= Fe, Mn, Ni, Cu) in the 1062, 1252, 1253, 1252-Mg alloys. Zr, Ti and V were detected in this phase in the 1252, 1253 and 1252-Mg alloys.

The volume fraction of aluminides changes correspondingly with the chemical composition of the alloy. The evolution with solution treatment of the 3D architecture of the alloys was investigated by synchrotron microtomography. The non-destructive nature of this technique allowed following univocally the evolution of the 3D microstructure of each alloy. Furthermore, the large coherence of the beam at the ID19 beamline of the ESRF resulted in enough phase contrast to resolve eutectic Si branches $>1\mu\text{m}$.

Changes during solution treatment were discussed in terms of volume fraction, interconnectivity (volume of the largest particle divided by total volume of the phase), surface curvature and specific Euler number of the individual and combined 3D networks of Si and aluminides:

- The volume fraction of aluminides in the 1062, 1252 and 1252-Mg alloys remains constant at $\sim 9.5 \pm 1 \text{ vol}\%$ after solution treatment. The aluminides in the 1253 alloy remain at $\sim 12 \pm 1 \text{ vol}\%$ in all studied conditions.
- Contrarily to the piston alloys, the volume fraction of the hypereutectic 1740 alloy shows a significant decrease from $5.7 \pm 0.8 \text{ vol}\%$ to $4 \pm 0.1 \text{ vol}\%$ of aluminides after 4h of solution treatment.
- The interconnectivity of the aluminides in the 1740 alloy decreases $\sim 21\%$ in the first hour of solution treatment and remains practically constant afterwards.

- The interconnectivity of the aluminides in the 1062, 1252, 1253 and 1252-Mg alloys remain highly maintained after 4h of solution treatment, i.e. 95-98%.
- The surface curvature distribution of the aluminides in the 1062 alloy shows a slight increase of spheroid-like region with large curvatures and a decrease in the number of flat regions during solution treatment.
- A slight broadening of the surface curvature distribution of aluminides in the 1252-Mg alloy after 1h of solution treatment at 500°C.
- The aluminides in the 1252 and 1253 alloys remain with constant surface curvature distribution during solution treatment.
- The morphology of the aluminides in the 1740 alloy exhibits a shift towards spheroid-like shapes combined with a broadening of the surface curvature distribution.
- The surface curvature distribution of the silicon in the 1062 and 1252 alloys shows an increase of pit-like and spheroid-like morphologies during solution treatment. The surface curvatures in the 1740 alloy show the formation of spheroid-like morphologies without an increase of pit-like shapes.
- The evolution of the specific Euler number, χ_v , of the aluminides in the 1252 and 1252-Mg alloys show ~10% increase, from $\sim -7 \times 10^{-3} \mu\text{m}^{-3}$ after 0h at 500°C to $\sim -6 \times 10^{-3} \mu\text{m}^{-3}$ after 1h at 500°C.
- The 1740 alloy exhibits a ~10% increase of χ_v of the aluminides after 1h of solution treatment. Due to the fibrous coral-like morphology of the aluminides (Al₂Cu) χ_v is more negative than for the piston alloys.

The evolution of the Euler number in the silicon network of the 1062, 1252 and 1740 was investigated during solution treatment:

- The specific Euler number, χ_v , of the silicon network shows an increase of more than 33% after 1h of solution treatment for the 1062 and 1252 alloys. This indicates a loss of connections within the silicon network provoked by diffusion-driven spheroidization.

The interface between aluminides and silicon in the 1062, 1252 and 1740 alloys showed the following behavior:

- In the 1062 and 1252 the interface remained stable during solution treatment. These results can be extrapolated to the 1253 and 1252-Mg alloys.

- The interface between aluminides and silicon in the 1740 alloy is significantly reduced to 50% and 25% with respect to the 0h/500°C condition after 1h and 4h of solution treatment, respectively.

5.3. Correlation of thermo-mechanical properties with internal architecture

The strength and thermo-mechanical fatigue resistance decreases with solution treatment time for all alloys. The fully interconnected hybrid network formed by Si and aluminides provides a higher strengthening effect than the structure with lower crosslinking of the network.

- The Brinell hardness after 1h of solution treatment with subsequent overaging up to 500h showed a significant decrease with respect to the non-solution treated condition.
- The results of nano indentations of the matrix of the piston alloys showed that the hardness of the matrix in overaged condition remains constant independently of the solution treatment time. This indicates that the precipitates embedded in the matrix are not responsible for the loss of strength of the alloys after 1h of solution treatment. This emphasizes the role of the 3D architecture of rigid networks on the strength of the investigated alloys.
- The range of the volume fraction of aluminides in the 1062, 1252, 1253 and 1252-mg alloys, i.e. ~8-13vol%, does not seem to affect the strength changes observed with solution treatment time.
- The 1740 alloy showed a dependence of strength with volume fraction of aluminides. This can be correlated to the considerable dissolution of Al₂Cu during solution treatment.
- The loss of connection within the hybrid network of Si and aluminides, expressed by the changes of the specific Euler number, χ_v , indicates that this is a relevant parameter influencing the observed changes of thermo-mechanical behavior.
- In the first hour of solution treatment the specific Euler number, χ_v , increases in the hybrid network of the 1252 alloy from $-7.7 \times 10^{-3} \mu\text{m}^{-3}$ to $-6.8 \times 10^{-3} \mu\text{m}^{-3}$.
- The 1062 alloy has a χ_v of $-6.3 \times 10^{-3} \mu\text{m}^{-3}$ in the 0h condition that results in thermo-mechanical properties similar to the ones of the solution treated 1252 alloy.

- For the piston alloys an χ_v of the hybrid network $< -7 \times 10^{-3} \mu\text{m}^{-3}$ is necessary to induce a strength increase ($\sigma_{0.2}$, σ_{max} and TMF resistance) compared with the solution treated alloys.
- The mechanical properties of the 1740 alloy are governed by the loss of volume fraction of aluminides, the interconnectivity and the loss of connection within the still connected large hybrid Si-aluminides particle and by the spheroidization of Si and aluminides.

6. References

- [1] J. Campbell, Castings 2nd ed., Oxford, U.K.: Butterworth Heinemann, 2003.
- [2] J. R. Davis, "ASM speciality handbook: Aluminium and aluminium alloys," 1993.
- [3] M. Day and A. Hellawell, *Proc. R. soc. A* 305, p. 473, 1968.
- [4] G. Requena, G. Garcés, Z. Asghar, E. Marks, P. Staron and P. Cloetens, "The Effect of the Connectivity of rigid Phases on Strength of Al-Si Alloys," *Advanced Engineering Materials*, pp. 674-684, 2011.
- [5] J. A. Bell and W. C. Winegard, *Nature*, p. 5006:177, 1965.
- [6] Al-Si phase diagram: <http://resource.npl.co.uk/mtdata/phdiagrams/alsi.htm>
- [7] T. Hosch, L. G. England and R. E. Napolitano, "Analysis of the high growth-rate transition in Al-Si eutectic solidification," *J. Mater Sci*, pp. 4892-4899, 2009.
- [8] S. Z. Lu and A. Hellawell, "The mechanism of silicon modification in aluminum-silicon alloys: impurity induced twinning," *Metall Trans A*, pp. 1721-1733, october 1987.
- [9] F. Lasagni, A. Lasagni, E. Marks, C. Holzapfel, F. Mücklich and H. P. Degischer, "Three-dimensional characterization of 'as-cast' and solution-treated AlSi(Sr) alloys by high-resolution FIB tomography," *Acta Materialia* 55, pp. 3875-3882, 2007.
- [10] T. H. Ludwig, E. Schonhøvd Dæhlen, P. L. Schaffer and L. Arnberg, "The effect of Ca and P interaction on the Al-Si eutectic," *Journal of Alloys and Compounds* 586, pp. 180-190, 2014.
- [11] K. Nogita, S. D. McDonald, K. Tsujimoto, K. Yasuda and A. K. Dahle, "Aluminium phosphide as a eutectic grain nucleus in hypoeutectic Al-Si alloys," *Journal of Electron Microscopy*, pp. 361-369, 2004.
- [12] A. Dahle, K. Nogita, S. McDonald, C. Dinnis and L. Liu, "Eutectic modification and microstructure development in Al-Si Alloys," *Materials Science and Engineering A* 413-414, pp. 243-248, 2005.
- [13] J. Asensio-Lozano and B. Suarez-Peña, "Effect of the addition of refiners and/or modifiers on the microstructure of die cast Al-12Si alloys," *Scripta Materialia* 54, pp. 943-947, 2006.

-
- [14] L. Yu, X. Liu, H. Ding and X. Bian, "A new nucleation mechanism of primary Si by peritectic-like coupling of AlP and TiB₂ in near eutectic Al-Si alloy," *Journal of Alloys and Compounds* 432, pp. 156-162, 2007.
- [15] W. Edwards, Microstructural and mechanical property modelling for the processing of Al-Si alloys, Loughborough, 2002.
- [16] S. Liang and R. Schmid-Fetzer, "Phosphorus in Al-Si cast alloys: thermodynamic prediction of the AlP and eutectic (Si) solidification sequence validated by microstructure and nucleation undercooling data," *Acta Materialia*, vol. 72, pp. 41-56, 2014.
- [17] T. O. Mbuya, I. Sinclair, A. J. Moffat and P. Reed, "Analysis of fatigue crack initiation and S-N response of model cast aluminium piston alloys," *Materials Science and Engineering A*, no. 528, pp. 7331-7340, 2011.
- [18] D. L. Zhang, L. H. Zheng and D. H. Stjohn, "Effect of a short solution treatment time on microstructure and mechanical properties of modified Al-7wt.%Si-0.3wt.%Mg alloy," *Journal of Light Metals*, no. 2, pp. 27-36, 2002.
- [19] A. Moffat, Micromechanistic analysis of fatigue in aluminium silicon casting alloys, Southampton, 2007.
- [20] P. Y. Zhu, Q. Y. Liu and T. X. Hou, "Spheroidization of eutectic Silicon in Aluminum-Silicon Alloys," *AFS Transactions*, no. 93, pp. 609-614, 1985.
- [21] H. Röhrig and E. Käpernick, "Über die beim Glühen von Al-Si Legierungen eintretende Gefügeveränderungen," *Aluminium*, no. 23, pp. 235-239, 1941.
- [22] G. Requena, G. Garcés, M. Rodríguez, T. Pirling and P. Cloetens, *Advanced Engineering Materials*, no. 11, p. 1007, 2009.
- [23] E. Werner, "Thermal shape instabilities of lamellar structures," *Zeitschrift für Metallkunde*, no. 81, pp. 790-798, 1990.
- [24] S. Manasijevic, R. Radisa, S. Markovic, Z. Acimovic-Pavlovic and K. Raic, "Thermal analysis and microscopic characterization of the piston alloy AlSi13Cu4Ni2Mg," *Intermetallics* 19, pp. 486-492, 2011.
- [25] A. Farkoosh, M. Javidani, M. Hoseini, D. Larouche and M. Pegguleryuz, "Phase formation in as-solidified and heat-treated Al-Si-Cu-Mg-Ni alloys: Thermodynamic assessment and experimental investigation for alloy design," *Journal of Alloys and Compounds* 551, pp. 596-606, 2013.

-
- [26] V. Zolotarevsky, N. Belov and M. Glazoff, *Casting Aluminum Alloys*, Elsevier Science & Technology, 2007.
- [27] C. Chen, G. West and R. Thomson, "Characterisation of intermetallic phases in multicomponent Al-Si casting alloys for engineering applications," *Materials Science Forum*, no. 519-521, pp. 359-364, 2006.
- [28] R. Gholizadeh and S. G. Shabestari, "Investigation of the effects of Ni, Fe and Mn on the formation of complex intermetallic compounds in Al-Si-Cu-Mg-Ni," *Metallurgical and Materials Transactions A*, no. 42A, pp. 3447-3458, 2011.
- [29] C. Chen and R. Thomson, "The combined use of EBSD and EDX analyses for the identification of complex intermetallic phases in multicomponent Al-Si alloys," *Journal of Alloys and Compounds*, no. 490, pp. 293-300, 2010.
- [30] M.V. Kral, H.R. McIntyre, M.J. Smillie, "Identification of intermetallic phases in a eutectic Al-Si casting alloy using electron backscatter diffraction pattern analysis," *Scripta Materialia*, no.51, pp. 215-219, 2004.
- [31] N. A. Belov, D. G. Eskin and N. N. Avxentieva, "Constituent phase diagrams of the Al-Cu-Fe-Mg-Ni-Si system and their application to the analysis of aluminium piston alloys," *Acta Materialia*, no. 53, pp. 4709-4722, 2005.
- [32] Z. Asghar, G. Requena and E. Boller, "3D interpenetrating hybrid network of rigid phases in an AlSi10Cu5NiFe piston alloy," *Praktische Metallographie*, no. 47, pp. 471-486, 2010.
- [33] Z. Asghar, G. Requena and F. Kubel, "The role of Ni and Fe aluminides on the elevated temperature strength of an AlSi12 alloy," *Materials Science and Engineering A*, no. 527, pp. 5691-5698, 2010.
- [34] Z. Asghar, G. Requena and E. Boller, "Three-dimensional rigid multiphase networks providing high-temperature strength to cast AlSi10Cu5Ni1-2 piston alloys," *Acta Materialia*, no. 59, pp. 6420-6432, 2011.
- [35] N. Belov, A. Alabin and I. Matveeva, "Optimization of phase composition of Al-Cu-Mn-Zr-Sc alloys for rolled products without requirement for solution treatment and quenching," *Journal of Alloys and Compounds*, no. 583, pp. 206-2013, 2014.
- [36] K. Knipling, D. Seidman and D. Dunand, "Ambient- and high-temperature mechanical properties of isochronally aged Al-0.06Sc, Al-0.06Zr and Al-0.06Sc-0.06Zr(at%) alloys," *Acta Materialia*, no. 59, pp. 943-954, 2011.

-
- [37] M. S. Zedalis and M. E. Fine, "Precipitation and oswald ripening in dilute Al Base-Zr-V alloys," *Metallurgical Trans A*, no. 17, pp. 2187-2198, 1986.
- [38] K. E. Knipling, D. C. Dunand and D. N. Seidman, "Precipitation evolution in Al-Zr and Al-Zr-Ti alloys during isothermal aging at 375-425°C," *Acta Materialia*, no. 56, pp. 114-127, 2008.
- [39] N. Vo, D. Dunand and D. Seidman, "Improving aging and creep resistance in a dilute Al-Sc alloy by microalloying with Si, Zr and Er," *Acta Materialia*, no. 63, pp. 73-85, 2014.
- [40] C. Booth-Morrison, Z. Mao, M. Diaz, D. Dunand, C. Wolverton and D. Seidman, "Role of silicon in accelerating the nucleation of Al₃(Sc,Zr) precipitates in dilute Al-Sc-Zr alloys," *Acta Materialia*, no. 60, pp. 470-4752, 2012.
- [41] W. Kasprzak, B. S. Amirkhiz and M. Niewczas, "Structure and properties of cast Al-Si based alloy with Zr-V-Ti additions and its evaluation of high temperature performance," *Journal of Alloys and Compounds*, no. 595, pp. 67-79, 2014.
- [42] S. K. Shaha, F. Czerwinski, W. Kasprzak and D. L. Chen, "Work hardening and texture during compression deformation of the Al-Si-Cu-Mg alloy modified with V, Zr and Ti," *Journal of Alloys and Compounds*, no. 593, pp. 290-299, 2014.
- [43] H. A. Elhadari, H. A. Patel, D. L. Chen and W. Kasprzak, "Tensile and fatigue properties of a cast aluminium alloy with Ti, Zr and V additions," *Materials Science and Engineering A*, no. 528, pp. 8128-8138, 2011.
- [44] A. M. Mohamed, F. H. Samuel and S. Al kahtani, "Microstructure, tensile properties and fracture behavior of high temperature Al-Si-Mg-Cu cast alloy," *Materials Science and Engineering A*, no. 577, pp. 64-72, 2013.
- [45] J. Hernandez-Sandoval, G. H. Garza-Elizondo, A. M. Samuel, S. Valtierra and F. H. Samuel, "The ambient and high temperature deformation behavior of Al-Si-Cu-Mg alloy with minor Ti, Zr, Ni additions," *Materials and Design*, no. 58, pp. 89-101, 2014.
- [46] K. E. Knipling, D. C. Dunand and D. N. Seidman, "Precipitation evolution in Al-Zr and Al-Zr-Ti alloys during aging at 450-600°C," *Acta Materialia*, no. 56, pp. 1182-1195, 2008.

-
- [47] E. Ogris, Development of Al-Si-Mg Alloys for Semi-solid processing and silicon spheroidization treatment (SST) for Al-Si cast alloys, Zürich: Shaker Verlag, 2002.
- [48] A. Dlouhy, N. Merk and G. Eggeler, *Acta mater*, no. 41, pp. 3245-3256, 1993.
- [49] T. Bidlingmeier, D. Vogt and A. Wanner, *Werkstoffe und Werkstoffverbunde*, p. 245, 1996.
- [50] G. Requena and H. P. Degischer, " Creep behaviour of unreinforced and short fibre reinforced AlSi12CuMgNi piston alloys," *Materials Science and Engineering A*, no. 420, pp. 265-275, 2006.
- [51] G. Requena, G. Gárces, S. Danko, T. Pirling and P. Cloetens, "3D Architecture and Load Partition in Eutectic Al-Si Alloys," *Adv. Eng. Mater.*, 11, no. 12, pp. 1007-1014, 2009.
- [52] G. Requena, G. Gárces , S. Danko, T. Pirling and E. Boller, "The effect of eutectic Si on the strength of short-fibre-reinforced Al," *Acta Materialia*, no. 57, pp. 3199-3210, 2009.
- [53] H. Winand, A. Whitehouse and P. Whitters, *Mat.Sci.Ang. A*, no. 284, p. 103, 2000.
- [54] F. Lasagni, J. A. Acuña and H. P. Degischer, "Interpenetrating Hybrid Reinforcement in Al₂O₃ short fiber preforms infiltrated by Al-Si alloys," *Metallurgical and Materials Transactions A*, no. 39, pp. 1466-1474, 2008.
- [55] C. L. Chen, A. Richter and R. C. Thomson, "Investigation of mechanical properties of intermetallic phases in multi-component Al-Si alloys using hot-stage nanoindentation," *Intermetallics*, pp. 1-10, 2009.
- [56] C. L. Chen, A. Richter and R. C. Thomson, "Mechanical properties of intermetallic phases in multi-component Al-Si alloys using nanoindentation," *Intermetallics*, no. 17, pp. 634-641, 2009.
- [57] P. K. Rohatgi, R. C. Sharma and K. V. Praphakar, "Microstructure and mechanical properties of unidirectionally solidified Al-Si-Ni ternary eutectic," *Metallurgical Transaction A*, no. 6, pp. 569-575, 1975.
- [58] F. Stadler, H. Antrekowitsch, W. Fagner, H. Kaufmann and P. J. Uggowitzer, "The effect of Ni on the high-temperature strength of Al-Si cast alloys," *Materials Science Forum*, no. 690, pp. 274-277, 2011.

-
- [59] Y. H. Cho, Y. R. Im, S. W. Kwon and H. C. Lee, "The effect of alloying elements on the microstructure and mechanical properties of Al-12Si cast alloys," *Materials Science Forum*, no. 426-432, pp. 339-344, 2003.
- [60] Y. Li, Y. Yang, Y. Wu, L. Wang and X. Liu, "Quantitative comparison of three Ni-containing phases to the elevated-temperature properties of Al-Si piston alloys," *Materials Science and Engineering A*, no. 527, p. 7132-7137, 2010.
- [61] Y. Yang, K. Yu, Y. Li, D. Zhao and X. Liu, "Evolution of nickel-rich phases in Al-Si-Cu-Ni-Mg piston alloys with different Cu additions," *Materials and Design*, vol. 33, pp. 220-225, 2012.
- [62] A. Tewari and A. M. Gokhale, "Application of three dimensional digital image processing for reconstruction of microstructural volume from serial sections," *Materials Characterization*, no. 44, pp. 259-269, 2000.
- [63] H. Singh, A. M. Gokhale, A. Tewari, S. Zhang and Y. Mao, "Three dimensional visualization and quantitative characterization of primary silicon particles in an Al-Si base alloy," *Scripta Materialia*, no. 61, pp. 441-444, 2009.
- [64] M. V. Kral and G. Spanos, "Three-dimensional analysis of proeutectic cementite precipitates," *Acta Materialia*, no. 47, pp. 711-724, 1999.
- [65] N. C. W. Kuijpers, J. Tirel, D. N. Hanlon and S. van der Zwaag, "Quantification of the evolution of the 3D intermetallic structure in a 6005A aluminium alloy during a homogenisation treatment," *Materials Characterization*, no. 48, pp. 379-392, 2002.
- [66] N. Chawla and K. K. Chawla, "Microstructure-based modeling of the deformation behavior of particle reinforced metal matrix composites," *Journal of Materials Science*, no. 41, pp. 913-925, 2006.
- [67] D. Tolnai, 3D characterization of microstructure evolution of cast AlMgSi alloys by synchrotron tomography, Wien: TU Wien, 2011.
- [68] N. Limodin, A. El Bartali, L. Wang, J. Lachambre, J. Y. Buffiere and E. Charkaluk, "Application of X-ray microtomography to study the influence of the casting microstructure upon the tensile behaviour of an Al-Si alloy," *Nuclear Instruments and Methods in Physics Research B*, 2013.
- [69] P. J. Withers, *Materials today*, no. 10, pp. 26-34, 2007.

-
- [70] T. Thüring, T. Zhou, U. Lundström, A. Burvall, S. Rutishauser, C. David, H. M. Hertz and M. Stampanoni, "X-ray grating interferometry with a liquid-metal-jet source," *Applied Physics Letters*, no. 103, 2013.
- [71] O. Hemberg, M. Otendal and H. M. Hertz, "Liquid-metal-jet anode x-ray tube," *Optical Engineering*, no. 43, pp. 1682-1688, 2004.
- [72] E. Maire and P. J. Withers, "Quantitative X-ray tomography," *International Materials Reviews*, no. 59, pp. 1-43, 2014.
- [73] S.M. Khopkar, "Basic Concepts of Analytical Chemistry," *New Age International, 1998*
- [74] P. Cloetens, R. Baret, J. Baruchel, J. P. Guigay and M. Schlenker, "Phase objects in synchrotron radiation hard X-ray imaging," *J.Phys. D: Appl.Phys*, no. 29, pp. 133-146, 1996.
- [75] S. C. Mayo, A. W. Stevenson and S. W. Wilkins, "In-line phase contrast X-ray imaging and tomography for materials science," *Materials*, no. 5, pp. 937-965, 2012.
- [76] D. Paganin, S. C. Mayo, T. E. Gureyev, P. R. Miller and S. W. Wilkins, "Simultaneous phase and amplitude extraction from a single defocused image of a homogenous object," *Journal Microsc.*, no. 206, pp. 33-40, 2002.
- [77] S. Sanchez, P. E. Ahlberg, K. M. Trinajstic, A. Mirone and P. Tafforeau, "Three dimensional synchrotron virtual paleohistology: a new insight into the world of fossil bone," *Microsc. Microanal.*, no. 18, pp. 1095-1105, 2012.
- [78] T. Weitkamp, D. Haas, D. Wegrzynek and A. Rack, "ANKAphase: software for single-distance phase retrieval from," *J. Synchrotron Rad.*, no. 18, p. 617-629, 2011.
- [79] R. S. Bradley, A. McNeil and P. J. Withers, "An examination of phase retrieval algorithms as applied to phase contrast tomography using laboratory sources," *Proc. SPIE*, vol. VII, no. 7804, 2010.
- [80] P. Thévenaz, "http://fiji.sc/StackReg," 2010. [Online]. Available: <http://bigwww.epfl.ch/thevenaz/stackreg/>.
- [81] J. C. Labiche, O. Mathon, S. Pascarelli, M. A. Newton, G. G. Ferre, C. Curfs, G. Vaughan, A. Homs and D. Fernandez Carreiras, "The fast readout low noise camera as a versatile x-ray detector for time resolved dispersive extended x-ray absorption fine structure and diffraction studies of dynamic

-
- problems in materials science, chemistry, and catalysis," *Review of Scientific Instruments*, no. 78, pp. 1-11, 2007.
- [82] G. Holst, "Noise in imaging: The good , the bad and the right," *Photonics Spectra*, December 2006.
- [83] P.-A. Douissard, A. Cecilia, X. Rochet, X. Chapel, T. Martin, T. V. D. Kamp, L. Helfen, T. Baumbach, L. Luquot, X. Xiao, J. Meinhardt, and A. Rack, "A versatile indirect detector design for hard X-ray microimaging," *J. Instrum.*, vol. 7, no. Issue 9, pp. 09016, 2012.
- [84] M. Boin and A. Haibel, "Compensation of ring artefacts in synchrotron tomographic images," *Optics Express*, no. 14, pp. 12071-12075, 2006.
- [85] H. C. Andrews and B. R. Hunt, "Digital image restoration," *Prentice-Hall Signal Processing Series*, 1977.
- [86] M. Sanchez del Rio and R. Dejus, "<http://www.esrf.eu/Instrumentation/software/data-analysis/xop2.3/download>," [Online]. Available: <http://ftp.esrf.eu/pub/scisoft/xop2.3/>
- [87] Principal curvature: [Online], Wikipedia
- [88] H.-J. Vogel, "Topological Characterization of Porous Media," *Morphology of Condensed Matter*, Lecture Notes in Physics Volume 600, pp 75-92, 2002
- [89] J. Ohser, F. Mücklich, "Statistical Analysis of Microstructures in Material Science," John Wiley & Sons, Ltd, 2000
- [90] A. Velichko, C. Holzapfel, A. Siefers, K. Schladitz, F. Mücklich, "Unambiguous classification of complex microstructures by their three-dimensional parameters applied to graphite in cast iron ," *Acta Materialia* 56, pp.1981-1990, 2008
- [91] M.J. Silva, L.J. Gibson, "The effect of non-periodic microstructure and defects on the compressive strength of two-dimensional cellular solids," *Int.J.Mech.Sci.*, vol. 39, no.5, pp.549-563, 1997